

Synthesis and Characterization of a Dicobalt Catalyst for the Silylation of Dinitrogen

A Thesis
SUBMITTED TO THE FACULTY OF
UNIVERSITY OF MINNESOTA
BY

Randall Bernard Siedschlag

IN PARTIAL FULFILLMENT OF THE REQUIREMENTS
FOR THE DEGREE OF
DOCTOR OF PHILOSOPHY

Connie Lu, Adviser

June, 2016

© Randall Bernard Siedschlag 2016

Acknowledgements

A big thank you to everyone I have encountered during my time at the University of Minnesota. A thank you to my high school chemistry teacher, Josh Knecht, for influencing me and my undergraduate research adviser, Jason D'Acchioli, for introducing me to inorganic chemistry and research. Thanks to Connie for accepting me into her lab, her help with attaining an NSF fellowship, and her constant guidance through the hurdles of graduate school. Thank you Lu lab members, past and present, for making graduate school less stressful – for the most part. Thanks to all of my collaborators, Eckhard, Andreas, Laura G., and Vic. A special thanks to: Kostas and Varinia for all of their computational work, the Tonks lab for the use of their Endeavor reactor, the Ellis lab for solvents and discussions, the Tolman lab for the use of their GC/MS, and finally Bill Tolman, for initially convincing me to pursue inorganic chemistry in graduate school.

Thank you to my committee: Kent, for getting me started at Minnesota the summer of 2011, John E. for insightful chemistry lectures and discussions, and John L. for use of the EPR instrument. Thank you to my parents and in-laws for their support and laughter throughout everything we have dealt with. Most of all, I owe a plethora of thanks to my wife, Amanda, who has been with me through thick and thin. She is my rock and without her, this would not have been possible.

Dedication

This thesis is dedicated to my wife, Amanda. Without her amazing love and support,
none of this would have been possible.

Table of Contents

List of Tables	vi
List of Figures	viii
List of Schemes.....	xix
List of Symbols and Abbreviations.....	xx
<i>Chapter 1</i> Dinitrogen Activation and Reduction: From Biology to Biomimetic Model	
Complexes	1
1.1 Motivation.....	2
1.1.1 Understanding Dinitrogen Activation.....	2
1.2 Biological N ₂ Fixation	6
1.3 Synthetic N ₂ Fixation Models	16
1.3.1 Molybdenum Systems.....	16
1.4 Cobalt N ₂ Compounds	26
1.5 Bimetallic Cooperativity	30
1.6 Thesis Scope	37
<i>Chapter 2</i> Synthesis and Characterization of Dicobalt Compounds	
2.1 Overview	39
2.2 Introduction.....	40
2.3 Results and Discussion	46
2.3.1 Synthesis and ¹ H NMR Spectroscopy.....	46
2.3.2 Solid-state Structures	50
2.3.3 Vis-NIR Data	53
2.3.4 Magnetic Measurements and EPR.....	58

2.3.5	Infrared Data	68
2.3.6	Cyclic Voltammetry	72
2.3.7	Theoretical Calculations	75
2.4	Conclusions	78
2.5	Experimental Procedures	79
2.5.1	General Considerations	79
2.5.2	Synthetic Procedures	79
2.5.3	X-ray Crystallographic Data Collection and Refinement of Structures ...	81
2.5.4	Physical Measurements	82
2.5.5	Computational Details	82
<i>Chapter 3</i>	<i>Catalytic Silylation of Dinitrogen Using Cobalt-Containing Catalysts</i>	<i>84</i>
3.1	Overview	85
3.2	Introduction	86
3.3	Results and Discussion	88
3.3.1	Catalytic Silylation of Dinitrogen	88
3.3.2	Elucidating the Active Catalytic Species	93
3.3.3	Theoretical Calculations and Mechanistic Insight	102
3.3.4	Electrocatalytic Dinitrogen Silylation	109
3.4	Conclusions	110
3.5	Experimental	111
3.5.1	General Considerations and Physical Methods	111
3.5.2	Catalytic Procedures	112
3.5.3	Computational Methods	116

<i>Chapter 4</i>	Synthesis and Characterization of Postulated Intermediates in Dinitrogen	
	Silylation	117
4.1	Overview.....	118
4.2	Introduction.....	119
4.3	Results and Discussion	127
4.3.1	Synthesis and ¹ H NMR Spectroscopy.....	127
4.3.2	Solid-state Structure of a Dicobalt Imido	132
4.3.3	Vis-NIR Data	136
4.3.4	EPR Data and Electronic Structure.....	143
4.3.5	Infrared Data	149
4.3.6	Cyclic Voltammetry.....	151
4.3.7	Catalytic Activity of the Silyldiazenido Intermediate	153
4.3.8	Preliminary Reactivity Scope of the Dicobalt Imido	154
4.4	Conclusions.....	157
4.5	Experimental	158
4.5.1	General Considerations.....	158
4.5.2	Synthetic Procedures.....	158
4.5.3	X-ray Crystallographic Data Collection and Refinement of Structure... ..	160
4.5.4	Physical Measurements.....	161
4.5.5	Computational Details	161
	Bibliography	162
	Appendix.....	176

List of Tables

Table 1.4.1 Comparison of Co(N ₂) compounds activation of N ₂ .	28
Table 2.3.1 Bond Metrics of 1-Br , 2 , and 3 .	51
Table 2.3.2 Crystallographic Details for 1-Br , 2 , and 3 .	52
Table 2.3.3 Vis and NIR transitions for 1-Cl , 2 , 3 , and 4 .	54
Table 2.3.4 TD-DFT (B3LYP, def2-TZVP) results with associated transitions	57
Table 2.3.5 Comparison of trigonal M-Co-N ₂ complexes	71
Table 2.3.6 Summary of Electrochemical data for 2 under N ₂ and Ar.	75
Table 3.3.1 Reaction of N ₂ (1 atm), Me ₃ SiCl (10.5 mmol), and KC ₈ (10.4 mmol) using different cobalt precatalysts (5.27 μmol, 0.13 mM) in 40 mL THF at 299 K for 12 hr.	91
Table 3.3.2 Variation of reductants or additives with complex 1 under standard catalytic conditions (see Table 3.3.1).	93
Table 3.3.3 High pressure N ₂ runs at 0.05% catalyst loading in 30 mL of THF	99
Table 3.3.4 Energy profile of the catalytic mechanism mediated by A with calculated intermediates and transition states for AlCo and CoCo For each structure, ΔG values relative to the reactants: A , N ₂ and six TMS radicals are indicated. Reaction barriers (ΔG [‡]) are shown in red within parenthesis. ΔG and ΔG [‡] are reported in kcal mol ⁻¹ .	107
Table 4.3.1 Comparison of structural metrics of 2 with LCo ₂ and LCo ₂ Br.	134
Table 4.3.2 Comparison of Co-NR compounds (R = alkyl)	134
Table 4.3.3 Crystallographic details for 2 .	135

Table 4.3.4 Vis transition seen in compounds 1-SiPh₃ , 1-SiPh₂Me , 1-SiPhMe₂ , and 1-SiMe₃	138
Table 4.3.5 TD-DFT Excitation Energies and their MO Interpretations for 1-SiPh₃ , 1-SiPh₂Me , 1-SiPhMe₂ , and 1-SiMe₃ anionic compounds (d ¹⁶) at the PBE level of theory.	141
Table 4.3.6 Calculated relative free energies of various possible spin states at the PBE and M06-L levels of theory. Bolded values are th lowest energy spin states.	145
Table 4.3.7 Comparisons of silyldiazenido stretching frequencies	150
Table A3.3.1 Results of Triplicate Runs for Each Compound for Catalytic N ₂ Silylation	177
Table A3.3.2. Spin density isosurfaces (0.02 a.u.) of intermediates and transition states. Blue and green density corresponds to alpha and beta spin, respectively. In all cases, Co _N (II) is $S = 3/2$	178
Table A3.3.3 Calculated Bond Lengths (Å), Angles (deg.), and N ₁ -N ₂ bond stretching frequencies (cm ⁻¹) through the reaction coordinate (path I). All species are in their anionic form, except neutral Co ₂ L and free N ₂	179
Table A3.5.1 A DFT benchmark study to compare various functionals and basis sets for [(N ₂)Co ₂ L] ⁻ ($S = 1$). Differences between the Co-Co, N-N, and Co-L (ligand) bond distances (Å) in the crystal structure and the various optimized geometries are given. The $\langle S^2 \rangle$ values are also reported.....	179

List of Figures

Figure 1.1.1 Example of dinitrogen bonding modes to transition metal centers.	2
Figure 1.1.2 Representation of dinitrogen activation across the periodic table. Taken from reference 4.	3
Figure 1.1.3 Schematic diagram seen in an industrial Haber-Bosch facility. Taken from reference 5d.	5
Figure 1.2.1 Protein crystal structure of Mo-dependent nitrogenase. Tan is the Fe protein, Green is the alpha subunit of the MoFe protein, Light blue is the beta subunit of the MoFe protein. Ball and stick models of the F-cluster, P cluster and FeMo-cofactor. PDB: 2AKF. Taken from reference 10.	7
Figure 1.2.2 Zoom of the FeMo-cofactor showing the location of two key residues to N ₂ reduction. Taken from reference 10.	9
Figure 1.2.3 Lowe-Thornely model to dinitrogen reduction. Adapted from reference 10.	10
Figure 1.2.4 Proposed structure of the E ₄ state of the FeMo-cofactor. Taken from reference 10.	11
Figure 1.2.5 Depiction of the electron transfer to the MoFe protein from A) Fe protein in nitrogenase B) CdS photoexcited nanorod. Taken from reference 19.	12
Figure 1.2.6 General schemes for catalytic dinitrogen functionalization	14
Figure 1.2.7 Q-band CW EPR spectrum of α -70Val \rightarrow Ala, α -195His \rightarrow Gln MoFe protein in resting state (S = 3/2) and trapped during turnover with ¹⁴ N ₂ H ₄ . Taken from reference 26.	15

Figure 1.3.1 Proposed mechanism for dinitrogen reduction using $P_4Mo(N_2)_2$ (center). Electrons are derived from Mo.	17
Figure 1.3.2 Structure of $HIPTN_3NMo(N_2)$ (Left) and spacefill of $HIPTN_3NMo(NH_3)$ (Right) (Blue = N, Yellow = Mo). Taken from ref 21.	18
Figure 1.3.3 Proposed intermediates in the reduction of dinitrogen at a $[HIPTN_3N]Mo$ (Mo) center through the stepwise addition of protons and electrons. Brackets denote nonisolated species Taken from reference 21.	19
Figure 1.3.4 PNP and PPP molybdenum pincer compounds used for ammonia catalysis. Adapted from reference 31.	20
Figure 1.3.5 Tetraphosphine iron compounds first seen to reduce dinitrogen to ammonia. Adapted from reference 35.	22
Figure 1.3.6 Top: Scheme depicting the formation of the tetrairon nitride from N_2 . Bottom: X-ray crystal structure 50% probability ellipsoids of the tetrairon nitride. Taken from reference 37a.	23
Figure 1.3.7 Left: Structure of $(N_2)FeP_3^E$ catalyst with equiv of NH_3 produced. Right: Qualitative comparison of $(N_2)FeP_3^E$ system compared to a proposed N_2 species in the FeMo-cofactor. Taken from ref 38.	24
Figure 1.3.8 Potential catalytic scenarios for ammonia catalysis using FeP_3^B . Blue compounds have been characterized. Dashed lines are hypothesized to not be feasible under catalytic conditions ($-78^\circ C$) although the crossover from $N-NH_2$ to NH_2-NH_2 is observed using FeP_3^{Si} and is believed to be a key intermediate in catalysis. Taken from ref 23.	25

Figure 1.4.3 Comparison of phosphine orbitals of Thomas and Lu ligands. Taken from ref 43b.....	29
Figure 1.5.1 Comparison of single site oxidative addition (left) and bimetallic cooperative oxidative addition (right). Taken from reference 53.....	31
Figure 1.5.2 Proposed catalytic cycle for hydrazine disproportionation using (THF) ₃ [NP] ₃ TiCo(N ₂) as the catalyst. Taken from reference 411.....	32
Figure 1.5.3 Depiction of the stoichiometric (top) aryl C-H borylation and catalytic (bottom) aryl C-H borylation using a Cu-Fe catalyst (M = Cu, L = IMes). Taken from reference 53.....	34
Figure 1.5.4 Example of how nucleophilicity changes product distribution. Taken from reference 47.....	35
Figure 1.5.5 Hypothetical mechanism for a) catalyst activation b) CO ₂ hydroboration c) CO ₂ – assisted formate decarbonylation. Taken from reference 53.....	35
Figure 2.2.1 Select examples of bimetallic cobalt compounds.....	41
Figure 2.2.2 Qualitative MO diagram for Co ₂ in a tetragonal (left) and trigonal (right) framework.....	42
Figure 2.2.3 Examples of dicobalt complexes in a localized ligand framework.....	44
Figure 2.2.4 Frontier molecular orbital diagram of (A) Thomas’s Co(I)Co(I) and (B) Co(II)Co(I) [BP86/LANL2TZ(F)/6-311+G(d)/D95V] Taken from ref 68.	45
Figure 2.2.5 Ligand scaffolds promoting metal-metal bonds in the Lu group.....	45
Figure 2.3.1 ¹ H NMR Spectrum (C ₆ D ₆ , 300 MHz) of 1-Cl	47
Figure 2.3.2 ¹ H NMR spectrum (300 MHz, d ⁸ -THF) of 2 in N ₂ (bottom) and Ar (top) *= THF, \$= benzene.....	48

Figure 2.3.3 ^1H NMR spectrum (300 MHz, d^8 -THF) of 3	49
Figure 2.3.4 ^1H NMR spectrum (300 MHz, d^8 -THF) of 4	50
Figure 2.3.5 X-ray crystal structures of 1-Br , 2 , and 3	51
Figure 2.3.6 Vis spectra ($\epsilon \times 10^4$ vs nm) at 293 K in THF of 1-Cl (purple, solid line), 2 (brown, dotted line), 3 (gold, long-dashed line) and 4 (red, short-dashed line) in THF. Insert: NIR spectra (ϵ vs nm) of 1-Cl (purple, solid line), 2 (brown, dotted line), 3 (gold, long-dashed line) and 4 (red, short-dashed line).....	54
Figure 2.3.7 TD-DFT result showing the vis transition in 3 (545 nm).....	57
Figure 2.3.8 Top: Temperature dependence of the effective magnetic moment, μ_{eff} , of 2 (1 Tesla, 2–290 K). The red line represents the spin-Hamiltonian simulation using a two-spin model with $S_1 = 3/2$, $S_2 = 1$, $g_1 = g_2 = 2.066$, $J_{12} = + 60.00 \text{ cm}^{-1}$, $D_1 = D_2 =$ 12.00 cm^{-1} with a correction for the underlying diamagnetism of -422.2×10^{-6} cm^3/mol	60
Figure 2.3.9 X-Band EPR spectrum (dX''/dB) of 2 in an N_2 atmosphere in a toluene glass (21 K). The solid line is the experimental spectrum. The dashed red line is the simulated spectrum with anisotropic g values $g = 2.14, 2.14$ and 1.898 . The spectrum is modeled with $A_{xx} = A_{yy} = 29.3126$ and $A_{zz} = 170 \times 10^{-4} \text{ cm}^{-1}$ and line widths of $W_x = W_y = 50$ and $W_z = 80$	61
Figure 2.3.10 X-Band EPR spectrum (dX''/dB) of 2 under an argon atmosphere in a toluene glass (21 K). The solid line is the experimental spectrum. The dashed red line is the simulated $S = 5/2$ spectrum (80%) with $g_{\text{eff}} = 6.5, 6.5$, and 1.80 and $W_x = W_y = 220$, $W_z = 300 \text{ G}$ and $A_{zz} = 80 \times 10^{-4} \text{ cm}^{-1}$. The spectrum is also modeled	

with a $S = \frac{1}{2}$ (20%) spectrum with $g_{\text{eff}} = 2.175, 2.175$ and 1.898 and $W_x=W_y= 50$, $W_z= 80$ Gauss and $A_{xx}=A_{yy}= 26.3056$ and $A_{zz}= 170 \times 10^{-4} \text{ cm}^{-1}$	61
Figure 2.3.11 Four potential qualitative molecular orbital diagrams explaining the electronic phenomena occurring when dinitrogen binds to 2 . Top: Covalent interactions	62
Figure 2.3.12 Top: Temperature dependence of the effective magnetic moment, μ_{eff} , of 3 [K(2,2,2-cryptand)]Co ₂ (N ₂)L (diamonds, 1 Tesla, 2–290 K). The red line represents the spin-Hamiltonian simulation with $S_{\text{tot}}= 1$, $g = 2.138$, zero-field splitting, $D =$ 42.432 cm^{-1} , with a correction for the underlying diamagnetism of -698.6×10^{-6} cm^3/mol	64
Figure 2.3.13 Calculated molecular orbital diagram of 3 (DFT, M06L)	65
Figure 2.3.14 X-Band EPR spectrum (dX''/dB) of 4 in THF glass (21K) shown as solid black line. The dashed red line is the simulated $S= 3/2$ spectrum with anisotropic g values $g = 2.1578, 2.1578$, and 1.898 and line widths of $W_x = 17$, $W_y = 50$, $W_z = 8$ G and z-hyperfine tensor for Co ($I = 7/2$) of $A_{zz} = 70 \times 10^{-4} \text{ cm}^{-1}$. * baseline impurity in cavity	66
Figure 2.3.15 Qualitative orbital diagrams showing anti-ferromagnetic coupling in 3 (left) and two potential reduction sites in 4 (right).	67
Figure 2.3.16 Correlation of dinitrogen stretching frequency to N-N bond strength. Blue circles represent mononuclear dinitrogen species and green squares represent dinuclear dinitrogen species. Taken from reference 4.	68

Figure 2.3.17 Solid state (KBr pellet) IR spectrum of the N ₂ region (1600 cm ⁻¹ to 2300 cm ⁻¹) for 2 (brown), 3 (yellow), and 4 (red). The asterisk denotes a small impurity of 3 in the spectrum of 4 due to decomposition.....	70
Figure 2.3.18 VTIR spectrum in THF of 2 at 303 K (top, solid), 2 at 173 K (middle, dashed, $\nu_{N_2} = 2120 \text{ cm}^{-1}$) and 3 at 173 K (bottom, light dashed, $\nu_{N_2} = 2000 \text{ cm}^{-1}$)	70
Figure 2.3.19 CV (DME, 0.1 M [TBA][PF ₆]) of 2 under a dinitrogen atmosphere with scan rate dependence shown (scan speed = 10, 50, 100, 250 and 500 mV/s.).....	73
Figure 2.3.20 Depiction of ECEC type mechanism observed in the CV of 2 . E = electron transfers, C = chemical events (i.e. N ₂ binding).	74
Figure 2.3.21 CV (DME, 0.1 M [TBA][PF ₆]) of 2 under an argon atmosphere with scan rate dependence shown (scan speed = 10, 50, 100, 250 and 500 mV/s.).....	74
Figure 2.3.22 Molecular orbitals of the dominant electronic configuration for ^{Me} LCO ₂ ..	76
Figure 2.3.23 Molecular orbitals of the dominant electronic configuration for [^{Me} LCO ₂]	76
Figure 2.3.24 Spin densities of calculated $S = 3/2$ state (left) and $S = 1/2$ state (right) of [^{iPr} LCO ₂ (N ₂)] ²⁻	77
Figure 3.2.1 Selected examples of dinitrogen silylation catalysts	87
Figure 3.3.1 GC trace of catalytic reaction products	89
Figure 3.3.2 MS result of GC signal at 8.53 min corresponding to amine product. Insert: zoom to see m/z for ⁺ N(SiMe ₃) ₃ = 234	89
Figure 3.3.3 Structures of [Co(N ₂)AIL] ⁻ (left) and 2 (right) with qualitative depiction of the <i>trans</i> -influence of the metallo-ligand and N ₂ activation at cobalt. Yellow arrows represent the qualitative direction of electron density. Hydrogens and counter ions are omitted for clarity.....	90

Figure 3.3.4 Example of poisoning test showing surface nature of nanoparticles and single site nature of molecules. The ellipses indicate binding sights of poisoning ligands	94
Figure 3.3.5 Visual depiction of the filtrate test using 1 as the pre-catalyst. Turnover numbers (TONs) are shown in blue in the figure, and were determined by GC-MS analysis of the worked up product, as described in the experimental section.	95
Figure 3.3.6 Vis overlay of observed indophenol formation from kinetic runs of 1 (0.65mM). Time = 2 min (red), 5 min (orange), 10 min (green), 15 min (blue), 20 min (purple). A 1 cm pathlength cell was used and the spectra were collected at 293 K.....	97
Figure 3.3.7 Plot of [TMS ₃ N] versus time at various [1] (0.026-0.65 mM) in reactions with N ₂ (1 atm), Me ₃ SiCl (21.3 mmol), and KC ₈ (20.7 mmol).	97
Figure 3.3.8 Plot of initial rates ($\Delta[N(\text{SiMe}_3)_3]/\Delta t$, mM min ⁻¹) versus [1] (0.026-0.65 mM) in reactions with N ₂ (1 atm), Me ₃ SiCl (21.3 mmol), and KC ₈ (20.7 mmol)....	98
Figure 3.3.9 Stacked ¹ H NMR (500 MHz, d ⁸ -THF) of <i>in operando</i> studies with precatalyst 1	100
Figure 3.3.10 Stacked ¹ H NMR (500 MHz, d ⁸ -THF) of <i>in operando</i> studies with precatalyst 1 . Zoom of the diamagnetic region (% = THF, \$= THF decomposition,	100
Figure 3.3.11 Three potential reactive pathways for silylation of dinitrogen Top: Nucleophilic attack; Middle: TMS radical attack; Bottom: TMS anion attack.	101
Figure 3.3.12 Energy profile of the catalytic mechanism mediated by A with calculated intermediates and transition states. For each structure, the lowest spin state is	

indicated, along with ΔG values (relative to the reactants: A , N_2 and six TMS radicals). Reaction barriers are shown in red within parenthesis. The drawing is roughly scaled to energy, except where denoted by a break “//”. For the reaction, $N_2 + 6 \text{ TMS}\bullet \rightarrow 2 \text{ N(TMS)}_3$, $\Delta G = -265.4 \text{ kcal/mol}$	103
Figure 3.3.13 Energy profile of the three possible mechanisms mediated by A with calculated intermediates and transition states. Since the reaction mechanism from A to D is the same for the three alternative paths (see Figure 3.3.12 for A to D pathway), D was chosen as the starting point. For each structure, the lowest spin state is indicated, along with ΔG values (relative to the reactants: A , N_2 and six TMS radicals). Reaction barriers are shown in red within parenthesis. The drawing is NOT scaled to energy. Color is used to distinguish the alternative pathways (II and III) from path I.	104
Figure 3.3.14 Energy profile of the catalytic mechanism mediated by $\text{Co(N}_2\text{)AIL}$ with calculated intermediates and transition states. For each structure, the ΔG values relative to the reactants: A , N_2 and six TMS radicals are shown. Reaction barriers (ΔG^\ddagger) are shown in red within parenthesis. The drawing is not scaled to energy. .	108
Figure 3.3.15 CV (DME, 250 mV/s, 0.2 M TBAPF ₆) of 1 (black trace) with varying equivalents of TMSCl.	108
Figure 3.4.1 Proposed catalytic cycle for dinitrogen silylation using 1	110
Figure 4.2.1 General schemes for catalytic dinitrogen functionalization	120
Figure 4.2.2 Select examples of low spin late transition metal-imido complexes.....	124
Figure 4.2.3 Representation of Betley’s Co(III) imidos that display open shell electron configurations. Taken from reference 117.....	125

Figure 4.2.4 Representative structures of 1-SiPh₃ , 1-SiPh₂Me , 1-SiPhMe₂ , 1-SiMe₃ , and 2	126
Figure 4.3.1 Potential pathways to functionalizing dinitrogen bound to a metal center	127
Figure 4.3.2 Top: ¹ H NMR Spectrum (d ⁸ -THF, 500 MHz) of 1-SiPh₃	129
Figure 4.3.3 Synthetic routes for formation of transition metal imidos.....	131
Figure 4.3.4 ¹ H NMR Spectrum (C ₆ D ₆ , 400 MHz) of 2	132
Figure 4.3.5 X-ray crystal structure of 2 at 50% probability. Hydrogen atoms were removed for clarity.....	132
Figure 4.3.6 Vis-NIR spectrum of 1-SiPh₃ (solid line) and 2 (dashed line) recorded in THF at 293 K.....	137
Figure 4.3.7 Vis spectrum of 1-SiPh₃ (red), 1-SiPh₂Me (green), 1-SiPhMe₂ (blue), and 1-SiMe₃ (purple).....	139
Figure 4.3.8 X-Band EPR spectrum (dX''/dB) of 1-SiPh₃ in THF glass (21K) shown as solid black line. The dashed red line is the simulated $S = 3/2$ spectrum with anisotropic g values $g = 2.20, 2.20, \text{ and } 2.02$ and line widths of $W_x = 200 = W_y = 50, W_z = 50$ G and z-hyperfine tensor for Co ($I = 7/2$) of $A_{zz} = 85 \times 10^{-4} \text{ cm}^{-1}$. * baseline impurity in cavity.....	144
Figure 4.3.9 X-Band EPR spectrum (dX''/dB) of 2 in toluene glass (7 K) shown as solid black line. The dashed red line is the simulated $S = 3/2$ spectrum with anisotropic g values $g = 2.16, 2.16, \text{ and } 2.01$ and line widths of $W_x = 100 = W_y = 100, W_z = 50$ G and z-hyperfine tensor for Co ($I = 7/2$) of $A_{zz} = 85 \times 10^{-4} \text{ cm}^{-1}$	144
Figure 4.3.10 Spin density isosurface (0.02 a.u.) of 2 , neutral quartet. Fuscia and green density correspond to alpha and beta spin, respectively.	146

Figure 4.3.11 Overlay of X-Band EPR spectrums (dX''/dB) in THF glass for [LCo] ⁻ (Black, bottom), [LCo ₂ (N ₂)] ²⁻ (Red, 2 nd from bottom), 1-SiPh₃ (Green, 2 nd from top), and 2 (Purple, top). Insert: Zoom of 3000 to 400 Gauss region highlighting Co (<i>I</i> = 7/2) hyperfine.	147
Figure 4.3.12 Qualitative orbital diagrams highlighting the differences in 1-SiPh₃ (top), 2 (middle) and [LCo ₂ (N ₂)] ²⁻ (bottom).....	148
Figure 4.3.13 Solution IR spectrum (THF, 293 K) of 1-SiPh₃ , ν(N=NR) : 1690 cm ⁻¹ ...	150
Figure 4.3.14 Full CV of 2 (0.1 M TBAPF ₆ , 50 mV/s)	151
Figure 4.3.15 Scan speed dependence (10 – 250 mV/s) for cathodic electrochemical event of 2 . Current was corrected by dividing by the square root of the scan speed.	152
Figure 4.3.16 Scan speed dependence (10 – 250 mV/s) for anodic electrochemical event of 2 . Current was corrected by dividing by the square root of the scan speed.	153
Figure 4.3.17 General scope of nitrene reactions attempted with complex 2	154
Figure 4.3.18 Positive mode ESI-MS spectrum in acetonitrile of reaction solution of 2 with PMe ₃ Solid line is experimental spectrum. Dashed line is a model of Me ₃ P=NH-Ad ⁺	155
Figure 4.3.19 ¹ H NMR spectra (500 MHz, C ₆ D ₆) of reaction of 2 with cyclo-octene ...	156
Figure A3.3.1 Indophenol calibration curve (λ _{max} = 625 nm) for NH ₃ quantification. ..	180
Figure A3.3.2 GC/MS calibration curve of N(SiMe ₃) ₃ using 9-fluorenone as the internal standard	180
Figure A3.3.3 Triplicate indophenol analysis of [N(TMS) ₃] (mM) vs time with [1]=0.13 mM. Standard deviation of the slope was used to determine the experimental error of 0.009 mM/min	181

Figure A4.3.1 Stack plot of ^{19}F NMR Spectrum ($\text{d}^8\text{-THF}$, 470 MHz) of ClSiPhAr (bottom), crude 1-SiPh₂Ar (1.5 equiv ClSiPhAr) (middle) and 1-SiPh₂Ar after 12 hr photolysis (top).....	181
Figure A4.3.2 ^1H NMR ($\text{d}^8\text{-THF}$, 500 MHz) for the photolysis of 1-SiPh₃ Top: Wide widow Bottom: Zoom between 240 – 150 ppm	182
Figure A4.3.3 Solution IR spectrum (THF , 298 K) of 1-SiPh₃ (blue) and 1-$^{15}\text{N}_2\text{SiPh}_3$ (red).....	183
Figure A4.5.1 ^1H NMR Spectrum (400 MHz, C_6D_6) of [K(2,2,2-cryptand)]CoL	183

List of Schemes

Scheme 1.1.1 Equation showing the reaction of N_2 and H_2 to form NH_3 at STP with the standard enthalpy of formation. Adapted from reference 3.....	4
Scheme 1.2.1 Equation for reduction of dinitrogen by nitrogenase	6
Scheme 1.5.1 Example of hydrosilylation catalysis using Zr-Co bimetallic. Note the fluxionality of the metal-metal bond. Taken from reference 51.....	31
Scheme 1.5.2 Scheme showing the reaction of $(THF)[NP]_3TiCo(N_2)$ with azobenzene or 1,2-diphenyl hydrazine. Taken from reference 411.....	33
Scheme 2.3.1 Reaction scheme for synthesis of 1-X , 2 , 3 , and 4	47
Scheme 3.3.1 Scheme showing products seen under standard catalytic conditions.....	89
Scheme 4.2.1 Scheme depicting the formation of a dihydrazido silyl complex isolated by Lu. Adapted from reference 41m.....	121
Scheme 4.2.2 Scheme of catalytic aziridination of olefins with aryl-iron-imidos. Adapted from reference 112.....	122
Scheme 4.3.1 General reaction scheme for the generation of 1-SiPh₃	128

List of Symbols and Abbreviations

*	antibonding
°	degree
2,2,2-cryptand	4,7,13,16,21,24-hexaoxa-1,10-diazabicyclo[8.8.8]hexacosane
Å	angstrom
abs	absorbance
Ad	adamantyl
ap	apical
atm	atmosphere
avg	average
$A_{xx, yy, zz}$	hyperfine tensor
B.M.	Bohr Magnetons
B3LYP	Becke, three-parameter, Lee-Yang-Parr functional
BArF	$[\text{B}(3,5\text{-}(\text{CF}_3)_2\text{C}_6\text{H}_3)_4]^-$
Bpin	boron pinacolate
C	Celsius
C_6D_6	deuterated benzene
calcd	calculated
CASSCF	complete active space self-consistent field
CCDC	Cambridge crystallographic data center
CD_2Cl_2	deuterated methylene chloride
CH_3CN	acetonitrile
cm	centimeter
cm^{-1}	wavenumber
CO	carbon monoxide
Cp	cyclopentadienyl ligand
Cp^*	pentamethyl cyclopentadienyl ligand
CP_3	$[\text{o-}(\text{}^i\text{Pr}_2\text{P})\text{C}_6\text{H}_4]_3\text{C}^-$
CSD	Cambridge structural data base
CV	cyclic voltammetry
D	zero-field splitting
$\text{d}^8\text{-THF}$	deuterated tetrahydrofuran
depf	1,1'-bis(diethylphosphino)ferrocene
DFT	density functional theory
DME	dimethoxyethane
DMeOPrPE	1,2-bis(bis(methoxypropyl)phosphino)ethane)
dmpe	1,2-bis(dimethylphosphino)ethane
DPhBz	diphenylbenzamidinate
DPhF	diphenylformamidinate
E/D	rhombicity
$E_{1/2}$	half-wave potential
EBO	effective bond order

EC	electron transfer, chemical event
EMAC	extended metal chains
ENDOR	electron nuclear double resonance
E_{pa}	anodic potential
E_{pc}	cathodic potential
EPR	electron paramagnetic resonance
equiv	equivalents
ESEEM	electron spin echo envelope modulation
ESI-MS	electrospray ionization mass spectrometry
Et_2O	diethyl ether
eV	electron volt
Fc	ferrocene
Fc^+	ferrocenium
Fp	$[\eta^5-C_5H_5Fe(CO)_2]^-$
FSR	formal shortness ratio
FTIR	fourier transform infrared
G	Gauss
g	anisotropic g factor
GC	gas chromatography
g_{eff}	effective g value
Gln	glutamine
hr	hour
HCl	hydrochloric acid
HIPT	hexaisopropylterphenyl
His	histidine
HOMO	highest occupied molecular orbital
I	nuclear spin quantum number
Ile	isoleucine
IMes	1,3-bis-(2,4,6-trimethylphenyl)imidazol-2-ylidene)
<i>in vacuo</i>	under vacuum
$i_{p,a} / i_{p,c}$	ratio of anodic peak current to cathodic peak current
IPr	1,3-bis-(2,6-diisopropylphenyl)imidazol-2-ylidene
iPr	isopropyl
IVCT	intervalence charge transfers
J_{12}	coupling constant
K	Kelvin
KC_8	potassium graphite
kcal	kilocalorie
kJ	kilojoule
K_p	equilibrium constant
L	$N(o-(NHCH_2P^iPr_2)C_6H_4)_3$
LA	Lewis acid

LMCT	ligand-to-metal charge transfer
LT	Lowe-Thornely
LUMO	lowest unoccupied molecular orbital
M	molarity
M06L	Minnesota 06 local functional
Me	methyl
Mes	mesityl
mg	milligram
MgADP	magnesium adenosine-diphosphate
MgATP	magnesium adenosine-triphosphate
MHz	megahertz
min	minute
mL	milliliter
MLCT	metal-to-ligand charge transfer
mM	millimolar
mmol	millimole
MO	molecular orbital
mol	mole
Mp	$[\eta^5\text{-C}_5\text{H}_5\text{Mo}(\text{CO})_3]^-$
MS	mass spectrometry
mV	millivolt
N(TMS) ₃	tris(trimethylsilyl)amine
N _{amide}	amide nitrogen
N _{ap}	apical nitrogen
nBuLi	n-butyl lithium
NIR	near infrared
NK	non-Krammers
nm	nanometer
NMR	nuclear magnetic resonance
NN	2,2,6,6-tetramethyl-3,5-bis(diisopropylphenylimido)- hept-4-yl
NP	(ⁱ Pr ₂ PNMes) ₃
NPs	nanoparticles
OTf	trifluoromethanesulfonate
P	pressure
P ₃ BPh	$[\text{PhB}(\text{CH}_2\text{PPh}_2)_3]^-$
PDB	protein data bank
PDI	2,6-(2,6- ⁱ Pr ₂ -C ₆ H ₃ -N=CMe) ₂ C ₅ H ₃ N
Ph	phenyl
PhB(^t BuIm) ₃	tris(1- <i>tert</i> butyl-2-ylidene)phenylborate
P _i	inorganic phosphate
PMe ₃	trimethylphosphine

PNP	$[\text{N}(\text{CH}_2\text{CH}_2\text{P}^i\text{Pr}_2)_2]^-$
ppm	parts per million
RASPT2	restricted active space multi-configurational second order perturbation
RASSCF	restricted active space self-consistent field
rds	rate-determining step
ref	reference
reflns	reflections
rt	room temperature
<i>S</i>	spin
SiP ₃	$[\text{o}-(^i\text{Pr}_2\text{P})\text{C}_6\text{H}_4]_3\text{Si}^-$
SQUID	super-conducting quantum interference device
STP	standard temperature and pressure
T	temperature
t	time
TBAPF ₆	tertabutylammonium hexafluorophosphate
tBu	tert-butyl
tBuCN	tert-butylisocyanide
TD-DFT	time dependent density functional theory
THF	tetrahydrofuran
TMS	trimethylsilyl
TMSCl	trimethylsilyl chloride
TON	turnover number
TPB	$[\text{o}-(^i\text{Pr}_2\text{P})\text{C}_6\text{H}_4]_3\text{B}$
Tp ^{tBu,Me}	tris(2-methyl, 4- <i>tert</i> butyl pyrazolyl)borate
UV	ultra violet
V	volt
Val	valine
vis	visible
vs	versus
VT	variable temperature
VTVH	variable temperature variable magnetic field
WBO	Wiberg bond order
W _{x, y, z}	line width
Z	number of independent structures in unit cell
δ	delta
δ	chemical shift
ΔE	difference in potential
ΔG	Gibbs free energy
ΔG [‡]	transition state Gibbs energy
ΔH ⁰	standard enthalpy of reaction
ε	molar absorptivity

η	hapticity
θ	degrees of data collection
λ	wavelength
λ_{max}	maximum absorbance wavelength
μ	bridging
μA	microamp
μ_{eff}	effective magnetic moment
μL	microliter
μmol	micromole
π	pi
σ	sigma
τ	tau

Chapter 1

**Dinitrogen Activation and Reduction: From Biology to Biomimetic Model
Complexes**

1.1 Motivation

A major societal goal is reducing our dependence on oil reserves due to their finite supply and the adverse effects of burning fossil fuels on climate change. As well, commodity products such as plastics, among others rely on petroleum feedstocks, which also suffer from the finite supply. In order to mitigate climate change, the development of new, cleaner fuel sources (i.e. NH_3 and H_2) and new chemical feedstocks (i.e. functionalized ammonia) derived from abundant small molecules (i.e. N_2) are a necessity.¹

1.1.1 Understanding Dinitrogen Activation

While dinitrogen is the most abundant gas in our atmosphere, its relative kinetic inertness makes its transformation to ammonia or other chemical feedstocks challenging.² The highest occupied molecular orbital (HOMO) – lowest unoccupied molecular orbital (LUMO) gap of N_2 is large (10.82 eV) making one- and two- electron reductions of N_2 challenging. Likewise, proton affinity of N_2 is substantially low such that direct protonation by strong acids is not feasible.³ To alleviate these barriers, electron-rich transition metals can be used to bind N_2 through σ - and more importantly π -back-bonding interactions (Figure 1.1.1), lowering the energy of and potentially populating the LUMO of N_2 , and thereby weakening the N-N bond.

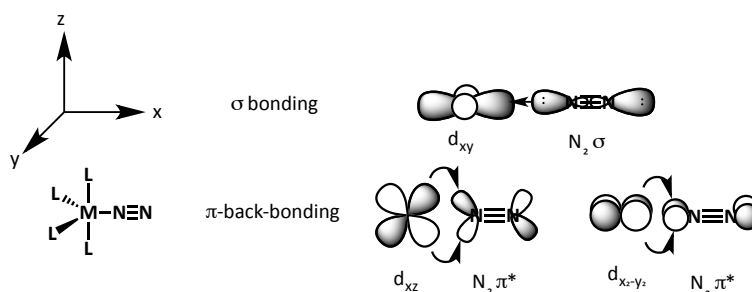


Figure 1.1.1 Example of dinitrogen bonding modes to transition metal centers.

Periodic trends derived from N_2 coordination complexes suggest that only certain transition metals are able to bind and activate N_2 towards reduction (Figure 1.1.1) based on their relative d-orbital energies.⁴ In order to raise the d-orbital energy levels to better match the $N_2 \pi^*$ orbitals, strong field ligands and low coordination environments can be utilized. Several synthetic examples using these strategies for iron and cobalt dinitrogen complexes will be discussed later in this chapter.

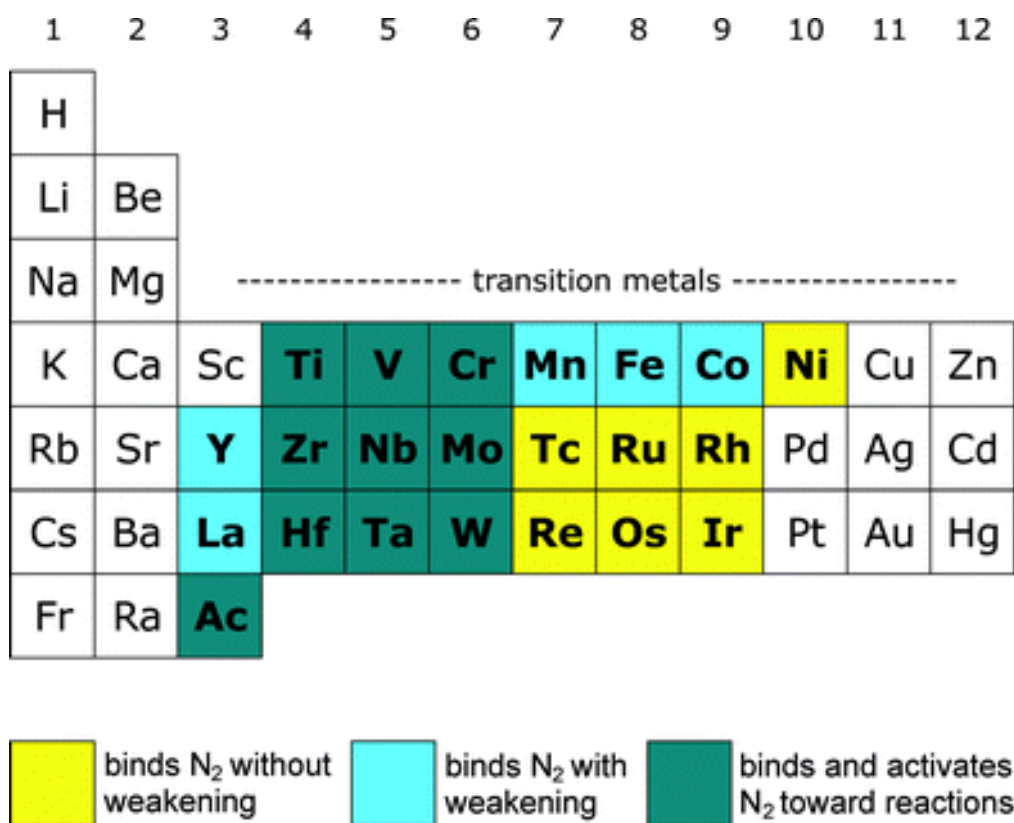
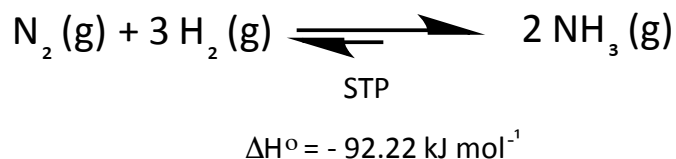


Figure 1.1.2 Representation of dinitrogen activation across the periodic table. Taken from reference 4.

1.1.2 The Haber-Bosch Process

Industrially, dinitrogen fixation has been achieved via the Haber-Bosch process.⁵ Here, dinitrogen and dihydrogen are flowed over a solid iron catalyst bed doped with Lewis acids (i.e. Al₂O₃, K₂O, CaO and MgO) at high temperatures and pressures (500 °C and 250 Bar). While the overall conversion of N₂ and H₂ to NH₃ is enthalpically favorable at STP (Scheme 1.1.1), it is entropically unfavorable. The use of high pressures, temperatures and a metal catalyst are needed to overcome the high barriers of the first steps of reduction and push the equilibrium to favor ammonia formation. Unfortunately, conversion is only 15 % over a single pass of the catalyst due to the equilibrium of the system ($K_p = 1.45 \times 10^{-5}$).⁶ However, recycling of the gas and removal of ammonia shift the equilibrium and allow for multiple catalytic passes yielding near quantitative conversion (Figure 1.1.3). Unfortunately, the conversion to ammonia comes at a very high economical and environmental cost due to the global demands for fertilizer. The amount of energy needed to perform Haber-Bosch is about 2% of the planet's annual energy output, which leads to potentially high operational costs.^{5c, 6a, 7} As well, the hydrogen generated for the reaction comes from steam reformation of natural gas, which creates an appreciable amount of CO₂.⁷ With N₂ being the most abundant gas in Earth's atmosphere, developing catalysts for its reduction, while mitigating the generation of green house gases would be beneficial.



Scheme 1.1.1 Equation showing the reaction of N₂ and H₂ to form NH₃ at STP with the standard enthalpy of formation. Adapted from reference 3.

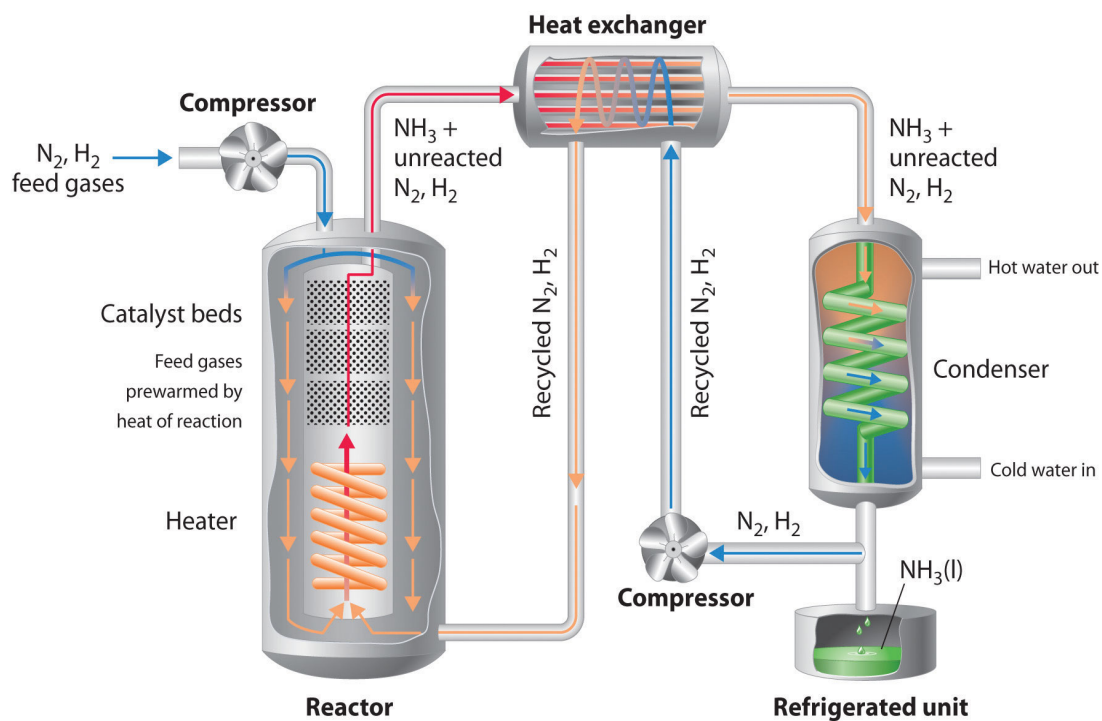
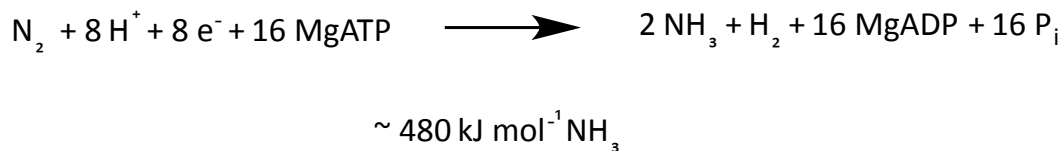


Figure 1.1.3 Schematic diagram seen in an industrial Haber-Bosch facility. Taken from reference 5d.

Ideally, it would be productive to find an alternative system that can compete with Haber-Bosch at lower pressures and temperatures. Likewise, developing a system in which N_2 can form bonds other than N-H (e.g. N-C and N-Si bonds) would be essential in the generation of new chemical feedstocks directly from dinitrogen. This chapter will focus on how steps are being taken to understand and generate catalysts that can perform the reduction of dinitrogen under mild conditions, where the primary inspiration is the multi-metallic enzyme nitrogenase. From there synthetic models derived from nitrogenase will be discussed, and finally alternative catalysts for dinitrogen reduction will be presented.

1.2 Biological N₂ Fixation

The bacteria *Azotobacter vinelandii* and *Klebsiella pneumoniae* as well as certain blue-green algae utilize the enzyme nitrogenase, which converts dinitrogen to ammonia and dihydrogen under ambient reaction conditions coupled with the hydrolysis of ATP (Scheme 1.2.1).⁸ At the heart of the nitrogenase enzyme is a multimetallic-sulfur cluster responsible for the fixation of dinitrogen. Three different forms of this co-factor have been discovered, all with a 7 iron- 9-sulfur -1 X atom core. The difference between the three cofactors is the identity of an eighth metal, which can either be iron, vanadium or molybdenum.⁹ Of these three cofactors, the FeMo-cofactor has been the most extensively studied and will be the one discussed in this chapter.



Scheme 1.2.1 Equation for reduction of dinitrogen by nitrogenase

1.2.1 Structural Aspects of Nitrogenase

Seminal work in the field of nitrogenase has advanced our understanding of the structural and functional properties of the FeMo-cofactor.^{8, 10} Of recent record, the identity of the interstitial X atom was elucidated to be a carbon atom through X-ray emission spectroscopy (XES) studies and electron spin echo envelope modulation (ESEEM) experiments.¹¹ Since its identification, synthetic inorganic chemists have sought out to create model systems bearing a Fe-C interaction and to study them for dinitrogen reduction (*vide infra*).

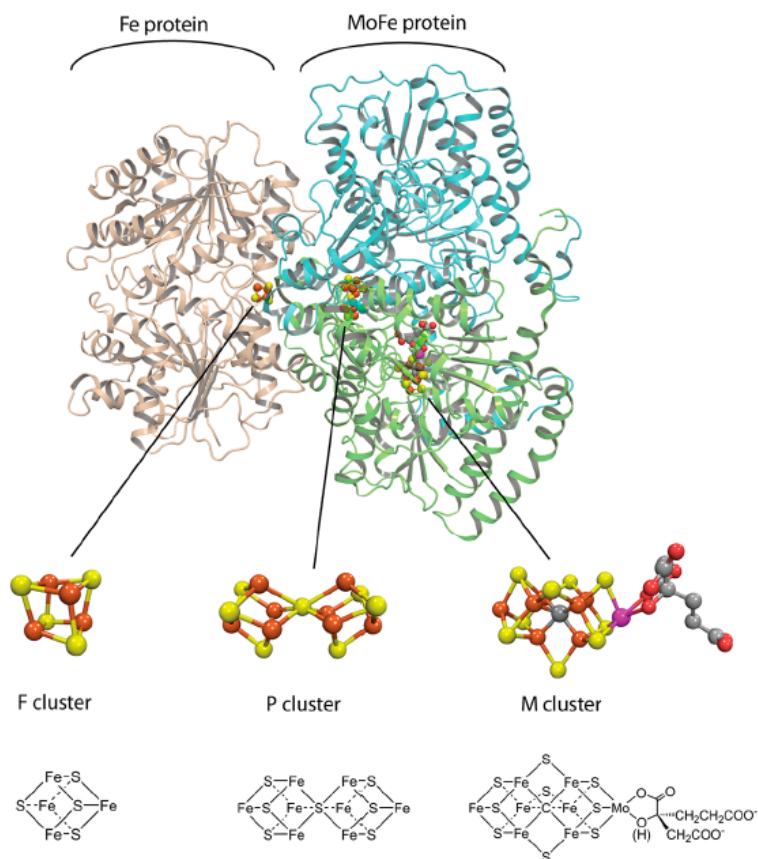


Figure 1.2.1 Protein crystal structure of Mo-dependent nitrogenase. Tan is the Fe protein, Green is the alpha subunit of the MoFe protein, Light blue is the beta subunit of the MoFe protein. Ball and stick models of the F-cluster, P cluster and FeMo-cofactor. PDB: 2AKF. Taken from reference 10.

The structure of Mo dependent nitrogenase has also been subject to extensive study. The enzyme consists of two proteins, a MoFe protein and Fe protein (Figure 1.2.1). The MoFe protein, which contains the FeMo-cofactor, is a $\alpha_2\beta_2$ -heterotetramer.⁸ This protein also contains a large iron-sulfur cluster (P cluster) that is believed to be responsible for electron transfer to the FeMo-cofactor (*vide infra*) from the Fe protein. The Fe protein is responsible for the hydrolysis of adenosine-triphosphate (ATP) to ADP as well as serving as electron transfer conduit to the FeMo-cofactor. The hydrolysis reduces a 4Fe-4S cluster (F cluster), which provides the reducing equivalents for nitrogenase activity.⁸

There are two aspects of particular interest when examining this electron transfer step. First, it was found that the Fe protein only binds to the MoFe protein once it has hydrolyzed ATP to ADP and inorganic phosphine.⁸ Upon transfer of electrons, the protein detaches. Secondly, the overall distance of the F cluster to the FeMo-cofactor is 23 Å, seemingly too long for efficient electron transfer. However, the addition of the P cluster (9 Å from the F Cluster and 13 Å from FeMo) allows for efficient electron transfer to the active site of nitrogenase.¹² Of note, the P cluster is a 7S:8Fe cluster which qualitatively is two fused 4Fe-4S clusters sharing a sulfur atom. Due to the large size of this cluster, storage of multiple electrons as well as controlled delivery to the co-factor for individual one-electron steps is possible.

Another key structural feature of the MoFe protein can be seen by studying two key second coordination sphere protein residues in the wild type (WT) enzyme, 195^{His} and 70^{Val} (Figure 1.2.2).¹³ These residues are believed to play an important role in the reduction of dinitrogen. It is well understood that 195^{His} is used as a proton shuttle whereas 70^{Val} serves as a gate-keeper for allowing substrate access to the cofactor.¹⁰ For

example, when 195^{His}→^{Gln} mutation is present, the enzyme is inactive. Likewise, when the 70^{Val}→^{Ile} mutation is present, the reduction of dinitrogen was shut down and only proton reduction was possible. The 70^{Val} residue is also located over the top Fe face of the cofactor, suggesting that Fe could be implemented as a site of N₂ binding.¹⁴

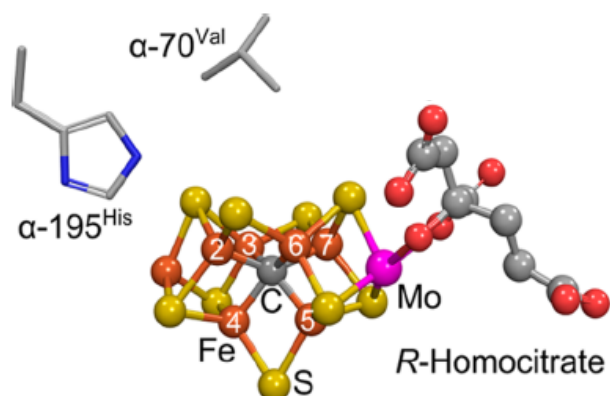


Figure 1.2.2 Zoom of the FeMo-cofactor showing the location of two key residues to N₂ reduction. Taken from reference 10.

1.2.2. Electron Loading of FeMo-cofactor

While the site of dinitrogen reduction is still debated, the key steps to generate ammonia have been investigated through spectroscopic studies. Early kinetic work laid out the base for understanding dinitrogen binding and its coinciding H₂ release, as well as the number of reduction steps needed for ammonia formation. The Lowe-Thorneley (LT) kinetic model (Figure 1.2.3) suggests that the cofactor must be preloaded with four reducing equivalences prior to dinitrogen binding.⁸ In each step of the model, the addition of a proton and an electron are invoked. To confirm this model, reduction steps were done under an atmosphere of argon to examine only the pre-dinitrogen steps. It was seen that reducing the cofactor with 4 reducing equivalents in a buffered solution under cyro-annealing conditions lead to the formation of two equivalents of H₂.¹⁵

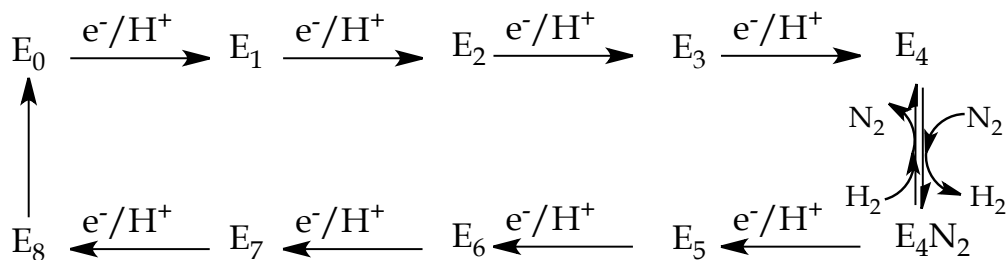


Figure 1.2.3 Lowe-Thornely model to dinitrogen reduction. Adapted from reference 10.

This observation led to a hypothesis that protons and hydrides must be stored within the cofactor in order to generate H_2 . It was found through freeze-quench EPR studies that three states of the cofactor were observed (E_0 , E_2 , and E_4 from Figure 1.2.3). It should be noted that the as isolated FeMo-cofactor has a spin state of $S = 3/2$, which would be active by EPR and is referred to as the E_0 state.⁸ Upon reduction a $S = 1/2$ EPR signal was observed.¹⁶ Upon slow warm up, the two signals grow in; one corresponding to the E_0 state, and another $S = 3/2$ signal believed to correspond to the E_2 state. Further evidence for these states was seen through labeling studies of the protons. This allowed for $^{1,2}H$ ENDOR studies to be performed, which provided structural information of paramagnetic species through the coupling of the spin of EPR active systems to the relaxation of nuclei of interest.¹⁰ The $^{1,2}H$ ENDOR results gave an isotropic hyperfine signal with a value of 24 MHz, indicative of transition metal hydrides. As well, a rhombic anisotropic hyperfine contribution was observed, which ruled out terminal hydrides that typically give rise to axial hyperfine signals.¹⁷ Finally, ^{95}Mo ENDOR measurements suggest that the hydrides are bridged between iron atoms, since no hyperfine interactions were observed.¹⁸ These experiments lead to the assignment of the E_4 state, $S = 1/2$, (Figure 1.2.4) as a doubly protonated dihydride species.

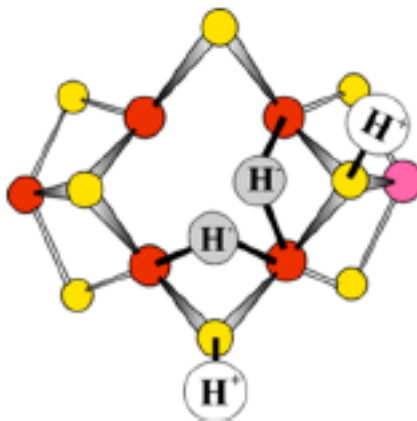


Figure 1.2.4 Proposed structure of the E₄ state of the FeMo-cofactor. Taken from reference 10.

Of note, a recent publication from King *et al.* demonstrated the substitution of the Fe protein with a photosensitive CdS nanocrystal.¹⁹ To make this process operational, the MoFe protein was grown on the nanocrystals. The system under buffered solution (pH 7) was then exposed to 405 nm diode light source to excite the nanocrystals and provide electrons to the MoFe protein (Figure 1.2.5). This system was found to have a turnover frequency (TOF) of 75 per minute of ammonia formed, which is 63% of the wild type enzyme under catalytic conditions. Like the wild type enzyme, H₂ was also formed in this hybrid system. This report was one of the first examples to show that nitrogenase can operate catalytically with a photochemical electron source. While other photosensitizers had lower reduction potentials, the electron transfers were slow and allowed for oxidation of the cofactor with contaminant released of H₂. However, for this system, it was hypothesized that the rapid delivery of electrons to the FeMo-cofactor from the strong light absorption of CdS nanorods allowed for sufficient reduction to the active E₄ state of the enzyme, which has been found to be the state of N₂ binding and eventual reduction.

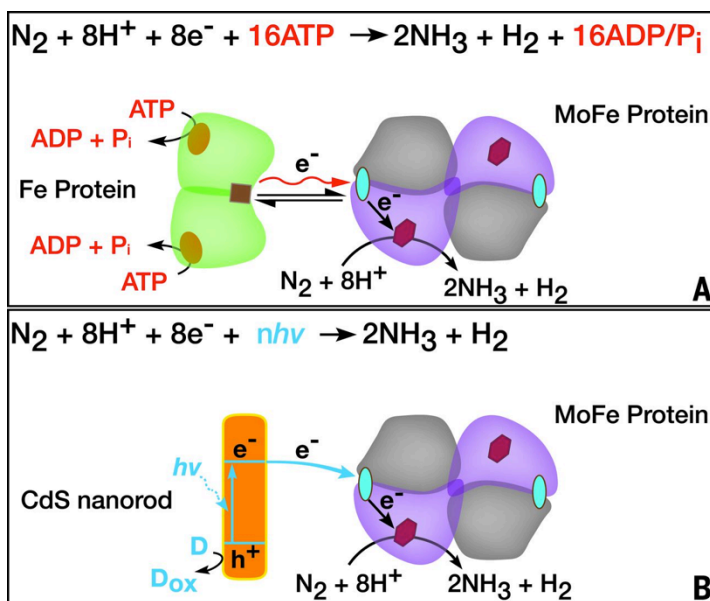


Figure 1.2.5 Depiction of the electron transfer to the MoFe protein from A) Fe protein in nitrogenase B) CdS photoexcited nanorod. Taken from reference 19.

1.2.3 Mechanism to Dinitrogen Reduction

After the formation of the E_4 state, the next proposed step from the LT model is binding of N_2 and release of H_2 . However, the mechanism in which N_2 is reduced is still ambiguous. There are three potential mechanistic pathways to the generation of ammonia from N_2 (Figure 1.2.6). The first pathway is a distal mechanism, which was first proposed by Chatt²⁰ and later amended by Schrock²¹ in synthetic molybdenum systems (*vide infra*). In this mechanism the N_2 unit is protonated at the distal position three times, leading to ammonia formation as well as a metal nitride, which can be further protonated to generate a second equivalent of ammonia. The second pathway is an alternating pathway, which was first proposed through theoretical calculations to be a thermodynamically viable alternative pathway for nitrogenase activity.¹² By that description, diazene ($HN=NH$) and hydrazine (H_2N-NH_2) would be generated until the final two steps, which would generate ammonia. The final pathway, mostly seen in synthetic systems that

perform reduction of dinitrogen via silylation using trimethylsilyl chloride (*vide infra*), goes through a disilylhydrazido (N-N(SiMe₃)₂) intermediate, followed by silylation of the proximal nitrogen. The latter steps of this mechanism are still under investigation as whether hydrazide (SiMe₃N-N(SiMe₃)₂⁻) release occurs or imido (M-N-SiMe₃) formation occurs.²² Of relevance to nitrogenase, a recent complex from the Peters group was hypothesized to go through a similar type of mechanism to generate ammonia, although the steps are different due to the use of protons instead of sterically encumbering trimethylsilyl moieties.²³ Synthetic N₂ fixation model systems will be discussed later in this chapter.

In the nitrogenase system, it was found that both diazene and hydrazine are reduced to ammonia in the wild type enzyme, suggesting that the alternating pathway is a viable pathway to N₂ reduction.^{8,24} As well, it is known that the V-dependent nitrogenase, which many believe has a similar mechanism to that of the Mo-dependent enzyme, generates a small amount of hydrazine under turnover conditions, again suggesting the alternating pathway.²⁵

To further elucidate the pathway, isotopic labeling of several reduced N₂ compounds (diazene, hydrazine, and methylhydrazine) lead to the spectroscopic understanding of the mechanism for ammonia formation. It was seen that when diazene and hydrazine are added to the mutated 70^{Val→Ile} and 195^{His→Gln} that a common intermediate, *I*, can be observed in EPR and ¹⁵N, ^{1,2}H ENDOR experiments. It was proposed that both substrates end at the same point down stream, both generate one equivalent of ammonia, and that *I* must be some trapped NH_x state of the system. Based on the pathways that are laid out from the alternating model, intermediate *I* can either be defined as a metal-amido or

metal-ammonia adduct. The true identity of *I* and eventually another intermediate *H* were confirmed through closer examination of the EPR data (Figure 1.2.7).²⁶ It was seen that a broad non-Kramers (NK) doublet (integer spin) signal, possibly intermediate *H*, was broadening the Kramers (non-integer spin) signal of *I* in the EPR.

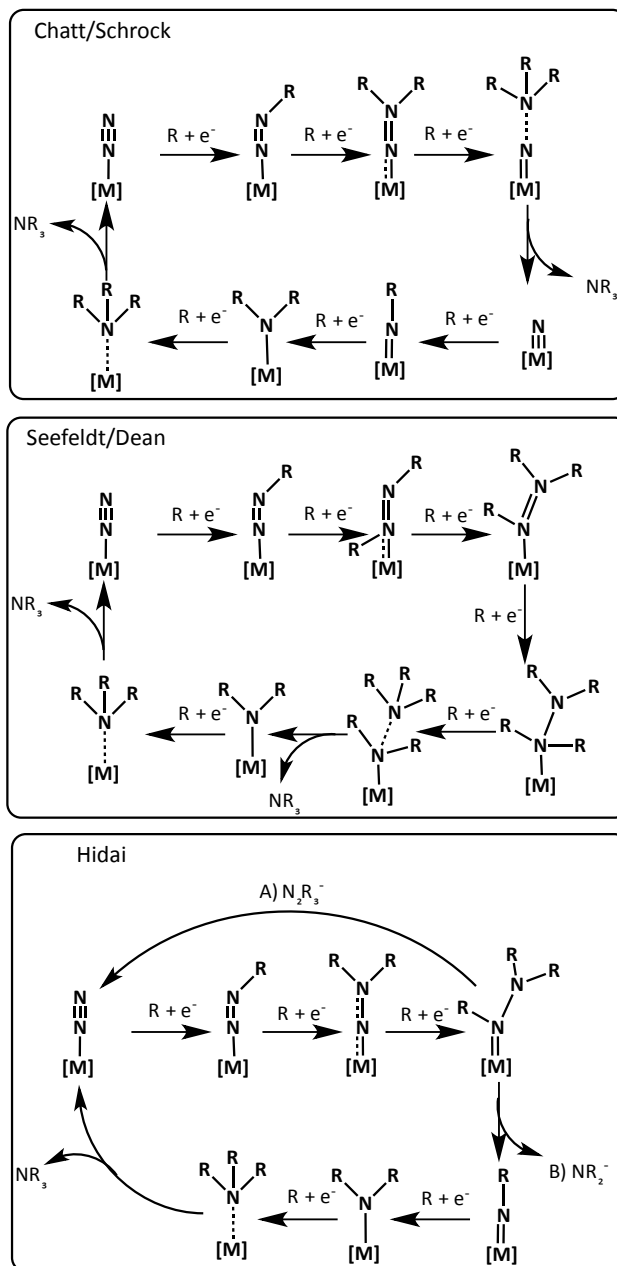


Figure 1.2.6 General schemes for catalytic dinitrogen functionalization
 Top: Chatt-Schrock Mechanism; Middle: Alternating Mechanism; Bottom: Silylation Mechanisms $R = \text{H}^+$ or Me_3SiCl

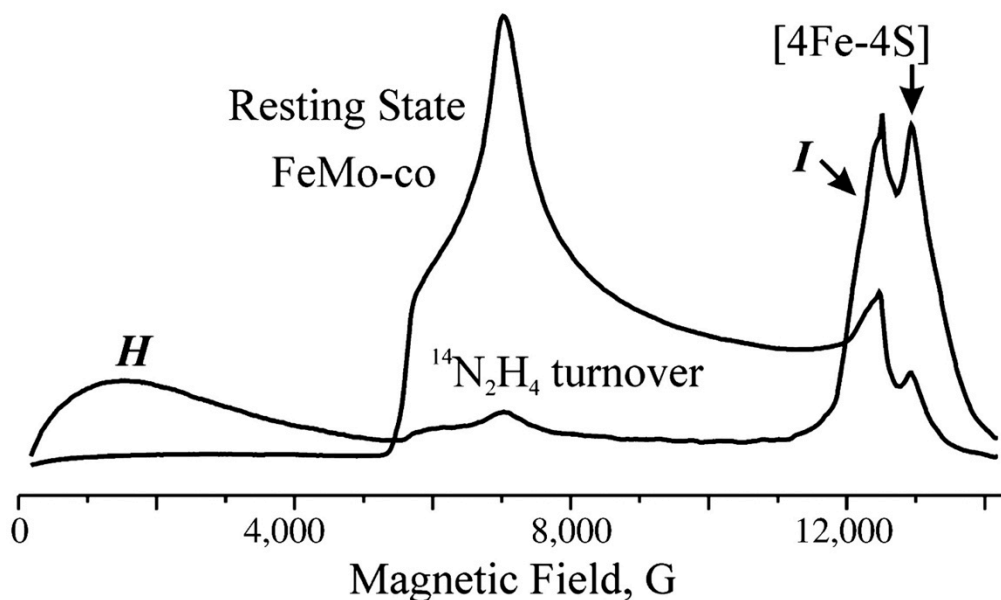


Figure 1.2.7 Q-band CW EPR spectrum of α -70Val \rightarrow Ala, α -195His \rightarrow Gln MoFe protein in resting state ($S = 3/2$) and trapped during turnover with $^{14}\text{N}_2\text{H}_4$. Taken from reference 26.

One way to characterize NK doublets is through ESEEM spectroscopy.²⁶ ESEEM is a pulsed experiment similar to ENDOR in which an electron spin echo is created and the decay is monitored. When weak interactions with other atoms exist around the paramagnetic center, the decay is modulated.²⁷ From labeling the atoms that are interacting, structural information can be attained and the environment around the paramagnetic center can be elucidated. Through the use of NK-ESEEM spectroscopy using labeled substrates and ^{95}Mo labeled cofactor, it was found that intermediate *H* was being formed at the FeMo-cofactor and was bound to the cofactor. Through examination of the quadrupole coupling extracted from the decay, intermediate *H* was believed to be an $-\text{NH}_2$ species.^{26, 28} This led to intermediate *I* being assigned the ammonia adduct trapped by the mutation of the protein residues.

From the examination of nitrogenase, several design principles for making effective dinitrogen reduction catalysts have been introduced. The first principle is the necessity of having a system that can effectively store reducing equivalents that later are used in the multi-electron reduction step. Secondly, effective proton and electron transfer is necessary to provide additional electrons to the N₂ unit and limit non-productive proton reduction to dihydrogen. Finally, the fact that nitrogenase utilizes multiple metal centers and electron-rich ligands suggest the potential of multimetallic synthetic compounds facilitating small molecule activation and reduction.

1.3 Synthetic N₂ Fixation Models

1.3.1 Molybdenum Systems

Taking lessons from the study of nitrogenase, several molybdenum and later iron compounds (*vide infra*) were developed and investigated to understand the reduction of nitrogen at a single metal center. Due to the observation of molybdenum in the cofactor of nitrogenase and its capability of allowing access to many redox states, scientists believed the catalytically active site of dinitrogen reduction was based at the molybdenum center. This sub-section will focus on molybdenum-based catalysts for dinitrogen reduction.

Early synthetic work by Chatt^{20a-d, 29} and Hidai³⁰ showed that several tetraphosphine molybdenum and tungsten dinitrogen compounds and protonated intermediates could be isolated through the direct protonation using sulfuric acid (Figure 1.3.1). These were the first examples of synthetic transition metal complexes reducing dinitrogen to ammonia, albeit sub-stoichiometrically. Interestingly, no added electrons were present in these ammonia-forming reactions, meaning the electrons were only derived from the

molybdenum center. These experiments led to the first proposed mechanism for dinitrogen reduction, in which molybdenum is cycled between Mo(0) to Mo(IV) oxidation states.³¹

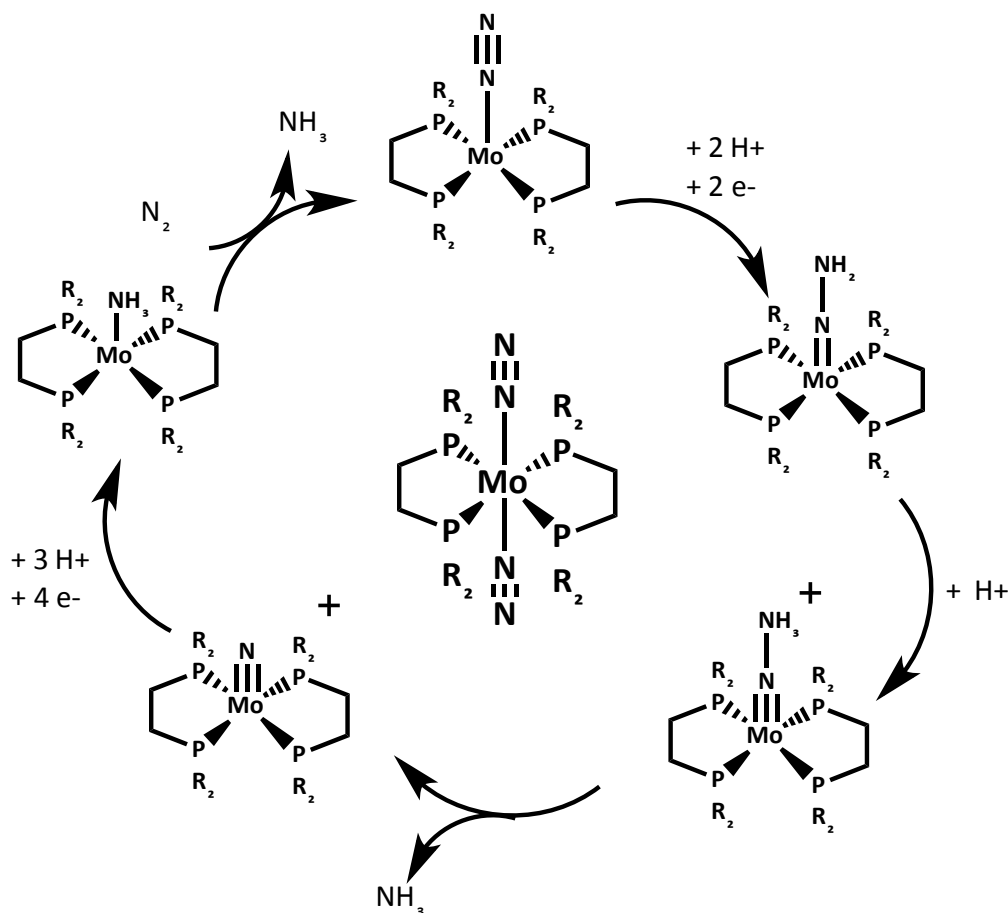


Figure 1.3.1 Proposed mechanism for dinitrogen reduction using P₄Mo(N₂)₂ (center). Electrons are derived from Mo.

In 2003, Yandulov and Schrock developed a triamidoamine molybdenum complex, [HIPTN₃N] (HIPT= hexaisopropylterphenyl, N₃N= tris(2-aminoethyl)amine) (Figure 1.3.2), in which catalytic N₂ reduction was achieved.^{21, 32} The bulky ligand design was important to allow for dinitrogen to bind to the Mo center and prevent the thermodynamically favorable formation of a bis(molybdenum)μ-(N₂) sandwich complex.

As well, the proton and electron sources along with the solvent choice were important in achieving maximum catalytic activity. The catalytic reduction of dinitrogen to ammonia proceeds with $\text{HIPTN}_3\text{NMo}(\text{N}_2)$ in a solution of heptane with [2,6-lutidinum]BArF (BArF = $[\text{B}(3,5\text{-}(\text{CF}_3)_2\text{C}_6\text{H}_3)_4]$). This was followed by the slow addition of the reductant decamethyl chromocene, Cp^*_2Cr , over a 6 hr period at room temperature to net 8 equivalents of NH_3 out of a possible 12.²¹ Not only was Schrock's system a competent homogeneous catalyst for ammonia production, it also allowed for the direct isolation of nine potential intermediates along the catalytic pathway (Figure 1.3.3), which provides information on the mechanism of dinitrogen formation. In this system, the prevailing mechanism is similar to that of Chatt's cycle proposed earlier. The one difference between the mechanisms is the higher oxidation states of molybdenum that are observed for the Schrock system ($\text{Mo}(\text{III}) \rightarrow \text{Mo}(\text{VI})$) compared to the Chatt mechanism ($\text{Mo}(0) \rightarrow \text{Mo}(\text{IV})$). The observance of these two mechanisms have led many to postulate that molybdenum may be the active metal in nitrogenase, although recent evidence suggests Fe is more likely the active metal (*vide supra*).²⁴

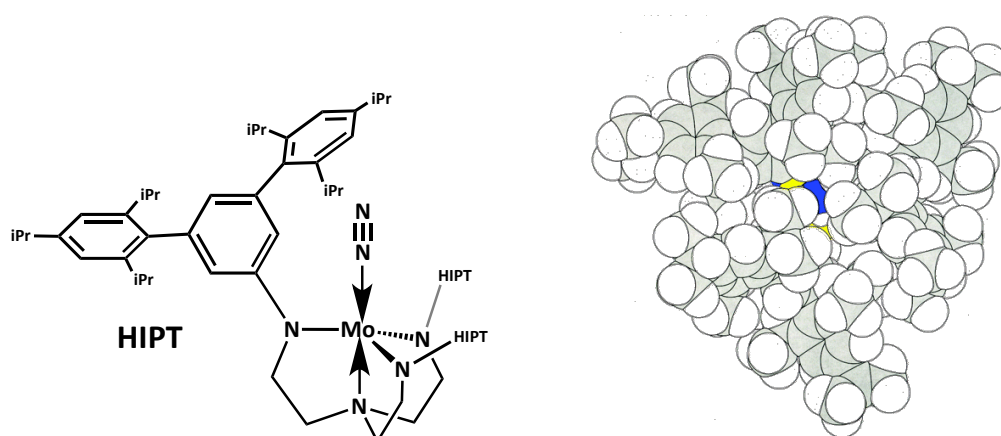


Figure 1.3.2 Structure of $\text{HIPTN}_3\text{NMo}(\text{N}_2)$ (Left) and spacefill of $\text{HIPTN}_3\text{NMo}(\text{NH}_3)$ (Right) (Blue = N, Yellow = Mo). Taken from ref 21.

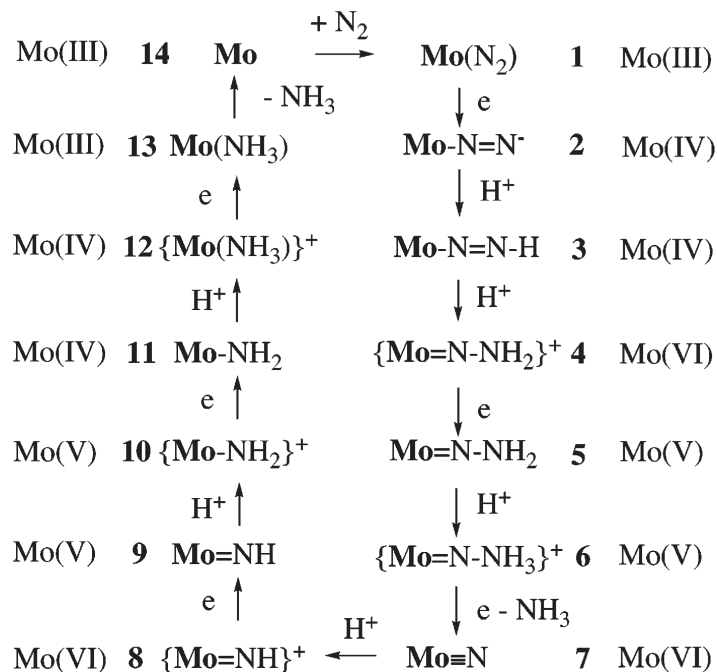


Figure 1.3.3 Proposed intermediates in the reduction of dinitrogen at a [HIPTN₃N]Mo (**Mo**) center through the stepwise addition of protons and electrons. Brackets denote nonisolated species Taken from reference 21.

More recently, Nishibayashi *et al.* have developed several dinitrogen-bridged dimolybdenum PNP-pincer, 2,6-bis(di-*tert*-butylphosphinomethyl)pyridine, and PPP-pincer, bis(di-*tert*-butylphosphineethyl)phenylphosphine, variants that are highly competent in the reduction of dinitrogen to ammonia (Figure 1.3.4).^{31,33} The catalytic conditions are similar to that of the Schrock system where cobaltocene Cp₂Co is the reductant instead of Cp^{*}₂Cr. In initial studies, with the PNP-system it was found when the *para* position of the pyridine ring was a proton (R = H), ammonia could be generated up to 23 equivalents.^{33b} However, by tuning the *para* position with electron donating groups (R = OMe) or a redox-mediator similar to nitrogenase (R = ferrocene, Fc) the amount of ammonia was greatly increased (52 and 45 equiv respectively). It was believed that electron donating substituents accelerated protonation, where as Fc accelerated electron transfer. Interestingly, the authors note that the bridging dinitrogen unit plays a role in

mediating the reactivity of the complex. When monometallic PNP-Mo(N) compounds are exposed to catalytic conditions, the resulting formation of ammonia is significantly lessened from the parent dimolybdenum compound. This result suggests synergy between the metals, similar to that seen in nitrogenase. It is uncertain whether the second molybdenum atom contributes electrons or just acts as a stabilizer to the catalytic species. Finally, when an isolated molybdenum nitride in the PPP-pincer is used, ammonia formation is maximized to 63 equivalences per molybdenum atom. It is hypothesized that the lower basicity and π -back bonding ability of the PPP-scaffold stabilizes a wide range of molybdenum oxidation states, making catalysis more facile.³¹ The authors also note that the complex is believed to form a similar dinitrogen-bridged dimolybdenum pincer as seen in the PNP systems, although to date they have not isolated such a species.³¹

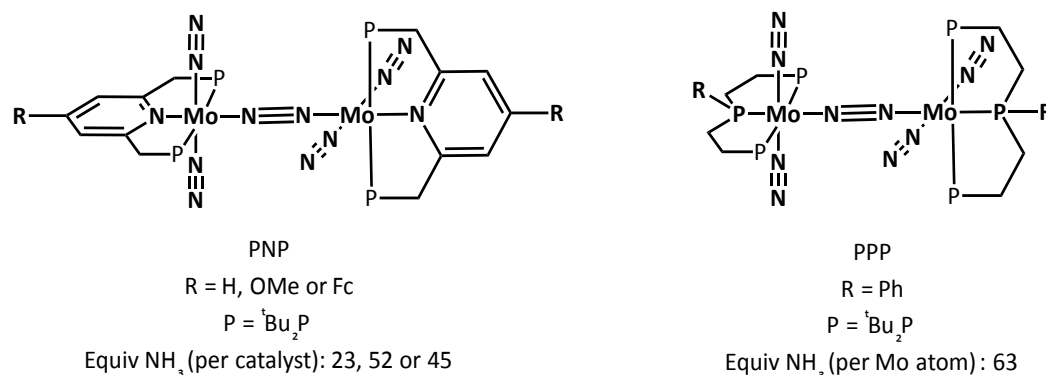


Figure 1.3.4 PNP and PPP molybdenum pincer compounds used for ammonia catalysis. Adapted from reference 31.

It should be noted that molybdenum also can serve as a catalyst for the silylation of dinitrogen to tris(trimethylsilyl)amine.^{22a} Information regarding those systems will be described in detail in chapters 3 and 4.

1.3.2. Iron Systems

Molybdenum has been a noteworthy metal for the reduction of dinitrogen in synthetic systems. In contrast, the synthetic dinitrogen reduction chemistry at iron, the metal seen in all types of nitrogenases, has been less thoroughly explored until recently. One reason for this may lie in the periodic trend of transition metal d-orbitals. While the high d-electron counts of the later transition metals (Fe, Co, Ni) would seem advantageous, their greater electronegativity results in lower energy d-orbitals, which are not typically amenable to N₂ activation.⁴ This periodic trend is at odds with the activation of dinitrogen, which requires high-energy filled d-orbitals to effectively π -back bond into the π^* orbitals of N₂. The use of strong field ligands and low coordinate geometries can promote high-energy d-orbitals for effective π -back bonding for late transition metals such as Fe.⁴ This subsection will primarily focus on select examples of iron compounds, which bind dinitrogen and can generate ammonia.

One of the first accounts of dinitrogen reduction via an iron complex came from the work of Leigh and Jimenez-Tenorio using a low-valent Fe(dmpe)₂ compounds (dmpe = 1,2-bis(dimethylphosphino)ethane).³⁴ They were able to synthesize a Fe(N₂) complex through ligand substitution of *trans*-[FeH(H₂)(dmpe)₂]⁺ with N₂ to generate [FeH(N₂)(dmpe)₂]⁺. This complex can readily react with base to generate a generate Fe(N₂)(dmpe)₂, which loses N₂ over time or under vacuum, owing to the weak interaction with Fe. Upon *in situ* generation of Fe(N₂)(dmpe)₂, followed by the addition of stoichiometric amounts of acid in THF gives a 12 % yield of ammonia (Figure 1.3.5). Ten years later, using a similar system, [Fe(DMeOPrPE)₂H(H₂)]⁺, (DMeOPrPE = 1,2-

bis(bis(methoxypropyl)phosphino)ethane), Tyler *et al.* looked to examine the reduction of N_2 .³⁵ Upon generation of $[Fe(DMeOPrPE)_2H(H_2)]^+$ from the dichloride precursor, base and H_2 , the exchange of H_2 with N_2 was observed similarly to the Leigh system.³⁶ The analogous reaction using HOTf produced only marginally better yields of ammonia (15%) but showed that iron can be primed for N_2 binding through reduction with H_2 .

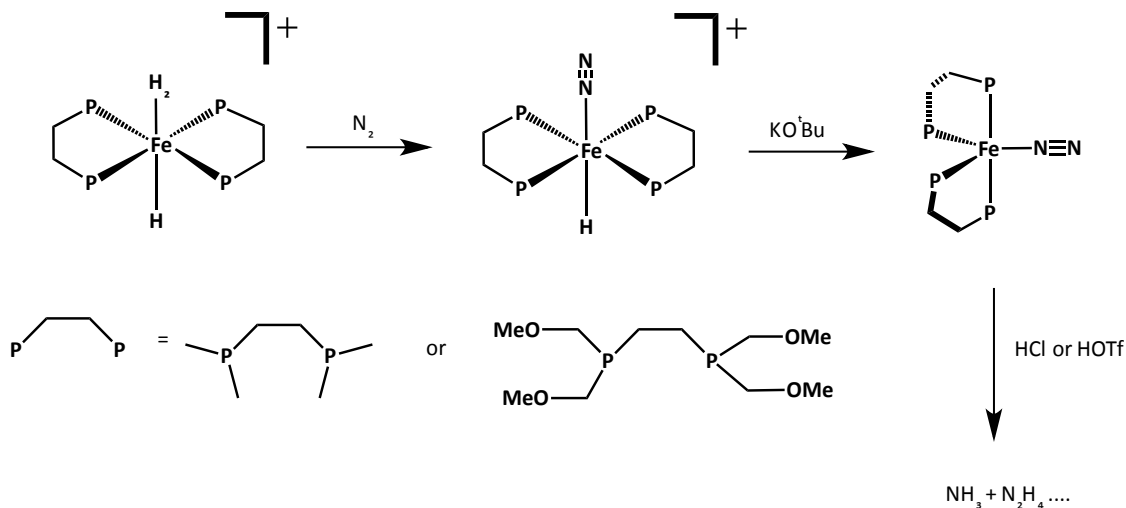


Figure 1.3.5 Tetraphosphine iron compounds first seen to reduce dinitrogen to ammonia. Adapted from reference 35.

One of the best systems for achieving the stoichiometric formation of ammonia from N_2 comes from the Holland group, which utilizes low coordinate bulky β -diketiminate ligands that can increase the energy of π^* symmetry orbitals.^{4, 37} When various β -diketiminate ligands are mixed with $FeCl_2$ and reduced with 4 equivalents of potassium, a highly activated $Fe_2K_2(N_2)$ species can be formed ($\nu_{N_2} = 1778-1810 \text{ cm}^{-1}$), indicative of a N_2^{2-} unit.⁴ It was found that the bulky aryl substituents on the ligand backbone allow for interaction with the potassium, which can then contribute to N_2 activation. When only 2 equivalents of potassium are added (β -diketiminate in this case is $MeC[C(Me)N(2,6-Me_2C_6H_3)]_2^-$), the dinitrogen unit can be split to generate a tetrairon bis(nitride) species

(Figure 1.3.6).^{37a} This complex can react with acid to generate ammonia in 84% yield with concomitant formation of a bridging diiron dihydride.

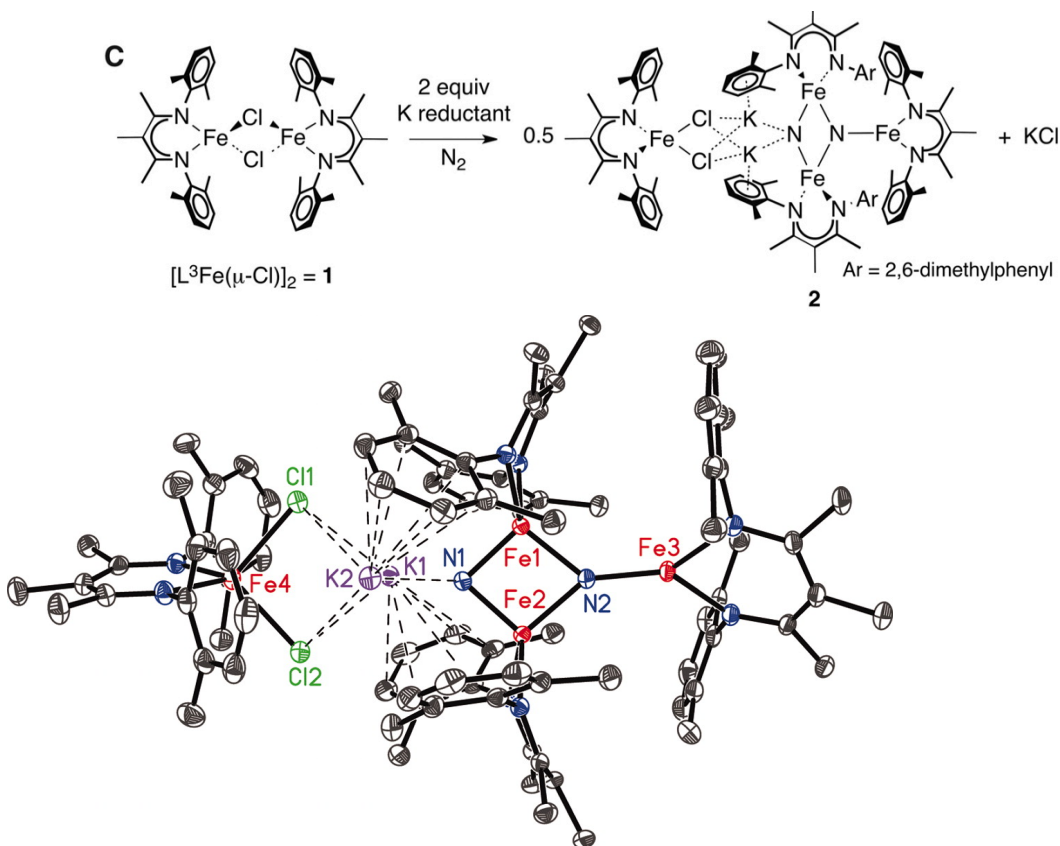


Figure 1.3.6 Top: Scheme depicting the formation of the tetrairon nitride from N_2 . Bottom: X-ray crystal structure 50% probability ellipsoids of the tetrairon nitride. Taken from reference 37a.

To the best of my knowledge, work from Peters *et al.* has been the only record of homogeneous catalytic dinitrogen reduction to ammonia using iron.^{23, 38} Several related systems from Peters (Figure 1.3.7) have shown mild to excellent activity with equivalents of ammonia when reacted with $(Et_2O)_2HBArF$ ($BArF = [B(3,5-(CF_3)_2C_6H_3)_4]^-$) and potassium graphite (KC_8) at $-78^\circ C$. Of relevance to this thesis, the compounds generating the highest amount of ammonia are all housed in similar tetradentate P_3^E ($P_3 = \text{tris}(o\text{-diisopropylphosphinophenyl})$, $E = \text{borane, methyl, or silyl}$) scaffolds. These scaffolds allow for flexible interaction with the metal center depending on oxidation state via a

trans-interaction involving E that can tune and/or cooperatively react with substrates. The best of these systems is the borane analog, which can generate 59(±6) equivalents of ammonia per Fe although the yield is low (12 % NH₃/H⁺). The reactivity was also susceptible to the quality of the reagents used, with crystalline (Et₂O)₂HBArF providing the best results. The catalysis was seen to be most efficient when potassium graphite (KC₈) was used as compared with alternative reductants such as sodium amalgam.

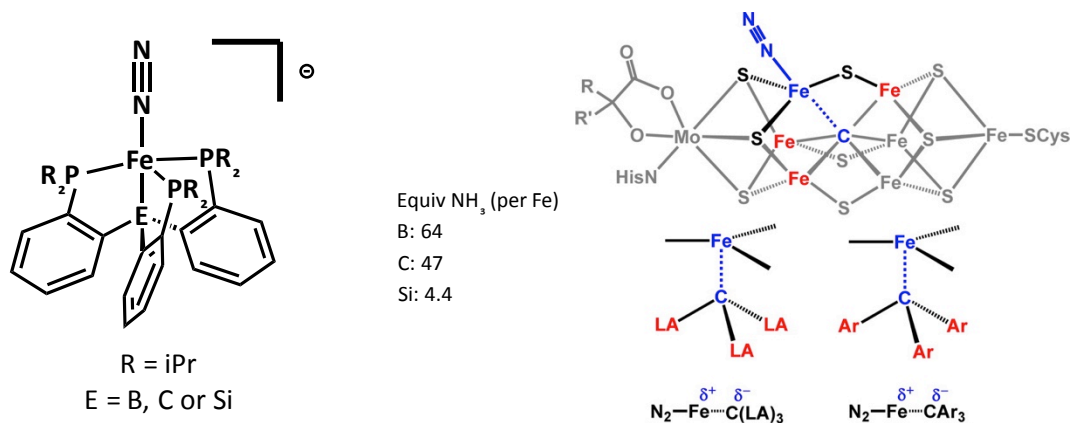


Figure 1.3.7 Left: Structure of (N₂)FeP₃^E catalyst with equiv of NH₃ produced. Right: Qualitative comparison of (N₂)FeP₃^E system compared to a proposed N₂ species in the FeMo-cofactor. Taken from ref 38.

The FeP₃^E system also allowed for mechanistic investigation into the catalytic reaction. Several potential intermediates have been independently characterized through Mössbauer spectroscopy.³⁹ The isolation of these prior species allowed for *in situ* monitoring of the reaction mixtures by freeze-quenching the solution and examination via Mössbauer spectroscopy.²³ From the Mössbauer data, a mechanism was proposed (Figure 1.3.8) which suggests a third mechanism for dinitrogen reduction. From this study, it was found that a dihydride species was the resting state of the catalyst. This dihydride species can be thought of as the pre-storage of 2 reducing equivalents at the iron center, similar to how nitrogenase stores hydrides prior to dinitrogen binding (*vide*

supra). When examining the N_2 reduction steps, it was found that a $Fe=N-NH_2$ species and a $Fe-NH_2-NH_2$ were present in the reaction solutions. These observations suggest that a possible third mechanism exists that is a combination of the Chatt/Schrock and alternating mechanisms.

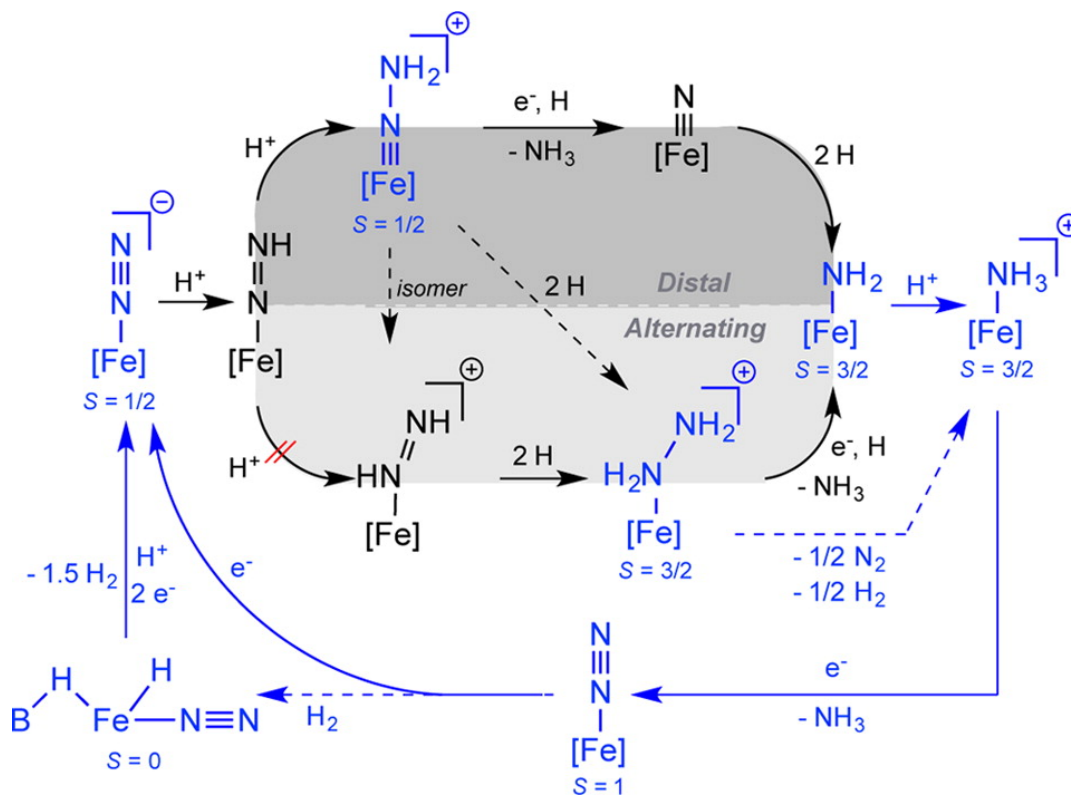


Figure 1.3.8 Potential catalytic scenarios for ammonia catalysis using FeP_3^B . Blue compounds have been characterized. Dashed lines are hypothesized to not be feasible under catalytic conditions ($-78^\circ C$) although the crossover from $N-NH_2$ to NH_2-NH_2 is observed using FeP_3^{Si} and is believed to be a key intermediate in catalysis. Taken from ref 23.

1.4 Cobalt N₂ Compounds

Although Co has lower energy d-orbitals for a given oxidation state than Fe, several examples of Co-N₂ compounds exist in the literature. In fact, a search of the Cambridge structural database⁴⁰ (CSD) harvests 58 structurally characterized Co-N₂ species, including one from the work in this thesis. Many of these compounds have unique ligand environments that tune the metal center as seen in Figure 1.4.1.⁴¹ As well, the majority of these compounds contain strong-field ligands and possess lower coordinate cobalt centers, which facilitate higher d-orbital energies due to the change in the ligand field. As expected by going across the period table, the N₂ units in these compounds are less activated than those in isostructural Fe compounds (Table 1.4.1). In fact, in all of the trigonal alkyl phosphine systems, the average $\Delta\nu_{N_2}$ between isostructural Fe and Co systems is 70 cm⁻¹, correlating with the differences in d-orbital energies between the respective metals.

Interestingly, this $\Delta\nu_{N_2}$ difference is much smaller in anionic β -diketimate and borate compounds. In the case of the β -diketimate systems, the N₂ unit is further activated through interactions with alkali cations (Na and K). This leads to the N₂ unit to be formally assigned as N₂²⁻ fragment in both the Fe₂ and Co₂ cases. It is believed that interactions of alkali metals in the N₂ coordination sphere account for the similar activation of N₂ between the two metals. This is further corroborated through the structural comparison of the neutral Fe₂ and Co₂ bridging N₂ compounds (no ν_{N_2} has been reported for the Co₂ system), in which the Fe₂ species was seen to have a longer N₂ distance compared to the isostructural Co₂ compound (1.189Å and 1.139Å respectively) corresponding to the observed periodic trend between Fe and Co.⁴² When examining the

N_2 fixation of these cobalt compounds to ammonia, only one compound, $TBPCo(N_2)^-$ from has been found to exhibit marginal activity (2.4 equiv per Co) relative to iron and molybdenum catalysts (Figure 1.4.2).^{41j}

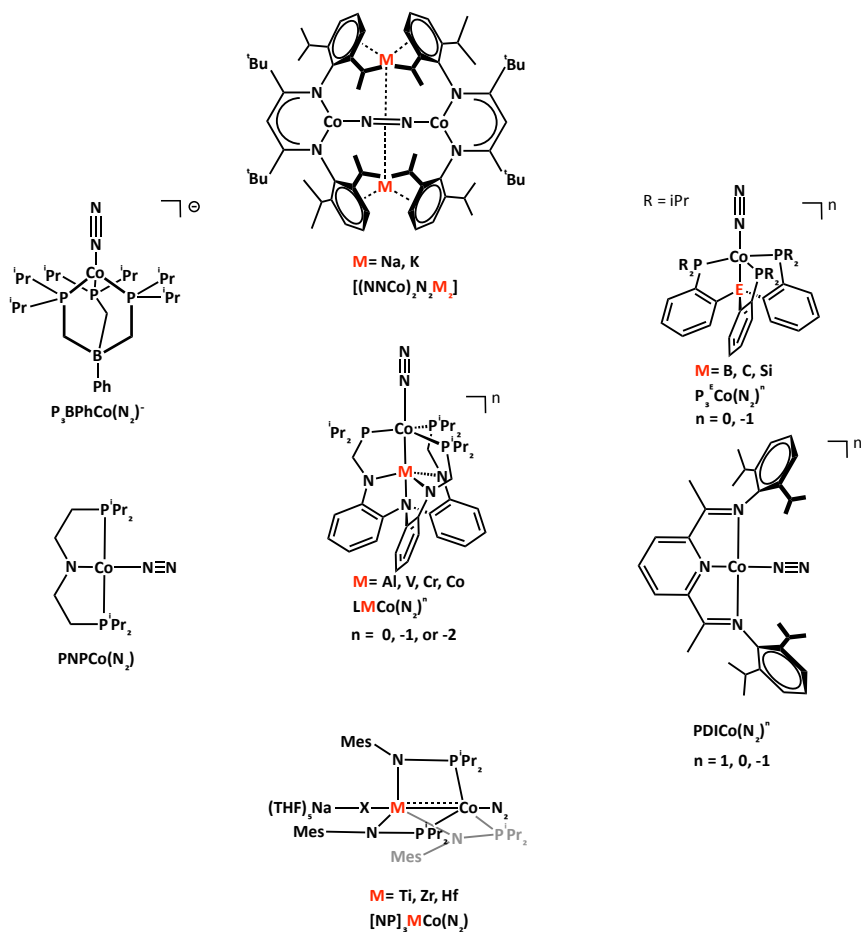


Figure 1.4.1 Select examples of $Co(N_2)$ compounds

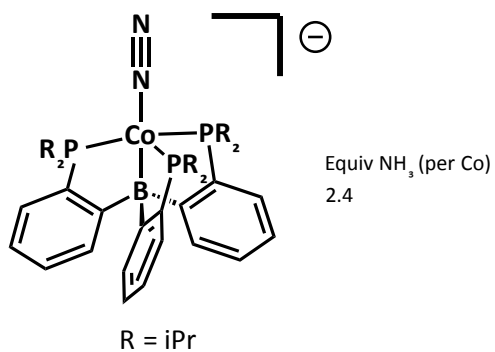


Figure 1.4.2 $TBPCo(N_2)$ and its equivalents of ammonia generated from the reduction of N_2 .

Table 1.4.1 Comparison of Co(N₂) compounds activation of N₂.

Complex	Co oxidation state	ν_{N_2} (cm ⁻¹)	$\Delta\nu_{\text{N}_2}$ (Co vs Fe) ^a (cm ⁻¹)	ref
(PDI)Co(N ₂) ⁺	1	2184	N/A	41c
(PDI)Co(N ₂)	1	2093	57	41c
(PDI)Co(N ₂) ⁺	1	2046	N/A	41c
(PNP)Co(N ₂)	1	1999	N/A	41a
(P ₃ C)Co(N ₂)	1	2057	67	41j
(P ₃ Si)Co(N ₂)	1	2063	60	41f
(P ₃ B)Co(N ₂)	0	2089	78	41i
(THF)[NP] ₃ TiCo(N ₂)	0	2045	N/A	41l
(THF)[NP] ₃ ZrCo(N ₂)	0	2023	N/A	41g
(THF)[NP] ₃ HfCo(N ₂)	0	1992	N/A	41h
K ₂ [(NNCo)(N ₂)]	0	1599	10	41d
Na ₂ [(NNCo)(N ₂)]	0	1598	15	41d
(P ₃ BPh)Co(N ₂)	0	1896	12	41e
LAiCo(N ₂)	0	2081	71	41m
LAiCo(N ₂) ⁻	-1	1995	70	41m
LCrCo(N ₂) ⁻	-1	1990	N/A	41b
(P ₃ B)Co(N ₂) ⁻	-1	1978	73	41i
LVCo(N ₂) ⁻	-1	1971	N/A	41b

a: when isostructural compound exists

PDI: 2,6-(2,6-ⁱPr₂-C₆H₃-N=CMe)₂C₅H₃N); PNP: [N(CH₂CH₂PⁱPr₂)₂]⁻

P₃E: (P₃ = tris(*o*-diisopropylphosphinophenyl), E = borane, methyl, or silyl)

NP: (ⁱPr₂PNMes)₃; NN: 2,2,6,6-tetramethyl-3,5-bis(diisopropylphenylimido)-hept-4-yl

P₃BPh: [PhB(CH₂PPh₂)₃]⁻; L: N(*o*-(NHCH₂PⁱPr₂)C₆H₄)₃

Interestingly, several of the compounds just described are contained within a bimetallic core in comparable ligands. However, the differences lie in the nature of the cobalt center. For example, in a phosphamide (2-atom bridge, bottom Figure 1.4.3) framework from the Thomas group, all of the $MCo(N_2)$ containing compounds have an overall neutral charge, with no reports to my knowledge of the isolation of further reduced species.^{41g, 43} Conversely, in an amide-phosphine scaffold from the Lu group (3-atom bridge, center Figure 1.4.3), it was seen that only the anionic species bind dinitrogen.^{41b} This difference can be attributed to the bimetallic cores in the 3-atom bridge having strong metal-metal bonds in the overall neutral complex. The bond strength can be qualitatively understood by examination of the lone pair orbitals on the phosphines of Lu's and Thomas's ligands (Figure 1.4.3). The near 90° angle in Lu's system pushes the metals closer together, causing better orbital mixing and stronger metal-metal bonds.

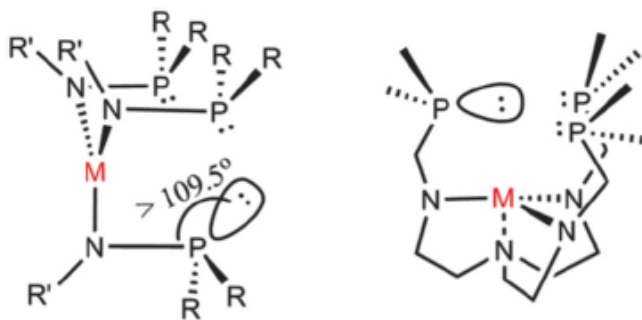


Figure 1.4.1 Comparison of phosphine orbitals of Thomas and Lu ligands. Taken from ref 43b.

However, through addition of an electron(s) the metal-metal bond is broken and the cobalt center is able to bind N_2 . Intriguingly, this phenomenon is not observed within the iron bimetallic compounds. One hypothesis is the d-electron count of iron upon

reduction is not high enough to disrupt the metal-metal bond, which are much stronger in the M-Fe cases (triple bonds) compared to M-Co bonds (double and single bonds). As well, it is likely that the lower polarity of the bonding in the M-Fe compounds vs the M-Co compounds also plays a role. These observations are mildly similar to the reductive activation of the FeMo-cofactor prior to dinitrogen binding. Reactivity with these MCo(N₂) species are currently under investigation for their reduction of dinitrogen to silyl amines.⁴⁴

1.5 Bimetallic Cooperativity

As seen in the previous sections, pairing a metal with a Lewis acid or other transition metal facilitates electron storage through reduction or activation of H₂ to form metal hydrides. In some cases, the storage of electrons also leads to binding of N₂ and the activation of the N₂ ligand can be tuned by changing the bimetallic pair. Those reactions with small molecules can be viewed as cooperativity between the metal pair. Likewise, many reactions involving metallo-enzymes that activate small molecules are possible due to two or more metal centers working in concert with one another.⁴⁵ Taking lessons from nature, this multimetallic cooperativity has been applied to synthetic systems (Figure 1.5.1). One way of promoting cooperativity is by having ligand scaffolds that can hold two different metals, allowing one to tune the other and/or interact with substrate.⁴⁶ Another way is through the formation of unsupported metal-metal bonds, which are then able to work in tandem with different substrates and eventually reform to regenerate the resting state of the catalyst.⁴⁷ An example of each of these strategies will be presented in the following paragraphs.

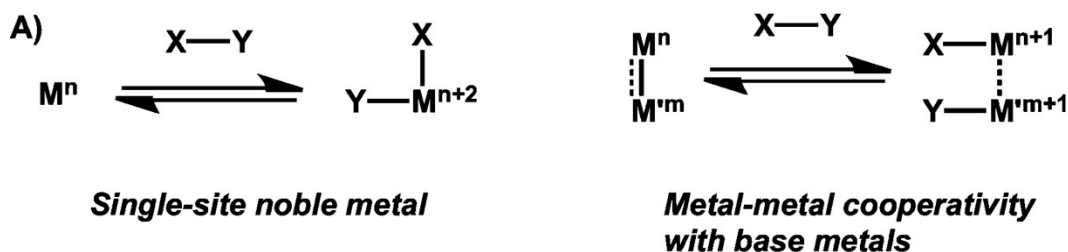
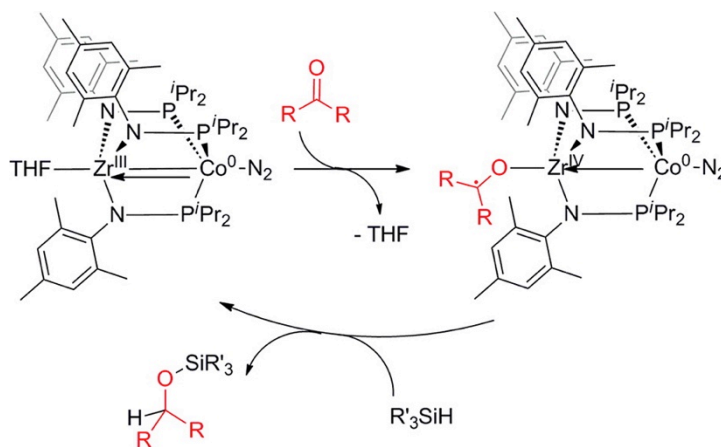


Figure 1.5.1 Comparison of single site oxidative addition (left) and bimetallic cooperative oxidative addition (right). Taken from reference 53.

As mentioned previously, the Thomas group has been able to synthesize several MCo as well as other various hetero- and homobimetallic compounds. Of note is a Zr-Co complex, which was observed to promote Kumada couplings⁴⁸, CO₂ activation⁴⁹, H₂ activation⁵⁰, and hydrosilylation⁵¹ of ketones. In all cases, the multiple bond between the metals, which is polarized, is disrupted either through substrate activation at one metal, or across the metal-metal bond. The polarized nature of the metal-metal bond allows the multiple bond to be more activated, similar to that of C=O bond. For example, in the hydrosilylation catalysis, the substrate can be activated via the polarized bond and upon reaction with substrate, is released with concomitant reformation of the metal-metal multiple bond (Scheme 1.5.1).



Scheme 1.5.1 Example of hydrosilylation catalysis using Zr-Co bimetallic. Note the fluxionality of the metal-metal bond. Taken from reference 51.

Another example bimetallic from the Thomas group, $(\text{THF})[\text{NP}]_3\text{TiCo}(\text{N}_2)$, can be used as a catalyst for the disproportionation of hydrazine (N_2H_4) to ammonia at room temperature.⁴¹¹ Interestingly, the isoelectronic Zr-Co complex does not fully disproportionate hydrazine and forms ammonia and a zirconium bound η^2 -hydrazido-ZrCo species.⁵² The Ti-Co complex is believed to operate through disproportionation to generate a bound diazene adduct ($\text{HN}=\text{NH}$) across the Ti-Co bond (Figure 1.5.2). It is then hypothesized to react with another molecule of hydrazine to generate ammonia and N_2 . This catalyst can generate 22 equivalents of ammonia at room temperature. When methylhydrazine (MeNHNH_2) is used, a 3:1 mixture of $\text{NH}_3/\text{MeNH}_2$ Ti-Co adducts are isolated. The authors report that similar product distribution is observed in other systems believed to go through diazene intermediates. Finally, when the Ti-Co bimetallic was reacted stoichiometrically with either azobenzene ($\text{Ph-N}=\text{N-Ph}$) or 1,2-diphenylhydrazine (Ph-NH-NH-Ph), the metal-metal bond was cleaved to generate an oxidized decomposition product (Scheme 1.5.2). The authors note that while the isolated product is a decomposition complex, the first step with the substituted substrates is likely binding across the metal-metal bond. The decomposition is likely due to the ineffective disproportionation due to the substitution of the substrates.

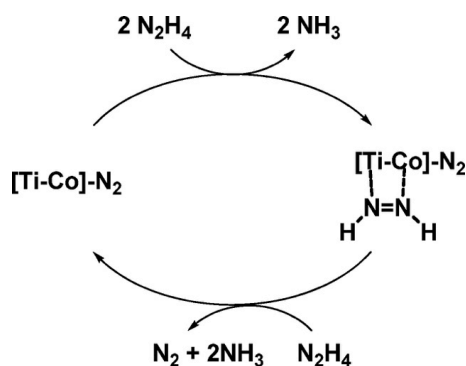
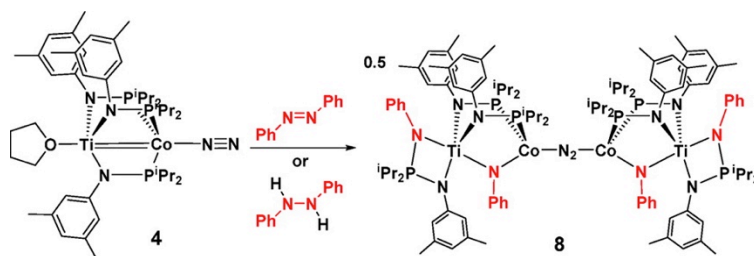


Figure 1.5.2 Proposed catalytic cycle for hydrazine disproportionation using $(\text{THF})[\text{NP}]_3\text{TiCo}(\text{N}_2)$ as the catalyst. Taken from reference 411.



Scheme 1.5.2 Scheme showing the reaction of $(\text{THF})[\text{NP}]_3\text{TiCo}(\text{N}_2)$ with azobenzene or 1,2-diphenyl hydrazine. Taken from reference 411.

One recent example from Mankad *et al.* utilizes electrophilic organometallic compounds (i.e. NaFp , $\text{Fp} = [\eta^5\text{-C}_5\text{H}_5\text{Fe}(\text{CO})_2]^+$) and nucleophilic metal N-heterocyclic carbenes (NHC) compounds (i.e. IMesCu , $\text{IMes} = 1,3\text{-bis-(2,4,6-trimethylphenyl)imidazol-2-ylidene}$) to promote a variety of catalytic processes including aryl C-H borylation⁵³ and CO_2 hydroboration⁵⁴. For example, a Fe-Cu (IMesCu-Fp) complex catalyzes aryl C-H borylation (Figure 1.5.4). The reformation of a metal-metal interaction and concomitant formation of H_2 facilitate the photochemical aryl C-H borylation catalysis. As well, incorporation of a Cu cation prevents the formation of the catalytically inert Fp-dimer, $([\eta^5\text{-C}_5\text{H}_5\text{Fe}(\text{CO})\mu\text{-CO}]_2)$ through reductive elimination of a FpH and IMesCuH fragment to give H_2 and the starting Fe-Cu bimetallic.

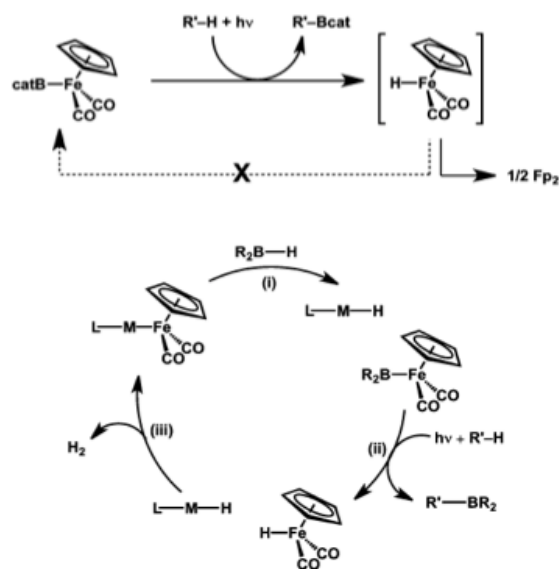


Figure 1.5.3 Depiction of the stoichiometric (top) aryl C-H borylation and catalytic (bottom) aryl C-H borylation using a Cu-Fe catalyst ($\text{M} = \text{Cu}$, $\text{L} = \text{IMes}$). Taken from reference 53.

A unique dichotomy exists with the bonding interactions of the Fe and Cu metal centers. While bond reformation is a key catalytic step, the bond has to be relatively weak to allow for oxidative addition across the metal-metal bond. The Fe-Cu bond distance is relatively short at 2.3462(5) Å suggesting a covalent single bond. However, DFT calculations performed for the Fe-Cu bimetallic suggest a different bonding interaction through analysis of the Wiberg bond order (WBO).⁵⁵ A WBO of 0.39 was calculated for the Fe-Cu bimetallic, suggestive of a dative $\text{Fe} \rightarrow \text{Cu}$ bond with significant ionic character and a polar metal-metal bond. The polarity of the bond is believed to allow the metals to readily react with polarized substrates and generate a reactive species.

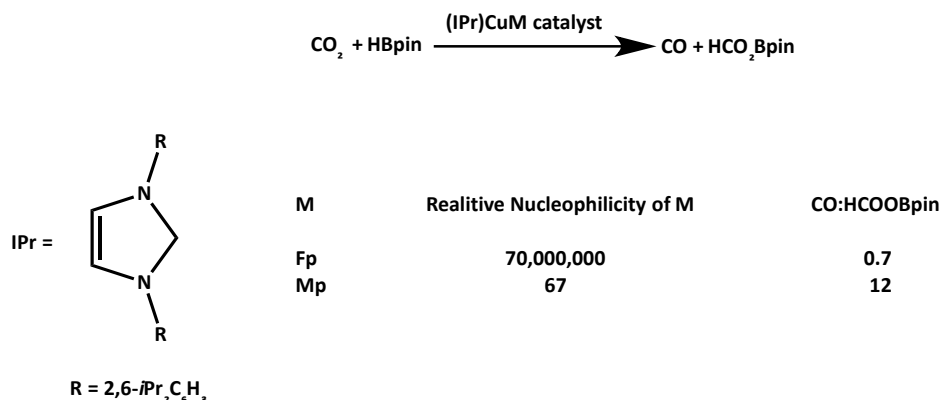


Figure 1.5.4 Example of how nucleophilicity changes product distribution. Taken from reference 47.

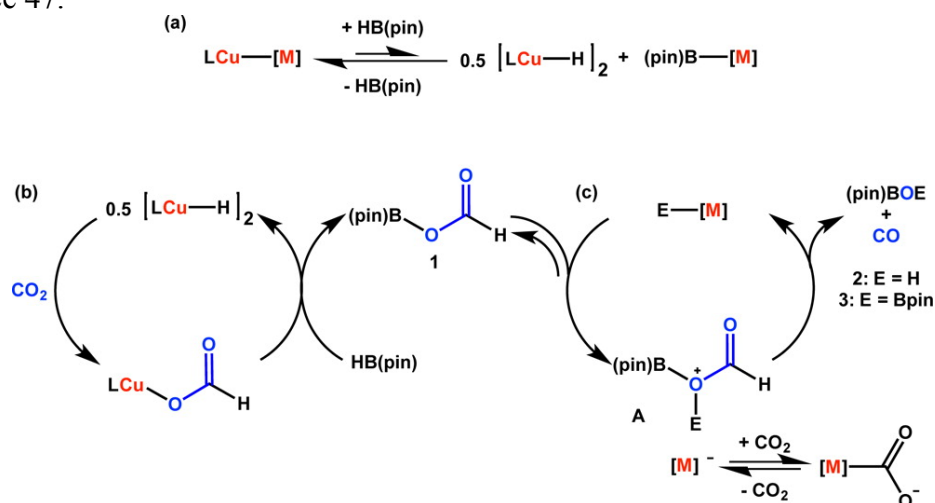


Figure 1.5.5 Hypothetical mechanism for a) catalyst activation b) CO₂ hydroboration c) CO₂ – assisted formate decarbonylation. Taken from reference 53.

Mankad's bimetallic system provides a unique template for designing different catalysts by modulation of the bimetallic pairs. In fact, a fine interplay exists between the metal pairs, with different combinations promoting certain reactions involving the same substrates. For example CO₂ hydroboration functions with the Cu-Fe combination (IPrCu-Fp, IPr = 1,3-bis-(2,6-diisopropylphenyl)imidazol-2-ylidene) and Cu-Mo (IPrCu-Mp, Mp = [η^5 -C₅H₅Mo(CO)₃]), but generates different products (Figure 1.5.4).

The catalyst works by activation of the bimetallic pair to form the IPrCu-H and M-Bpin (M = Fe or Mo Figure 1.5.5 (a)), which is in equilibrium with the starting bimetallic

(IPrCu-M, M = Fp or Mp). The catalysis then proceeds in tandem with first hydroboration of CO₂ by IPrCu-H to generate the borylated formate product (Figure 1.5.5 (b)). Finally, decarbonylation of the formate via M generates CO and the diborylether (Figure 1.5.5 (c)).

When the Cu-Fe pair is used, a mixture of the borylformate product (3.0 equiv) and the diborylether (2.1 equiv) are formed with very little CO (0.7:1, CO:HCO₂Bpin). However, upon swapping the catalyst to a Cu-Mo pair, the tandem catalysis is more facile and is selective toward the formation of CO and the diborylether (3.5 equiv).⁵⁴ Interestingly, when the NHC is changed to the less sterically hindered IMes NHC, both Cu-Fe and Cu-Mo pairs were competent in generating CO from CO₂ (>20:1, CO:HCO₂Bpin). This result was due to the increased accessibility of the bimetallic core by H-Bpin to generate the catalytically active species.

These pairs function differently due to the change in nucleophilicity of the second metal (Figure 1.5.4). It is hypothesized that the decarbonylation step is related to the lability of the M-Bpin fragment to form a M⁻ fragment, which is sequestered by CO₂. The trend is inverse of the nucleophilicity with Mp⁻ > Fp⁻. The nucleophilicity also causes changes in the metal-metal interaction, making the Cu-Mo bond weaker, thus pushing the equilibrium with H-Bpin toward the catalytically active species.

1.6 Thesis Scope

The scope of this thesis consists of the synthesis and characterization of several dicobalt compounds. It is hypothesized that pairing two electron-rich transition metals could help promote the activation and reduction of dinitrogen. This hypothesis arises from the lessons learned from biological dinitrogen fixation and how the multi-metallic core of the FeMo-cofactor is essential to storing electrons and priming the enzyme for dinitrogen fixation.

Although cobalt is not traditionally the target metal for N_2 activation due to its relatively low-energy d-orbitals, the use two cobalts would potentially tune the d-orbitals through orbital mixing and storing of electrons in high lying orbitals. The increase in electrons would lead to higher energy d-orbitals, which then can interact more strongly with the N_2 π system. The greater electron counts then can donate into the dinitrogen ligand, thus priming it for activation and reduction. At the start of this thesis work, the use of cobalt to catalytically reduce dinitrogen was scarcely explored. This thesis will show that, in fact, cobalt can reduce dinitrogen and become a viable metal in the silylation of dinitrogen to tris(trimethylsilyl)amine. It will also be shown that the cobalt center can be tuned by changing the *trans* metallo-ligands, which leads to changes in dinitrogen activation and reactivity. Finally, exploration of the dinitrogen silylation mechanism will be discussed.

Chapter 2

Synthesis and Characterization of Dicobalt Compounds

In part from:

Siedschlag, R. B.; Bernales, V.; Vogiatzis, K. D.; Planas, N.; Clouston, L. J.; Bill, E.;
Gagliardi, L. ^{*}; Lu, C. C. “Catalytic Silylation of Dinitrogen with a Dicobalt Complex.” *J.*
Am. Chem. Soc. **2015**, *137*, 4638-4641

2.1 Overview

Through the use of a heptadentate scaffold, a bimetallic cobalt complex has been synthesized. The scaffold, $N(o\text{-(NHCH}_2\text{P}(\text{iPr})_2)\text{C}_6\text{H}_4)_3$, abbreviated as H_3L , was deprotonated using *n*-butyl lithium and subsequently metallated with two equivalents of a cobalt dihalide, CoCl_2 or CoBr_2 , to yield a bimetallic cobalt complex, LCo_2X (**1-Cl** or **1-Br**), respectively. Through chemical reduction of the bimetallic halide, a mixed-valent coordinatively unsaturated dicobalt complex can be isolated, LCo_2 (**2**). Through electrochemical analysis and chemical reduction, two other reduced states for the bimetallic core can be observed and synthesized, $[\text{LCo}_2(\text{N}_2)]^-$ (**3**), and $[\text{LCo}_2(\text{N}_2)]^{2-}$ (**4**). It was found that **2** has a high spin electronic configuration despite having the shortest mixed-valent cobalt-cobalt bond. Compound **2** was also found to bind N_2 at low temperatures providing a series of a dicobalt- N_2 compounds in three different oxidation states. The metal-metal bonding and electronic structure of these complexes were examined.

2.2 Introduction

Understanding the interactions between two transition metals is important for explaining various phenomena within biological⁵⁶ and heterogeneous catalysts,⁵⁷ electron transfer within semi-conductor materials and electron sources in photovoltaics.⁵⁸ More specifically, interactions between first-row transition metals have the potential for multi-electron reactions that are typically only attainable by 2nd and 3rd row transition metal compounds. However, direct metal-metal interactions between first-row metal are challenging to accomplish due to compacted 3d orbitals, which result in poor orbital overlap with other first-row metals. Furthermore, a dichotomy exists between orbital overlap and electron-electron repulsion, especially in high-spin first-row bimetallics. While overlap increases covalency, electron-electron repulsion becomes greater resulting in weaker bonds compared to 2nd and 3rd row bimetallic pairs.⁵⁹

In line with the quandary that limits the strength of bonds between first row metals is the fact that there are still few examples of first-row metal-bonded compounds compared to 2nd and 3rd row species. Specifically, dirhodium is one of the most extensively studied homobimetallic (more than 1800 complexes as of 2005), not only for characterization but reactivity as well.⁶⁰ When examining dicobalt compounds with short Co-Co bonds, many exist as adducts of $\text{Co}_2(\text{CO})_8$ to alkyne, alkene or carbonyl moieties or as extended metal chains (EMACs).^{60b} Only a small set of bimetallic cobalt compounds (13 as of early 2015) are present in the literature. These compounds have interesting magnetic properties and a potential for multi-electron redox chemistry. Select examples are shown in Figure 2.2.1.

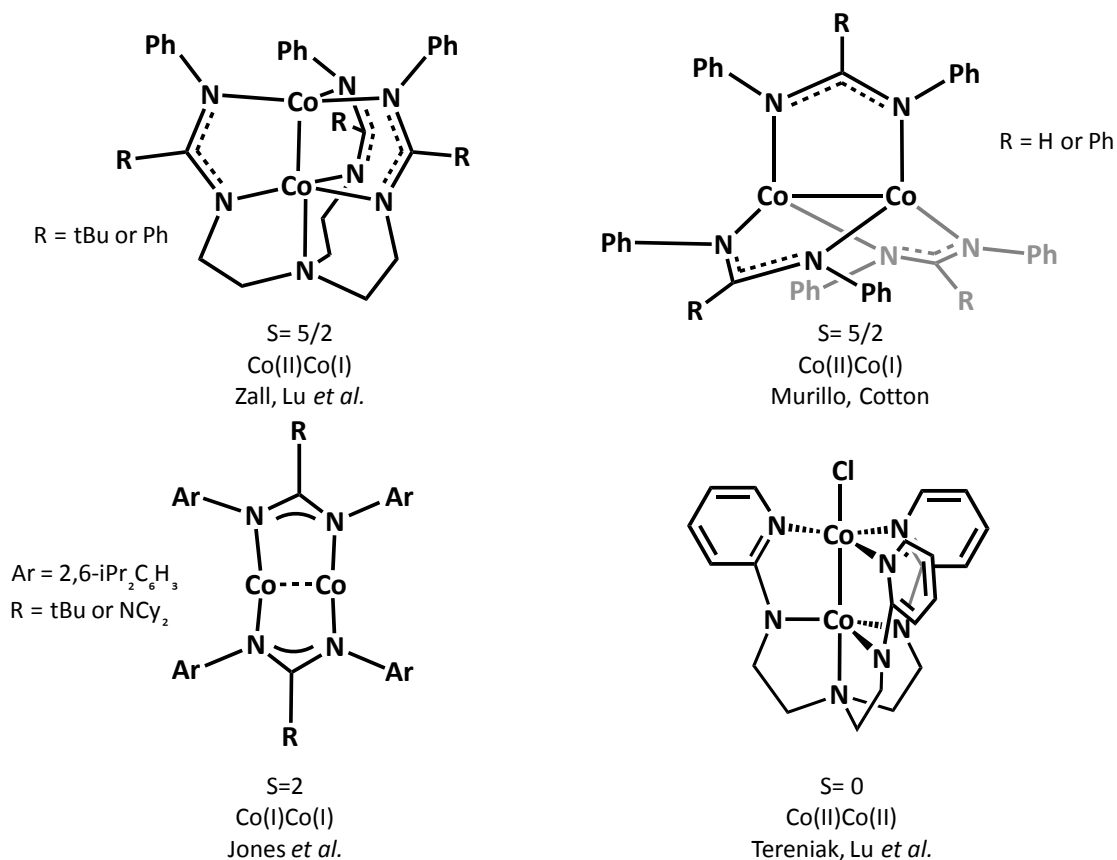


Figure 2.2.1 Select examples of bimetallic cobalt compounds.

The first examples of supported bimetallic cobalt compounds containing a Co-Co bond were a formamidinate trigonal and tetragonal paddlewheel complexes synthesized and characterized by Cotton *et al.*⁶¹ The trigonal and tetragonal paddlewheels are interesting due to the paramagnetism of the former and the diamagnetism of the latter. Isostructural Fe_2 compounds are known and offer interesting comparison. One difference between the diiron and dicobalt complexes is the diiron tetragonal and trigonal variants are high spin ($S = 4$ and $S = 7/2$ respectively).⁶² The reason for the differences in the dicobalt systems can be seen in the electronic structure of the trigonal and tetragonal systems (Figure 2.2.2). The tetragonal dicobalt compound has an electronic structure of $(\sigma)^2(\pi)^4(\delta)^2(\delta^*)^2(\pi^*)^4(\sigma^*)^2$ with the second set of δ -symmetry orbitals being destabilized

by anti-bonding interactions with the ligands. When going from tetragonal to trigonal symmetry, all of the δ orbitals are accessible and lead to an electronic configuration of $(\sigma)^2(\pi)^4(\pi^*)^4(\sigma^*)^1(\delta)^2(\delta^*)^2$. This leads to the π^* orbitals being doubly occupied leading to purely σ contributions to the metal-metal bond. Preliminary magnetic measurements indicated a $S = 3/2$ ground state, which was later revisited and found to be $S = 5/2$.⁶³ These results lead to the assignment of a Co-Co bond-order of 0.5. Similar to the diiron complexes, it is believed that the Co_2^{3+} core is not a localized Co(II)Co(I) core but rather a delocalized Co(1.5)Co(1.5) core.

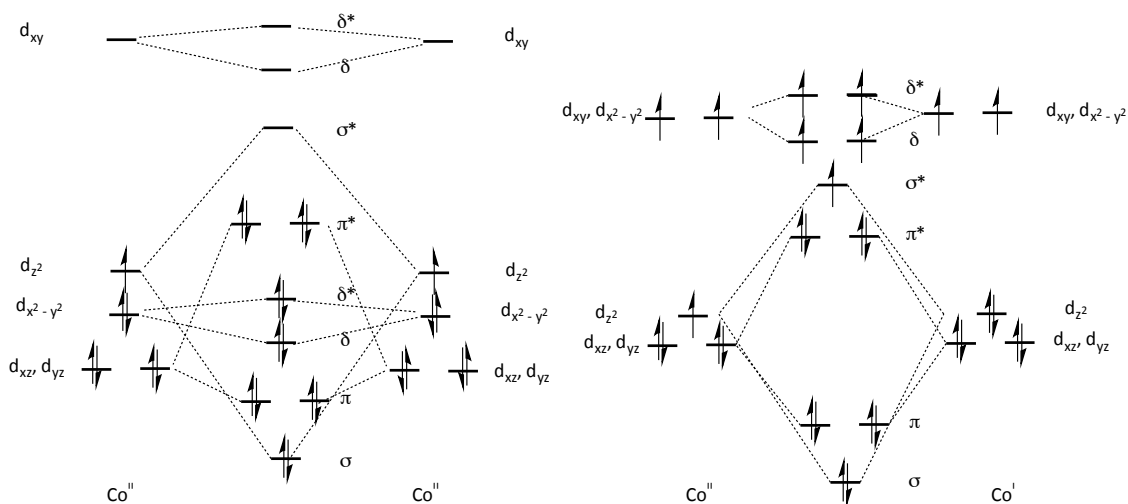


Figure 2.2.2 Qualitative MO diagram for Co_2 in a tetragonal (left) and trigonal (right) framework.

Recently, the Lu group was able to examine trigonal dicobalt species in a similar delocalized ligand frameworks.⁶³ It was found in that a dicobalt species in a tris(amidinato)amine ligand could be isolated and that it had a Co-Co bond shorter than that of the formamidinate dicobalt compounds (2.2944(7) Å vs 2.320(1) Å respectively). In addition, a well-isolated $S = 5/2$ ground state was found to be the primary configuration of the Co_2^{3+} , which was formally assigned analogously to the trigonal lantern dicobalt species.

By making the scaffold more electron-localized (i.e. removing charge localization within the backbone), tris(amidinato)amine to tris(2-(2-pyridylamino)ethyl)amine, the Lu group could isolate a Co_2^{4+} core.⁶⁴ This complex was found to have a $S = 0$ ground state with thermally accessible paramagnetic excited states at room temperature. Like the amidinate systems, a Co_2^{3+} was accessible but only as a transient species. Interestingly, attempts to reduce the core with Grignard reagents resulted in the formation of a cobalt-cobalt organometallic with a $S = 1$ ground state.⁶⁵

The shortest Co-Co bonds to date (2.13 and 2.14 Å) were isolated by Jones et al. using amidinato-and guanidinato ligands.⁶⁶ Surprisingly, despite the short Co-Co bond, these compounds were found to have high-spin $S = 2$ Co_2^{2+} cores. While the Co-Co bond was believed to be multiple in nature based on structural evidence, the multi-configurationality of the bonding through theoretical calculations made the bond-order assignment ambiguous.

Up to this point, the dicobalt compounds discussed were in similar delocalized ligand sets. As was seen in the examples from the Lu group, changing the ligand donors on each metal center can cause changes in the properties of the metal-metal interactions. An example of even greater ligand localization comes from Thomas *et al.* (Figure 2.2.3), which utilized a phosphino-amide (NP) ligand to provide to unique ligand environments for two cobalts. This ligand was previously utilized for the formation of trigonal heterobimetallic compounds (e.g. ZrCo^{41g} and CrCo^{43}). The pairings has also been extended to homobimetallic of late metals, diiron⁶⁷ and dicobalt.⁶⁸

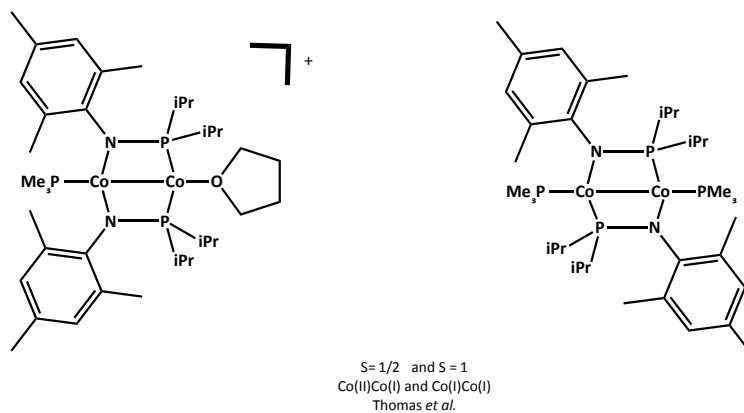


Figure 2.2.3 Examples of dicobalt complexes in a localized ligand framework.

In the case of diiron, trigonal compounds can be isolated and characterized in the NP scaffold, whereas to date only low-coordinate a Co(I)Co(I) complex and a Co(II)Co(I) complex have been isolated (Figure 2.2.4). In these complexes, the Co(I)Co(I) complex is symmetric with an intermediate $S = 1$. The Co-Co bond is also longer (2.5536(3) Å) relative to other Co(I)Co(I) complexes. This is most likely due to the orientation of the phosphorous lone pairs, inhibiting closer metal-metal interactions. Upon oxidation with ferrocenium hexafluorophosphate, the ligand rearranges in which the amides bind a formally Co(II) center and the phosphines bind a formally Co(I) center. The Co-Co distance contracts and the spin-state decreases to $S = 1/2$.

2.3 Results and Discussion

2.3.1 Synthesis and ^1H NMR Spectroscopy

Dicobalt species containing direct metal-metal interactions have been achieved through various synthetic methods. The most forward route to the homobimetallic is through a one-pot salt metathesis synthesis, in which two equivalents of cobalt precursor are added to the deprotonated ligand. Thomas *et al.*, were able to use to this synthetic route to generate a low coordinate dicobalt core with two equivalents of deprotonated ligand and a bridging halide.⁶⁸ Of note, the two amide-phosphine ligands are bound symmetrically to the cobalt centers. Alternatively, the two cobalt metals can be discriminately added one at a time to form the corresponding monometallic and bimetallic species. Prior work in the Lu group has shown this to be a feasible route to the generation of bimetallic cobalt species.⁶³⁻⁶⁴

Using the one-pot synthetic method, we have successfully synthesized dicobalt(II,II) chloride (**1-Cl**) by adding two equivalents of CoCl_2 to Li_3L (Scheme 2.3.1). Complex **1-Cl** is isolated with a 95% yield as a dark purple solid. Complex **1-Cl** can be crystallized from a toluene solution layered with pentane in ~60% crystalline yield. The ^1H NMR spectrum of **1-Cl** exhibits 11 paramagnetically shifted resonances between -3 and 76 ppm (Figure 2.3.1). A completely symmetric complex (C_{3v} solution symmetry) would display 8 proton resonances for the 4 aryl protons, the 1 methine proton, 1 methylene and 2 methyl protons. Prior work with bimetallic complexes containing H_3L have shown the C_3 solution symmetry with 12 proton resonances which would disrupt the mirror plane, making all methyl, methylene and methine protons inequivalent.^{41m, 69} Due to crystallographic structural data, (*vide infra*) **1-Cl** is believed to be C_3 symmetric and the corresponding 12th proton signal is either paramagnetically broadened or coincident

The addition of potassium graphite (KC_8) to **1** in THF causes a color change from purple to brown to yield complex **2** in high crude yield (89%). Product **2** can be further purified through bulk crystallization via layering a concentrated THF solution of **2** with diethyl ether to yield about ~50% of crystalline **2**. The ^1H NMR of **2** in d^8 -THF is shown in Figure 2.3.2. While structural analysis shows a nearly $\text{C}_{3\text{V}}$ symmetric molecule (*vide infra*), only six of the expected eight paramagnetically shifted proton resonances can be observed in the solution state, ranging from 60 ppm to -48 ppm. The remaining two resonances are buried under residual solvent resonances. Interestingly, when the NMR solution is degassed and the spectrum is run, the ^1H resonances sharpen, and paramagnetically shift to give a range of resonances from 63 ppm to -51 ppm. As will be discussed in later sections of this chapter, this phenomenon is likely due to dinitrogen binding to the bimetallic core.

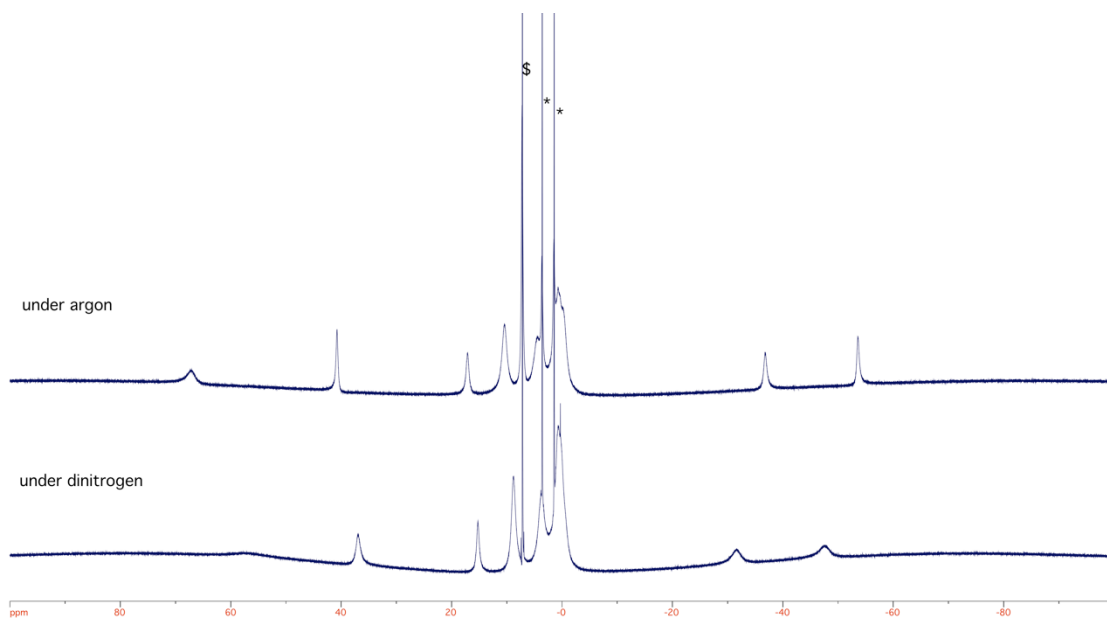


Figure 2.3.2 ^1H NMR spectrum (300 MHz, d^8 -THF) of **2** in N_2 (bottom) and Ar (top) *= THF, \$= benzene.

It was found through electrochemical measurements (*vide infra*) that complex **2** can be reduced by one and two electrons to give the respective mono-anionic and di-anionic species. The mono-anionic species, **3**, can be obtained through reacting **2** with one equivalent of KC_8 at room temperature for four hours. The reaction mixture changes from brown to yellow almost instantaneously. The reaction is filtered into a vial containing one equivalent of 4,7,13,16,21,24-hexaoxa-1,10-diazabicyclo[8.8.8]hexacosane (2,2,2-cryptand) and the solvent is removed to give complex **3**. Complex **3** can be further purified through by washing with benzene to give a crude yield of 89%. Bulk crystals of **3** can be obtained through the layering of diethyl ether onto a concentrated THF solution of **3** in 50% crystalline yield. The ^1H NMR of **3** in d^8 -THF is shown in Figure 2.3.3. The spectrum shows 8 paramagnetically shifted resonances from 202 ppm to -34 ppm. This is indicative of C_{3v} solution - state symmetry with the signals corresponding to 2,2,2-cryptand being masked by solvent resonances.

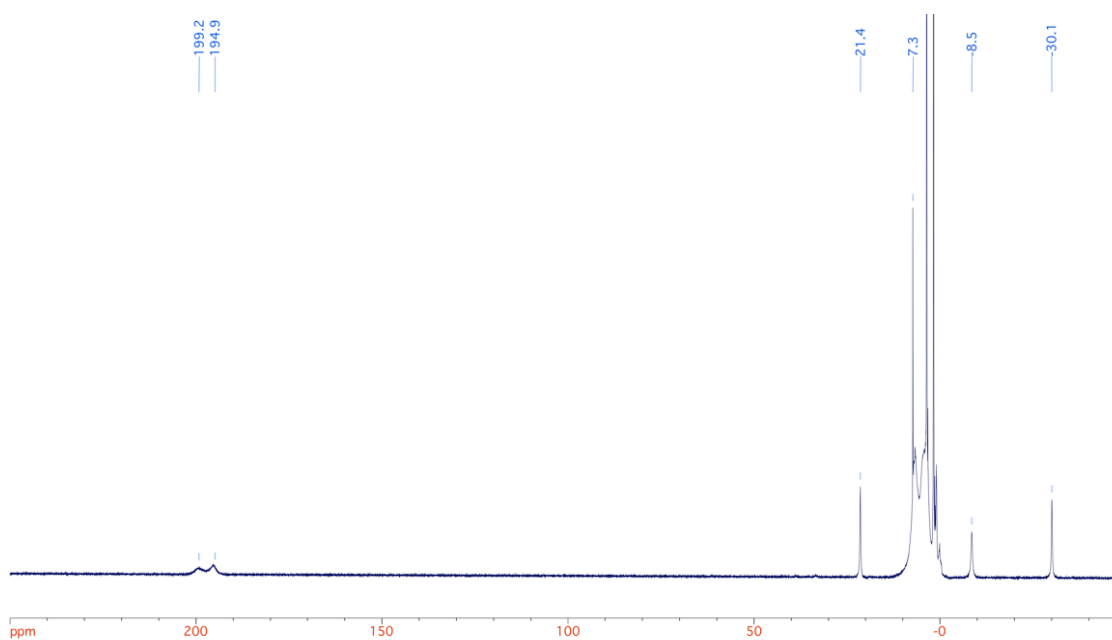


Figure 2.3.3 ^1H NMR spectrum (300 MHz, d^8 -THF) of **3**

The addition of two equivalents of KC_8 to **2** in THF after 12 hours results in a color change from brown to dark yellow. The resulting solution is filtered into a vial of 2,2,2-cryptand in which the solution changed colors from yellow to orange. The solution is removed *in vacuo* to give crude **4**. The ^1H NMR of **4** in d^8 -THF shows the expected 8 proton resonances for a C_{3v} symmetric molecule (Figure 2.3.4). The resonances range from 88 ppm to -28 ppm and have a similar splitting pattern to that of **3**. This can be attributed to the structural similarities of each complex.

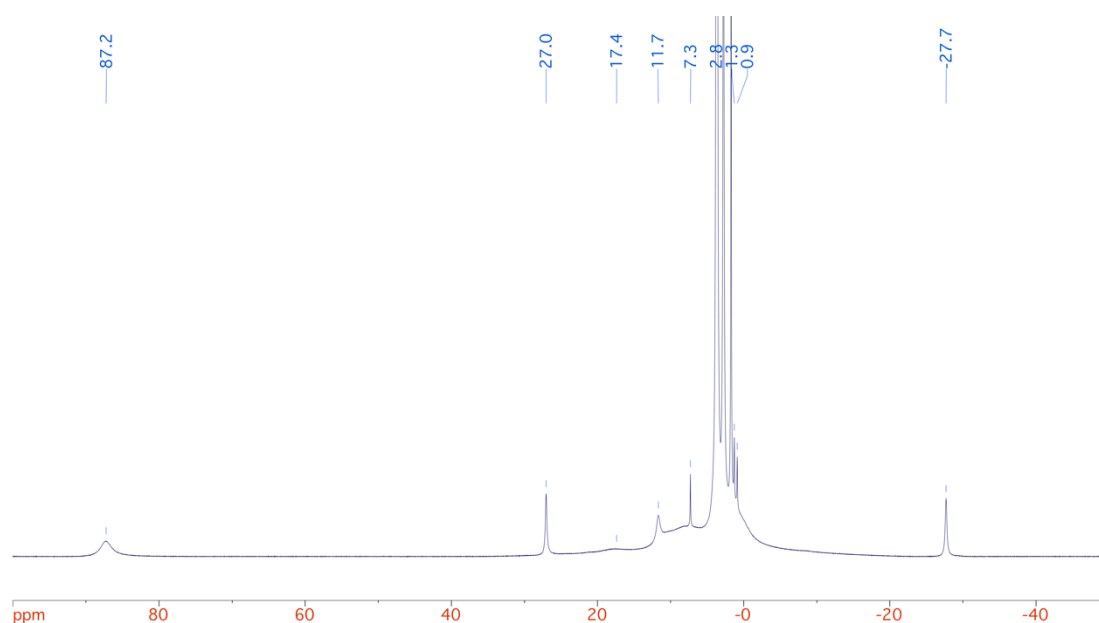


Figure 2.3.4 ^1H NMR spectrum (300 MHz, d^8 -THF) of **4**

2.3.2 Solid-state Structures

The molecular structures of **1-Br**, **2** and **3** have all been characterized through single-crystal X-ray diffraction and are shown in Figure 2.3.6. Attempts to attain single X-ray quality crystals for **4** have been unsuccessful to date. Each complex crystallizes in a different space group (Table 2.3.2): **1-Br** in the monoclinic space group $\text{P}2_1/\text{n}$, **2** in the monoclinic space group C_2 , and **3** in the orthorhombic space group P_{bca} . Important bond metrics can be found in Table 2.3.1. Structures are shown in Figure 2.3.5.

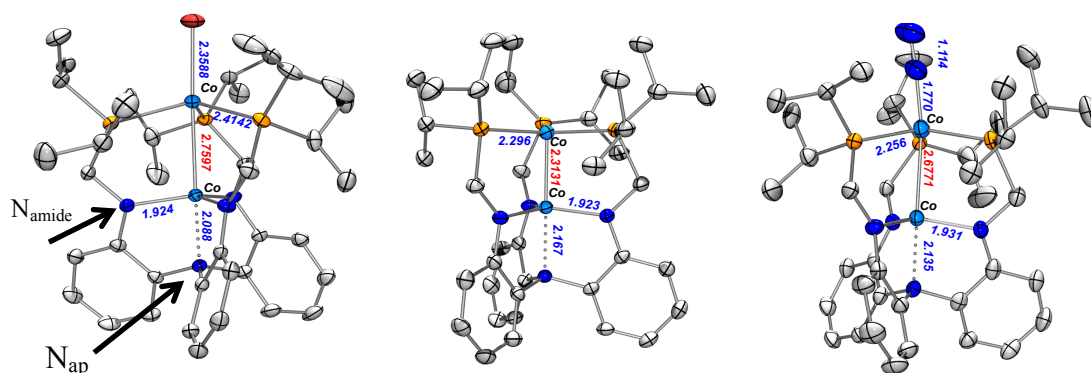


Figure 2.3.5 X-ray crystal structures of **1-Br**, **2**, and **3** at 50% probability. Hydrogen atoms and counterions were removed for clarity.

Table 2.3.1 Bond Metrics of **1-Br**, **2**, and **3**.

	1-Br	2	3
Co-Co	2.7597(4)	2.3131(6)	2.6771(7)
Co-X (X= Br or N ₂)	2.3588(4)	--	1.770(4)
N-N	--	--	1.114(4)
Co-P	2.4067(6), 2.4128(6), 2.4231(6)	2.288(1), 2.298(1), 2.303(1)	2.251(1), 2.252(1), 2.265(1)
Σ P-Co-P angles	343.84	358.64	351.47
Co-N _{amide}	1.917(2), 1.921(2), 1.936(2)	1.922(3), 1.923(3), 1.926(3)	1.929(3), 1.931(3), 1.933(3)
Σ N-Co-N _{amide} angles	355.99	357.45	355.1
Co-N _{ap}	2.088(2)	2.167(2)	2.135(3)

An important structural metric between complexes **1-3** is the Co-Co bond. Of note, the Co-Co bond can be modulated not only by the oxidation states of the metals themselves, but the axial donor on the phosphine coordinated cobalt (Co_P). For example, the Co-Co distance in **1-Br** is 2.7597(4) Å. Upon reduction, the Co-Co bond distance contracts to 2.3131(6) Å in **2** even though an electron is added to a formally σ* orbital (*vide infra*). Finally, upon reduction of **2** to **3**, the Co-Co bond distance elongates again to 2.6771(1) Å with concomitant binding of dinitrogen. The elongation of the cobalt-cobalt bond is hypothesized to be an effect of a trans-axial donor, which modulates the

metal-metal interaction. One way to understand the metal-metal interaction is through the formal shortness ratio, FSR⁷⁰, which is the quotient of metal-metal bond distance and sum of the covalent radii⁷¹ of the ions involved. For example, when a FSR is 1, it is interpreted as corresponding to a covalent single bond. As the sum of the metallic radii of two cobalt atoms is 2.314 Å, complex **2** has an FSR = 1 consistent with a Co-Co single bond, while complexes **1-Br** and **3** have a weak Co-Co interaction (FSR=1.16 and 1.14 respectively).

Table 2.3.2 Crystallographic Details for **1-Br**, **2**, and **3**.

	1-Br	2	3
chemical formula	C ₃₉ H ₆₀ BrCo ₂ N ₄ P ₃	C ₃₉ H ₆₀ N ₄ Co ₂ P ₃	C ₅₇ H ₉₆ Co ₂ KN ₈ O ₆ P ₃
formula weight	875.59	795.68	1239.33
crystal system	monoclinic	monoclinic	orthorhombic
space group	P2 ₁ /n	C ₂	P _{bca}
a (Å)	11.2942(5)	24.600(2)	21.5306(17)
b (Å)	23.5381(11)	14.009(1)	19.8037(15)
c (Å)	15.3249(7)	12.681(1)	31.964(3)
α (deg)	90	90	90
β (deg)	95.878(1)	97.223(1)	90
γ (deg)	90	90	90
V (Å ³)	4052.6(3)	4335.2(7)	13629.0(18)
Z	4	4	8
D _{calcd} (g cm ⁻³)	1.435	1.219	1.208
λ (Å), μ (mm ⁻¹)	0.71073, 1.956	0.71073, 0.906	0.01073, 0.668
T (K)	173(2)	173(2)	173(2)
θ range (deg)	2.308 to 27.480	1.67 to 27.50	1.27 to 27.55
reflns collected	9243	9837	15693
unique reflns	7342	8155	8464
data/restraints/ parameters	9243 / 0 / 454	9837 / 1 / 447	8464 / 0 / 702
R1, wR2 (I > 2σ(I))	R ₁ = 0.0471, wR ₂ = 0.0704	R ₁ = 0.0432, wR ₂ = 0.1013	R ₁ = 0.0582, wR ₂ = 0.1410

From the structural data, conclusions can be drawn as to where the reduction occurs in complexes **1**, **2**, and **3**. The reduction of **1** to **2** results in a large contraction of the Co-P bonds of $\Delta d_{\text{Co-P}} = 0.1179$ Å (an average of 2.4142 Å to an average of 2.2963 Å) indicative of increased π -back bonding to a more reduced cobalt center to the phosphine

ligands. However, the reduction of **2** to **3** only has a contraction of $\Delta d_{\text{Co-P}} = 0.0403 \text{ \AA}$ (an average of 2.2963 \AA to an average of 2.256 \AA). This contraction is lessened due to the binding of a dinitrogen ligand that can also participate in π -back bonding. When examining the bonding differences of the Co-N_{amide} bonds, going from **1** to **3** only has a change of $\Delta d_{\text{Co-N}} = 0.0063 \text{ \AA}$ (an average of 1.9247 \AA to an average of 1.9310 \AA), supporting the hypothesis of the reduction being localized to the phosphine bound cobalt.

Compared to literature compounds (*vide supra*), **2** was found to possess the shortest cobalt-cobalt bond in a trigonal framework. For comparison, **1-Br** possesses a surprisingly long cobalt-cobalt distance relative to a trigonal Co(II)Co(II) compound from Lu.⁶⁴ These differences in metal-metal interactions between **1-Br** and **2** are due to the flexibility of the ligand scaffold⁷² and the observation that apical ligands attenuate metal-metal bonding.^{41b, 69a}

2.3.3 *Vis-NIR Data*

Due to the range of colors and spin-states of complexes **1-4**, electronic absorption spectra were taken to lend insight into the electronic structure of the complexes. As shown in Figure 2.3.6, **1-4** have varying electronic absorptions (Table 2.3.3). Complex **1-Cl** has three absorptions in the visible (vis) region. A shoulder at $\lambda_{\text{max}} = 448 \text{ nm}$ ($\epsilon = 4000 \text{ M}^{-1} \text{ cm}^{-1}$), a primary absorbance at $\lambda_{\text{max}} = 554 \text{ nm}$ ($\epsilon = 5800 \text{ M}^{-1} \text{ cm}^{-1}$) and shoulder at $\lambda_{\text{max}} = 720 \text{ nm}$ ($\epsilon = 1230 \text{ M}^{-1} \text{ cm}^{-1}$) while complex **2** only has one intense absorption at $\lambda_{\text{max}} = 450 \text{ nm}$ ($\epsilon = 9800 \text{ M}^{-1} \text{ cm}^{-1}$). Complexes **3** and **4** also have features in the vis region albeit less defined. Complex **3** has an absorption at $\lambda_{\text{max}} = 560 \text{ nm}$ ($\epsilon = 1400 \text{ M}^{-1} \text{ cm}^{-1}$) and a shoulder at $\lambda_{\text{max}} = 637 \text{ nm}$ ($\epsilon = 980 \text{ M}^{-1} \text{ cm}^{-1}$), whereas complex **4** has two vis features at $\lambda_{\text{max}} = 564 \text{ nm}$ ($\epsilon = 1600 \text{ M}^{-1} \text{ cm}^{-1}$) and $\lambda_{\text{max}} = 653 \text{ nm}$ ($\epsilon = 640 \text{ M}^{-1} \text{ cm}^{-1}$).

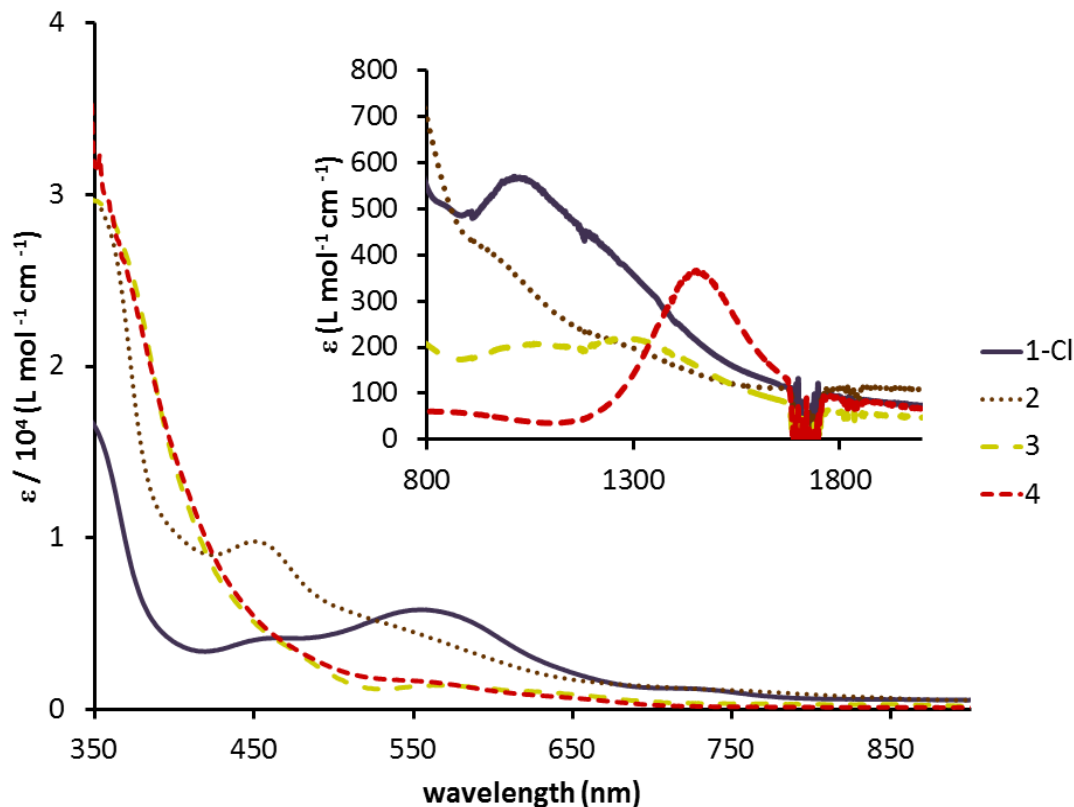


Figure 2.3.6 Vis spectra ($\epsilon \times 10^4$ vs nm) at 293 K in THF of **1-Cl** (purple, solid line), **2** (brown, dotted line), **3** (gold, long-dashed line) and **4** (red, short-dashed line) in THF. Insert: NIR spectra (ϵ vs nm) of **1-Cl** (purple, solid line), **2** (brown, dotted line), **3** (gold, long-dashed line) and **4** (red, short-dashed line).

Table 2.3.3 Vis and NIR transitions for **1-Cl**, **2**, **3**, and **4**

Complex	Vis transitions nm (ϵ , $M^{-1} \text{ cm}^{-1}$)	NIR transitions nm (ϵ , $M^{-1} \text{ cm}^{-1}$)
1-Cl	448 (4000), 554 (5800), 720 (1230)	953 (640)
2	450 (9800)	958 (400), 1200 (200)
3	560 (1400), 637 (980)	1035 (205), 1271 (220)
4	564 (1600), 653 (640)	1450 (360)

When examining the near-infrared (NIR) region of the electronic spectrum, several transitions are seen for complexes **1-4**. **1-Cl** has a single feature at $\lambda_{\text{max}} = 953 \text{ nm}$ ($\epsilon = 640 \text{ M}^{-1} \text{ cm}^{-1}$) which tails off further into the NIR region. Mixed-valent complexes **2** and **3** show two NIR features around $\lambda_{\text{max}} = 958 \text{ nm}$ and a broad shoulder around 1200 nm ($\epsilon = 400 \text{ M}^{-1} \text{ cm}^{-1}$ and $200 \text{ M}^{-1} \text{ cm}^{-1}$) and $\lambda_{\text{max}} = 1035 \text{ nm}$ and 1271 nm ($\epsilon = 205 \text{ M}^{-1} \text{ cm}^{-1}$ and $220 \text{ M}^{-1} \text{ cm}^{-1}$) respectively. Finally, mixed-valent complex **4** shows one sharp NIR absorbance at $\lambda_{\text{max}} = 1450 \text{ nm}$ ($\epsilon = 360 \text{ M}^{-1} \text{ cm}^{-1}$).

To our knowledge, **1-Cl** is the second trigonal Co(II)Co(II) bimetallic species in the literature, so there is limited compounds containing only cobalt to draw comparisons from. Fortunately, the Lu group has synthesized isostructural Fe(II)Fe(II) and Fe(II)Co(II) halide complexes in the same ligand framework.^{69a} In those compounds, all the visible electronic transitions were believed to arise from metal-ligand charge transfers (MLCT) bands as a blue shift was observed from going from Fe(II)Fe(II) to Fe(II)Co(II). One caveat to this assignment is the lack of similitude between the electronic configurations of the late-late bimetallics in this ligand scaffold. Complex **1** has an intermediate-spin electronic configuration (*vide supra*) whereas the isostructural Fe(II)Fe(II) and Fe(II)Co(II) complexes both have high-spin electronic configurations. By analogy to other bimetallic complexes synthesized in the Lu group, the NIR transitions are tentatively assigned as spin- and dipole-allowed inter or intrametal electronic transitions.

Interpretation of **2** is interesting due to the mixed-valent nature of the bimetallic core. Based on the molar absorptivity of the vis transition, the band at 450 nm can be attributed to a MLCT or LMCT band. The two NIR features for **2** can be attributed to d-d

transitions although it is ambiguous if they are intervalence charge transfers (IVCT) or intra-metal transitions. Thomas *et al.* have seen a similar NIR feature with similar molar absorptivity in a Co(II)Co(I) bimetallic, thus an assignment for an IVCT is not unreasonable.⁶⁸

Anionic **3** and dianionic **4** both have weak vis transitions. The transitions associated to **3** are either d-d transitions or weak MLCT or LMCT transitions based on molar absorptivities. The transitions of **3** were examined through time dependent – density functional theory (TD-DFT) calculations. The weak visible feature at 560 nm was attributed as an excitation from Co_P to the $\pi^*\text{-N}_2$ orbitals (Figure 2.3.7). Complex **3** has two weak NIR transitions, most likely d-d transitions, although it is unknown whether it is related to IVCT or intra-metal transitions.

The vis transitions in complex **4** are similar to those of **3** and likely the same. Interestingly, one of the transitions in **4** is likely a MLCT transition to the dinitrogen ligand since the solution changes color upon the addition of 2,2,2-cryptand (see experimental). The NIR absorption in **4**, is relatively strong and can be assigned to a d-d transition in Co_N since Co_P is believed to be fully occupied with ten d-electrons based on spectroscopic evidence (Section 2.3.4).

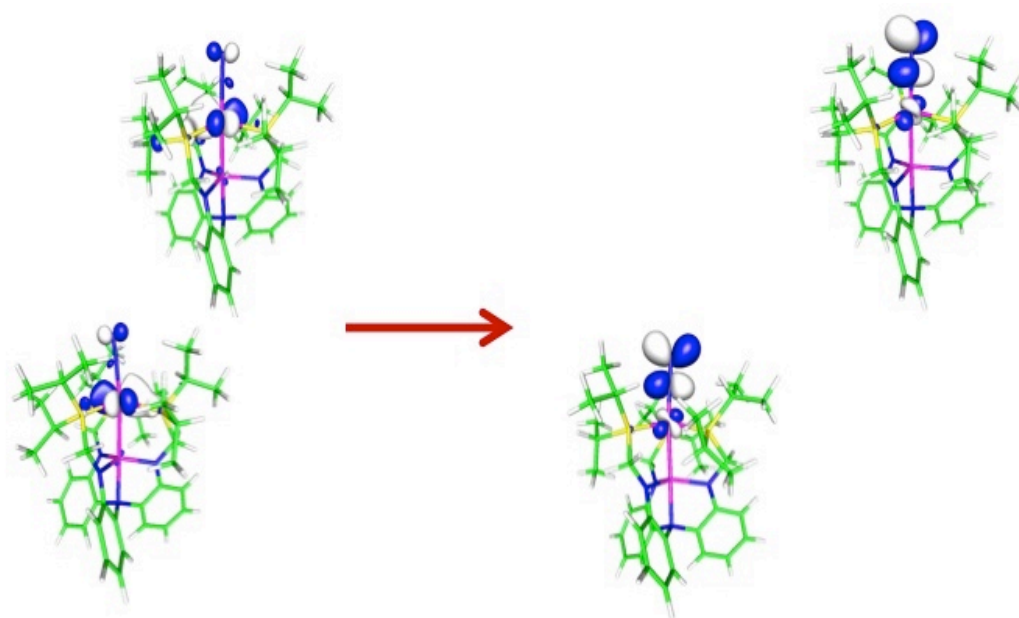


Figure 2.3.7 TD-DFT result showing the vis transition in **3** (545 nm) (B3LYP, def2-TZVP).

Table 2.3.4 TD-DFT (B3LYP, def2-TZVP) results with associated transitions

Wavelength (nm)	MOs involved	Percentage	Oscillation strength
545	$\alpha: d \rightarrow \pi^* - N_2$	75%	0.24×10^{-2}
534	$\alpha: d \rightarrow \pi^* - N_2$	88%	0.33×10^{-4}
532	$\alpha: d \rightarrow \pi^* - N_2$	90%	0.76×10^{-4}
521	$\alpha: d \rightarrow \pi^* - N_2$	77%	0.15×10^{-2}

2.3.4 Magnetic Measurements and EPR

Complexes **1-Cl** and **2** were examined through solution state magnetic moment to elucidate the spin state of the bimetallic core to help under the electronic structure of each complex. **1-Cl** had a solution state magnetic moment of $\mu_{\text{eff}} = 4.51$ B.M. which is slightly lower than the spin-only magnetic moment of $\mu_{\text{SO}} = 4.90$ B.M for $S = 2$. We are thus able to assign **1-Cl** as an intermediate spin $S = 2$ bimetallic core with four unpaired electrons. Complex **2** gave a solution state magnetic moment of $\mu_{\text{eff}} = 6.14$ B.M. which is slightly higher than the spin-only magnetic moment of $\mu_{\text{SO}} = 5.92$ B.M for $S = 5/2$. From this result, we were able to assign **2** as a high spin $S = 5/2$ bimetallic core with five unpaired electrons. This result for **2** was confirmed through SQUID magnetometry and EPR spectroscopy (*vide infra*).

The magnetic susceptibility of **2** was measured from 2 to 290 K through SQUID magnetometry measurements, and are consistent with $S = 5/2$. The effective magnetic moment for sextet **2** decreases slightly from 6.1 to 5.8 B.M. from 50-290 K. This value agrees closely with the spin-only magnetic moment for a $S = 5/2$ system (5.92 B.M.). To fit the data, a two-spin model is needed with ferromagnetic coupling ($J = 60 \text{ cm}^{-1}$) between Co(II), $S = 3/2$, and Co(I), $S = 1$, centers. Interestingly, compound **2** has a high spin configuration although it contains a strong covalent Co-Co bond through structural analysis (*vide supra*). Below 50 K, the effective magnetic moment is inconsistent with the high temperature magnetic moments. This deviation is possibly due to zero-field splitting, which can be simulated (Figure 2.3.8). The best fit can be obtained with zero-field splitting parameter $D_{5/2} = 12 \text{ cm}^{-1}$.

The EPR spectrum of **2** has also been collected in frozen toluene at 20 K. The expected EPR spectrum for an $S = 5/2$ system is predicted to have signals at effective g -values of $g_{\text{eff}} = 6, 6, \text{ and } 2$ for an axial spectrum due to the C_3 symmetry of the molecule.⁷³ However, when the spectra is prepared under a dinitrogen atmosphere, the corresponding spectrum reveals a $S = 1/2$ spin system with effective g -value around $g_{\text{eff}} = 2$ (Figure 2.3.9). We believe this to be due to dinitrogen binding at low temperature and this hypothesis is further investigated in Section 2.3.5. This leads to anti-ferromagnetic coupling of the metal centers when dinitrogen is bound. A qualitative molecular orbital diagram for these compounds can be seen in Figure 2.3.11. The spectrum can be modeled as a $S = 1/2$ axial spectrum with anisotropic g -values $g = 2.14, 2.14, \text{ and } 1.898$. The spectrum can be fit by modeling a hyperfine interaction of one cobalt nucleus ($I = 7/2$) with $A_{xx} = A_{yy} = 29.3126$ and $A_{zz} = 170 \times 10^{-4} \text{ cm}^{-1}$ and line widths of $W_x = W_y = 50$ and $W_z = 80 \text{ G}$. In contrast, when the EPR sample is prepared in an argon atmosphere, the corresponding EPR spectrum shows an axial signal with effective g -values of $g_{\text{eff}} = 6, 6, \text{ and } 2$, which agree with an expected $S = 5/2$ signal with a small trace (20%) of dinitrogen bound complex as well (Figure 2.3.10). The spectrum can be modeled as an axial $S = 5/2$ system with anisotropic g -values of $g = 2.1578, 2.1578 \text{ and } 1.898$ which agree with solid-state magnetic measurements which give a g -value of $g = 2.066$.

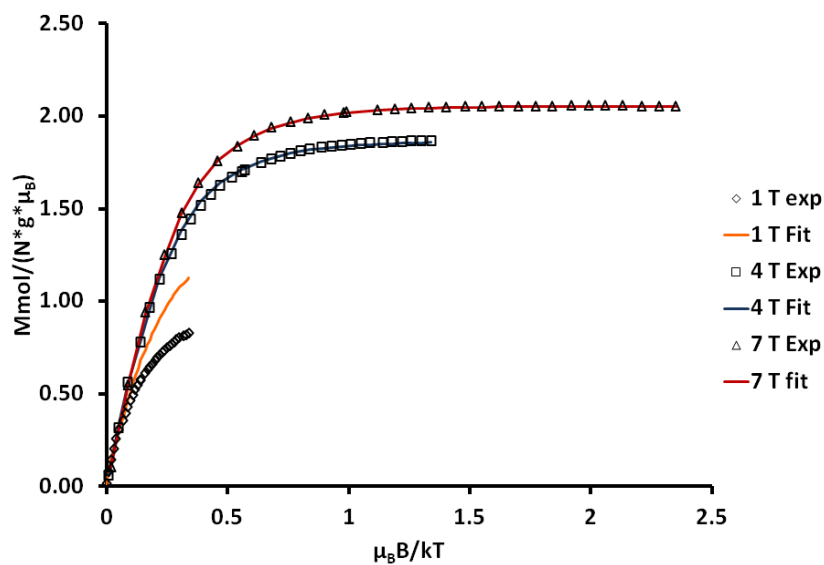
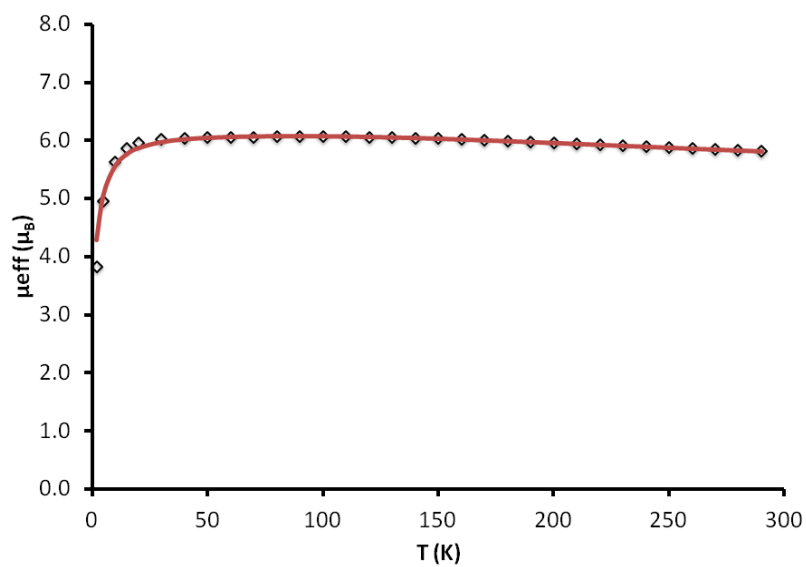


Figure 2.3.8 Top: Temperature dependence of the effective magnetic moment, μ_{eff} , of **2** (1 Tesla, 2–290 K). The red line represents the spin-Hamiltonian simulation using a two-spin model with $S_1=3/2$, $S_2=1$, $g_1=g_2=2.066$, $J_{12}=+60.00\text{ cm}^{-1}$, $D_1=D_2=12.00\text{ cm}^{-1}$ with a correction for the underlying diamagnetism of $-422.2 \times 10^{-6}\text{ cm}^3/\text{mol}$. Bottom: VTVH dependence of μ_{eff} , of **2** (1 Tesla, 2–50 K). The colored lines (orange 1 T, blue 4 T and red 7 T) represents the spin-Hamiltonian simulation using a two-spin model with $S_1=3/2$, $S_2=1$, $g_1=g_2=2.066$, $J_{12}=+60.00\text{ cm}^{-1}$, $D_1=D_2=12.00\text{ cm}^{-1}$ with a correction for the underlying diamagnetism of $-422.2 \times 10^{-6}\text{ cm}^3/\text{mol}$.

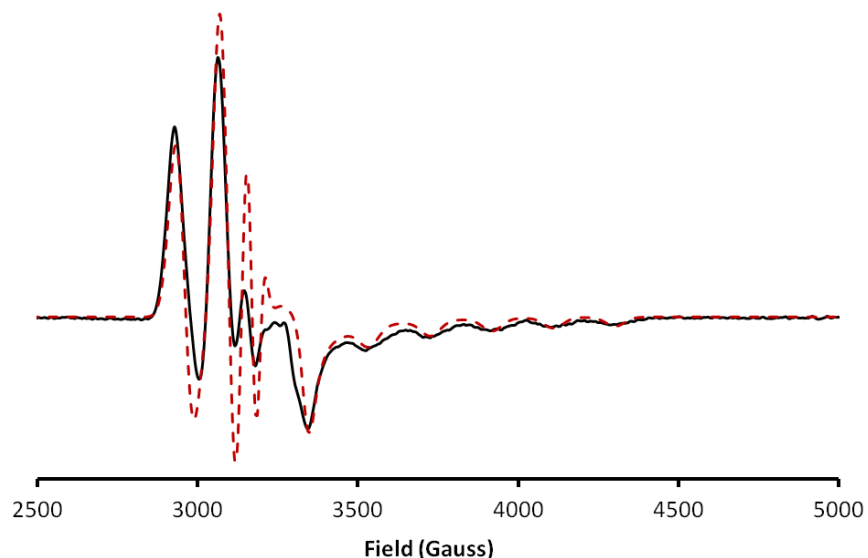


Figure 2.3.9 X-Band EPR spectrum (dX''/dB) of **2** in an N_2 atmosphere in a toluene glass (21 K). The solid line is the experimental spectrum. The dashed red line is the simulated spectrum with anisotropic g values $g = 2.14, 2.14$ and 1.898 . The spectrum is modeled with $A_{xx}=A_{yy}= 29.3126$ and $A_{zz}= 170 \times 10^{-4} \text{ cm}^{-1}$ and line widths of $W_x=W_y=50$ and $W_z= 80$.

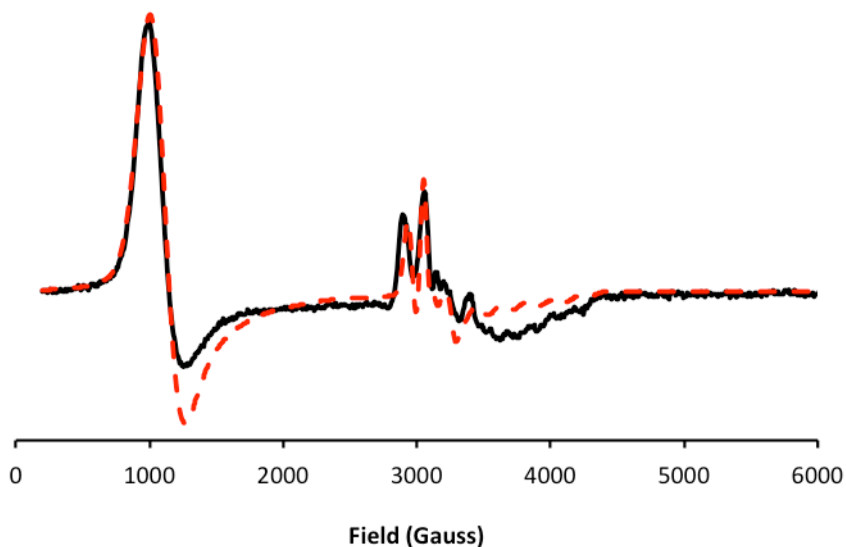


Figure 2.3.10 X-Band EPR spectrum (dX''/dB) of **2** under an argon atmosphere in a toluene glass (21 K). The solid line is the experimental spectrum. The dashed red line is the simulated $S = 5/2$ spectrum (80%) with $g_{\text{eff}} = 6.5, 6.5,$ and 1.80 and $W_x=W_y= 220$, $W_z= 300 \text{ G}$ and $A_{zz}= 80 \times 10^{-4} \text{ cm}^{-1}$. The spectrum is also modeled with a $S = 1/2$ (20%) spectrum with $g_{\text{eff}} = 2.175, 2.175$ and 1.898 and $W_x=W_y= 50$, $W_z= 80 \text{ Gauss}$ and $A_{xx}=A_{yy}= 26.3056$ and $A_{zz}= 170 \times 10^{-4} \text{ cm}^{-1}$.

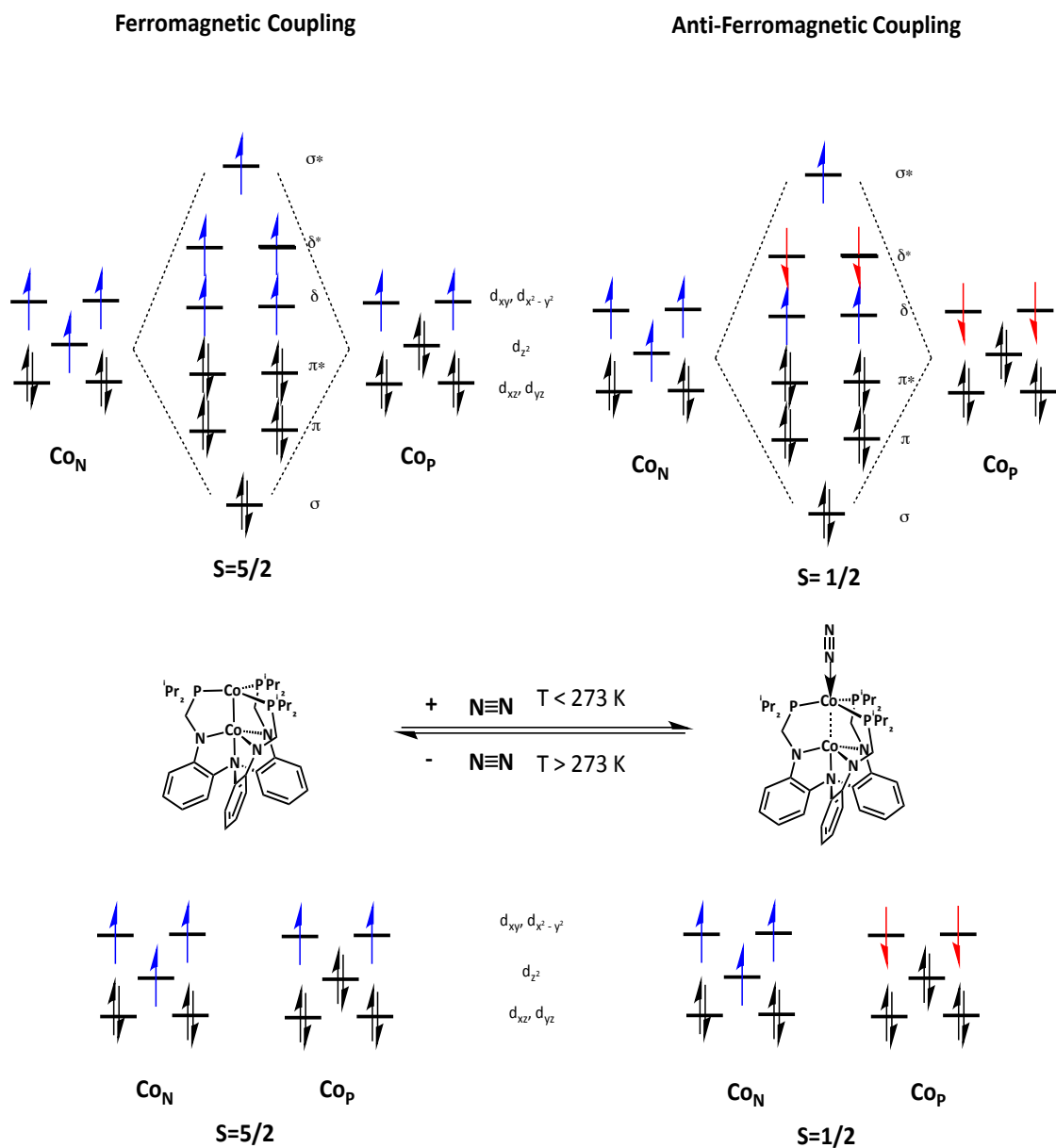


Figure 2.3.11 Four potential qualitative molecular orbital diagrams explaining the electronic phenomena occurring when dinitrogen binds to **2**. Top: Covalent interactions Bottom: Separate metal electron coupling

The magnetic susceptibility of **3** was measured from 2 to 290 K through SQUID magnetometry and is consistent with $S = 1$. The triplet state of **3** is energetically isolated, with a g -value of 2.14 and a zero-field splitting of 42 cm^{-1} (Fig. 2.3.12), and can formally arise from anti-ferromagnetic coupling between $S = 3/2$ Co(II) and $S = 1/2$ Co(0) spins. It is hypothesized that the binding of an axial donor to Co_P changes the interactions between the two cobalt centers from ferromagnetic coupling to anti-ferromagnetic coupling (Figure 2.3.14, Section 2.3.7). A similar phenomenon is seen with **3** (*vide supra*) when dinitrogen is bound.

Theoretical calculations were performed to provide understanding of the electronic structure (Figure 2.3.13). In a recent paper published by the Lu group, complex **3** was examined computationally through a DFT analysis and compared to other heterobimetallic M-Co (M = Ti, V, Cr) anions that also bind dinitrogen.^{41b} It was seen that due to the late-late homobimetallic nature of the dicobalt combination, the oxidation states of the bimetallic core were different ($\text{Co}_N(\text{II})\text{Co}_P(0)$ vs $M_N(\text{III})\text{Co}_P(-I)$) than the cores in the heterobimetallic species and the d-orbital overlap was energetically favored. These differences lead to a more delocalized Co-Co σ -bonding molecular orbital ($\text{Co}_N\text{-Co}_P$ 63%/37% vs $M_N\text{-Co}_P \sim 20\%/80\%$). Hence, a formal single bond was predicted. Formally, the triplet ground state is derived from an anti-ferromagnetic coupling of $S_1 = 3/2$ Co(II) and $S_2 = 1/2$ Co(0), corresponding to Co_N and Co_P , respectively. Due to the multi-configurational electronic structure of first-row bimetallic complexes, the electronic structure of **3** is most likely a combination of anti-ferromagnetic coupling and Co-Co bonding interactions.

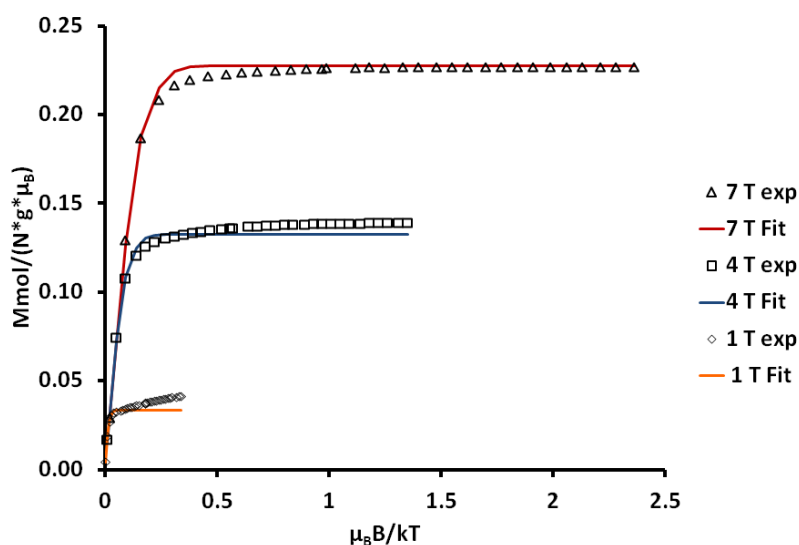
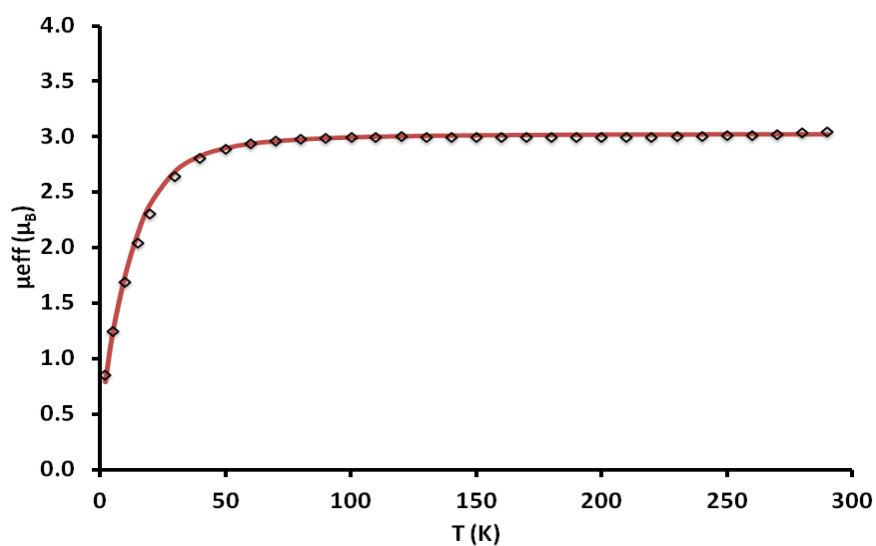


Figure 2.3.12 Top: Temperature dependence of the effective magnetic moment, μ_{eff} , of **3** [K(2,2,2-cryptand)]Co₂(N₂)L (diamonds, 1 Tesla, 2–290 K). The red line represents the spin-Hamiltonian simulation with $S_{\text{tot}}=1$, $g = 2.138$, zero-field splitting, $D = 42.432 \text{ cm}^{-1}$, with a correction for the underlying diamagnetism of $-698.6 \times 10^{-6} \text{ cm}^3/\text{mol}$. Bottom: VTVH dependence of μ_{eff} of **3** [K(2,2,2-cryptand)]Co₂(N₂)L (1, 4, 7 Tesla, 2-50 K). The colored lines (orange 1 T, blue 4 T and red 7 T) represents the spin-Hamiltonian simulation with $S_{\text{tot}}=1$, $g = 2.138$, $D = 42.432 \text{ cm}^{-1}$ with a correction for the underlying diamagnetism of $-698.6 \times 10^{-6} \text{ cm}^3/\text{mol}$.

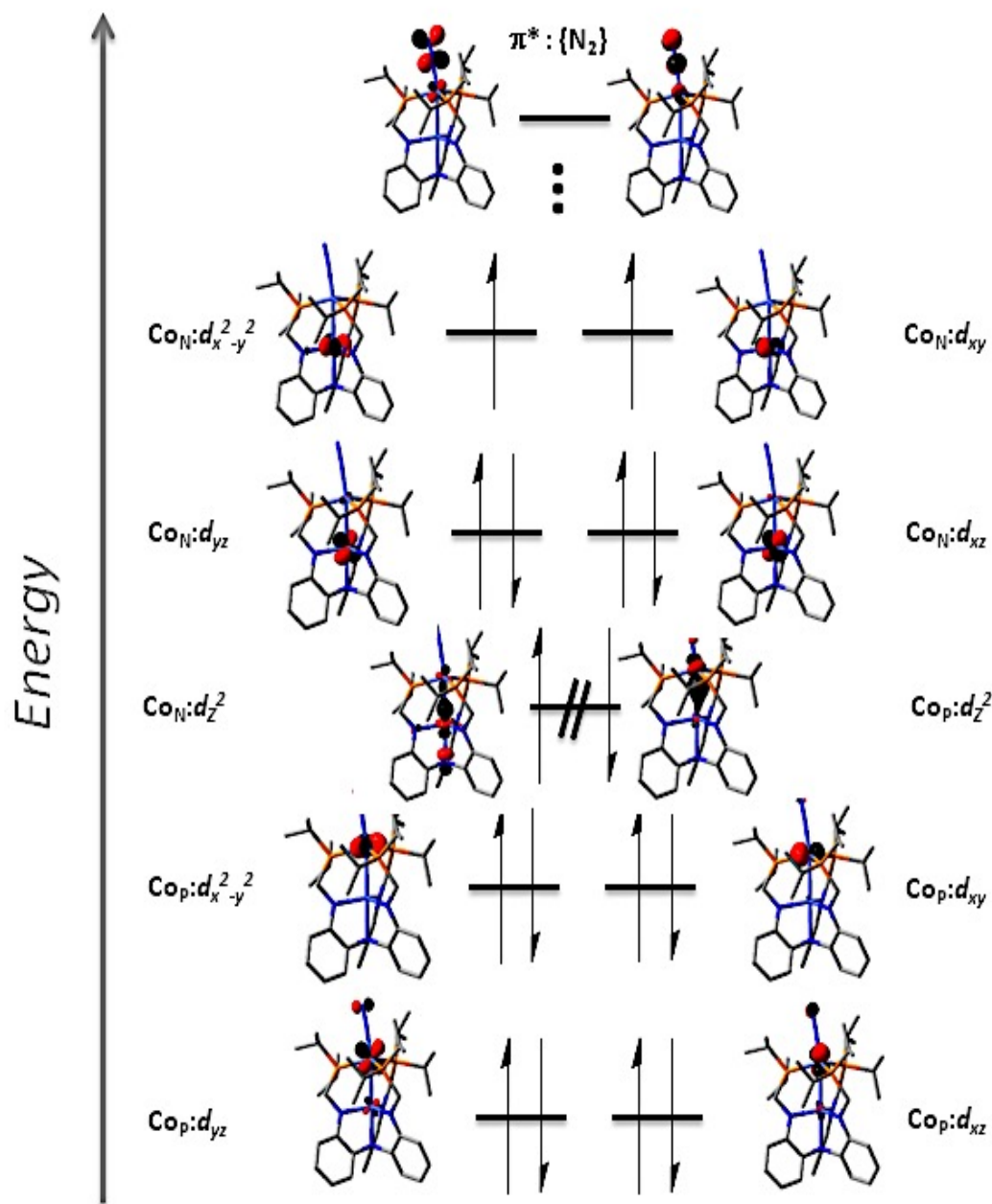


Figure 2.3.13 Calculated molecular orbital diagram of **3** (DFT, M06L)

The EPR spectrum of **4** has been collected in frozen THF at 20 K (Figure 2.3.14). The spectrum shows an axial signal with effective g-values of $g_{\text{eff}} = 4, 4$ and 2 , indicative of a $S = 3/2$ bimetallic core. The spectrum can be modeled as an $S = 3/2$ spin with anisotropic g-values of $2.2, 2.2$, and 2.07 , and $A_{zz} = 70 \times 10^{-4} \text{ cm}^{-1}$. There are two possible interpretations of the oxidation states of each cobalt center (Figure 2.3.15), a $\text{Co}_N(\text{I})\text{Co}_P(0)$ or $\text{Co}_N(\text{II})\text{Co}_P(-\text{I})$ combination. Based on FTIR data (*vide infra*) for the associated dinitrogen stretch, as well as the unfavorable possibility of a mono-cationic metal in a tri-anionic pocket, the more reasonable assignment is $\text{Co}_N(\text{II})\text{Co}_P(-\text{I})$. The hyperfine interaction in the z-vector only corresponds to unpaired electrons on Co_N .

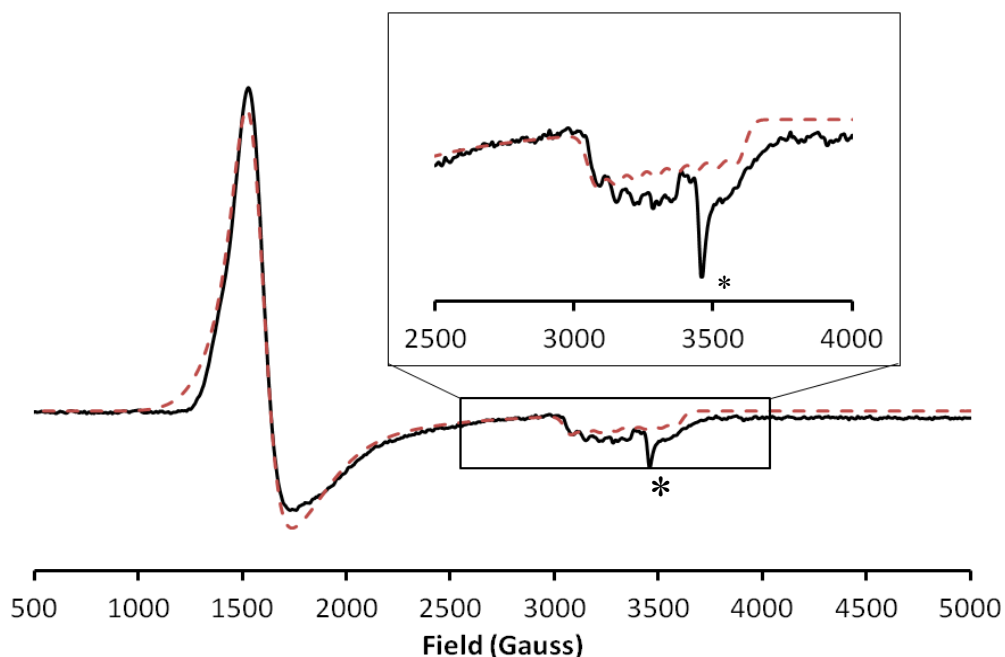


Figure 2.3.14 X-Band EPR spectrum (dX''/dB) of **4** in THF glass (21K) shown as solid black line. The dashed red line is the simulated $S = 3/2$ spectrum with anisotropic g values $g = 2.1578, 2.1578$, and 1.898 and line widths of $W_x = 17$, $W_y = 50$, $W_z = 8$ G and z-hyperfine tensor for Co ($I = 7/2$) of $A_{zz} = 70 \times 10^{-4} \text{ cm}^{-1}$. * baseline impurity in cavity.

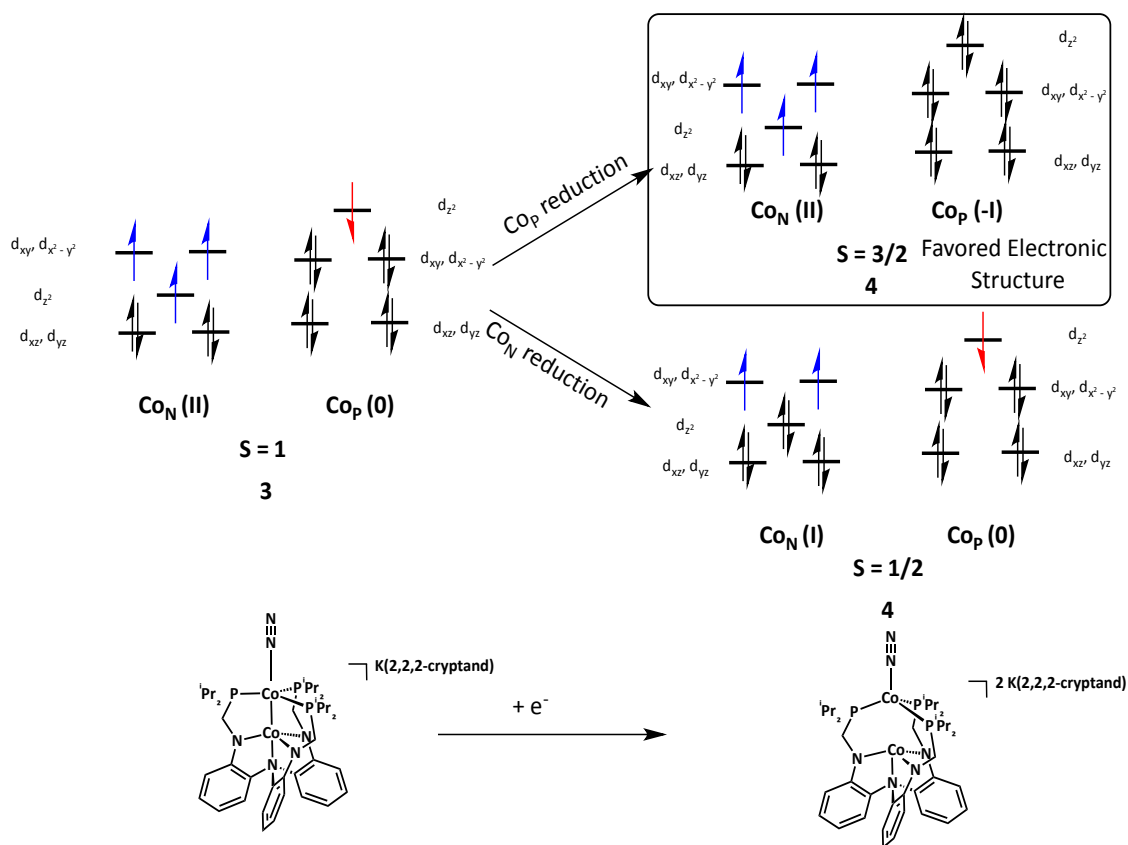


Figure 2.3.15 Qualitative orbital diagrams showing anti-ferromagnetic coupling in **3** (left) and two potential reduction sites in **4** (right).

2.3.5 Infrared Data

The activation of the N-N bond can be correlated to the N-N stretching frequency as stated by Badger's rule.^{4, 74} This correlation was plotted comparing crystallographic data with the dinitrogen stretching frequency (Figure 2.3.16). It shows that an activated yet still neutral bound dinitrogen ligand has $\nu(\text{N}_2)$ between 2200 and 1850 cm^{-1} and the two electron reduced N_2 with a wide range of frequencies of 1800 to 1300 cm^{-1} . Another feature of the plot is that the mononuclear dinitrogen compounds (blue circles) only exhibit weak dinitrogen activation, whereas the dinuclear compounds (green squares) mostly correlate to more reduced dinitrogen ligands. This increased activation is due to increased electron donation to the dinitrogen π^* system. In the case of group 8 and 9 metals, it was found that unique ligand fields are required to raise the d-orbital energies to induce π -back donation.

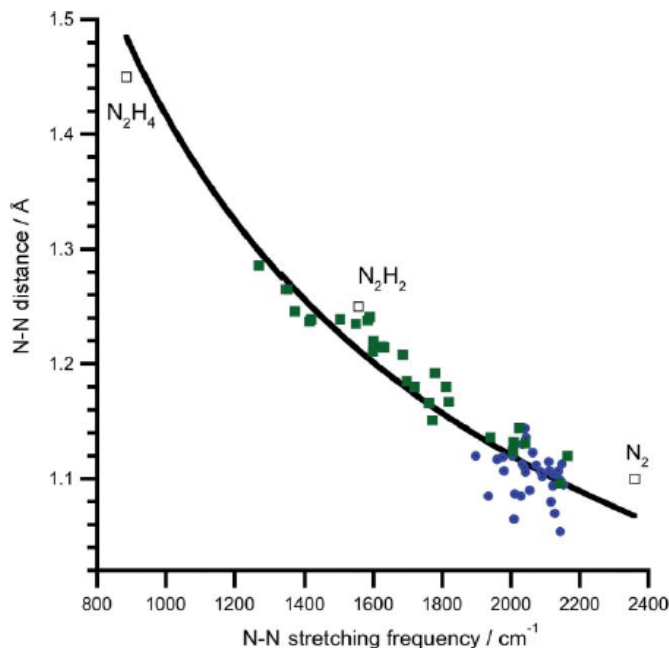


Figure 2.3.16 Correlation of dinitrogen stretching frequency to N-N bond strength. Blue circles represent mononuclear dinitrogen species and green squares represent dinuclear dinitrogen species. Taken from reference 4.

The infrared vibrational spectrum between 1600 and 2300 cm^{-1} was examined for the binding of dinitrogen with complexes **2**, **3**, and **4** (Figure 2.3.17). Crushed crystalline solid of **2** shows no significant signal corresponding to a bound dinitrogen unit. However, interesting solution state phenomena occurs at lower temperature (*vide infra*). Upon one and two electron reduction to **3** and **4** a dinitrogen signal is observed in the solid state at 1994 cm^{-1} and 1925 cm^{-1} . These stretches correspond to slight activation of a dinitrogen ligand through π -back donation into the dinitrogen π^* orbitals. However, the stretching frequency still corresponds to a neutral bound dinitrogen unit.

Complex **2** was examined using a variable-temperature (VT) IR instrument to examine the binding of dinitrogen at low temperatures (Figure 2.3.18). For experimental details, refer to section 2.5.4. At room temperature (303 K), **2** exhibited no vibrational features corresponding to dinitrogen binding. When the solution was cooled to 175 K, an absorbance feature at 2120 cm^{-1} was observed. This stretching frequency is indicative of a weakly bound dinitrogen ligand. As the temperature was increased, the signal diminished and ultimately disappeared at 303 K. For comparison, **3** was subjected to the exact VTIR conditions and displays a consistent absorbance at 2000 cm^{-1} , slightly blue-shifted from the solid state measurement of 1994 cm^{-1} .

Complexes **2**, **3**, and **4** represent a series of compounds that have dinitrogen bound through three different oxidation states. It is believed that this series is possible due to the influence of the electron-rich bimolecular core. When compared to Co-N₂ compounds with a *trans*-Lewis acids (LA)^{41j, m, 69b} (i.e. B or Al), it can be seen that going from a formal Co(0) to Co(-1) leads to a weakening of the N-N bond by 111 cm^{-1} and 86 cm^{-1} respectively (Table 2.3.5). However, while going from **3** (formally Co_P(0)) to **4** (formally

Co_P(-I)) shows a N-N weakening of only $\Delta\nu_{N_2} = 71 \text{ cm}^{-1}$, the dinitrogen ligand is significantly more activated in **4** when compared to the LA-Co(-I)-N₂ species ($\nu_{N_2} = 1925$ vs LA = A 1995 and LA = B 1978 cm^{-1}). It is hypothesized that the increase in activation is caused by the greater electron density of the *trans*-cobalt metallo-ligand relative to the *trans*-Lewis acid ligand.

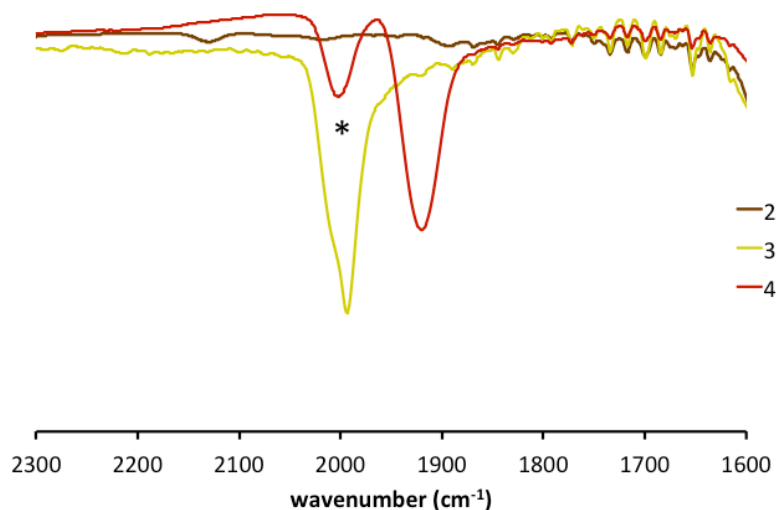


Figure 2.3.17 Solid state (KBr pellet) IR spectrum of the N₂ region (1600 cm^{-1} to 2300 cm^{-1}) for **2** (brown), **3** (yellow), and **4** (red). The asterisk denotes a small impurity of **3** in the spectrum of **4** due to decomposition.

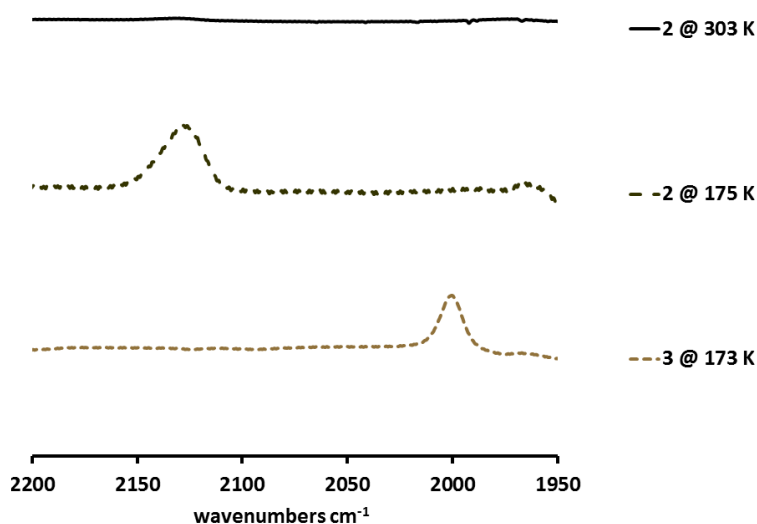


Figure 2.3.18 VTIR spectrum in THF of **2** at 303 K (top, solid), **2** at 173 K (middle, dashed, $\nu_{N_2} = 2120 \text{ cm}^{-1}$) and **3** at 173 K (bottom, light dashed, $\nu_{N_2} = 2000 \text{ cm}^{-1}$)

When comparing to *trans*-transition metal cobalt species, there is an apparent inverse relationship on electron richness (d-count) of the *trans* metallo-ligand and N₂ activation (i.e. for M = V, Cr, Co $\nu_{N_2} = 1971, 1990, 1994 \text{ cm}^{-1}$).^{41b} There is also a correlation of the anion reduction potential and N₂ activation; the harsher the reduction potential of the anion, the more activated N₂ is. One hypothesis for these relationships is the π orbitals involved in M-Co bonding and Co-N₂ bonding match in symmetry. This symmetry match means that the interactions between the transition metals can potentially modulate filled d_{xz} and d_{yz} orbitals of the cobalt interacting with N₂ to higher energy. In turn, the orbitals would closer match the π^* orbitals of the N₂ ligand, allowing for better π -back donation. However, theoretical calculations do not justify this hypothesis.^{41b}

Table 2.3.5 Comparison of trigonal M-Co-N₂ complexes

Complex	Co oxidation state	N ₂ frequency (cm ⁻¹)	ref
[CP ₃ Co(N ₂)] ⁺	2	2182	40j
2-N ₂	1	2120	this work
CP ₃ Co(N ₂)	1	2057	40j
SiP ₃ Co(N ₂)	1	2063	40j
3	0	1994	this work
LAICo(N ₂)	0	2081	40m
[LCrCo(N ₂)] ⁻	0	1990	40b
[LVCo(N ₂)] ⁻	0	1971	40b
[PhB(CH ₂ ^{iPr} P) ₃ Co(N ₂)] ⁻	0	1896	40j
TPBCo(N ₂)	0	2089	40j
4	-1	1925	this work
[LAICo(N ₂)] ⁻	-1	1995	40m
[NP] ₃ ZrCo(N ₂)	-1	2023	40g
[TPBCo(N ₂)] ⁻	-1	1978	40j

L = N(*o*-(NHCH₂P(ⁱPr)₂)C₆H₄)₃; TPB = [*o*-(ⁱPr₂P)C₆H₄]₃B;

CP₃ = [*o*-(ⁱPr₂P)C₆H₄]₃C; SiP₃ = [*o*-(ⁱPr₂P)C₆H₄]₃Si; NP = ⁱPr₂PNMes

2.3.6 Cyclic Voltammetry

The electrochemical properties of dicobalt (II,I) **2** were investigated using cyclic voltammetry (CV). The CV of **2** was measured in a 0.1 M [TBA][PF₆] solution in dimethoxyethane (DME) and the redox potentials were referenced against an internal ferrocene standard. At 100 mV/s **2** exhibits two reductive features, one irreversible feature at $E_{pc} = -2.18$ V and a reversible feature at $E_{1/2} = -2.54$ V ($\Delta E = 100$ mV, $i_{p,c}/i_{p,a} = 0.92$) (Figure 2.3.19). The first reductive event is attributed to a one-electron reduction of the complex to form a one electron reduced species, $[LCo_2(N_2)]^-$. It was shown that this species is chemically accessible and has been structurally characterized as described in Section 2.3.2. The most cathodic event has been formally assigned to the two electron reduced dicobalt dianion, $[LCo_2(N_2)]^{2-}$, which can be synthesized and has been characterized through spectroscopy (*vide supra*).

The first reductive feature has a corresponding anodic return feature that is far separated from the initial reduction ($E_{pa} = -1.80$ V, $\Delta E = 387$ mV). As the scan speed is increased, the peak-to-peak separation increases, while the current ratios become closer to unity (Figure 2.3.19). This can be attributed to the inability of the reduced species formed at the electrode to diffuse away prior to the subsequent return oxidation. This anomaly is attributed to a chemical reaction of the reduced species with the dinitrogen atmosphere. The Lu group had previously published a chromium-cobalt bimetallic species in which a similar feature was observed and was later confirmed to be due to interactions with dinitrogen by running the electrochemical experiment under an argon atmosphere^{41b, 75}. Schrock *et al.*, observed a similar phenomenon when looking at $HIPTN_3NMo(THF)$ electrochemically in which upon reduction,⁷⁶ THF is replaced by

dinitrogen and the return oxidation is shifted due to a chemical change of the analyte. This type of electrochemical mechanism is known as an ECEC mechanism in which an electron transfer happens, followed by a chemical transformation, and then having an electron transfer attributed to the new species and return to the original analyte.⁷⁷ It is hypothesized that **2** goes through a similar ECEC type mechanism under a dinitrogen atmosphere (Figure 2.3.20) in which **2** is reduced by one electron to generate $[\text{LCo}_2]^-$. $[\text{LCo}_2]^-$ then binds dinitrogen to form $[\text{LCo}_2(\text{N}_2)]^-$ and upon the anodic return, the one electron oxidation is shifted more anodically due to the binding of dinitrogen to the species and followed by N_2 release.

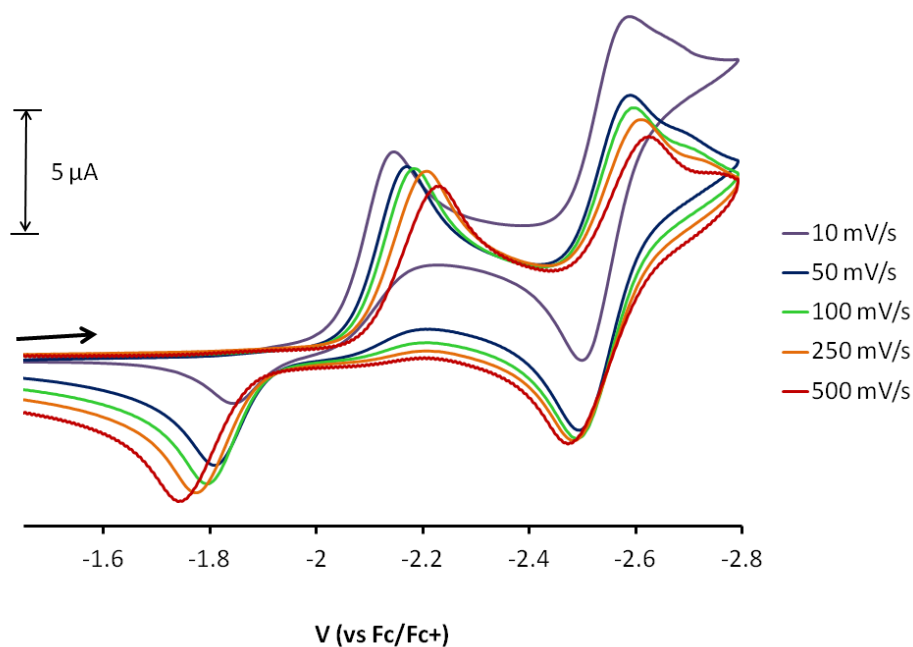


Figure 2.3.19 CV (DME, 0.1 M $[\text{TBA}][\text{PF}_6]$) of **2** under a dinitrogen atmosphere with scan rate dependence shown (scan speed = 10, 50, 100, 250 and 500 mV/s.)

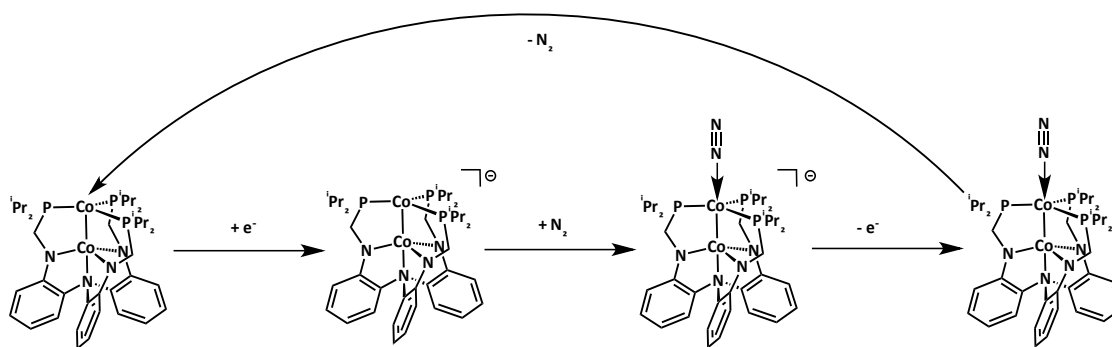


Figure 2.3.20 Depiction of ECEC type mechanism observed in the CV of **2**. E = electron transfers, C = chemical events (i.e. N_2 binding).

Analogously, the electrochemistry of **2** was examined under an argon atmosphere (Figure 2.3.21). It was found that the first cathodic event now becomes quasi-reversible ($E_{1/2} = -2.12$ V, $\Delta E = 111$ mV) while the second reduction event is shifted more cathodically and appears now as a quasi-reversible event ($E_{1/2} = -2.73$ V, $\Delta E = 230$ mV). The comparison of the CVs under each atmosphere are summarized in Table 2.3.6.

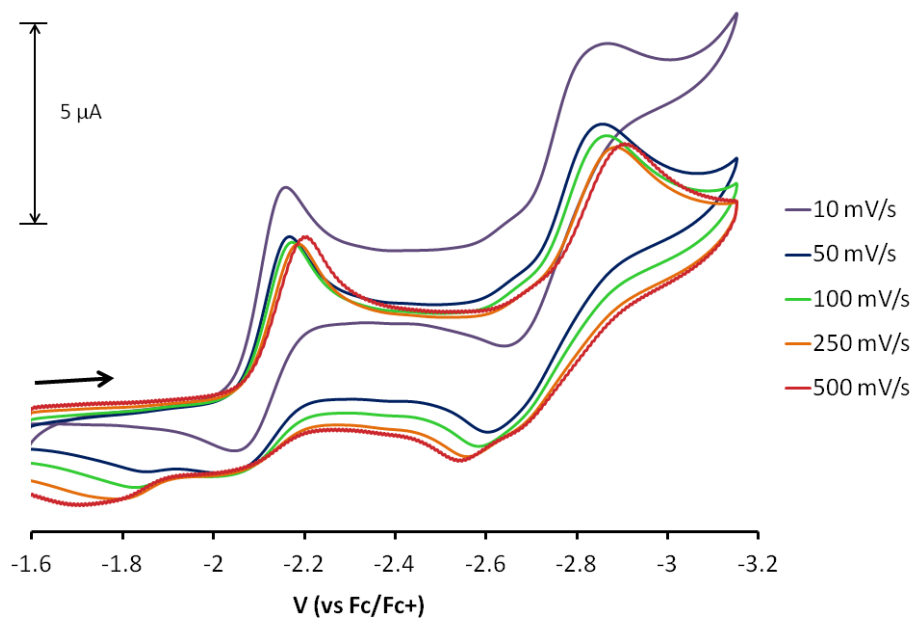


Figure 2.3.21 CV (DME, 0.1 M [TBA][PF₆]) of **2** under an argon atmosphere with scan rate dependence shown (scan speed = 10, 50, 100, 250 and 500 mV/s.)

Table 2.3.6 Summary of Electrochemical data for **2** under N₂ and Ar.

Redox Couple / total electrons	Complex-Atmosphere	E _{1/2} or	Δ(E) mV	i _{pa} / i _{pc}
		E _{pc} , E _{pa} (V) (vs Fc/Fc ⁺)		
[LCo ₂] ^{15/16}	2- N ₂	-2.18, -1.80	387	0.64
	2- Ar	-2.12	111	0.34
[LCo ₂] ^{16/17}	2- N ₂	-2.54	100	0.92
	2- Ar	-2.73	230	0.11

2.3.7 Theoretical Calculations

Theoretical calculations were performed for compounds **2**, **3**, and **4** to help understand the nature of the metal-metal interactions within this localized ligand framework. In some cases, the compounds were truncated by replacing the isopropyl groups appended to the phosphines to methyl groups (^{Me}L). Truncation has been shown to have a negligible effect on the electronic structure of the complexes as well as lowering computational cost.

Three species, ^{Me}LCo₂, [^{Me}LCo₂]⁻, and [^{Me}LCo₂(N₂)]⁻, were further interrogated by multi-reference methods to gain insight into their electronic structures (see Section 2.5.5). RASSCF / RASPT2 calculations of ^{Me}LCo₂ and [^{Me}LCo₂]⁻ generated the qualitative MO diagrams in Figure 2.3.22 and 2.3.23 respectively. The Co 3d-orbitals are primarily localized at each Co center, and the only delocalized MOs are the σ and σ*. Therefore, the metal-metal interaction is predicted to be weak. For ^{Me}LCo₂, the sextet (*S*_{total} = 5/2) ground state is formally derived from ferromagnetic coupling of *S*₁ = 3/2 Co(II) and *S*₂ =

1 Co(I), where the former is Co_N and the latter is Co_P. In support, the d-electron occupation of the two Co atoms is d^{8.02} and d^{6.98} for Co_P and Co_N, respectively.

For its anionic counterpart, [^{Me}LCO₂]⁻, the quintet (*S*_{total} = 2) ground state is predicted to be more stable than the triplet state, which is the both the experimental and computed ground state of its dinitrogen adduct [^{Me}LCO₂(N₂)]⁻. For [^{Me}LCO₂]⁻, the *S*_{total} = 2 ground state is formally derived from ferromagnetic coupling of *S*₁ = 3/2 Co(II) and *S*₂ = 1/2 Co(0), corresponding to Co_N and Co_P, respectively. Hence, the one-electron reduction of Co₂L is hypothesized to be localized at the phosphine-ligated Co site, which changes oxidation states from Co(I) to Co(0).

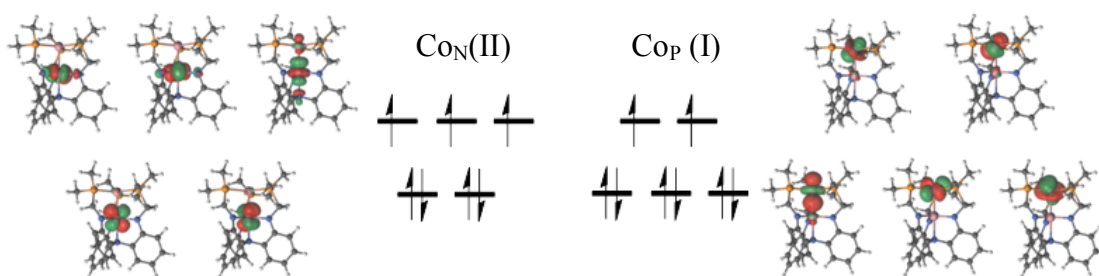


Figure 2.3.22 Molecular orbitals of the dominant electronic configuration for ^{Me}LCO₂

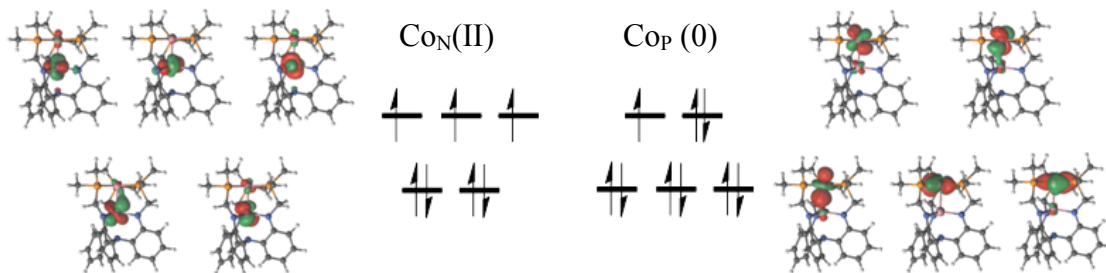


Figure 2.3.23 Molecular orbitals of the dominant electronic configuration for [^{Me}LCO₂]⁻

The binding of dinitrogen to complex **2** was investigated through theoretical calculations (DFT, M06L).⁷⁸ These preliminary results found that the *S* = 1/2 configuration was the lowest in energy. The high spin *S* = 5/2 and intermediate spin *S* = 3/2 ground states were 3.3 kcal/mol and 13.8 kcal/mol higher in energy. However, a large, yet

acceptable spin contamination for the $S = \frac{1}{2}$ configuration of $S^2 = 1.17$ ($S^2_{(1/2)} = 0.75$).

The contamination is likely due to the multi-configurational nature of the bimetallic core. A binding energy for dinitrogen of 2.94 kcal/mol at 273 K was found, which supports the low temperature dependence seen experimentally. Further theoretical investigation is in progress to fully understand the nature of dinitrogen binding.

Dianionic complex **4** was examined through theoretical calculations using the M06L functional and the basis sets def2-TZVP (Co, N, P) def2-SVP (C, H).⁷⁹ A spin state of $S = 3/2$ was found to be the most stable configuration by about 20 kcal/mol ($S = \frac{1}{2}$). This result is in good agreement with experimental EPR data also showing a ground state of $S = 3/2$ for **4**. The site of reduction was also elucidated by examining the spin density plots for the $S = 3/2$ state (Figure 2.3.24). It was seen that the majority of the unpaired spin was seen on Co_N . This would formally lead to the assignment of a Co(II)Co(-1) core, which was also hypothesized through experimental IR data examining the dinitrogen stretching frequency (*vide supra*).

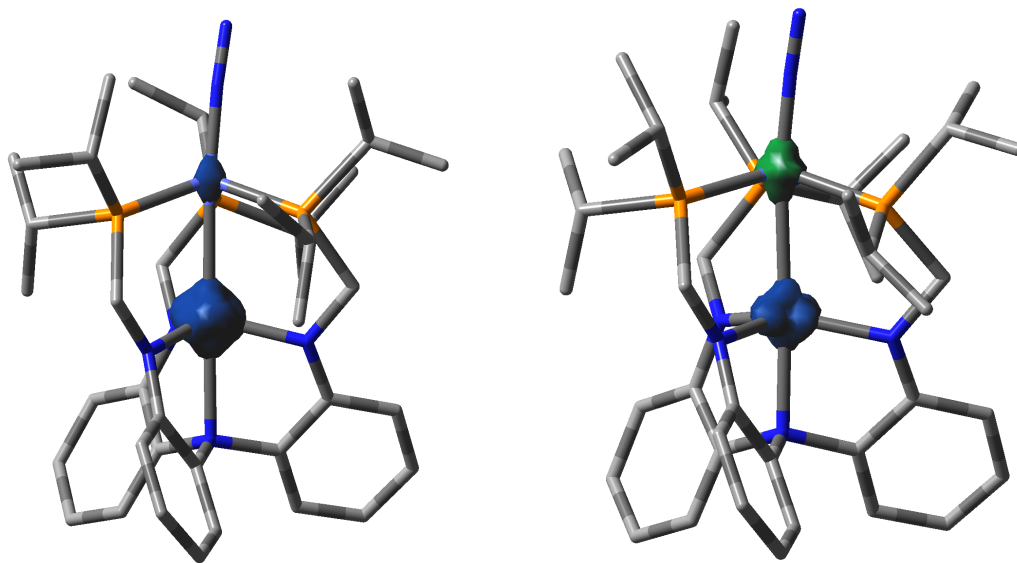


Figure 2.3.24 Spin densities of calculated $S = 3/2$ state (left) and $S = \frac{1}{2}$ state (right) of $[\text{iPr}]\text{LCO}_2(\text{N}_2)]^{2-}$.

2.4 Conclusions

Herein a series of five dicobalt species were synthesized and characterized: dicobalt(II,II) halide, **1-Cl**, dicobalt(II,I), **2**, dicobalt(II,I)-N₂, **2-N₂**, dicobalt(II,0)-N₂, **3**, and dicobalt(II,-I)-N₂ **4**. A range of low, intermediate and high-spin bimetallic cores were seen ranging in spin states from $S = 1$ to $S = 5/2$, of which the $S = 5/2$ had the shortest metal-metal bond. It was found that the localized electronics of the ligand scaffold allowed for the various charge states of the bimetallic species to be isolated. Most interestingly was the elucidation of dinitrogen binding to complex **2**. With that three different charge states of the dicobalt core are able to bind with dinitrogen, each with a different degree of N-N bond activation with dinitrogen stretching frequencies of 2120, 1994 and 1925 cm⁻¹ for **2-N₂**, **3**, and **4** respectively. It was also seen that binding of an axial dinitrogen ligand changes the spin state of complex **2** from $S = 5/2$ to $S = 1/2$. Similarly, theoretical calculations of **3** without N₂ bound predict a $S = 2$ ground state. Experimentally, **3** has a $S = 1$ spin system with N₂ bound which is also validated through theoretical calculations. Catalytic dinitrogen reduction will be examined more in depth in Chapter 3.

2.5 Experimental Procedures

2.5.1 General Considerations

Unless otherwise stated, all manipulations were performed under a dinitrogen atmosphere in a Vac Atmosphere glovebox or using standard Schlenk techniques.

Standard solvents were deoxygenated by sparging with dinitrogen and dried by passing through activated alumina columns of a SG Water solvent purification system.

Deuterated solvents were purchased from Cambridge Isotope Laboratories, Inc., degassed via freeze-pump-thaw cycles, and stored over activated 4 Å molecular sieves. ^1H and ^{31}P NMR spectra were recorded on Varian 300, and 500 MHz spectrometers at ambient temperature unless otherwise stated. Proton chemical shifts were referenced to residual solvent, ^{31}P NMR was referenced to 85% H_3PO_4 at 0 ppm.

The synthesis of 2,2,2-tri(diisopropylphosphinomethylamino)triphenylamine ((N(o-(NHCH₂PiPr₂)C₆H₄)₃) (abbreviated as LH₃) has been reported previously.^{69b}

2.5.2 Synthetic Procedures

Synthesis Protocol of Co₂Cl(L), (1-Cl): LH₃ (0.0344 g, 0.051 mmol) was dissolved in 2 mL of diethyl ether and cooled to -40 °C. nBuLi (2.5 M, 62 μL, 0.15 mmol) was added to the ether solution. The solution is immediately allowed to warm to room temperature and stirred for 1 h. The solution was then frozen and slowly thawed. It was then added to a frozen slurry of CoCl₂(THF)_{1.5} (24.3 mg, 0.102 mmol) (THF 4 mL). The solution was warmed to rt and stirred 1 hr to which the solvent was removed *in vacuo*. The solid was dissolved in toluene and filtered through Celite using a glass fiber filter. The solvent was then removed *in vacuo* overnight to yield a dark purple powder **2** (0.0404 g, 95 %). ^1H NMR (300 MHz, C₆D₆): δ 75.6, 53.8, 18.0, 12.2, 5.9, 4.8, 32., 2.1, 1.4, -2.4, -2.7. Evans'

Method: $\mu_{\text{eff}} = 4.51$ B.M ($S = 2$). UV-vis-NIR (THF) $\lambda_{\text{max}}/\text{nm}$ ($\epsilon / \text{M}^{-1} \text{cm}^{-1}$): 448 (4000), 554 (5800), 720 (1230), 953 (640). Analysis (calcd., found) for $\text{C}_{39}\text{H}_{60}\text{N}_4\text{P}_3\text{Co}_2\text{Cl}$: C (56.36, 56.44), H (7.28, 7.39), N (6.74, 6.65). The bromide analogue can be prepared by substituting CoBr_2 for $\text{CoCl}_2(\text{THF})_{1.5}$.

Synthesis Protocol of Co_2L (2): Potassium graphite (0.0067 g, 0.049 mmol) was added to a THF solution (4 mL) of **2** (0.0404 g, 0.048 mmol). The solution was stirred for 2.5 hrs in which the solution changed from dark purple to dark brown. The solution was filtered through Celite. The solvent was then removed *in vacuo* to give a brown solid. The solid was dissolved in toluene and filtered through Celite using a glass fiber filter. The solvent was removed *in vacuo* overnight to yield a brown solid **3** (0.034 g, 89%). Single crystals suitable for X-ray diffraction analysis were grown from a THF solution layered with pentane. ^1H NMR (300 MHz, C_6D_6): δ 60.0, 36.9, 15.2, 8.80, -31.6, -47.8. Evans' Method: $\mu_{\text{eff}} = 6.14$ B.M. ($S = 5/2$). UV-vis-NIR (THF) $\lambda_{\text{max}}/\text{nm}$ ($\epsilon / \text{M}^{-1} \text{cm}^{-1}$): 450 (9800), 958 (400), 1200 (200). Analysis (calcd., found) for $\text{C}_{39}\text{H}_{60}\text{N}_4\text{P}_3\text{Co}_2$: C (58.87, 58.86), H (7.60, 7.74), N (7.04, 7.07).

Synthesis of $[\text{K}(2,2,2\text{-cryptand})]\text{Co}_2(\text{N}_2)\text{L}$ (3): KC_8 (0.0041 g, 0.030 mmol) was added to a solution of **3** (0.024 g, 0.030 mmol) in 5 mL of THF. The solution was allowed to stir for 4 hr in which the solution changed from brown to yellow-brown. The solution was then filtered through a celite plug into a vial containing 2,2,2-cryptand (0.0113 g, 0.030 mmol). The solution then changed from yellow-brown to orange-brown. The solvent was removed *in vacuo* to give an orange-yellow solid. The solid was washed with benzene

and dried to give a yellow powder **3** (0.0331 g, 89 %). Single crystals suitable for X-ray diffraction analysis were grown from a THF solution layered with diethyl ether. ^1H NMR (300 MHz, d^8 -THF): δ 202.4, 196.6, 21.5, 6.8, 3.6, 2.6 -8.9, -30.4 IR (KBr pellet): $\nu(\text{N}_2)$ = 1994 cm^{-1} . UV-vis-NIR (THF) $\lambda_{\text{max}}/\text{nm}$ ($\epsilon / \text{M}^{-1} \text{cm}^{-1}$): 560 (1400), 637 (980), 1035 (205), 1271 (220). Analysis (calcd., found) for $\text{C}_{57}\text{H}_9\text{N}_8\text{P}_3\text{O}_6\text{KCO}_2$: C (55.24, 54.96), H (7.81, 7.75), N (9.04, 8.73).

Synthesis of $[\text{K}(\text{2,2,2-cryptand})]_2\text{Co}_2(\text{N}_2)\text{L}$ (4**):** KC_8 (0.0496 g, 0.367 mmol) was added to a solution of **2** (0.146 g, 0.184 mmol) in 10 mL of THF. The solution was allowed to stir for 12 hr in which the solution changed from brown to yellow-green. The solution was then filtered through a Celite plug into a vial containing 2,2,2-cryptand (0.138 g, 3.67 mmol). The solution changed from green to red-orange. The solvent was removed *in vacuo* to give an orange foam. The solid was reconstituted in THF and layered with diethyl ether to give orange-brown blobs (0.1156 g, 38%). ^1H NMR (300 MHz, d^8 -THF): δ 87.2, 27.0, 17.4, 11.7, 2.8, 1.3, 0.9, -27.7 IR (KBr pellet): $\nu(\text{N}_2)$ = 1925 cm^{-1} . UV-vis-NIR (THF) $\lambda_{\text{max}}/\text{nm}$ ($\epsilon / \text{M}^{-1} \text{cm}^{-1}$): 564 (1600), 653 (640), 1450 (360). Analysis (calcd., found) for $\text{C}_{75}\text{H}_{132}\text{N}_{10}\text{P}_3\text{O}_{12} \text{K}_2\text{CO}_2$: C (54.43, 55.26), H (8.04, 8.29), N (8.46, 7.36).

2.5.3 X-ray Crystallographic Data Collection and Refinement of Structures

A purple block of **1-Br**, a brown block of **2**, and an orange needle of **3** were placed on the tip of a 0.1 mm diameter glass capillary and mounted on a Bruker APEX II CCD diffractometer for data collection at 173(2) K. The data collection was carried out using Mo $K\alpha$ radiation (graphite monochromator). The data intensity was corrected for absorption and decay (SADABS). Final cell constants were obtained from least-squares

fits of all measured reflections and the structure was solved using SHELXS-08 and refined using SHELXL-08. A direct-methods solution was calculated which provided most non-hydrogen atoms from the E-map. Full-matrix least-squares/difference Fourier cycles were performed to locate the remaining non-hydrogen atoms and all non-hydrogen atoms were refined with anisotropic displacement parameters. Hydrogen atoms were placed in ideal positions and refined as riding atoms with relative isotropic displacement parameters. Disordered THF solvent molecules were removed from the unit cell of **2** and **3** using Platon SQUEEZE2. Solid-state structures of **1-Br**, **2**, and **3** have been deposited into the Cambridge Crystallographic Data Centre (CCDC 962873-962875).

2.5.4 *Physical Measurements*

Elemental analyses were performed by Complete Analysis Laboratories, Inc. (Parsippany, NJ). Cyclic voltammetry was performed with a CH Instruments 600 electrochemical analyzer with a one-cell setup, comprising a glassy carbon working electrode, a platinum wire counter electrode, and Ag/AgNO₃ reference electrode in acetonitrile. Analytes were measured in 0.1 M [TBA]PF₆ DME solutions and internally referenced to the Cp₂Fe/Cp₂Fe⁺ redox couple. Low temperature Fourier transform infrared (FTIR) spectra were collected on a Nicolet 6700 FTIR spectrometer (Thermo Scientific) with at least 16 scans and a resolution of 1 cm⁻¹ and kept in a cryostat regulated by liquid nitrogen and heater.

2.5.5 *Computational Details*

Three species, **2**, **3**, and **3-N₂**, were interrogated by multi-reference calculations using their DFT-optimized geometries in the MOLCAS-7.8 program.⁸⁰ In some cases, the compounds were truncated by replacing the isopropyl groups appended to the phosphines

to methyl groups ($^{\text{Me}}\text{L}$). The geometries of all species were derived from DFT optimizations (*vide supra*). The complete active space self-consistent field (CASSCF)⁸¹ and the restricted active space self-consistent field (RASSCF)⁸² methods were used, followed by multi-configurational second order perturbation theory, CASPT2⁸³ and RASPT2⁸⁴, respectively. The following relativistic all-electron basis sets were used: ANO-RCC-VTZP for Co, ANO-RCC-VDZP for P and N, and ANO-RCCMB for C and H atoms.⁸⁵ Scalar relativistic effects were included by using the Douglas–Kroll–Hess Hamiltonian.⁸⁶ The two-electron integral evaluation was simplified by using the Cholesky decomposition technique.⁸⁷ To avoid intruder states, an imaginary level shift of 0.2 au was used in the CASPT2 calculations.⁸⁸ For $^{\text{Me}}\text{LCo}_2$ and $[\text{Me}^{\text{L}}\text{Co}_2]^-$ species, a large configuration interaction space was investigated with RASSCF and RASPT2 calculations. The configuration interaction space is described as (N,20)/(N,10)/p, where the first parentheses corresponds to the total number of electrons (N, where N=15 and 16 for $^{\text{Me}}\text{LCo}_2$ and $[\text{Me}^{\text{L}}\text{Co}_2]^-$, respectively) and the total number of orbitals (20) in all RAS spaces, and the second parenthesis corresponds to the number of active electrons and orbitals in RAS2. The number of particles (p) in RAS3, which comprise the 4d orbitals of the two cobalt atoms, was restricted to 2. Multi-configurational calculations on the full $[\text{Me}^{\text{L}}\text{Co}_2(\text{N}_2)]^-$ species are computationally expensive and time-intensive. However, a CASSCF/CASPT2 study with an active space of 12 electrons in 13 orbitals was completed. For both the full and truncated structures, calculations using all valence 3d-electrons (N = 16) have not been successful.

Chapter 3

Catalytic Silylation of Dinitrogen Using Cobalt-Containing Catalysts

In part from:

Siedschlag, R. B.; Bernales, V.; Vogiatzis, K. D.; Planas, N.; Clouston, L. J.; Bill, E.;
Gagliardi, L.*; Lu, C. C.* “Catalytic Silylation of Dinitrogen with a Dicobalt Complex.”

J. Am. Chem. Soc. **2015**, 137, 4638-4641

3.1 Overview

A dicobalt complex, LCo_2 (**1**), catalyzes N_2 silylation with Me_3SiCl and KC_8 under 1 atm of N_2 at ambient temperature. Tris(trimethylsilyl)amine is formed with an initial turnover frequency of one $\text{N}(\text{TMS})_3/\text{min}$, ultimately reaching a turnover number of ~ 200 . The dicobalt species features a metal-metal interaction, which we postulate is important to its function. Although N_2 functionalization occurs at a single cobalt site, the second cobalt center modifies the electronics at the active site. It was found through a series of heterobimetallic cobalt species (Co-M , where $\text{M} = \text{Al, Ti, V, Cr}$) that the reactivity can be tuned through interactions between the two metal centers. Density functional calculations reveal that the Co-Co interaction evolves during the catalytic cycle: weakening upon N_2 binding, breaking with silylation of the metal-bound N_2 , and re-forming with expulsion of $[(\text{Me}_3\text{Si})_2\text{N}-\text{N}(\text{SiMe}_3)]^-$. It was also found through calculations that an isostructural $\text{LaCo}(\text{N}_2)$ complex is mechanistically similar but kinetically different.

3.2 Introduction

The N-Si bond has long been recognized as a useful linkage in organic synthesis for masking primary and secondary amines. Catalytic schemes to construct such bonds directly from N₂ are underdeveloped and would revolutionize the manufacturing of silylamines, which are increasingly important as industrial chemicals. For example, trisilylamines are used to fabricate silicon-nitride semi-conductors in front-end electronic applications, and Si-N based polymers are incorporated into ceramic materials to impart thermal resistance.⁸⁹ Developing N₂ silylation catalysts^{22a, 30e, 90} also complements ongoing research in N₂ fixation to ammonia, as they share the challenge of functionalizing N₂, a molecule that is both thermodynamically stable and kinetically inert, in an efficient and selective manner.^{5a, 21, 30f, 56b, 91}

A known catalyst for N₂ silylation is Mo(dep_f)₂(N₂)₂ (dep_f = 1,1'-bis(diethylphosphino)ferrocene) (Figure 3.2.1 top left), which produces N(SiMe₃)₃ from an atmosphere of N₂, Me₃SiCl, and Na_(s), with a turnover number (TON) of 150.^{22a} The catalytic mechanism was calculated to proceed through the attack of TMS radicals on the dinitrogen ligand. However, definitive experimental evidence for that radical mechanism was not provided. Recently, a molybdenum catalyst ligated in a tridentate phosphine scaffold was able to net a TON of 22 of N(SiMe₃)₃ with K_(s) as the reducing agent.^{22b} Unlike the previous molybdenum catalyst, this catalyst was proposed to functionalize dinitrogen with electrophilic Me₃SiCl opposed to Me₃Si radical. Specifically, it was found that the complex can functionalize dinitrogen twice in the distal position and cleave the N-N bond with the addition of two electrons to generate a Mo(IV) nitride.

Efforts to surpass the Mo catalysts with a first-row transition metal have met with limited success. A survey of simple iron^{90e} and cobalt⁹² coordination complexes showed subdued TONs, attaining a maximum of 40 (Figure 3.2.1 right). In this chapter, a dicobalt catalyst, **1** (**2** from chapter 2), that achieves relatively high TON of N(SiMe₃)₃ at 299 K will be discussed (Figure 3.2.1 center). The catalyst features a hemi-labile metal-metal interaction, which is, to our knowledge, is a unique hallmark in catalytic N₂ functionalization. This labile interaction can be perceived similarly to the interstitial carbide of nitrogenase, and its lability promoting catalytic reduction of dinitrogen.⁹³

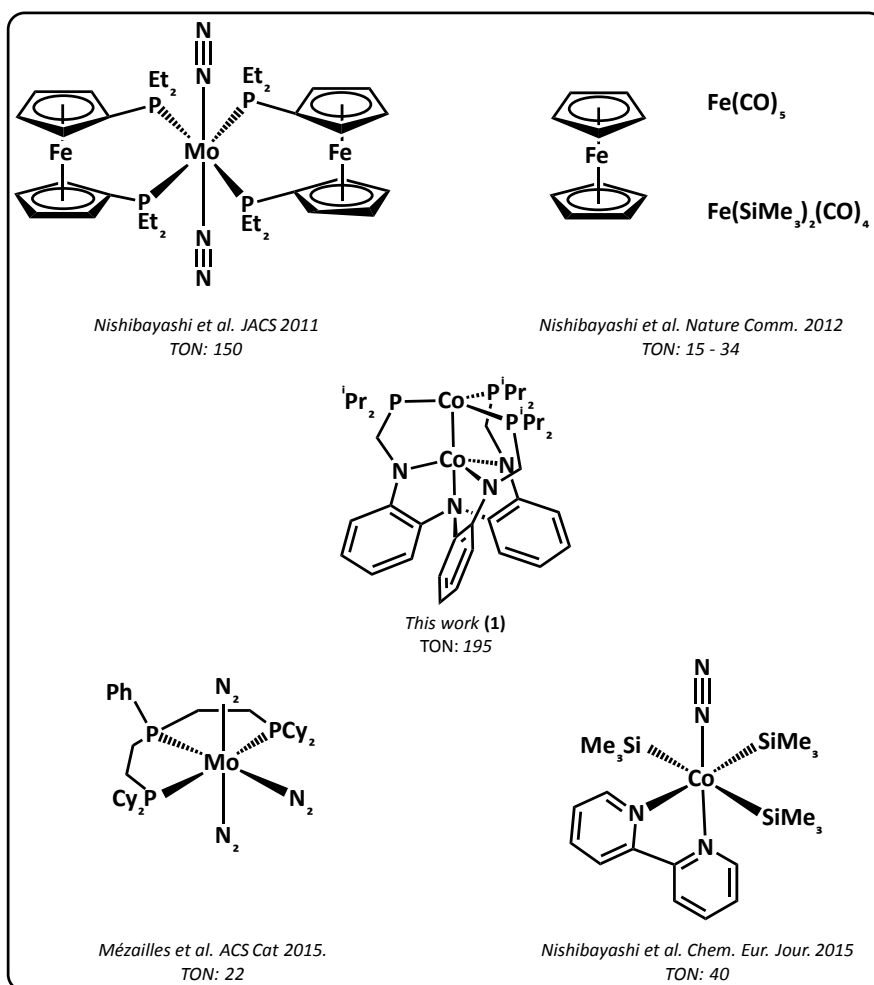
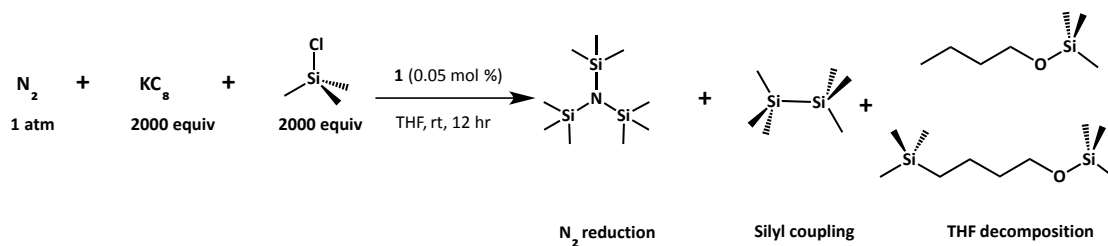


Figure 3.2.1 Selected examples of dinitrogen silylation catalysts
TON = turnover number

3.3 Results and Discussion

3.3.1 Catalytic Silylation of Dinitrogen

Since the anionic dicobalt N₂-adduct is stable to vacuum, we postulated that [LCo₂(N₂)]⁻ (**2**) could mediate the catalytic reduction of dinitrogen by using LCo₂ (**1**) as the precatalyst. Complex **1** was tested in catalytic N₂-silylation using a large excess of Me₃SiCl and reductant, KC₈, under an atmosphere of N₂. Standard catalytic conditions use a low-catalyst loading (0.13 mM, 0.05 mol%) at 299 K for 12 h in THF. Under these conditions, **1** generated N(SiMe₃)₃ in 30% yield, with a TON of 195 ± 25 (Table 3.3.1). The product was quantified via GC/MS (Figures 3.3.1 and 3.3.2). Based on the TON, **1** is one of the most active N₂-silylation catalysts with comparable activity to Mo(depf)₂(N₂)₂. Besides the desired product, N(SiMe₃)₃, other side-products are typically formed under these conditions, including Me₃SiSiMe₃, and mono- and bis-silylated THF, i.e. Me₃SiO(CH₂)₃CH₂R, where R = H, or SiMe₃ (Scheme 3.3.1). Formation of the latter two byproducts can be suppressed by performing the catalysis in DME (DME = dimethoxyethane), but the TON for N(SiMe₃)₃ is slightly lower at 140 ± 8 (Table A3.3.1). Anionic complex **2** was also catalytically competent and gave an identical TON as **1** (Table 3.3.1, entry 2). To test the robustness of the catalyst, we performed two consecutive catalytic cycles (i.e. living catalysis) using a 0.16 mM solution of **1**. In each cycle, Me₃SiCl and KC₈ (2000 equiv. each) were added to the reaction flask, and the reaction stirred for 12 h. The overall TON was 320 ± 18. If the first cycle generates 195 turnovers, then ~65% of the activity was retained in the second cycle (*vide infra*). When compared to living catalysis performed by Nishibayashi et al. in the Mo(depf)₂(N₂)₂ system (TON 226, ~50% activity), **1** is slightly more robust and overall performs better than the previous state-of-the-art system.



Scheme 3.3.1 Scheme showing products seen under standard catalytic conditions

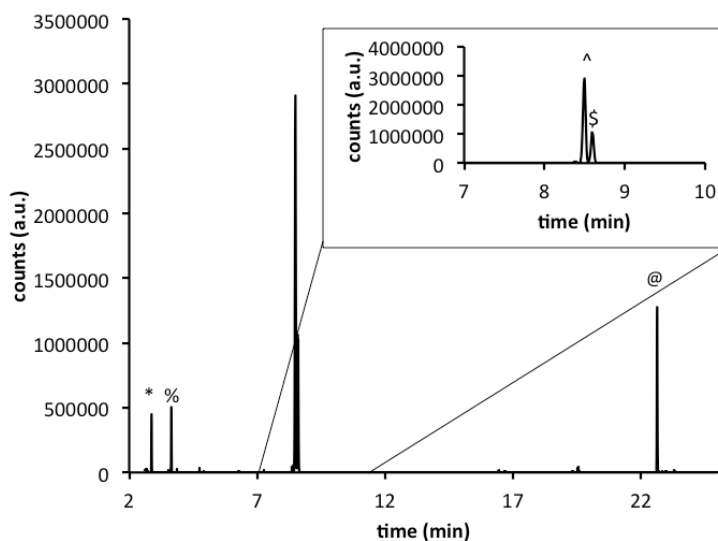


Figure 3.3.1 GC trace of catalytic reaction products

* = $\text{Me}_3\text{SiSiMe}_3$, % = $\text{Me}_3\text{SiOCH}_2\text{CH}_2\text{CH}_2\text{CH}_3$, ^ = $\text{Me}_3\text{SiOCH}_2\text{CH}_2\text{CH}_2\text{CH}_2\text{SiMe}_3$,
 \$ = $\text{N}(\text{SiMe}_3)_3$, @ = 9-fluorenone

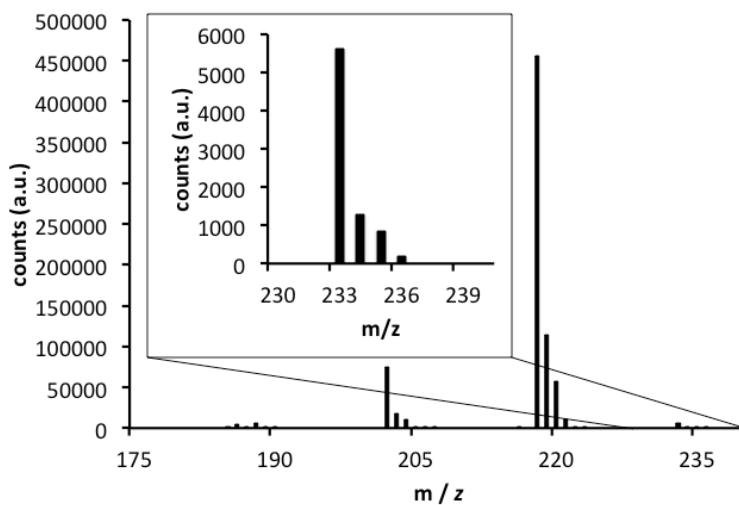


Figure 3.3.2 MS result of GC signal at 8.53 min corresponding to amine product. Insert: zoom to see m/z for $^+\text{N}(\text{SiMe}_3)_3 = 234$

We also tested an isostructural Co-Al compound, $\text{Co}(\text{N}_2)\text{AIL}$, to gauge the effect of the supporting metal on catalysis.^{41m} Under standard conditions, $\text{Co}(\text{N}_2)\text{AIL}$ produced substantially less amine with a TON of 30 ± 9 (entry 3). There are two possible factors that contribute to the poor catalytic performance of $\text{Co}(\text{N}_2)\text{AIL}$. The first factor is the apparent *trans* influence that aluminum imposes on the catalysis. In neutral and anionic cases, $\text{Co}(\text{N}_2)\text{AIL}$ and $\text{Co}(\text{N}_2)\text{AIL}^-$ have dative $\text{Co} \rightarrow \text{Al}$ interactions. The Lewis acidic aluminum center removes electron density from the cobalt center (Co_P), making the cobalt less basic and limiting the ability of the cobalt to donate electron density into the dinitrogen ligand (Figure 3.3.3, left). In contrast, anionic **2** has a *trans* metallo-ligand that is less Lewis acidic, which removes little, if any, electron density from Co_P , promoting the activation of dinitrogen (Figure 3.3.3, right). The second factor is a possible difference in the catalytic mechanism of $\text{Co}(\text{N}_2)\text{AIL}$ and **1**. Through computational studies of the mechanism, it is believed that the rate-determining-step (r.d.s) is different between the two catalysts (*vide infra*). This difference, which will be discussed in Section 3.3.4, also is hypothesized to lead to faster rates of catalyst degradation in the case of $\text{Co}(\text{N}_2)\text{AIL}$. The experimental evidence for the hypothesized degradation is preliminary and will be addressed in future communications.

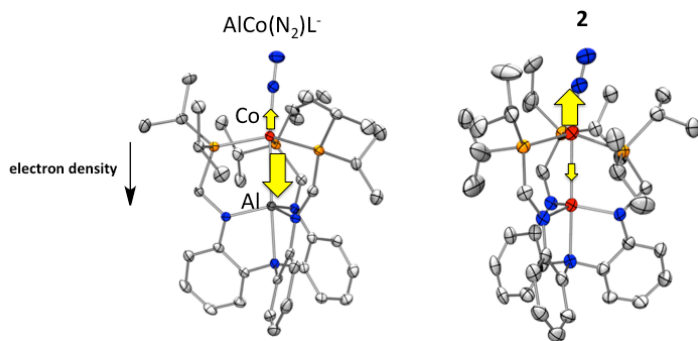
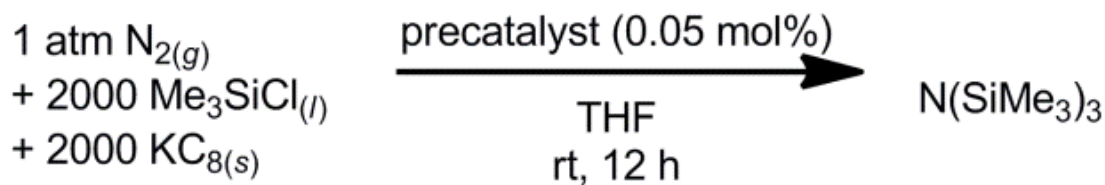


Figure 3.3.3 Structures of $[\text{Co}(\text{N}_2)\text{AIL}]^-$ (left) and **2** (right) with qualitative depiction of the *trans*-influence of the metallo-ligand and N_2 activation at cobalt. Yellow arrows represent the qualitative direction of electron density. Hydrogens and counter ions are omitted for clarity

Table 3.3.1 Reaction of N₂ (1 atm), Me₃SiCl (10.5 mmol), and KC₈ (10.4 mmol) using different cobalt precatalysts (5.27 μmol, 0.13 mM) in 40 mL THF at 299 K for 12 hr.



entry	precatalyst	% yield ^a	TON ^b
1	Co ₂ L (1)	30	195 ± 25
2	K(crypt)[(N ₂)Co ₂ L] (2)	27	178 ± 37
3	Co(N ₂)AIL	5	30 ± 9
4	CoCl ₂	1	6 ± 2
5	Co(PPh ₃) ₃ Cl	7	44 ± 11
6	CoCl ₂ + 3 PMe ₃	13	86 ± 6
7	CoCl ₂ + 3 PMe(<i>i</i> -Pr) ₂	14	94 ± 19
8	2 CoCl ₂ + LH ₃	25	172 ± 16
9	CoCl ₂ + LH ₃	16	103 ± 20
10	Co nanopowder ^c	0 ^d	0 ^d

^a % yield (ave of 3 trials) is calculated for N(SiMe₃) relative to Me₃SiCl.

^b TON (ave of 3 trials) = [N(SiMe₃)₃]/[precatalyst].

^c Co nanopowder (carbon-coated, < 50 nm particle size)

^d No amine detected by GC-MS.

The catalytic functionalization of N₂ by cobalt complexes is unconventional, though low-valent cobalt complexes are known to bind N₂.^{41e, 42, 94} Following our report, Nishibayashi et al. also reported that simple low-valent cobalt compounds can be competent in the silylation of N₂.⁹² To investigate whether simple cobalt complexes can perform N₂ silylation, we screened some cobalt precursors (Table 3.3.1, entries 4-7).

Even CoCl_2 is catalytic, although its activity is limited to a few turnovers (entry 4).^{90a} The Co(I) complex, $\text{CoCl}(\text{PPh}_3)_3$, is modestly active, with a TON of 44 ± 11 (entry 5). Increasing the Lewis basicity of the phosphine ligands dramatically raises the yield of $\text{N}(\text{SiMe}_3)_3$, and the TONs reach ~ 100 for the trialkylphosphines, PMe_3 and $i\text{-Pr}_2\text{PMe}$ (entries 6-7). The Lewis basicity of the trialkyl phosphine ligands is hypothesized to cause greater σ donation and lesser π -back donation in the Co-P bond. This dichotomy leads to an increase in electron density around the cobalt center to π donate into a dinitrogen ligand, which leads to increased N_2 activation and increased reactivity. While the ligand (LH_3) does not generate any amine under standard catalytic conditions, mixing the ligand with two equivalents of CoCl_2 is as effective as **1** (entry 8). Due to the large excess of reductant around, it is hypothesized that **1** is generated *in situ* in this case. Of note, a 1:1 ratio of the ligand to CoCl_2 halves the TON relative to **1** (entry 9), further providing evidence for the *in situ* generation of **1** with LH_3 and CoCl_2 . Finally, the only cobalt precursor in this screening that did not generate any detectable amine was cobalt nanopowder (entry 10).

Catalytic N_2 functionalization can be highly sensitive to the reductant,^{21-22, 90b, 91b, c} and so we investigated catalysis by **1** with various alkali metals: $\text{Li}_{(s)}$, $\text{Na}_{(s)}$, and $\text{K}_{(s)}$. Using standard catalytic conditions, the alkali metals significantly depressed the yield of $\text{N}(\text{SiMe}_3)_3$ (Table 3.3.2, entries 1-3). However, by prolonging the reaction time with $\text{K}_{(s)}$ from 12 to 95 h, the TON increases to 135 ± 29 (entry 4). It is hypothesized that catalysis is more facile with KC_8 compared to the alkali metal counterparts due to the increased surface area of KC_8 leading to a kinetically more favorable electron transfer process.

Table 3.3.2 Variation of reductants or additives with complex **1** under standard catalytic conditions (see Table 3.3.1).

entry	reductant	% yield ^a	TON ^a
1	Li _(s)	2.92	19 ± 6
2	Na _(s)	1.07	7 ± 5
3	K _(s)	4.49	29 ± 3
4	K _(s) (t = 95 h)	20.58	135 ± 29
additive ^b			
5	PMe ₃	27.01	178 ± 4
6	<i>t</i> -BuNC	18.36	120 ± 13

^a Calculation of % yield and TON is the same as for data in Table 3.3.1.

^b Additives are exogenous ligands. KC₈ is the reductant.

3.3.2 Elucidating the Active Catalytic Species

A difficult problem in catalysis is pinpointing the speciation of the active species, whether it be homogeneous or heterogeneous.⁹⁵ Though cobalt nanoparticles (NPs) were inactive for N₂ silylation, the elusive nature of the active species and the ambiguity surrounding any single speciation test prompted us to investigate this problem. To this end, we have probed the speciation of the catalyst through selective poisoning, a filtration test, initial rate studies, and *in operando* studies.

Since catalytic NPs have a smaller fraction of active metal sites relative to the bulk metal, they are readily poisoned by sub-stoichiometric, exogenous ligands (per metal). For late metal NPs, phosphine ligands can be effective poisons.^{27,28} In contrast, homogeneous metal catalysts require at least one equiv. of phosphine to completely

inhibit activity (Figure 3.3.4). The addition of one equiv. PMe_3 per **1** effected no change in TON (Table 3.3.2, entry 5). The use of a π -acceptor ligand, *t*-BuNC (1 equiv), however, did lower the TON to 120 ± 13 , but the preservation of significant activity argues against a heterogeneous catalyst.

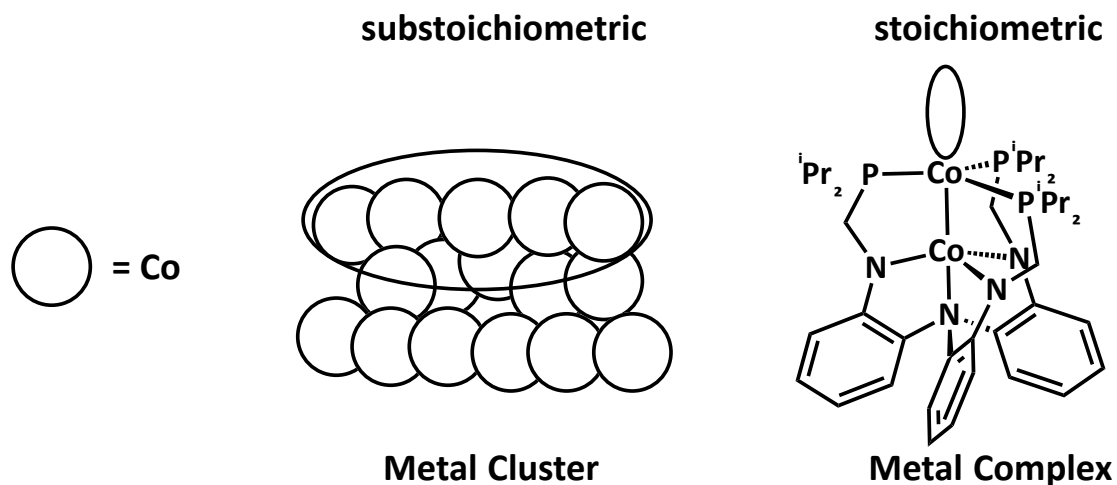


Figure 3.3.4 Example of poisoning test showing surface nature of nanoparticles and single site nature of molecules. The ellipses indicate binding sites of poisoning ligands

We also conducted a filtration test, whereby soluble and insoluble fractions are separated by filtration and then independently assayed for catalytic activity. In our variation of this test, one catalytic cycle is completed prior to filtration (0.13 mM **1**, 2000 equiv. Me_3SiCl , 2000 equiv. KC_8 , 80 mL THF, 12 hr). After filtering through a graphite pad, the resulting precipitate and half of the filtrate are each subjected to a second cycle of catalysis (Figure 3.3.5). The other half of the filtrate serves to exactly quantify the amine formed after the first cycle, and gave a TON of 166.^{38b} If the active species is insoluble, then at the conclusion of the second cycle, the TON will be ~ 166 for both the precipitate and the filtrate, as the latter carries the amine generated in the first cycle. On the other hand, if the active species is soluble, then the precipitate should not generate any amine, and the TON of the filtrate should double. Following work up, the overall

TON of the filtrate reaction was 316, versus 30 for the precipitate. Hence, we conclude that the active species is soluble.

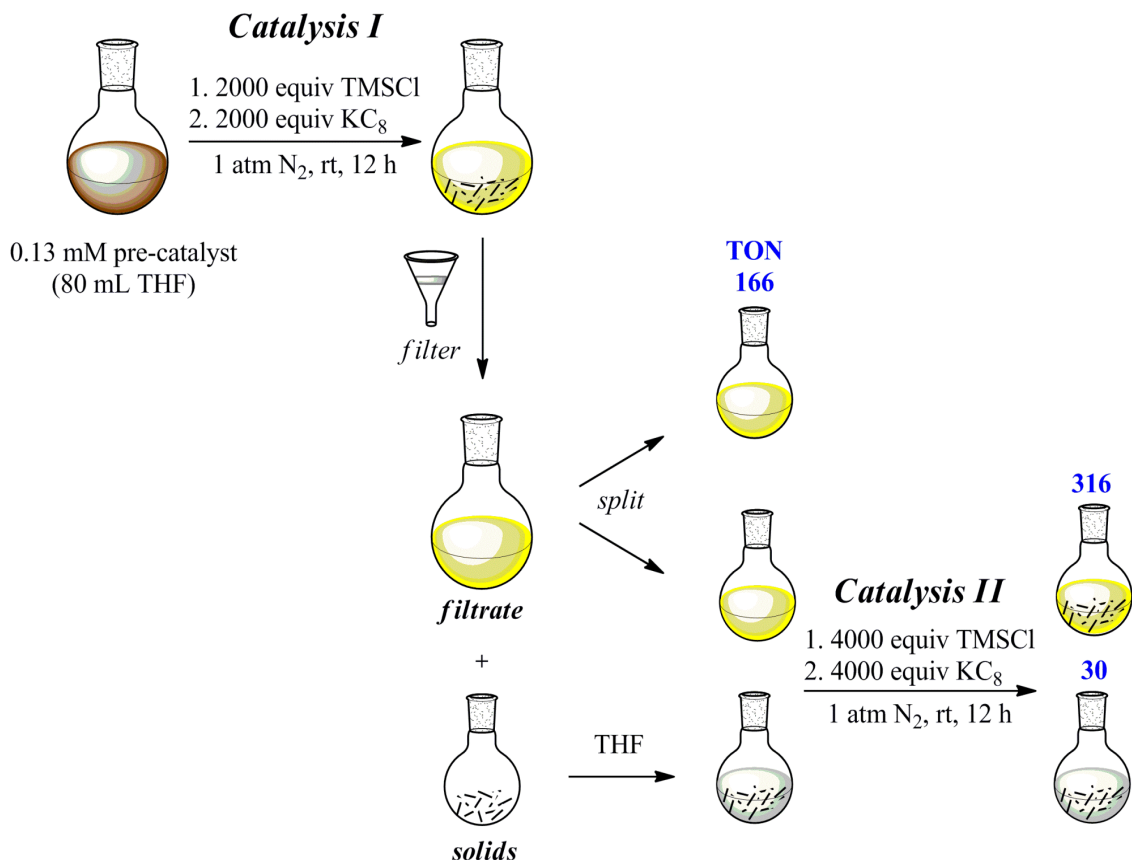


Figure 3.3.5 Visual depiction of the filtrate test using **1** as the pre-catalyst. Turnover numbers (TONs) are shown in blue in the figure, and were determined by GC-MS analysis of the worked up product, as described in the experimental section.

Though NPs and/or insoluble aggregates are discredited as active component(s) in the catalysis, cobalt nanoclusters, by virtue of their smaller size, can be soluble and more challenging to detect or to exclude. Formation of active nanoclusters may manifest in an induction period and/or irreproducible kinetic data. Initial rate experiments were conducted to determine the reaction order with respect to **1**. Amine formation was monitored by sampling the reaction mixture at discrete time points ($t = 2, 5, 10, 15,$ and 20 min). For each sample, the amount of $\text{N}(\text{SiMe}_3)_3$ was determined by converting

$\text{N}(\text{SiMe}_3)_3$ into NH_4Cl with acid, and then quantifying the ammonium by the indophenol method (Section 3.5).⁹⁶ A sample vis spectra of an indophenol run is shown in Figure 3.3.6 ($[\mathbf{1}] = 0.65 \text{ mM}$ at 293K). Rates of $\text{N}(\text{SiMe}_3)_3$ production were measured at four different concentrations of **1** (0.026, 0.13, 0.32, and 0.65 mM) (Figure 3.3.7), and the initial rates show a pseudo-first order dependence on catalyst concentration (Figure 3.3.8). The linear dependence of initial rates on **1**, as well as the absence of a lag period, is most consistent with a well-behaved homogeneous catalyst. We can also extract a turnover frequency of approximately one $\text{N}(\text{SiMe}_3)_3$ molecule per minute by performing the catalysis for one hour and examining the amount of product formed.

Further evidence of direct bimetallic catalyst was obtained through catalytic runs with various hetrobimetallic (MCoL) cobalt complexes ($\text{M} = \text{Ti}, \text{V}, \text{Cr}$). Under standard catalytic conditions, it was observed that the homobimetallic cobalt complex still performed the best. As the *trans* metalloligand is varied from cobalt to the left on the periodic table, the TON decreased ($\text{Cr} = 107$, $\text{V} = 86$, and $\text{Ti} = 81$). Interestingly, the TON of the heterobimetallics are within experimental error of one another. Experiments are on going to understand the differences in the catalytic competency of the heterobimetallic species.⁴⁴

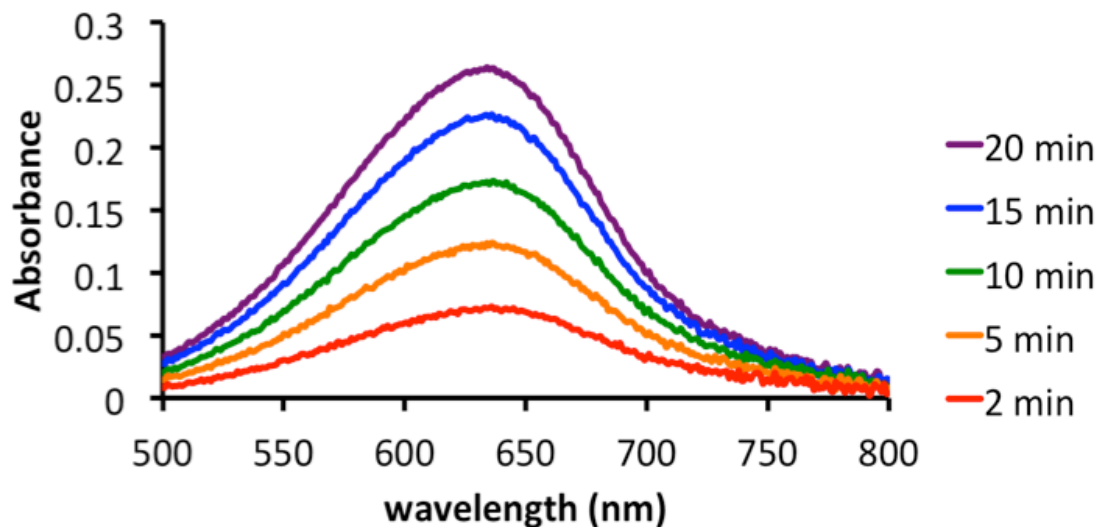


Figure 3.3.6 Vis overlay of observed indophenol formation from kinetic runs of **1** (0.65 mM). Time = 2 min (red), 5 min (orange), 10 min (green), 15 min (blue), 20 min (purple). A 1 cm pathlength cell was used and the spectra were collected at 293 K.

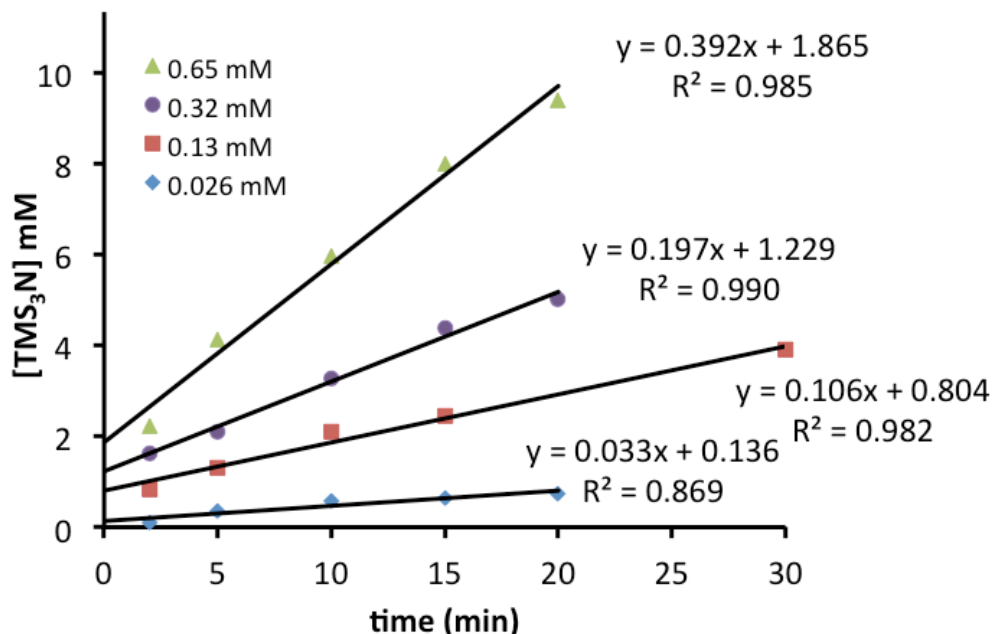


Figure 3.3.7 Plot of $[TMS_3N]$ versus time at various **1** (0.026-0.65 mM) in reactions with N_2 (1 atm), Me_3SiCl (21.3 mmol), and KC_8 (20.7 mmol).

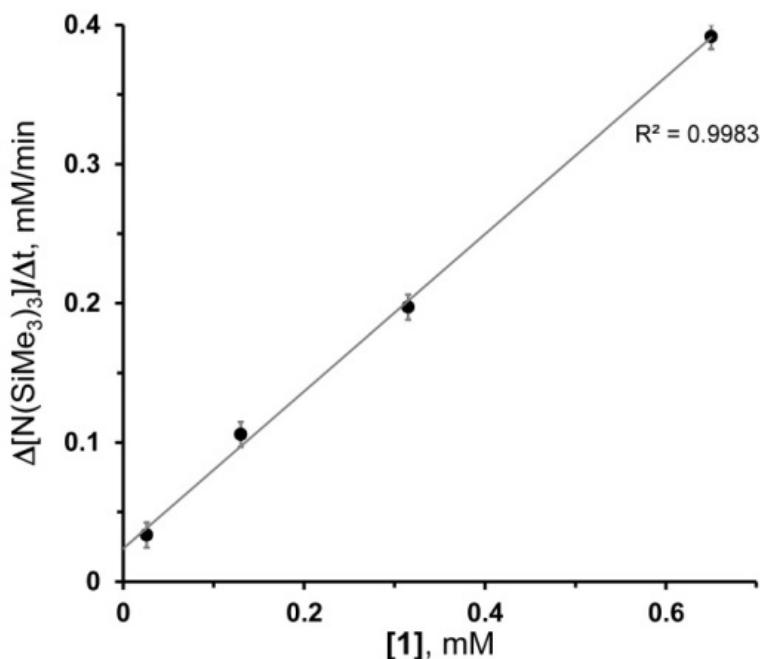


Figure 3.3.8 Plot of initial rates ($\Delta[\text{N}(\text{SiMe}_3)_3]/\Delta t$, mM min^{-1}) versus [1] (0.026-0.65 mM) in reactions with N_2 (1 atm), Me_3SiCl (21.3 mmol), and KC_8 (20.7 mmol).

As well as examining the catalyst dependence on rate of catalysis, the dependence on dinitrogen was also examined. Sub-atmospheric dinitrogen pressures as well as high-pressure dinitrogen runs were performed. The preliminary data suggests no dependence of $[\text{N}_2]$ at pressures greater than 1 atm (Table 3.3.3). To do this, **1** was subjected to various pressures of N_2 ($P = 1, 25, 50$ and 100 atm). Entries 1-4 were run at standard catalytic conditions using 30 mL of THF. Since turnovers are not improved with increased pressure of dinitrogen, it is believed that the reaction is saturated with dinitrogen and dinitrogen binding is not rate limiting.

To further investigate dinitrogen dependence, sub-atmospheric dinitrogen runs were run. By mixing different pressures of argon and dinitrogen in a high-pressure reactor and bleeding the mixture into the reaction vessels, mixtures of 25% and 10% dinitrogen were

used (75% and 90% Ar respectively). The preliminary data suggests that sub-atmospheric N₂ gave lowered TONs of 84(11) and 72(22) respectively. However, the control trial using the same experimental setup with 100 % N₂ gave a TON of 105(10). The different experimental setup could be the reason for the lowered TON from that of the reported 195(25) TON. Further investigation is needed to confirm a sub-atmospheric N₂ dependence.

Table 3.3.3 High pressure N₂ runs at 0.05% catalyst loading in 30 mL of THF

Entry	[1] mM	Pressure (atm)	TON ^a
1	0.13	1	195(25) ^b
2	0.13	25	161(15)
3	0.13	50	181(8)
4	0.13	100	184(9)

a) duplicate trials TON = mmol cat/ mmol N(TMS)₃

b) reported TON

In operando studies were conducted to assess whether the active species is truly bimetallic. Complex **1** was mixed with a small excess of Me₃SiCl and KC₈ (10 equiv.) under N₂ in THF-d₈ for 90 min. ¹H NMR analysis showed the presence of N(SiMe₃)₃ and multiple paramagnetic species (Figure 3.3.9, C and Figure 3.3.10 C), one of which is complex **2**. If the reaction is quenched with a drop of CD₂Cl₂, then only one paramagnetic species is observed, namely Co₂(Cl)L (Figure 3.3.9, B). These observations are consistent with a bimetallic active species during catalysis.

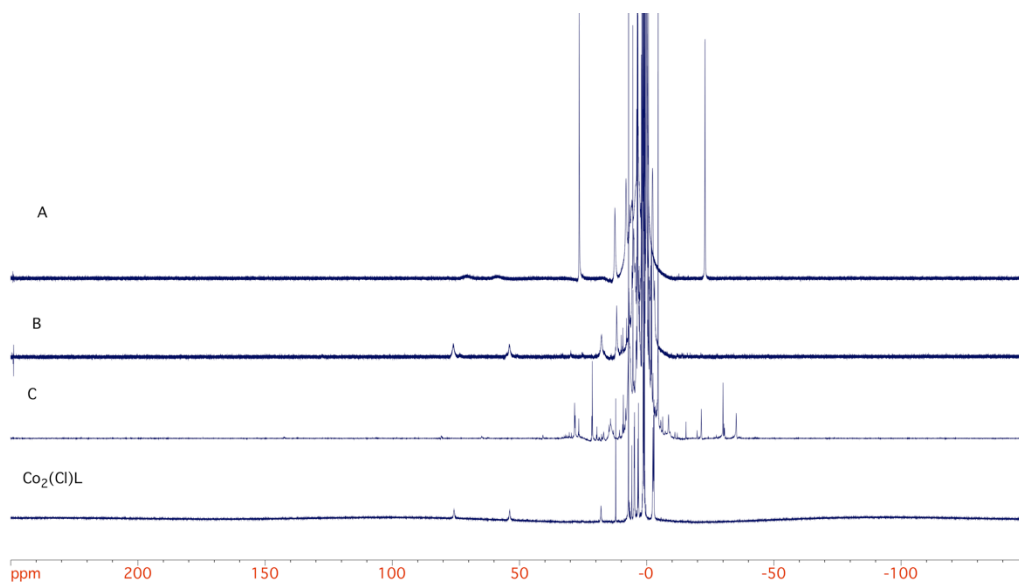


Figure 3.3.9 Stacked ^1H NMR (500 MHz, d^8 -THF) of *in operando* studies with precatalyst **1**
 Reaction A: **1** + 10 KC_8 + 5 $\text{Me}_3\text{SiSiMe}_3$ (90 min stirring under N_2 , filter prior to NMR)
 Reaction B: **1** + 10 KC_8 + 10 Me_3SiCl
 (90 min stirring under N_2 , filter, quench with one drop of CD_2Cl_2)
 Reaction C: **1** + 10 KC_8 + 10 Me_3SiCl (90 min stirring under N_2 , filter prior to NMR)

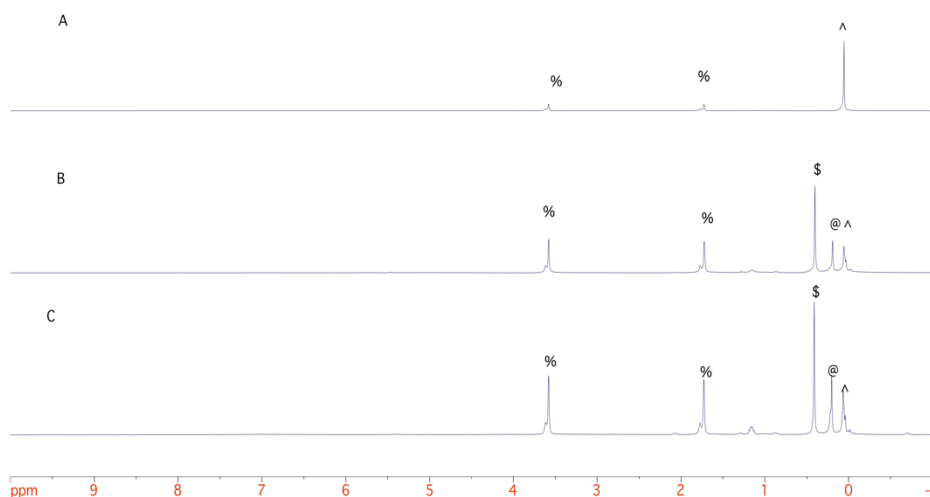


Figure 3.3.10 Stacked ^1H NMR (500 MHz, d^8 -THF) of *in operando* studies with precatalyst **1**.
 Zoom of the diamagnetic region (% = THF, \$= THF decomposition,
 @ = TMS_3N , ^ = hexamethyl disilane)
 Reaction A: **1** + 10 KC_8 + 5 $\text{Me}_3\text{SiSiMe}_3$ (90 min stirring under N_2 , filter prior to NMR)
 Reaction B: **1** + 10 KC_8 + 10 Me_3SiCl
 (90 min stirring under N_2 , filter, quench with one drop of CD_2Cl_2)
 Reaction C: **1** + 10 KC_8 + 10 Me_3SiCl (90 min stirring under N_2 , filter prior to NMR)

The mechanism for silylation of dinitrogen is ambiguous. The substrate, TMSCl, can react in three different reaction pathways (Figure 3.3.11). One pathway is through nucleophilic attack of the bound dinitrogen on TMSCl through a transient $[\text{TMS}]^+$.^{22b} A second pathway involves the generation of TMS radicals which then attack the bound dinitrogen.^{22a} The final potential pathway is one in which TMSCl dimerizes and forms hexamethyldisilane, $\text{Me}_3\text{SiSiMe}_3$, in the presence of potassium graphite.⁹⁷ The dimer then can be cleaved to generate $[\text{TMS}]^-$, which could then nucleophilically attack the bound dinitrogen. To rule out the reactive TMS anion, the catalysis was examined through an *in operando* ^1H NMR experiment with **1**, $\text{Me}_3\text{SiSiMe}_3$ as the silyl source and KC_8 (Figure 3.3.9 A). It was seen that the dianionic species, $[(\text{N}_2)\text{Co}_2\text{L}]^{2-}$, was the only species observed. When examining the ^1H diamagnetic region, only the starting disilane was observed with no proton signals corresponding to the amine product being present (Figure 3.3.10A).

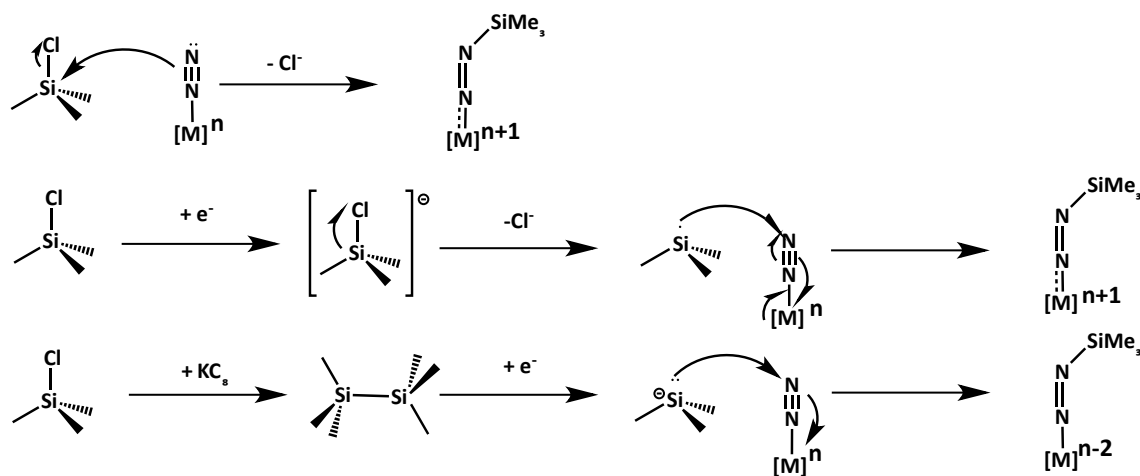


Figure 3.3.11 Three potential reactive pathways for silylation of dinitrogen Top: Nucleophilic attack; Middle: TMS radical attack; Bottom: TMS anion attack.

3.3.3 Theoretical Calculations and Mechanistic Insight

Theoretical calculations were performed to gain insight into catalytic mechanism and the electronic structures of **1** and **2**. The pre-catalyst, Co_2L , and potential active species, $[\text{Co}_2\text{L}]^-$ (**A**) and $[(\text{N}_2)\text{Co}_2\text{L}]^-$ (**B**) were found to have spin ground-states of $S = 5/2$, 2, and 1, respectively. The ground states of Co_2L and **B** match that of their experimental counterparts, **1** and **2**. In all three structures, the Co-Co interaction is weak: the only delocalized molecular orbitals are $(\sigma)^2$ and $(\sigma^*)^1$, and their occupancies predict a bond order of 0.5. The pre-catalyst, Co_2L , contains an $S = 3/2$ $\text{Co}_\text{N}(\text{II})$ and $S = 1$ $\text{Co}_\text{P}(\text{I})$ (where Co_N and Co_P denote the Co sites in the N_3 - and P_3 -plane), in agreement with the magnetic data. In the “naked” anion, **A**, Co_P is reduced to $S = 1/2$ $\text{Co}_\text{P}(0)$, while the $S = 3/2$ $\text{Co}_\text{N}(\text{II})$ center remains unchanged. The primary effect of N_2 -binding (**A**→**B**) is to change the nature of the magnetic coupling, leading to a lower overall spin state.

A catalytic mechanism and its energy profile are presented in Figure 3.3.12. As proposed previously,^{22a, 30e} the SiMe_3 radical is the active silyl reagent under reducing conditions. The overall mechanism begins with N_2 -binding (**A**→**B**), followed by three sequential additions of $\cdot\text{SiMe}_3$ to the N_2 ligand, and then expulsion of $[(\text{Me}_3\text{Si})_2\text{N}-\text{N}(\text{SiMe}_3)]^-$ to regenerate Co_2L . It has been calculated that $[\text{N}_2(\text{SiMe}_3)_3]^-$ converts spontaneously to two $\text{N}(\text{SiMe}_3)_3$ via an un-catalyzed pathway.^{22a} Lastly, Co_2L is easily reduced to **A** with KC_8 , closing the catalytic cycle. Alternative pathways, e.g. via a dicobalt nitride intermediate, were ruled out due to high activation barriers (>50 kcal/mol, Figure 3.3.13).

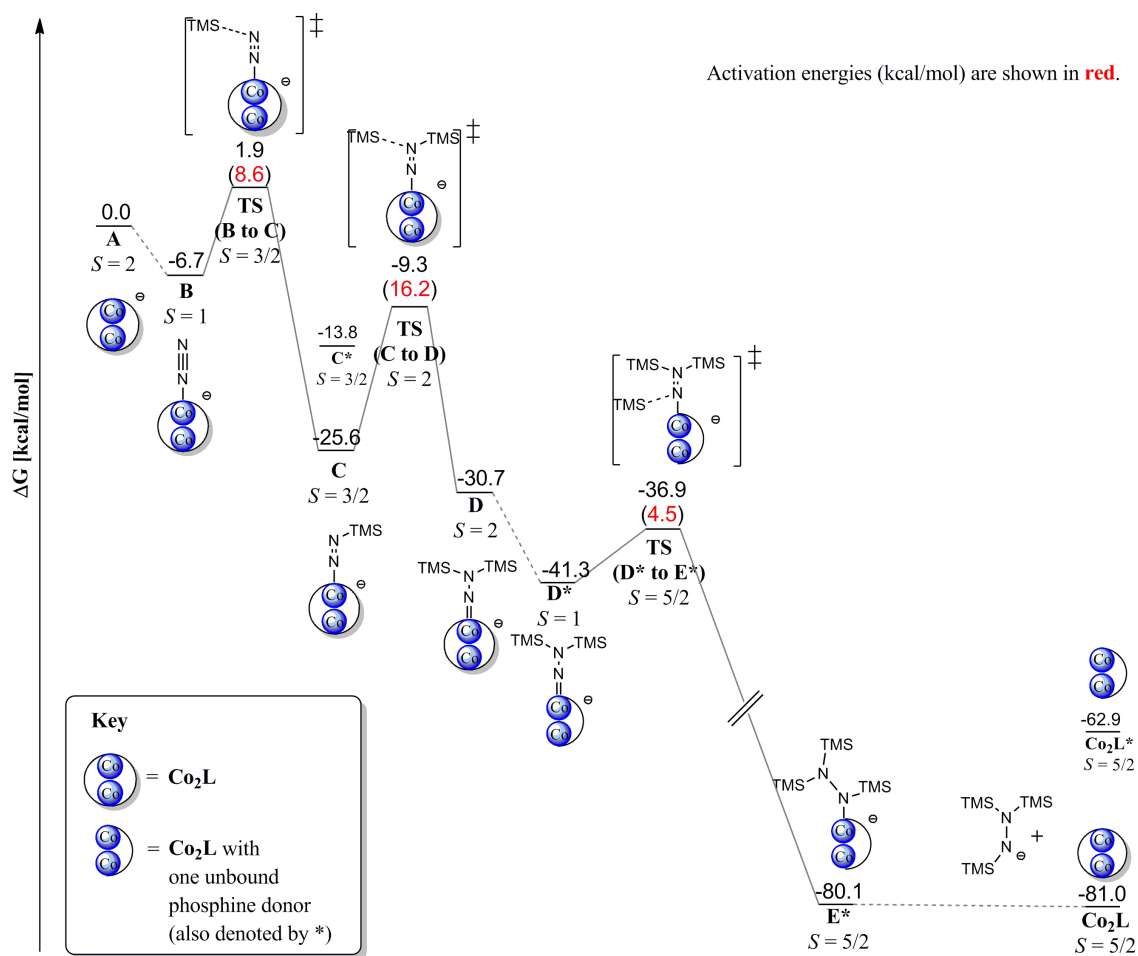


Figure 3.3.12 Energy profile of the catalytic mechanism mediated by **A** with calculated intermediates and transition states. For each structure, the lowest spin state is indicated, along with ΔG values (relative to the reactants: **A**, N_2 and six TMS radicals). Reaction barriers are shown in red within parenthesis. The drawing is roughly scaled to energy, except where denoted by a break “//”. For the reaction, $\text{N}_2 + 6 \text{TMS}\bullet \rightarrow 2 \text{N}(\text{TMS})_3$, $\Delta G = -265.4 \text{ kcal/mol}$.

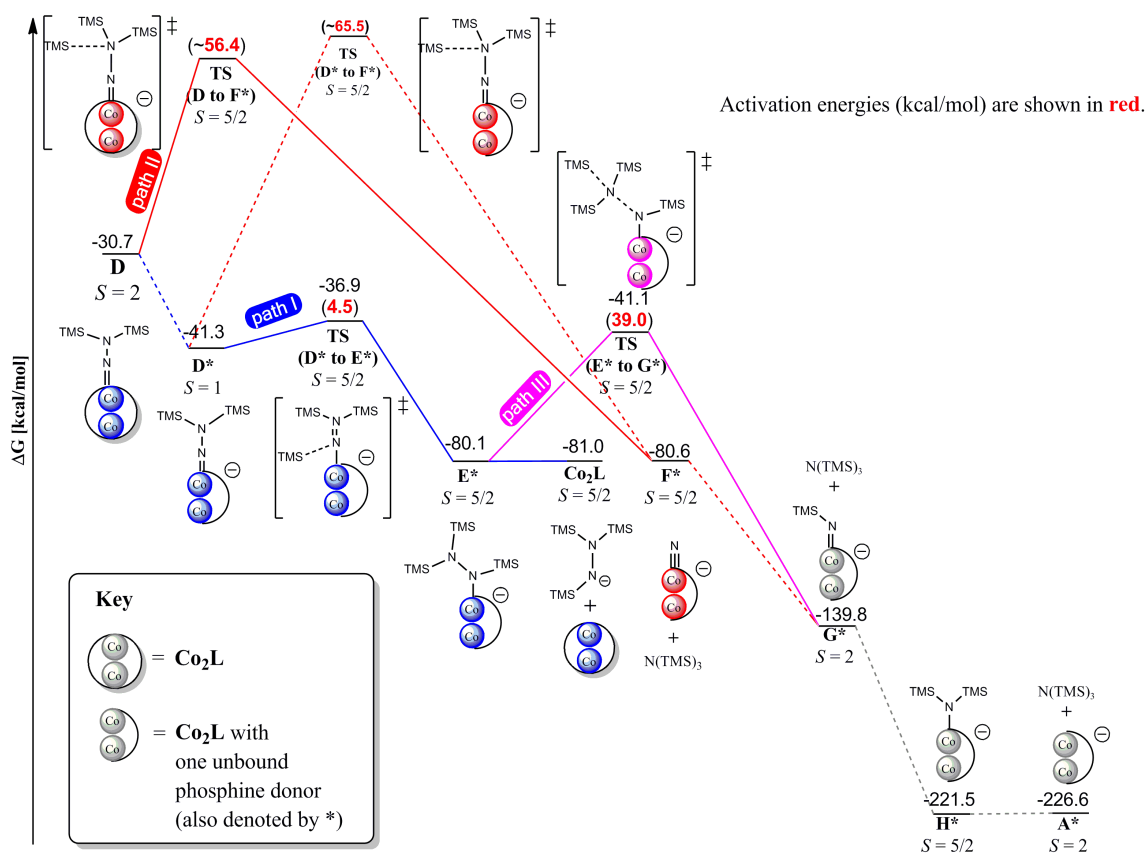


Figure 3.3.13 Energy profile of the three possible mechanisms mediated by **A** with calculated intermediates and transition states. Since the reaction mechanism from **A** to **D** is the same for the three alternative paths (see Figure 3.3.12 for **A** to **D** pathway), **D** was chosen as the starting point. For each structure, the lowest spin state is indicated, along with ΔG values (relative to the reactants: **A**, N_2 and six TMS radicals). Reaction barriers are shown in red within parenthesis. The drawing is NOT scaled to energy. Color is used to distinguish the alternative pathways (**II** and **III**) from path **I**.

The interesting section of the catalytic cycle is the cobalt-mediated reduction of N_2 by a total of four electrons to $[\text{N}_2(\text{SiMe}_3)_3]^-$. The three $\cdot\text{SiMe}_3$ equivalents add to the cobalt-bound N_2 in a distal-distal-proximal sequence, which is similar to the DFT-calculated mechanism for $\text{Mo}(\text{depf})_2(\text{N}_2)_2$.^{22a} The first $\cdot\text{SiMe}_3$ reacts with **B** to form the silyldiazenido(1-) intermediate **C**, with a barrier of 8.6 kcal/mol. The second addition of $\cdot\text{SiMe}_3$ generates the disilylhydrazido(2-) species **D**, with $\Delta G^\ddagger = 16.2$ kcal/mol, making this the rate-determining step. Intermediate **D** then undergoes an endergonic dissociation of one phosphine donor, presumably to lessen the steric repulsion between the phosphine substituents and the disilylhydrazido ligand to give intermediate **D***, where the asterisk denotes one dangling phosphine arm. The third $\cdot\text{SiMe}_3$ preferentially attacks the proximal N-atom, to form trisilylhydrazido **E*** with a low ΔG^\ddagger of 4.5 kcal/mol. Finally, phosphine association expels $[\text{N}_2(\text{SiMe}_3)_3]^-$ and regenerates Co_2L . No transition state could be found for this step (**E*** \rightarrow Co_2L), so we presume that this step is essentially barrierless.^{22a}

Notably, the $\text{Co}\cdots\text{Co}$ distance changes dramatically in this elementary step, from 3.547 Å in **E*** to 2.522 Å in Co_2L , whereby formation of the Co-Co bond may assist in releasing the $[\text{N}_2(\text{SiMe}_3)_3]^-$ product. Though Co_N is potentially redox-active, our calculations show that this is not the case here (Table A3.3.2). In the mechanism, Co_P cycles between $\text{Co}(0)$ and $\text{Co}(\text{II})$ in discrete one-electron steps, while Co_N maintains a constant oxidation state of +2 and a spin-state of $S = 3/2$. Although the reducing equivalents are stored only at the active cobalt, Co_N plays a significant role in stabilizing various $\text{Co}_\text{P}(\text{N}_2(\text{SiMe}_3)_x)$ ($x = 0$ to 2) intermediates, similar to the postulated mechanism of Rh_2 -catalyzed diazo-transfer reactions.⁹⁸ Indeed, the Co-Co interaction increasingly

weakens as N₂ binds and is functionalized to disilylhydrazido intermediate **D**, wherein the metal-metal bond is fully cleaved (Table A3.3.3). In the final step, the release of trisilylhydrazide is concomitant with Co-Co and Co-P bond formations.

Considering the bimetallic nature of the catalyst, it is intriguing to examine the role of the second cobalt. The supporting metal clearly affects the overall catalysis, as substituting Co with Al yields an isostructural Co-Al bimetallic that is less active by 6.5 fold. The Co oxidation states and the nature of the Co-M bonds are quite different between these two systems. For the Co-Al system, the (CoM)³⁺ and (CoM)²⁺ species are consistent with Co(0)Al(III) and Co(-I)Al(III),⁹⁹ whereas in dicobalt, they are better described as Co(I)Co(II) and Co(0)Co(II). In [Co(N₂)AIL]⁻, a strong inverse dative bond is present, Co(-I)→Al(III), whereas in [(N₂)Co₂L]⁻, the cobalt centers are weakly interacting. The Lewis acidic Al(III) metalloligand suppresses the catalytic activity at Co, and this is consistent with the opposite scenario that increasingly basic phosphine ligands increase TON (Table 3.3.1, entries 4-6). Hence, the supporting metal can effectively tune the electron density at the active cobalt center, where Al(III) and Co(II) represent two electronic differences of a metalloligand.

Another reason for the differences in the catalytic activity of **1** and Co(N₂)AIL is can be seen in the calculated reaction mechanism. By examining the reaction coordinate, it is seen that two things are different when Al is swapped out for Co in the bottom pocket (Figure 3.3.14). For Co(N₂)AIL, the phosphine arm dissociates at intermediate **C** to give **C***, whereas for **1**, the phosphine arm does not dissociate off until intermediate **D**. In **1**, the phosphine arm dissociating at **C** is 12 kcal/mol less favorable than it staying bound (Table 3.3.4). Since the phosphine arm dissociates early for Co(N₂)AIL, it is hypothesized

that the intermolecular decomposition of the dangling phosphine arm can be more facile, thus leading to poorer catalytic turnover.⁴⁴ A second difference is while the rate determining step in both complexes are the second addition of TMS radical, the transition state following the rate determining step for Co(N₂)AIL has a similar barrier to that of the rate determining step. This could lead to slower overall reaction kinetics. These findings along with the differences in the electronics of the two catalysts provide a solid hypothesis for the differences in catalytic activity.

Table 3.3.4 Energy profile of the catalytic mechanism mediated by **A** with calculated intermediates and transition states for AlCo and CoCo For each structure, ΔG values relative to the reactants: **A**, N₂ and six TMS radicals are indicated. Reaction barriers (ΔG^\ddagger) are shown in red within parenthesis. ΔG and ΔG^\ddagger are reported in kcal mol⁻¹.

Co M L Intermediate	M = Al (ΔG)	M = Co (ΔG)
A	0	0
B	-20.8	-6.7
B to C	-9.5 (11.3)	1.9 (8.6)
C	-17.7	-25.6
C*	-31.2	-13.8
C to D (C* to D* for M= Al)	-10.9 (20.3)	-9.3 (16.3)
D	N/A	-30.7
D*	-39.5	-41.3
D to E	-22.0 (17.5)	-36.9 (4.4)
E*	-67.8	-80.1
F*	-61.5	-62.9
G	-78.4	-81

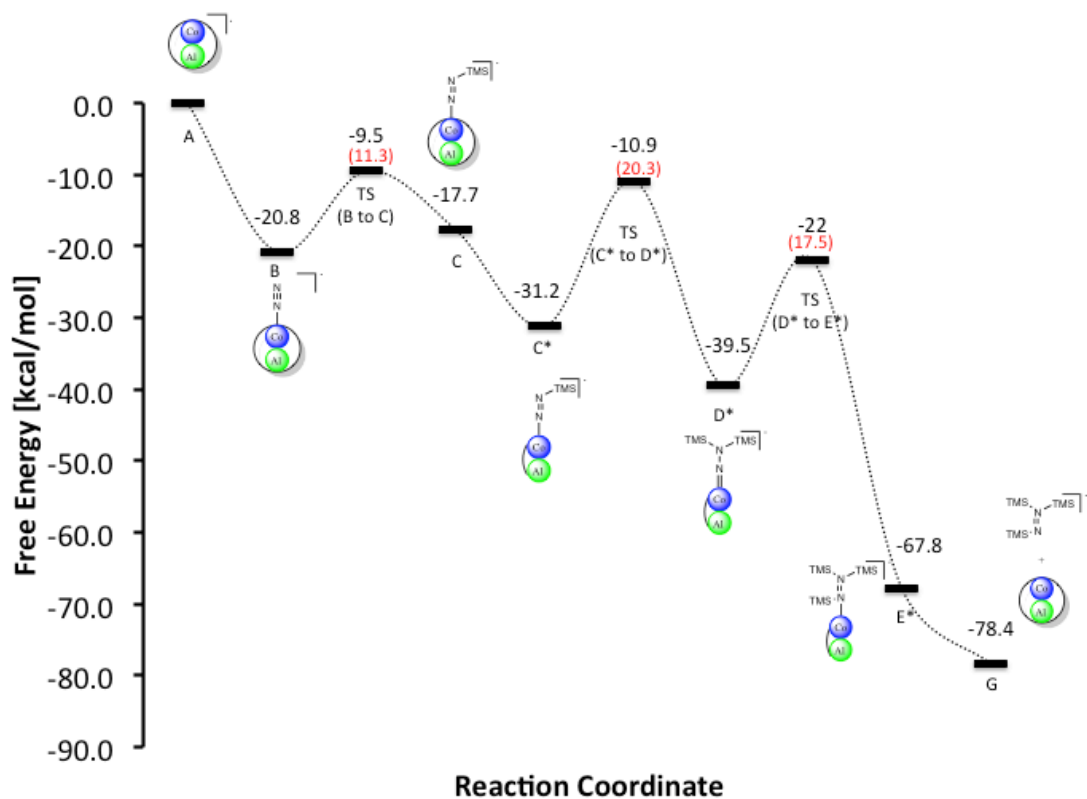


Figure 3.3.14 Energy profile of the catalytic mechanism mediated by $\text{Co}(\text{N}_2)\text{AIL}$ with calculated intermediates and transition states. For each structure, the ΔG values relative to the reactants: **A**, N_2 and six TMS radicals are shown. Reaction barriers (ΔG^\ddagger) are shown in red within parenthesis. The drawing is not scaled to energy.

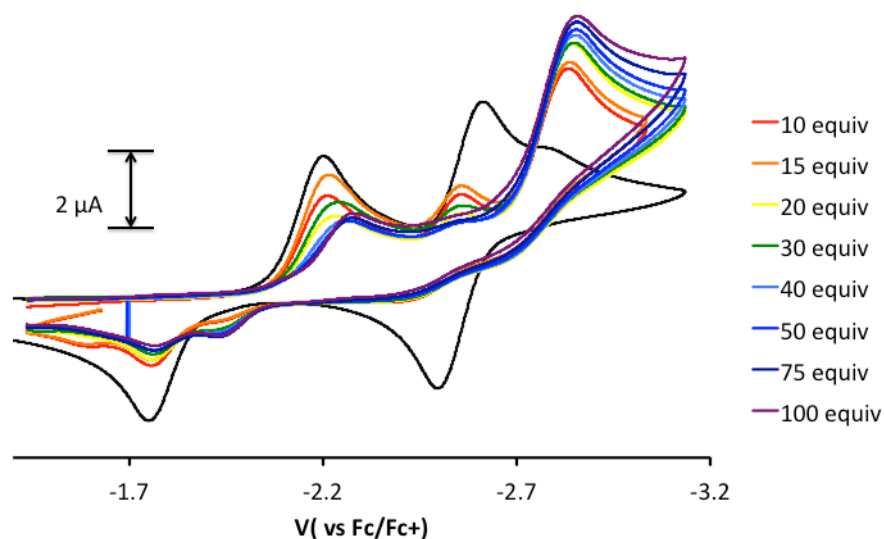


Figure 3.3.15 CV (DME, 250 mV/s, 0.2 M TBAPF₆) of **1** (black trace) with varying equivalents of TMSCl.

3.3.4 *Electrocatalytic Dinitrogen Silylation*

Lowering the atom economy for homogeneous reactions allows for the possibility of industrial applications. One way to achieve atom economy is by performing the reaction or catalysis electrochemically. In the case of dinitrogen silylation, the need for an outer sphere chemical electron source could be mitigated. To see if a catalyst can perform as an electrocatalyst, cyclic voltammetry (CV) experiment would yield a response of large current (catalytic current) when the reaction is occurring. As the amount of substrate is increased, the catalytic response should also increase. To that end, electrocatalysis using **1** as a pre-catalyst was explored. As can be seen in Figure 3.3.15, there is a change in the electrochemical response corresponding to an analyte-substrate interaction at the electrode.

However, the CV data suggests low or zero electrocatalytic activity due to the minute increase in current upon addition of substrate. One hypothesis for this result is the multi-step mechanism for dinitrogen silylation, where separate steps generating TMS[•] or nucleophilic attack of TMSCl by a reduced bimetallic N₂X_n species are required. Alternatively, the scan rate could be faster than the catalytic rate and/or the rate of diffusion of catalyst and substrate, thus no catalysis is observed. Further investigation of electrocatalysis is needed using a bulk electrolysis setup.

3.4 Conclusions

The silylation of dinitrogen was accomplished using a dicobalt catalyst, **1**. This catalyst out-performed the prior state of the art species by having a TON of 195 (25). Catalyst **1** was also shown to be robust in that it could under go a second set of catalytic conditions to have a total TON of 325 and ~65 % activity is retained when comparing the TONs between runs. Evidence was provided through various experiments that catalyst **1** is a well-behaved molecular bimetallic species. Theoretical calculations provided vital understanding for the catalytic mechanism. The reaction was found to proceed in a similar manner to previously studied silylation catalysts (Figure 3.3.16). The calculations also provided insight into the potential differences in catalytic activity for (N₂)CoAIL and **1**, showing that the timing of phosphine dissociation plays an important role in catalytic activity and potentially overall catalyst robustness. Preliminary data also suggests a *trans* metallo-ligand influence on the catalytic activity of several heterobimetallic complexes. The final chapter will discuss the isolation of potential intermediates along the catalytic pathway in hopes of lending insight into the type of transformation that is occurring.

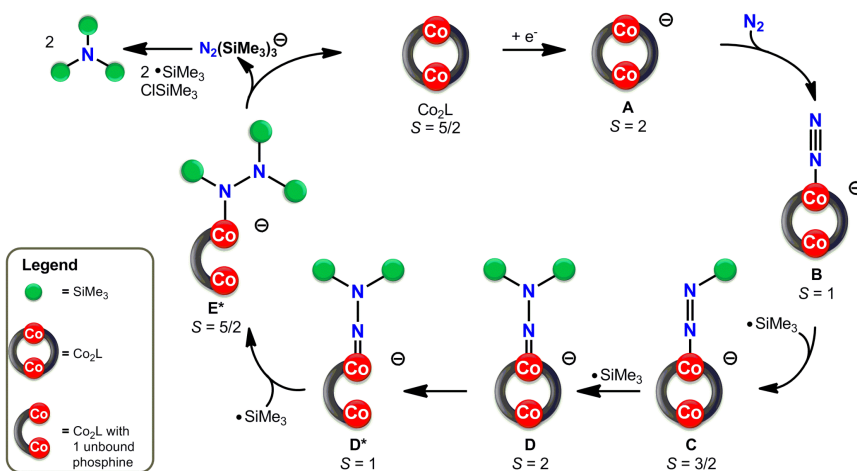


Figure 3.4.1 Proposed catalytic cycle for dinitrogen silylation using **1**

3.5 Experimental

3.5.1 General Considerations and Physical Methods

Unless otherwise stated, all manipulations were performed under a dinitrogen atmosphere in a Vac Atmosphere glovebox or using standard Schlenk techniques. Standard solvents were deoxygenated by sparging with dinitrogen and dried by passing through activated alumina columns of a SG Water solvent purification system. Deuterated solvents were purchased from Cambridge Isotope Laboratories, Inc., degassed via freeze-pump-thaw cycles, and stored over activated 4 Å molecular sieves. ^1H and ^{31}P NMR spectra were recorded on Varian 300, and 500 MHz spectrometers at ambient temperature unless otherwise stated. Proton chemical shifts were referenced to residual solvent, ^{31}P NMR was referenced to 85% H_3PO_4 at 0 ppm. Cyclic voltammetry was performed with a CH Instruments 600 electrochemical analyzer with a one-cell setup, comprising a glassy carbon working electrode, a platinum wire counter electrode, and Ag/AgNO_3 reference electrode in acetonitrile. Analytes were measured in 0.1 M $[\text{TBA}]\text{PF}_6$ DME solutions and internally referenced to the $\text{Cp}_2\text{Fe}/\text{Cp}_2\text{Fe}^+$ redox couple. All GC-MS experiments were conducted on an Agilent Technologies 7890A GC system and 5975C VLMSD. The GC column was a HP-5 ms with dimensions 30 m x 0.25 mm. The standard method used for all runs involved an initial oven temperature of 50°C (held for 2 min) followed by a 20°C min^{-1} ramp to 80°C (held for 4 min), followed by a by a 20°C min^{-1} ramp to 150 °C (held for 6 min) and a final 20°C min^{-1} ramp to 230°C (held for 10 min).

3.5.2 *Catalytic Procedures*

Typical procedure for the catalytic reduction of N₂ into N(SiMe₃)₃ using **1:** The precatalyst **1** (12.6 mg, 15.8 mmol) was dissolved in THF (12 mL) to make a concentrated stock solution. A 4 mL aliquot of the solution (5.27 mmol) plus 36 mL THF was transferred to a 100 mL sealable, cylindrical, thick-walled reaction flask (0.13 mM). To the flask, Me₃SiCl (1.3 mL, 10.5 mmol) and KC₈ (1.4 g, 10.4 mmol) were added. The reaction flask was sealed and stirred at rt for 12 hrs. At the end of the catalytic run (12 hrs), the reaction solution was filtered through a paper-lined Büchner funnel, and the residue was washed with THF (2 x 15 mL). The combined filtrate was first condensed by rotary evaporation to ~5 mL, and then subjected to vacuum transfer with heating to 100 °C to collect the organic volatiles. The volatiles were then diluted in THF to 25.0 mL. From this solution, a 1.0 mL aliquot was mixed with 9-fluorenone as an internal standard (1.0 mL of a 30.0 mM THF) and then analyzed by GC-MS to quantify the concentration of N(SiMe₃)₃. This procedure was used to determine TON for **1** and other cobalt precatalysts.

Living catalysis for the catalytic reduction of N₂ into N(SiMe₃)₃ using **1:** The precatalyst **1** (12.6 mg, 15.8 mmol) was dissolved in THF (12 mL) to make a concentrated stock solution. A 4 mL aliquot of the solution (5.27 mmol) plus 36 mL THF was transferred to a 100 mL sealable, cylindrical, thick-walled reaction flask (0.13 mM). To the flask, Me₃SiCl (1.3 mL, 10.5 mmol) and KC₈ (1.4 g, 10.4 mmol) were added. The reaction flask was sealed and stirred at rt for 12 hrs. A second set of reagents (KC₈, TMSCl and THF) was added to the reaction flask, sealed and stirred at RT for 12 hr. At

the end of the catalytic run (12 hrs), the reaction solution was filtered through a paper-lined Büchner funnel, and the residue was washed with THF (2 x 15 mL). The combined filtrate was first condensed by rotary evaporation to ~5 mL, and then subjected to vacuum transfer with heating to 100 °C to collect the organic volatiles. The volatiles were then diluted in THF to 25.0 mL. From this solution, a 1.0 mL aliquot was mixed with fluorenone as an internal standard (1.0 mL of a 30.0 mM THF) and then analyzed by GC-MS to quantify the concentration of $\text{N}(\text{SiMe}_3)_3$. This procedure was used to determine TON for **1** and other cobalt precatalysts.

Filtration test for the catalytic reduction of N_2 into $\text{N}(\text{SiMe}_3)_3$ using **1:** The precatalyst **1** (8.2 mg, 10.3 mmol) was dissolved in 80 mL THF (0.13 mM) and transferred to a 100 mL sealable, cylindrical, thick walled reaction flask. To the flask, Me_3SiCl (2.7 mL, 21.3 mmol) and KC_8 (2.8 g, 20.7 mmol) were added. The reaction was stirred for 24 hrs, and then the reaction solution was filtered through a graphite-lined frit. The residue was rinsed with 5 mL THF, and the combined filtrate was divided into two equal aliquots of 40 mL. One of the aliquots was worked up as described above to determine the TON of the first catalytic run. The second aliquot was transferred to a sealable reaction flask, and subjected to a second catalytic run by adding Me_3SiCl (2.7 mL, 21.3 mmol) and KC_8 (2.8 g, 20.7 mmol) and stirring for an additional 24 hrs. The precipitate from the filtration step was also subjected to a second catalytic run by adding 40 mL THF, Me_3SiCl (2.7 mL, 21.3 mmol), and KC_8 (2.8 g, 20.7 mmol), and stirring for 24 hrs. All reaction solutions were worked up as described above and analyzed by GC-MS.

Kinetic studies of the catalytic reduction of N₂ to N(SiMe₃)₃ using varying

concentrations of 1: The precatalyst **1** (2.3, 10.7, 28.8 and 57.6 mg) was dissolved in 110 mL THF (0.026, 0.13, 0.32, and 0.65 mM) and transferred to a 120 mL glass jar with a Teflon cap. To the jar, Me₃SiCl (2.7 mL, 21.3 mmol) and KC₈ (2.8 g, 20.7 mmol) were added. Periodically, 3.0 mL aliquots were removed from the stirring reaction (t = 1, 2, 5, 10, 15, 20, 30, 40, 50 and 60 min). Each aliquot was filtered through a filter pipette. To the resulting filtrate, ~4 mL of a 20% HCl solution was added and the mixture was stirred overnight to convert N(SiMe₃)₃ into NH₄Cl. The reaction mixtures were diluted with de-ionized H₂O to 10.0 mL, from which an 80.0 μL aliquot was subjected to the indophenol method to quantify ammonia, wherein the aliquot was mixed with aqueous solutions of nitroprusside/phenol (10 mL) and NaOH/NaOCl (10 mL). After 30 min, the mixture was analyzed by UV-vis spectroscopy to determine the concentration of indophenol ($\lambda_{\text{max}} = 625\text{-}635$ nm).

Procedure for high-pressure N₂ studies using 1: In a glovebox, three 60 mL bottles was charged with the precatalyst **1**, KC₈ and Me₃SiCl in 30 mL of THF. The jar was placed inside of a 1 L high-pressure reactor and removed from the glovebox. The reactor was then charged with 100 atm of dinitrogen and stirred overnight at rt. At the end of the catalytic run (12 h), the reaction solution was filtered through a paper-lined Büchner funnel, and the residue was washed with THF (2 x 15 mL). The combined filtrate was first condensed by rotary evaporation to ~2 mL. To the resulting solution, ~6 mL of a 1.6 M HCl solution was added and the mixture was stirred overnight to convert N(SiMe₃)₃ into NH₄Cl. The reaction mixtures were diluted with de-ionized H₂O to 10.0 mL, from

which an 20.0 μL aliquot was subjected to the indophenol method to quantify ammonia, wherein the aliquot was mixed with aqueous solutions of nitroprusside/phenol (5 mL) and NaOH/NaOCl (5 mL). After 30 min, the mixture was analyzed by UV-vis spectroscopy to determine the concentration of indophenol ($\lambda_{\text{max}} = 625\text{-}635 \text{ nm}$).

Procedure for sub-atmospheric N_2 studies using 1: A 1 L high-pressure reactor was charged with 180 atm of Ar and 20 atm of N_2 . The resulting mixture was slowly vented into a Schlenk line at a rate of 1 bubble per second for 10 minutes. The precatalyst **1** (12.6 mg, 15.8 mmol) was dissolved in THF (12 mL) to make a concentrated stock solution. A 4 mL aliquot of the solution (5.27 mmol) plus 36 mL THF was transferred to a 100 mL sealable, cylindrical, thick-walled reaction flask (0.13 mM). To the flask, Me_3SiCl (1.3 mL, 10.5 mmol). The reaction was frozen using a liquid nitrogen bath and a coldwell. To the frozen solution was added KC_8 (1.4 g, 10.4 mmol). The reaction flask was then evacuated and sealed. The flask was then exposed to the gas mixture and stirred at rt for 12 hs. At the end of the catalytic run (12 hrs), the reaction solution was filtered through a paper-lined Büchner funnel, and the residue was washed with THF (2 x 15 mL). The combined filtrate was first condensed by rotary evaporation to ~ 2 mL. To the resulting solution, ~ 4 mL of a 1.6 M HCl solution was added and the mixture was stirred overnight to convert $\text{N}(\text{SiMe}_3)_3$ into NH_4Cl . The reaction mixtures were diluted with de-ionized H_2O to 10.0 mL, from which an 20.0 μL aliquot was subjected to the indophenol method to quantify ammonia, wherein the aliquot was mixed with aqueous solutions of nitroprusside/phenol (5 mL) and NaOH/NaOCl (5 mL). After 30 min, the mixture was analyzed by UV-vis spectroscopy to determine the concentration of indophenol ($\lambda_{\text{max}} = 625\text{-}635 \text{ nm}$).

3.5.3 Computational Methods

DFT Mechanistic Study

The gas-phase geometries of all structures, including transition states, were optimized on the full structures (without truncation) using density functional theory (DFT) with the M06-L⁷⁸ functional and def2-TZVP⁷⁹ (for N, P, Si, Cl and Co atoms) / def2-SVP (for C, H atoms) basis sets. (Note: The choice of the M06-L functional was based on a benchmark DFT study of [(N₂)Co₂L]⁻ comparing different functionals: PBE,¹⁰⁰ PBE-D3,¹⁰⁰⁻¹⁰¹ PBE0-D3,¹⁰¹⁻¹⁰² B3LYP-D3,^{101, 103} M06-L,⁷⁸ and N12.¹⁰⁴ (Table A3.5.1) The experimental crystal structures of **1** and **2** were used as initial geometries for their corresponding calculated structures. All optimized intermediate structures were found to have only real frequencies. All optimized transition states were found to have a single imaginary frequency along the reaction coordinate. Gibbs free energies (ΔG) at 298.15 K were computed by adding zero-point vibrational energies, and thermal vibrational-rotational entropy in the quasi-harmonic approximation calculated at the M06-L/def2-TZVP(for N, P, Si, Cl and Co)/def2-SVP(for C, H) level. Solvation effects were also considered by performing single-point calculations for all intermediates and transition states using the SMD solvation model¹⁰⁵ with the diffuse basis set, def2-TZVPD¹⁰⁶ (for N, P, Si, Cl and Co atoms)(def2-SVP for C and H) and THF as the solvent. In summary, the energies of all calculated structures were determined at the M06-L/def2-TZVP and M06-L/def2-TZVPD/SMD levels of theory, where the former is used for geometry optimizations, and the latter for single-point energy calculations. The *Gaussian09* suite of program¹⁰⁷ was used for all DFT calculations.

Chapter 4

**Synthesis and Characterization of Postulated Intermediates in
Dinitrogen Silylation**

4.1 Overview

The previous chapter introduced a dicobalt complex, LCo_2 , and its ability to catalyze the reductive silylation of dinitrogen. The catalysis is proposed to be facilitated by a bimetallic species, and the individual steps of the catalytic mechanism are not well understood. This chapter will provide insight into the catalytic steps by exploring the stoichiometric reactivity with relevant substrates starting with LCo_2 . As well, a dicobalt imido species will be presented as a model complex of a potential intermediate. As a stand-alone molecule, the dicobalt imido was tested for nitrene group transfer to phosphines, CO and olefins. The driving force of cobalt-cobalt bond formation is hypothesized to facilitate nitrene transfer. The characterization of a silylhydrazido and dicobalt imido will be discussed within.

4.2 Introduction

Dinitrogen metal complexes and their functionalized derivatives are important molecules for understanding the mechanism of dinitrogen reduction. For example, the mechanism in which nitrogenase reduces dinitrogen to ammonia while also generating an equivalent of hydrogen remains ambiguous.^{10, 108} While most now believe the nitrogenase operates through the FeMo-cofactor, only a few intermediates have been characterized *in situ* and some uncertainty resonates with the site of dinitrogen binding.

There are three potential pathways in which nitrogenase can operate (Figure 4.2.1). In the first proposed pathway to dinitrogen reduction, which was proposed by Chatt and later amended by Schrock, the dinitrogen unit is functionalized in the distal position three times, displacing an equivalent of ammonia and proceeding through a metal nitrido.^{21, 108a} The nitrido can further react with proton and electron equivalents to generate another equivalent of ammonia. This mechanism was based on the isolation of several intermediates with a molybdenum model system that reduces dinitrogen to ammonia.^{32b}

The second pathway is a theoretical mechanism proposed by Seedfeldt *et al.*¹² This mechanism was calculated to be an energetically favorable alternative for nitrogenase reduction of N₂, and recently experimental evidence suggests this mechanism to be highly plausible.¹⁰ The proposed mechanism involves attack by reagents at alternating distal and proximal positions.

The third pathway is a combination of these two mechanisms and was first examined by Hidaï.^{30a, f, 109} This mechanism is typically invoked for the catalytic reduction of dinitrogen through silylation using synthetic catalysts.^{22b, 41k, 90e, 110} In this mechanism, the dinitrogen unit is first functionalized in the distal position twice. The substrate then attacks

the proximal nitrogen and the complex can either dissociate $[\text{NR}_2]^{-22\text{b}}$ or $[\text{NRNR}_2]^{-41\text{k}, 90\text{e}}$,¹¹⁰ to give the resulting metal-imido or starting catalyst respectively. A similar mechanism has recently been observed by the Peters group in the examination of dinitrogen reduction to ammonia using a Fe-model system.²³

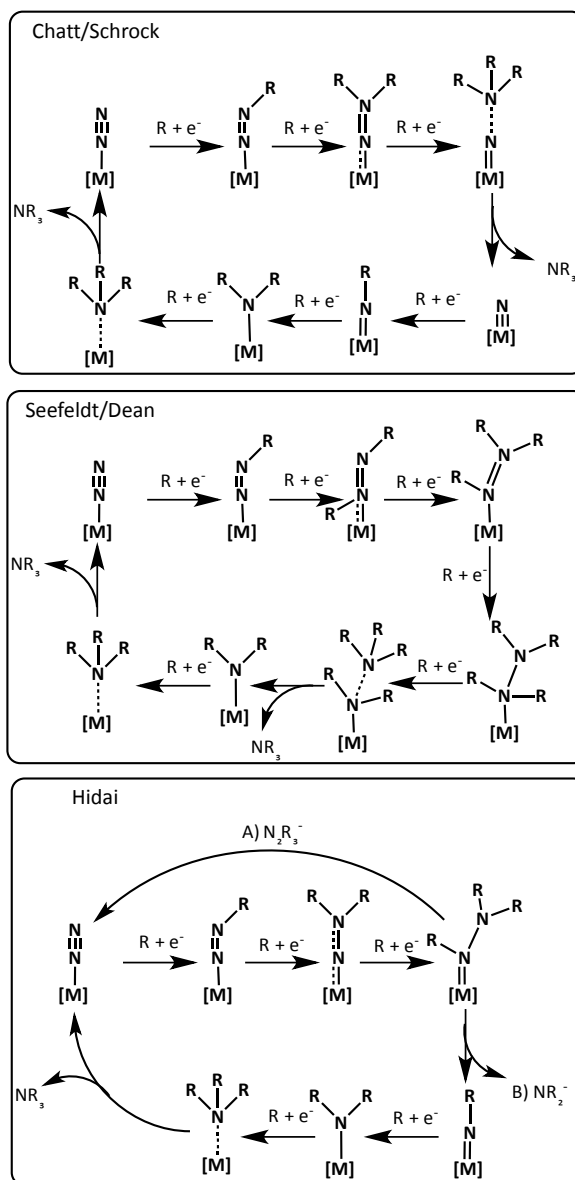
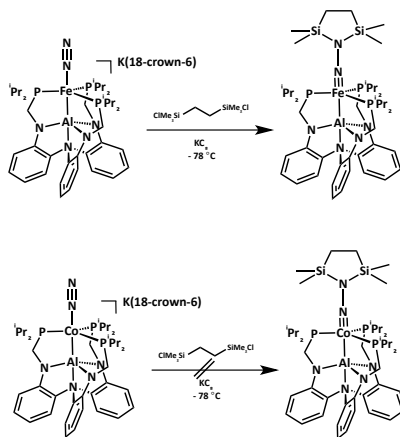


Figure 4.2.1 General schemes for catalytic dinitrogen functionalization
 Top: Chatt/Schrock Mechanism Middle: Alternating Mechanism Bottom: Silylation Mechanisms. $\text{R} = \text{H}^+$ or Me_3SiCl

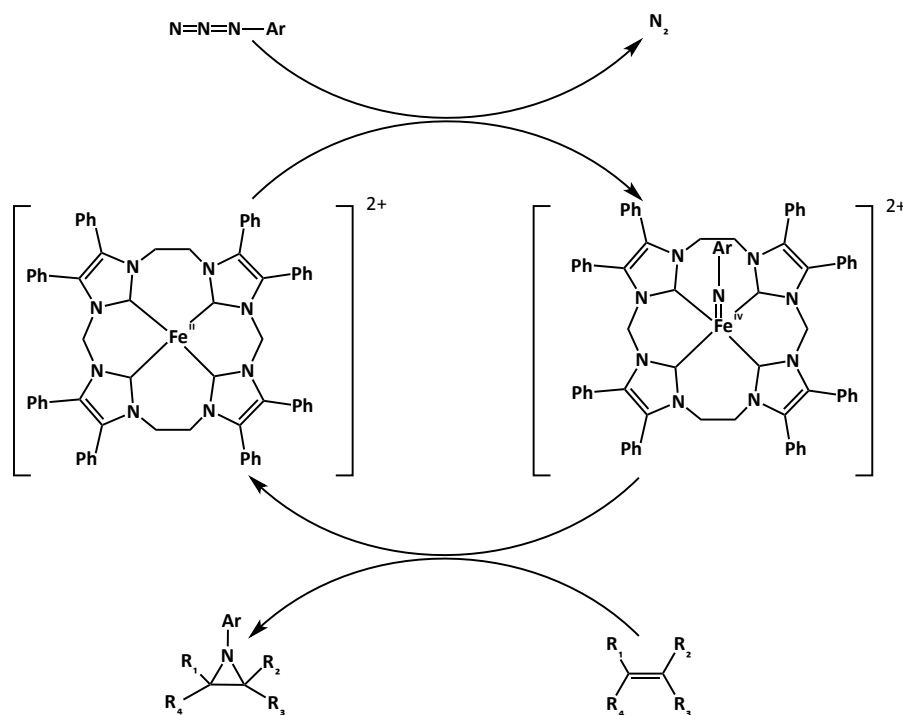
Isolation of any of these intermediates could prove beneficial in understanding the mechanism in which dinitrogen silylation occurs through LCo_2 . To that end, previous work in the Lu lab has found that a doubly silylated dinitrogen aluminium-iron product ($\text{LAIFe}[\text{N}_2(\text{SiMe}_2\text{CH}_2)_2]$) can be isolated from a reaction with the disilyl electrophile 1,2-bis(chlorodimethylsilyl)ethane and 2 equivalents of potassium graphite with the parent $\text{LAIFe}(\text{N}_2)$ complex (Scheme 4.2.1).^{41m} To date, an analogous $\text{LAICo}[\text{N}_2(\text{SiMe}_2\text{CH}_2)_2]$ product has not been isolated either structurally or spectroscopically. Interestingly, although a dihydrazido product could be generated from the parent $\text{LAIFe}(\text{N}_2)$ complex, the parent complex was found to be significantly less catalytically active for dinitrogen silylation than $\text{LAICo}(\text{N}_2)$.

Mono functionalized products, specifically silyldiazenido ($\text{M-N}=\text{NSiMe}_3$) compounds, have been observed for trigonal phosphine systems containing Fe and Co from the Peters lab.^{39d, 41e} To the best of my knowledge, a silyldiazenido product has not been isolated for either of the parent $\text{LAIFe}(\text{N}_2)$ or $\text{LAICo}(\text{N}_2)$ complexes, although attempts have been renewed in light of the catalytic activity of $\text{LAICo}(\text{N}_2)$ and LCo_2 toward dinitrogen silylation to tris(trimethylsilyl)amine.¹¹¹



Scheme 4.2.1 Scheme depicting the formation of a dihydrazido silyl complex isolated by Lu. Adapted from reference 41m.

In addition to elucidating the catalytic mechanism for dinitrogen functionalization, these potential intermediates can serve as useful molecules for other chemical transformations. For example, transition metal-imido species have the potential to insert into unsaturated C-C bonds. Jenkins *et al.* have developed iron and ruthenium catalysts that can perform aziridation reactions with alkenes and aryl azides (Scheme 4.2.2).¹¹² Typically, aziridation reactions involve the use of hypervalent iodine species to insert into the C-C bond.¹¹³ However, these reactions are non-catalytic and have poor functional group tolerance. Jenkins' catalysts were found to tolerate various aryl functional groups on the azide to generate the desired aziridation products. In the iron catalyst, the reaction is proposed to proceed through a Fe(IV) imido species. The catalyst was also found to be very robust since it could be recycled with only a marginal loss in activity.



Scheme 4.2.2 Scheme of catalytic aziridination of olefins with aryl-iron-imidos. Adapted from reference 112.

Transition metal imidos are also of interest due to their metal-ligand multiple bonds and understanding how the bonding can be tuned by the transition metal. Transition metal imidos have predominately been seen in early transition metals due to the low d-electron count and metal Lewis acidity that helps stabilize the basic NR fragment.¹¹⁴ Over the last 15 years, the synthesis and reactivity of late transition metal imidos (e.g. Co, Ni) have been explored.¹¹⁵ It was hypothesized that the high d-electron counts of the late transition metals would promote more facile nitrene transfer.¹¹⁴ However, the high electron counts also pose a problem in the synthesis of the metal-imidos. Unlike the early metal species, the later transition metals high electron counts can lead to having electrons in d-orbitals that are π^* anti-bonding with respect to the imido fragment. While this would promote reactivity, it also is a caveat in the formation and isolation of a transition metal imido altogether.

To address these issues, several factors must be considered to even conceive the formation of a late transition metal imido. One factor is the nature of the ligand donors. In order to stabilize the π^* symmetry orbitals, the use of strong field ligands are advantageous. These types of ligands allow for low spin singlet configurations promoting vacant π^* symmetry orbitals, thus stabilizing the metal-imido.¹¹⁴ A second factor is the coordination geometry about the metal. Hillhouse^{115b-e} and Holland¹¹⁶ and others have shown that using low coordinate precursors allows for facile formation of the desired transition metal-imido. These low coordination environments allow for different electronic structures that could tolerate higher d-electron counts. Several examples are shown in Figure 4.2.2.

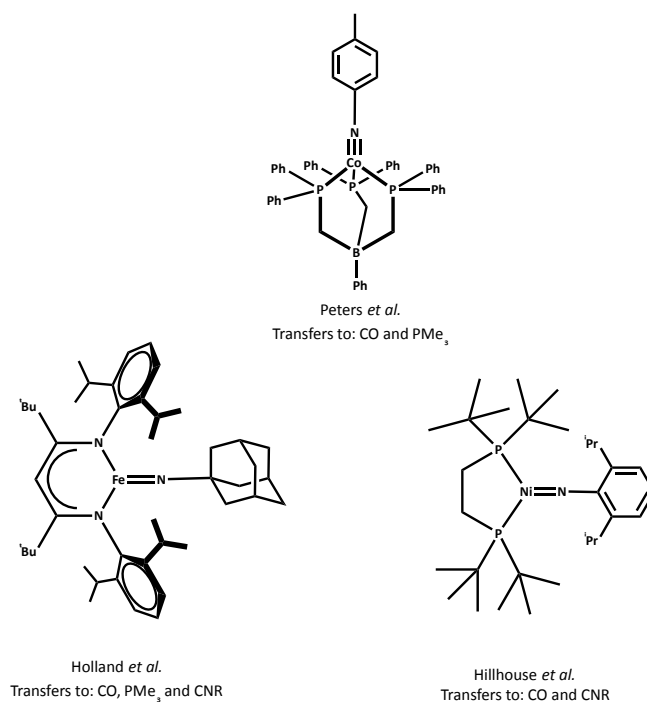
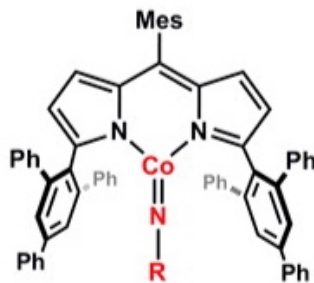


Figure 4.2.2 Select examples of low spin late transition metal-imido complexes.

However, there is one example from Betley *et al.* where a low coordinate cobalt imido was isolated using weak-field dipyrinato ligands (Figure 4.2.3).¹¹⁷ It was found that the weak-ligand field allowed for small population of the π^* orbitals of the imido fragment at room temperature. This allowed for a high-spin *tert*-butyl imido ($S = 2$) and an intermediate-spin mesityl imido ($S = 1$) to both be reactive at room temperature. In fact, the mesityl imido was able to perform facile intermolecular H-atom abstraction at room temperature while the *tert*-butyl imido could undergo facile transfer to phosphine. This result validates the hypothesis that late transition metal imidos can be highly reactive under the right ligand environments.



R = tBu or mesityl

Figure 4.2.3 Representation of Betley's Co(III) imidos that display open shell electron configurations. Taken from reference 117.

As mentioned prior, transition metal imidos have utility as nitrene transfer reagents to unsaturated C-C bonds. Transition metal imidos can also act as electrophiles and nucleophiles depending on electron density of the metal-imido. For example, it is well known that some transition metal imidos can do nitrene transfer to nucleophilic trialkyl or triaryphosphines to generate phosphinimines.¹¹⁸ Likewise, transition imidos have also been found to react with isocyanides and carbon monoxide to form carbodiimides and isocyanates respectively.¹¹⁴ Of note, the ability to modulate the R group on the imido fragment offers a unique synthetic strategy towards asymmetric carbodiimides, which serve as useful precursors for the generation of asymmetric amidinates.¹¹⁹ Likewise, isocyanates are precursors for the generation of urethane linkages.¹²⁰ By modulating the R group of the imido, various urethane linkages can now be attained.

The work described in this chapter is a continuation of our efforts to understand dinitrogen functionalization using a dicobalt catalyst, LCo_2 . The chapter will focus on the research into the synthesis, characterization, and reactivity studies of potential intermediates along the dinitrogen silylation mechanism. The intermediates here include silyldiazenido compounds (**1-SiPh₃**, **1-SiPh₂Me**, **1-SiPhMe₂**, and **1-SiMe₃**) as well as a dicobalt adamantylimido complex, **2** (Figure 4.2.4). Complex **1-SiPh₃** was also examined as a catalytically active species for the silylation of dinitrogen. Nitrene transfer chemistry was examined for complex **2** to see if the nature of the bimetallic unit could promote more facile reactivity versus monocobalt imidos.

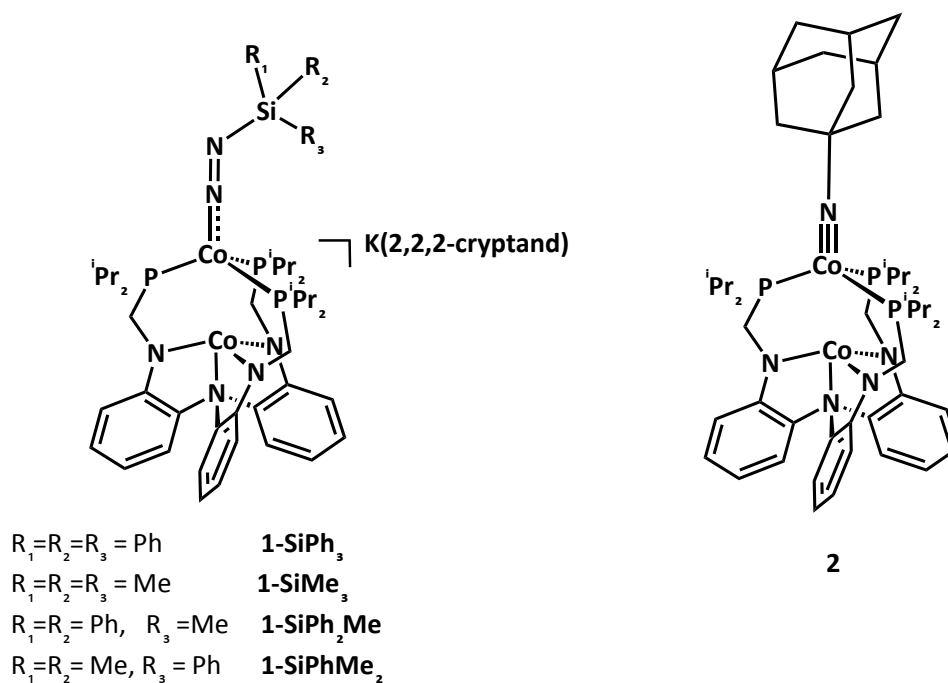


Figure 4.2.4 Representative structures of **1-SiPh₃**, **1-SiPh₂Me**, **1-SiPhMe₂**, **1-SiMe₃**, and **2**

4.3 Results and Discussion

4.3.1 Synthesis and ^1H NMR Spectroscopy

Mono-functionalized metal dinitrogen species have been well characterized as coordination compounds.^{22a, 39d, 41e} Two potential reaction pathways are possible for the addition of silyl groups to dinitrogen (Figure 4.3.1). One pathway is through nucleophilic attack of a bound dinitrogen unit via SiR_3X (R = alkyl or aryl, X = Cl or OTf) substrates.^{39d, 121} A second pathway is through the generation of silyl radicals which attack the dinitrogen unit.^{22a, 41k} These silyl radicals can be generated *in situ* through outer sphere electron transfer or through a silyl radical source (e.g. bis(trimethylsilyl mercury)). The actual reaction pathway for dinitrogen silylation remains unknown due to limited experimental evidence.^{22, 41k, 121}

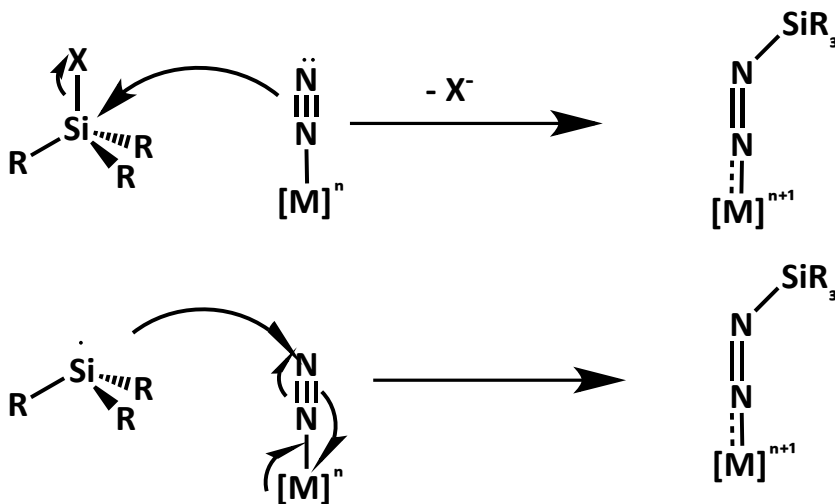
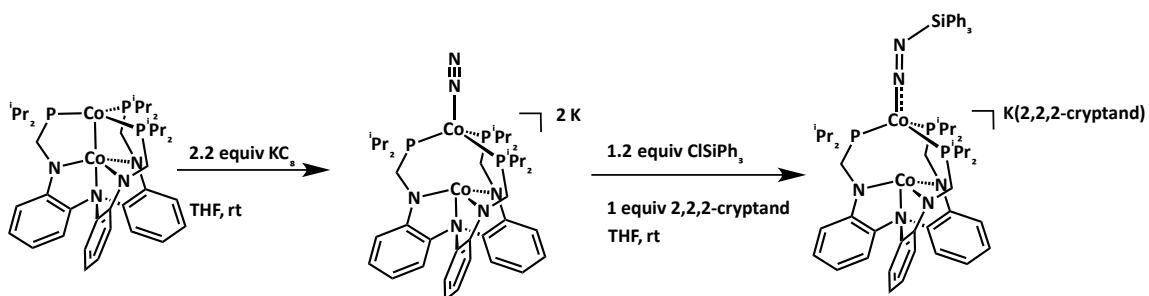


Figure 4.3.1 Potential pathways to functionalizing dinitrogen bound to a metal center

The synthesis of a silyldiazenido dinitrogen complex can be accomplished through reacting dicobalt dianion $[\text{LCO}_2(\text{N}_2)]^{2-}$ with 1 equivalent of SiPh_3Cl in THF at room temperature to generate a green solution of **1-SiPh₃** after 1 hour (Scheme 4.3.1). The ^1H NMR spectrum shows seven paramagnetically shifted resonances (Figure 4.3.2) that have

a similar pattern to that of $[\text{LCo}_2(\text{N}_2)]^-$. The desired product is believed to be a silyldiazenido product due to changes in the IR spectrum (*vide infra*). The reaction can also proceed with other silyl chloride reagents to generate yellow-green **1-SiPh₂Me**, **1-SiPhMe₂**, and **1-SiMe₃** after 1 hour. When the number of aryl groups are fewer, product stability is diminished due to the increased observation of $[\text{LCo}_2(\text{N}_2)]^-$ in the ^1H NMR spectrum. Alternatively, it is possible that a greater amount of outer sphere electron transfer to the ClSiR_3 substrate occurs leading to the increase in monoanion formed. Similar outer sphere electron transfer is observed when silylation reactions with heterobimetallic $\text{M-Co}(\text{N}_2)^-$ are attempted resulting in the formation of MCo neutral species.⁴⁴



Scheme 4.3.1 General reaction scheme for the generation of **1-SiPh₃**

A fluorine tagged silyl chloride, ClSiPh_2Ar ($\text{Ar} = 4\text{-CF}_3\text{C}_6\text{H}_4$) was synthesized to monitor the formation of the functionalized intermediate. The starting silane has a ^{19}F NMR chemical shift of -63.9 ppm. When ClSiPh_2Ar is reacted with $[\text{LCo}_2(\text{N}_2)]^{2-}$, a green product is observed with similar ^1H NMR chemical shifts (Figure 4.3.2). However, examination of the ^{19}F NMR shift shows little change compared to the starting material (^{19}F δ -64.6 ppm) (Figure A4.3.1). Due to the paramagnetic nature of the molecule and the change in electronic environment of the silicon, a shift in the ^{19}F NMR was expected.

One hypothesis for the lack of fluorine chemical shift arises from the similarity of a N_2^- vs Cl^- and the possibility that the paramagnetic center only affecting the relaxation time of the ^{19}F nucleus and not its chemical shift. Although a review of ^{19}F NMR in paramagnetic systems explains how the latter can be possible, t_1 measurements should be taken to confirm this hypothesis.¹²² Likewise, an EPR measurement of **1-SiPh₃** (*vide infra*) suggests a negatively charged N_2SiPh_3 fragment (overall complex is -1 with Co(II)Co(I) core), which further supports the hypothesis. It should be noted that when excess $ClSiPh_2Ar$ is used, two ^{19}F signals are present, separated by ~ 0.6 ppm (Figure A4.3.1).

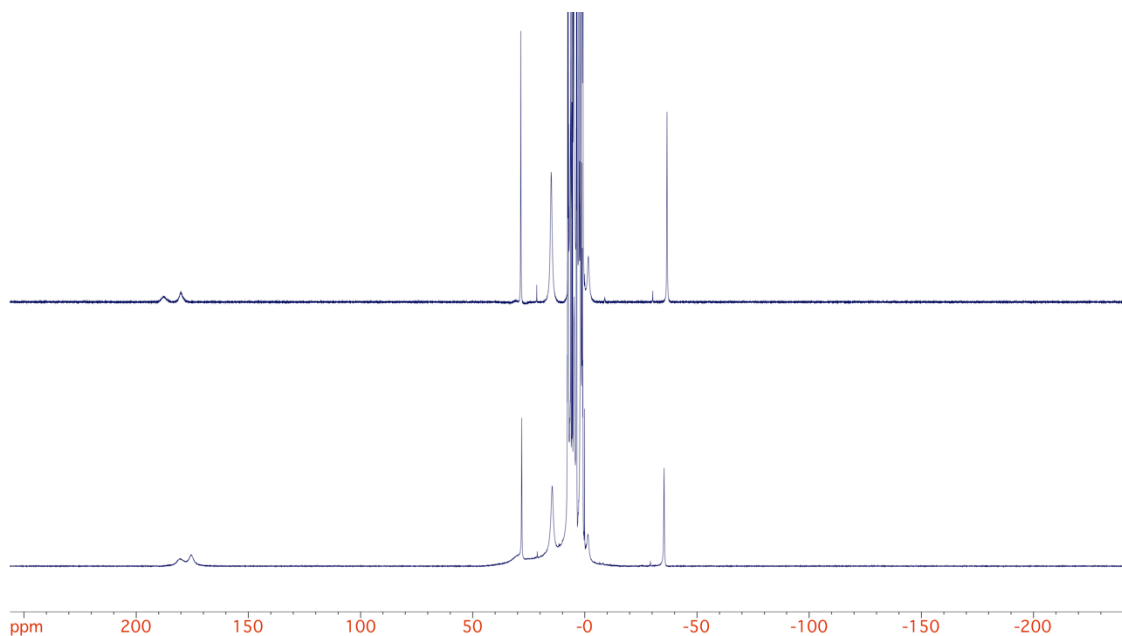


Figure 4.3.2 Top: 1H NMR Spectrum (d^8 -THF, 500 MHz) of **1-SiPh₃**
 Bottom: 1H NMR Spectrum (d^8 -THF, 500 MHz) of **1-SiPh₂Ar** (Ar = 4-CF₃C₆H₄)

Due to bleaching of the color of a sample of **1-SiPh₃** during Vis-NIR analysis (*vide infra*), **1-SiPh₃** and **1-SiPh₂Ar** was examined photochemically under both Ar and N_2 .

Exposure of **1-SiPh₃** to photolysis led to decomposition to the mono-anion, [LCO₂(N₂)]⁻, and a unidentified paramagnetic species after 4 hours (Appendix Figure 4.3.2) under Ar and N₂ atmospheres. Further photolysis leads to full formation of the unidentified paramagnetic species. The mono-anion, [LCO₂(N₂)]⁻, on its own is photochemically stable, so the most likely source of decomposition involves a silicon moiety, either from **1-SiPh₃** or residual ClSiPh₃. Tracking the photolysis of **1-SiPh₂Ar** yields a broad ¹⁹F resonance centered at -63 ppm (Figure A4.3.1 top). A control reaction with ClSiPh₂Ar and potassium graphite to generate the disilane (Ph₂ArSi-SiPh₂Ar), a potential outer sphere reduction product, shows no change from starting material by ¹⁹F NMR, suggesting either no reaction occurred or the disilane product has a coincident ¹⁹F NMR shift to that of the starting material.

Another potential intermediate in catalytic silylation mechanism is the formation of a metal-imido. The identification of a dicobalt imido intermediate *in operando* has not been experimentally accomplished. To that end, we set out to synthesize a dicobalt imido independently. Typically, metal-imido species can be formed through several synthetic routes (Figure 4.3.3). One route commonly found in the literature is reacting the metal complex with an organic azide (N₃R).^{41e, 114} This reaction proceeds through the two-electron NR group transfer to the transition metal center with concomitant formation of dinitrogen serving as the driving force for the reaction. A second route pioneered by Bergman¹²³ for Ir and later for Ni and Co by Hillhouse^{115b-e, 124} and others^{115a, 118} proceeds through metathesis of a metal-X (X = Cl or OTf) species with amide (NHR) precursors. The bound amide species can then be deprotonated or undergo H-atom abstraction to form the desired metal imido.

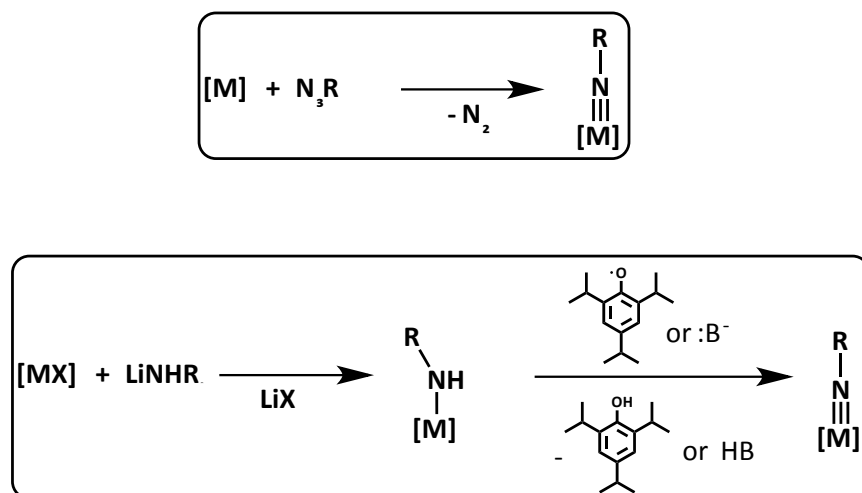


Figure 4.3.3 Synthetic routes for formation of transition metal imidos

When crystalline LCO_2 is subjected to adamantylazide, the solution changes color from brown to red. However, work-up of the solution yields a 1H NMR spectrum with multiple products. Serendipitously, it was found that generating LCO_2 *in situ* from LCO_2Cl and then adding adamantylazide produces a dicobalt imido, **2**, in 24-50% crude yields after a diethyl ether wash and reconstitution of the solid in benzene. These results suggest the role of Lewis acid salts for promoting N_2 loss and imido formation.

Analogously, Peters *et al.* can generate a cobalt imido in the $PhB(CH_2P^iPr_2)_3^-$ framework by *in situ* reduction of $PhB(CH_2P^iPr_2)_3CoI$ followed by an addition of tolyl azide.^{41e} The 1H NMR spectrum of **2** shows 15 signals from 272 to -39 ppm (Figure 4.3.4). The 15 proton signals are indicative of C_3 solution symmetry with 12 protons belonging to the ligand scaffold and 3 protons for the bound adamantyl group.

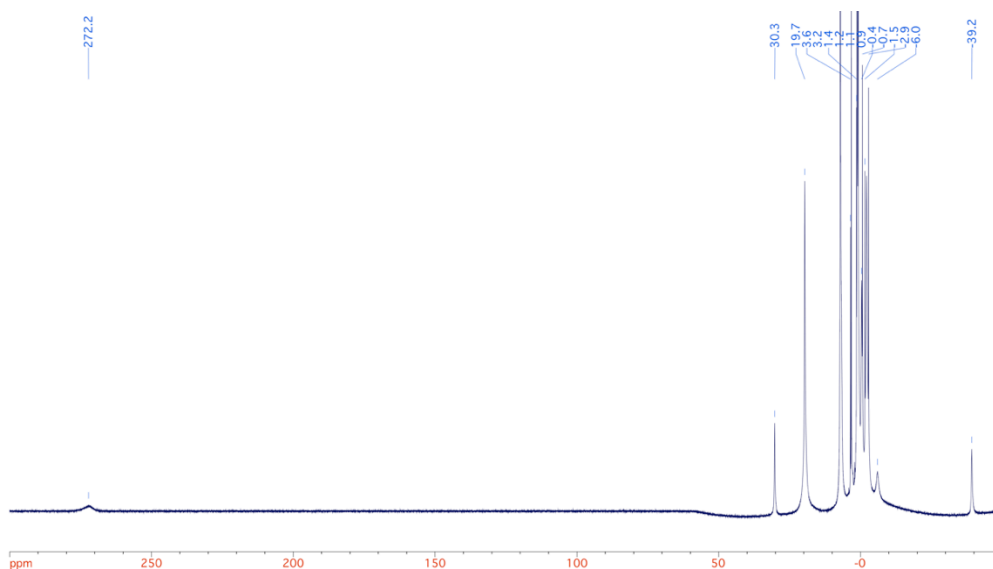


Figure 4.3.4 ^1H NMR Spectrum (C_6D_6 , 400 MHz) of **2**

4.3.2 Solid-state Structure of a Dicobalt Imido

The molecular structure of **2** has been characterized through single-crystal X-ray diffraction and is shown in Figure 4.3.5. Attempts to attain single crystals for **1-SiPh₃**, **1-SiPh₂Me**, **1-SiPhMe₂**, and **1-SiMe₃** have so far been thwarted due to the instability of the complexes in solution over days. Compound **2** crystallizes in the monoclinic space group $\text{P}2_{1/n}$ (Table 4.3.3) with two molecules of benzene in the unit cell. The important structural metrics can be found in Table 4.3.1 with comparisons to other dicobalt species.

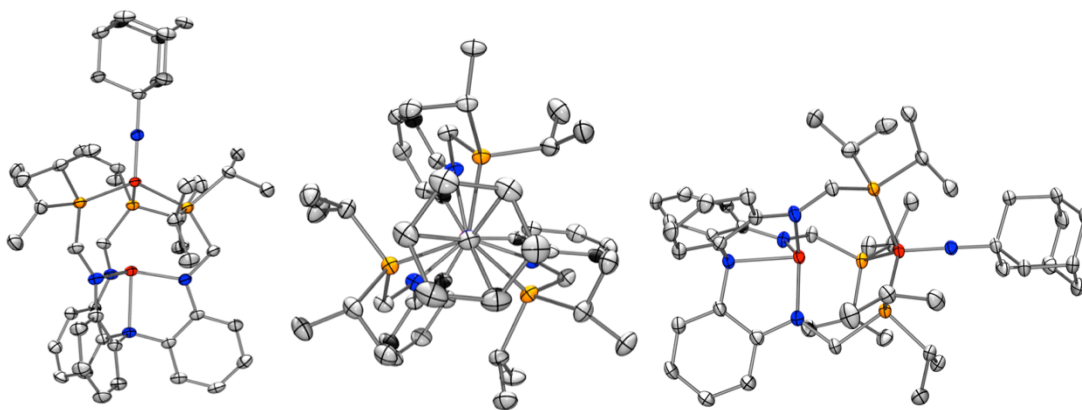


Figure 4.3.5 X-ray crystal structure of **2** at 50% probability. Hydrogen atoms were removed for clarity.

As shown in Table 4.3.1, the cobalt-cobalt distance is long at 3.124 Å. This distance is well out of the sum of the covalent radii (2.31 Å), suggesting the cobalt centers are non-interacting.⁷⁰⁻⁷¹ However, the inter atomic distance of the two cobalts are still within the sum of the van der Waals radii for two cobalt atoms (4.0 Å).¹²⁵ By comparing **2** to other dicobalt compounds in the L scaffold, the oxidation state of each metal can be qualitatively elucidated. When examining the average Co-N_{amide} distance (1.918 Å), a slight contraction is observed from that of the parent compound LCo(II)Co(I) (avg Co-N_{amide} 1.924 Å) as well as LCo(II)Co(II)Br (avg Co-N_{amide} 1.925 Å). While the Co-N_{amide} contraction might suggest a change in oxidation state from Co(II) to Co(III), the observed change is within e.s.d. of the distances, suggesting that likely no change in oxidation state has occurred. EPR evidence also suggests a Co(II) assignment for Co_N (*vide infra*).

Analogously, complex **2** has an average Co-P bond distance (2.300 Å) similar to that of LCo₂ (avg Co-P 2.296 Å) and ~ 0.1 Å shorter than LCo₂Br, suggesting a similar Co_P oxidation state between **2** and LCo₂. However, analysis of the P-Co-P angles shows a drastic geometry change from LCo₂ to **2** (Σ P-Co-P angles 358.64 and 324.39 respectively), which makes the oxidation state analysis ambiguous via comparison to LCo₂. Of greater note, literature precedent supports the assignment of a Co_P(III) assignment, making the overall dicobalt core Co(II)Co(III). Further evidence for the assignment of a Co₂⁵⁺ core is provided in Section 4.3.4.

Table 4.3.1 Comparison of structural metrics of **2** with LCo₂ and LCo₂Br

	2	LCo₂	LCo₂Br
Co-Co	3.124	2.3131(6)	2.7597(4)
Co _P -NAd or Br	1.645(2)	--	2.3588(4)
Co-N-C angle	178.9(2)	--	--
Co-P	2.2829(7), 2.2991(7), 2.3188(7)	2.288(1), 2.298(1), 2.303(1)	2.4067(6), 2.4128(6), 2.4231(6)
Σ P-Co-P angles	324.39	358.64	343.84
Co-N _{amide}	1.915(2), 1.919(2), 1.919(2)	1.922(3), 1.923(3), 1.926(3)	1.917(2), 1.921(2), 1.936(2)
Σ N-Co-N _{amide} angles	355.84	357.45	355.99
Co-N _{ap}	2.162(2)	2.167(2)	2.088(2)

Complex **2** has a short Co_P-N bond distance of 1.645(2) Å as well as the Co_P-N-C angle of 178.9(2)^o. These metrics suggest multiple bonding between the cobalt and imido fragment. The geometry about the cobalt center can be viewed as distorted tetrahedral with a τ_4 value¹²⁶ = 0.97 with 1 corresponding to tetrahedral and 0 corresponding to square planar. The cobalt is also displaced from the P₃ plane by nearly a full angstrom (0.816 Å) which again differs from the prior dicobalt compounds with axial bound ligands as discussed previously.

Table 4.3.2 Comparison of Co-NR compounds (R = alkyl)

Complex	Co-NR distance (Å)	Co-N-C angle	ref
2	1.645(2)	178.9(2)	<i>this work</i>
[PhB(CH ₂ P ^{Ph}) ₃]Co(N ^t Bu)	1.633(2)	176.7(1)	<i>121b</i>
(Tp ^{tBu,Me})Co(N ^t Bu)	1.660(3)	179.4(3)	<i>121a</i>
(Tp ^{tBu,Me})Co(NAd)	1.655(2)	178.3(2)	<i>121c</i>
[PhB(^t BuIm) ₃]Co(N ^t Bu)	1.659(3)	179.7(3)	<i>113a</i>

(Tp^{tBu,Me}) : tris(2-methyl, 4-*tert*butyl pyrazolyl)borate
 [PhB(^tBuIm)₃]: tris(1-*tert*butyl-2-ylidene)phenylborate

Table 4.3.3 Crystallographic details for **2**

	2
chemical formula	C ₅₈ H ₈₄ Co ₂ N ₅ P ₃
formula weight	1062.07
crystal system	monoclinic
space group	P2 ₁ /n
a (Å)	12.8703(3)
b (Å)	21.9784(5)
c (Å)	19.5698(4)
α (deg)	90
β (deg)	97.7620(13)
γ (deg)	90
V (Å ³)	5484.0(2)
Z	4
D _{calcd} (g cm ⁻³)	1.286
λ (Å), μ (mm ⁻¹)	1.54178, 5.876
T (K)	123(2)
θ range (deg)	3.88 to 74.674
reflns collected	11203
unique reflns	9176
data/restraints/ parameters	11203 / 0 / 635
R ₁ , wR ₂ (I > 2σ(I))	R ₁ = 0.0603, wR ₂ = 0.1232

There are several examples throughout the literature that cobalt-imidos possess a Co-N triple bond and the oxidation state of cobalt is trivalent.^{115a, 127} Comparison of **2** to other cobalt alkylimidos can be seen in Table 4.3.2. Compared to the literature examples, **2** has the second shortest Co-NR bond despite having electron rich phosphine ligands. This leads to increased electron density around the cobalt center, potentially making the imido more reactive. This hypothesis will be examined further in Section 4.3.8.

4.3.3 Vis-NIR Data

Due to their vibrant green color and to help elucidate their electronic structure, compounds **1-SiPh₃** and **2** was examined by visible-near-infrared electronic absorbance spectroscopy. The vis-NIR spectra for **1-SiPh₃** and **2** can be seen in Figure 4.3.6. Compound **2** has three absorbances of which include a shoulder at $\lambda_{\text{max}} = 450 \text{ nm}$ ($\epsilon = 1700 \text{ M}^{-1} \text{ cm}^{-1}$), a primary vis absorbance at $\lambda_{\text{max}} = 636 \text{ nm}$ ($\epsilon = 950 \text{ M}^{-1} \text{ cm}^{-1}$) and a prominent NIR feature at $\lambda_{\text{max}} = 903 \text{ nm}$ ($\epsilon = 650 \text{ M}^{-1} \text{ cm}^{-1}$). The low molar absorptivity of the features and the proposed electronic structure of **2** (*vide infra*) suggest the absorbances are d-d transitions, although weak MLCT or LMCT transitions should not be ruled out for the vis absorbances. Similar absorbances attributed to d-d transitions have been observed in other Co(III)-NR (R = tBu or tolyl) imidos, albeit blue-shifted from the prominently observed vis feature of **2**.¹²⁸ Due to the large interatomic distance of the cobalt centers (3.124 Å), IVCT transitions are also unlikely. The NIR transition is tentatively assigned as a spin- and dipole-allowed intra-metal d-d transition on Co_N, analogous to LCo₂Cl (Chapter 2). Further analysis provided from TD-DFT calculations would be valuable in understanding the observed transitions in **2**.

Compound **1-SiPh₃** has two absorbances with a primary vis absorbance at $\lambda_{\text{max}} = 590 \text{ nm}$ ($\epsilon = 1200 \text{ M}^{-1} \text{ cm}^{-1}$) and prominent NIR feature at $\lambda_{\text{max}} = 1340 \text{ nm}$ ($\epsilon = 250 \text{ M}^{-1} \text{ cm}^{-1}$). The vis transition is tentatively assigned as a metal-to-ligand charge transfer (MLCT) from Co_P to the π^* orbitals for the N₂SiPh₃ fragment. This assignment was corroborated through time-dependent density functional theory (TD-DFT) calculations, which suggest a similar transition. The NIR transition was assigned as a d-d transition. Due to the electronic structure of the **1-SiPh₃** (*vide infra*), the d-d transition is believed to an intra-

metal d-d transition on Co_N , similar to **2**. Color bleaching of the sample was observed after several scans of varying concentrations owing to the instability of **1-SiPh₃** to light (*vide supra*). The bleaching is believed to be light driven due to room temperature stability studies showing zero decomposition over several hours.

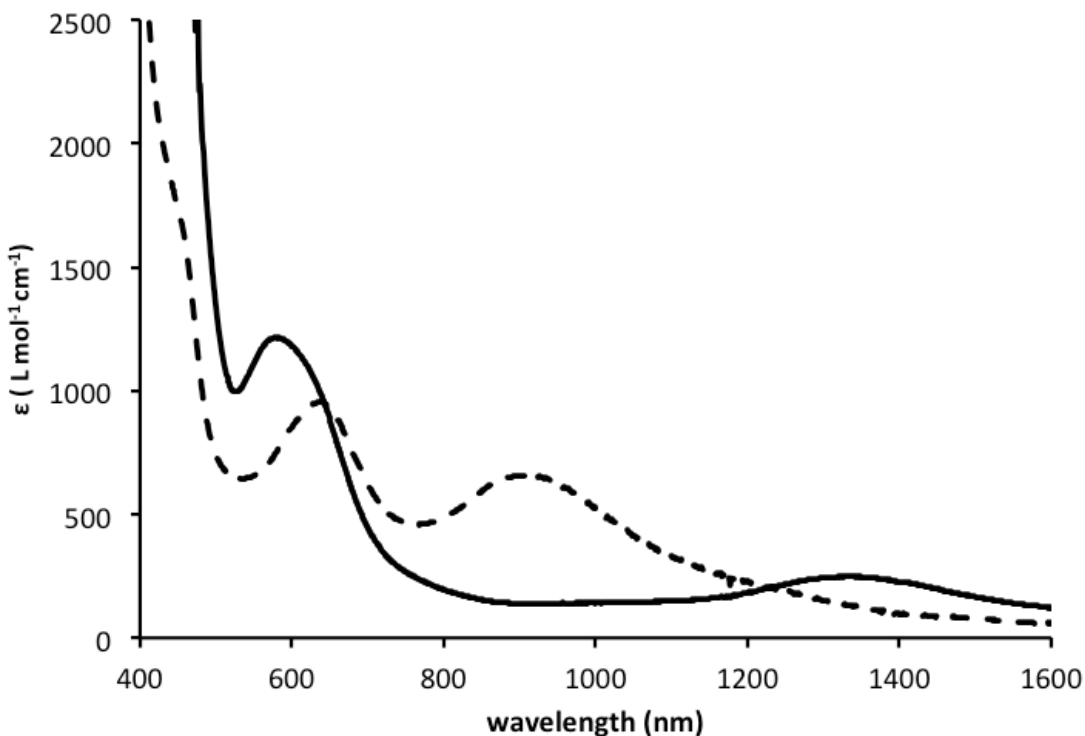


Figure 4.3.6 Vis-NIR spectrum of **1-SiPh₃** (solid line) and **2** (dashed line) recorded in THF at 293 K

Owing to the different R groups of the silyldiazenido products, **1-SiPh₃**, **1-SiPh₂Me**, **1-SiPhMe₂**, and **1-SiMe₃** were *in situ* generated and examined in the vis region (Figure 4.3.7) to see if there is an effect on the R substituent of the silyl group. All of the compounds have a similar absorbance with similar molar extinction coefficients (1000 – 1200 L mol⁻¹ cm⁻¹ assuming 100% conversion, Table 4.3.4). Interestingly, as phenyl

groups are removed from the silyl substrate, the electronic absorbance blue shifts (590 nm for **1-SiPh₃** to 570 nm for **1-SiMe₃**). To try and rationalize the observed blue shift, TD-DFT calculations of the varying R groups on the silyl moiety were performed (Table 4.3.5). It should be noted that some of the excited energies correspond to a single transition. Many of the excited energies correspond to multiple transitions, and the major contributing transitions are shown with their percent contributions and most atomic orbital contributions (up to 5%) to the complexes are included. TD-DFT predicted that the observed transition corresponds to a Co_p to N₂SiR₃ MLCT. The excitation energy for this group of dicobalt complexes decreases from 1.97 eV (630 nm) for **1-SiMe₂Ph** to 1.79 eV (692 nm) **1-SiPh₃**, consistent with monotonic substitution of the methyl groups (from 0 - 2) with phenyl groups.

Table 4.3.4 Vis transition seen in compounds **1-SiPh₃**, **1-SiPh₂Me**, **1-SiPhMe₂**, and **1-SiMe₃**

Complex	λ_{max} (nm)	molar absorptivity ($\text{M}^{-1} \text{cm}^{-1}$)
1-SiPh₃	590	1200
1-SiPh₂Me	583	1130
1-SiPhMe₂	571	1060
1-SiMe₃	550	970

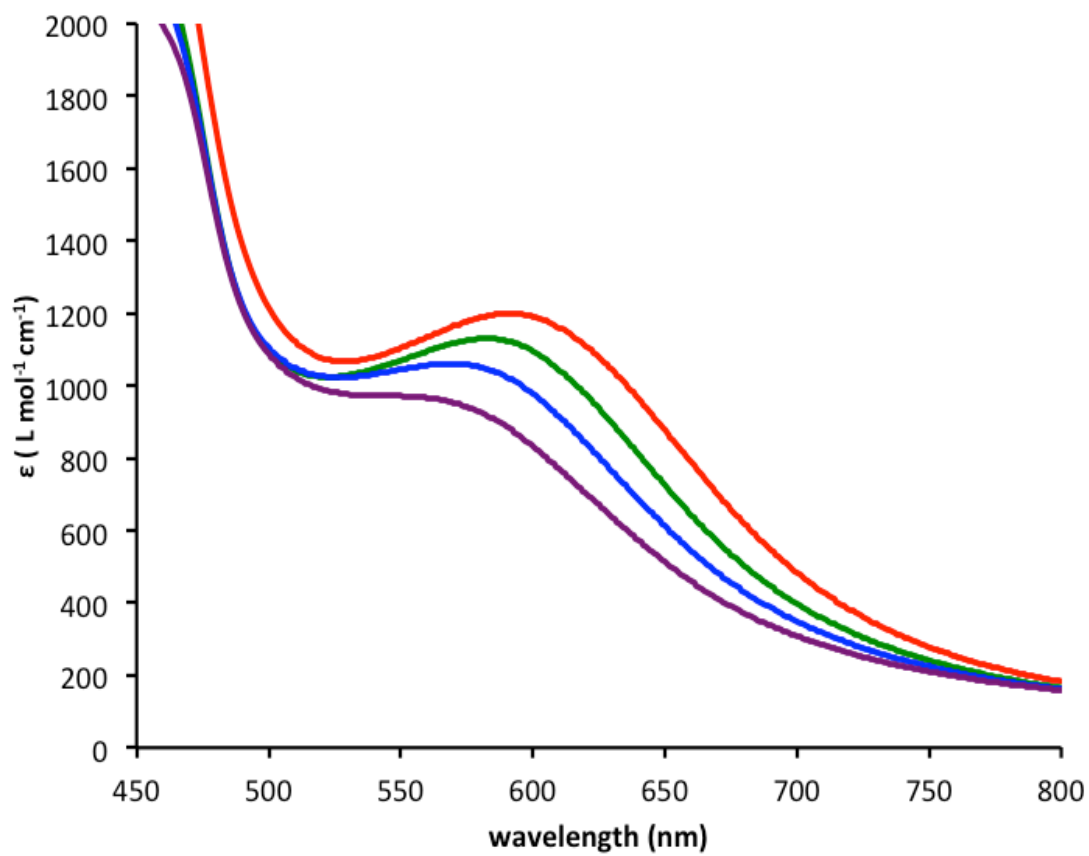
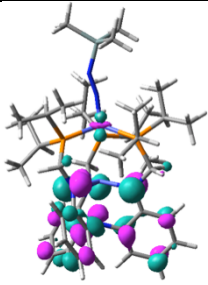
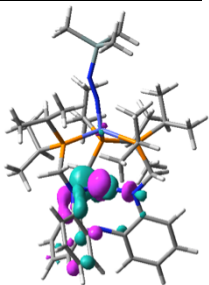
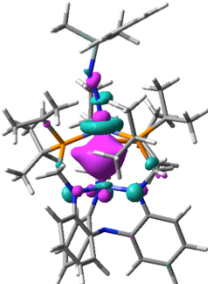
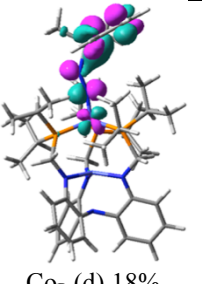
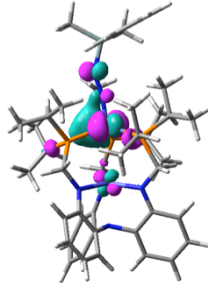
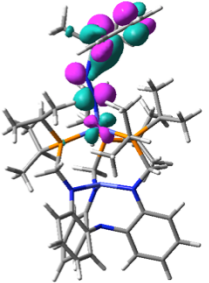
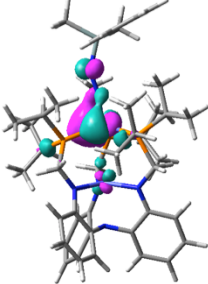
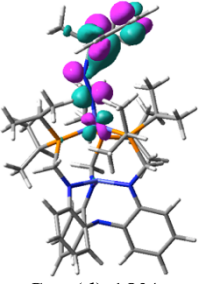


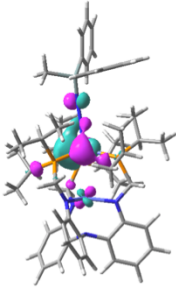
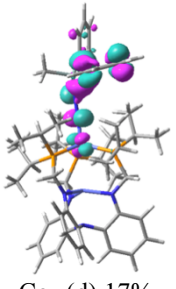
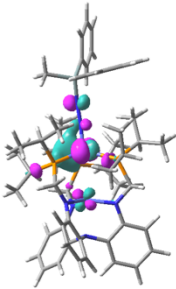
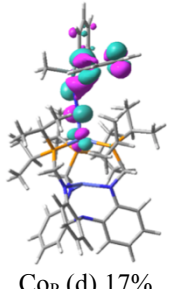
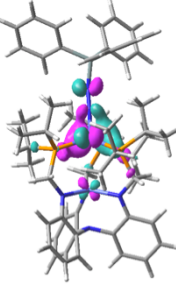
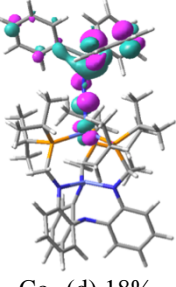
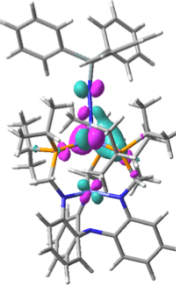
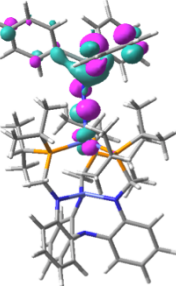
Figure 4.3.7 Vis spectrum of **1-SiPh₃** (red), **1-SiPh₂Me** (green), **1-SiPhMe₂** (blue), and **1-SiMe₃** (purple).

The predicted blue shift is hypothesized to be attributed to the destabilization of the $N_2 \pi^*$ orbitals as more electron rich groups are present. This can be seen in the predicted MLCT transitions, which show initial contributions from Co_P (~60%) to the whole N_2SiR_3 fragment (~65%) for **1-SiPh₃**, **1-SiPh₂Me**, and **1-SiPhMe₂**. As the number of phenyl groups are increased, the percentage of the transition to the N_2SiR_3 fragment localized on the N_2 portion decreases (27 % for **1-SiPhMe₂** and 12 % for **1-SiPh₃**) indicative of the delocalization through the phenyl rings.

However, the major transition seen for **1-SiMe₃** was predicted to be a LMCT band from the phenyl amine backbone to Co_N . Analogous to the phenyl silyl moieties, a MLCT from Co_P to N_2SiR_3 transition was also predicted but has much lower intensity compared to the LMCT transition. Akin to the understanding gained from the phenyl systems, the $N_2 \pi^*$ orbitals become higher energetically as the silyl becomes more electron donating. In the case of **1-SiMe₃**, this energy difference causes the primary transition observed in TD-DFT calculations to be LMCT at Co_N rather than MLCT at Co_P .

Table 4.3.5 TD-DFT Excitation Energies and their MO Interpretations for **1-SiPh₃**, **1-SiPh₂Me**, **1-SiPhMe₂**, and **1-SiMe₃** anionic compounds (d¹⁶) at the PBE level of theory.

λ_{max} (nm) (Energy in eV)	Oscillator strength	Orb. Transition (Percent)	Transition	
			From:	To:
1-SiMe₃ 625.35 (1.98)	0.0085	235B -> 240B (98%)	 Co _P (d) 13% N (p) 30%	 Co _N (d) 56%
			 Co _P (d) 43% Co _N (d) 5%	 Co _P (d) 18% N ₂ (p) 21% C ^{Phenyl} (p) 30% Si (p) 5%
1-SiPhMe₂ 629.88 (1.97)	0.0144	251A -> 257A (24%)	 Co _P (d) 57% Co _N (d) 6% P (p) 5%	 Co _P (d) 18% N ₂ (p) 27% C ^{Phenyl} (p) 30% Si (p) 5%
			 Co _P (d) 59%	 Co _P (d) 18% N ₂ (p) 21% C ^{Phenyl} (p) 30% Si (p) 5%

λ_{max} (nm) (Energy in eV)	Oscillator strength	Orb. Transition (Percent)	Transition	
			From:	To:
1-SiPh₂Me 651.17 (1.90)	0.0267	265B -> 270B (44%)		
			Co _P (d) 60%	Co _P (d) 17% N ₂ (p) 13% C ^{Phenyl} (p) 30% Si (p) 6%
		267A -> 273A (41%)		
			Co _P (d) 58% Co _N (d) 7% P (p) 5%	Co _P (d) 17% N ₂ (p) 13% C ^{Phenyl} (p) 30% Si (p) 6%
1-SiPh₃ 692.04 (1.79)	0.0154	281B -> 286B (34%)		
			Co _P (d) 59%	Co _P (d) 18% N ₂ (p) 12% C ^{Phenyl} (p) 26% Si (p) 7%
		283A -> 289A (23%)		
			Co _P (d) 57% Co _N (d) 7%	Co _P (d) 17% N ₂ (p) 13% C ^{Phenyl} (p) 24% Si (p) 7%

4.3.4 EPR Data and Electronic Structure

Due to the inability to structurally characterize a silyldiazenido intermediate, EPR spectroscopy was useful in providing evidence for the formation of **1-SiPh₃** and understanding the electronic structure of **1-SiPh₃**. Theoretical calculations laid out in Chapter 3 predict that the anionic silyldiazenido species should have a non-integer $S = 3/2$ spin state which would be observable via EPR. In fact, the EPR spectrum of **1-SiPh₃** shows an axial signal with the expected $g_{\text{eff}} = 4, 4, 2$ pattern indicative of a $S = 3/2$ system (Figure 4.3.8). The spectrum can be modeled as an $S = 3/2$ system with anisotropic g -values of $g = 2.200, 2.200, \text{ and } 2.02$. An 8-line hyperfine splitting is observed at $g_{\text{eff}} = 2$. This coupling can be modeled as one cobalt nucleus ($I = 7/2$) with a A_{zz} hyperfine of $85 \times 10^{-4} \text{ cm}^{-1}$. The origin of the unpaired spin comes from a cobalt(II) center with three unpaired electrons.

A possible electronic configuration for this model intermediate, $[\text{LCo}_2\text{N}_2\text{SiPh}_3]^-$, is a $\text{Co}_\text{N}(\text{II})\text{Co}_\text{P}(\text{I})$ species with non-interacting metals. The $\text{Co}_\text{N}(\text{II})$ center, would be a high-spin d^7 cobalt with $S = 3/2$. The $\text{Co}(\text{I})$ center would be a low-spin d^8 cobalt and diamagnetic. This assignment is further corroborated by theoretical calculations that predict a mixed-valent $\text{Co}(\text{II})\text{Co}(\text{I})$ system that is $S = 3/2$. Energies of **1-SiPh₃**, **1-SiPh₂Me**, **1-SiPhMe₂**, and **1-SiMe₃** in various spin states are reported in Table 4.3.6. A quartet ground spin state was found to be the ground spin-state for all systems at the PBE and M06-L level of theory.

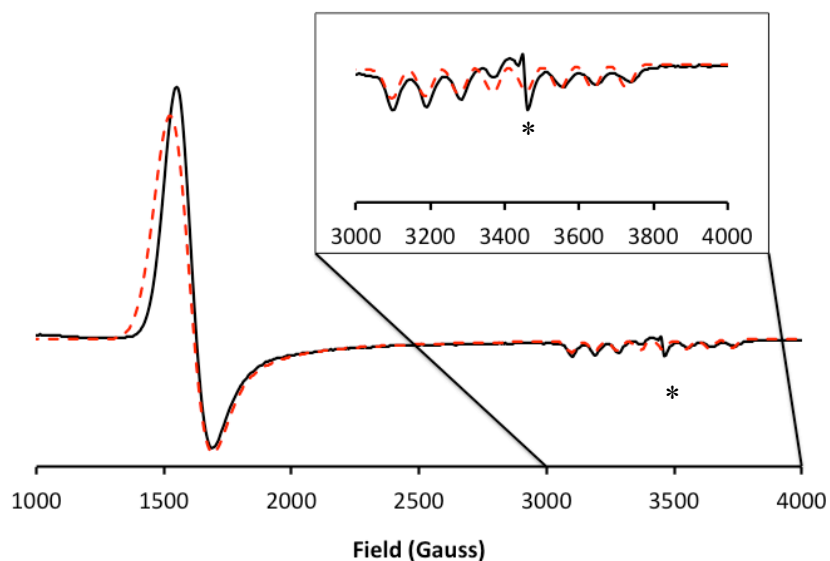


Figure 4.3.8 X-Band EPR spectrum (dX''/dB) of **1-SiPh₃** in THF glass (21K) shown as solid black line. The dashed red line is the simulated $S = 3/2$ spectrum with anisotropic g values $g = 2.20, 2.20,$ and 2.02 and line widths of $W_x = 200 = W_y = 50, W_z = 50$ G and z -hyperfine tensor for Co ($I = 7/2$) of $A_{zz} = 85 \times 10^{-4} \text{ cm}^{-1}$. * baseline impurity in cavity.

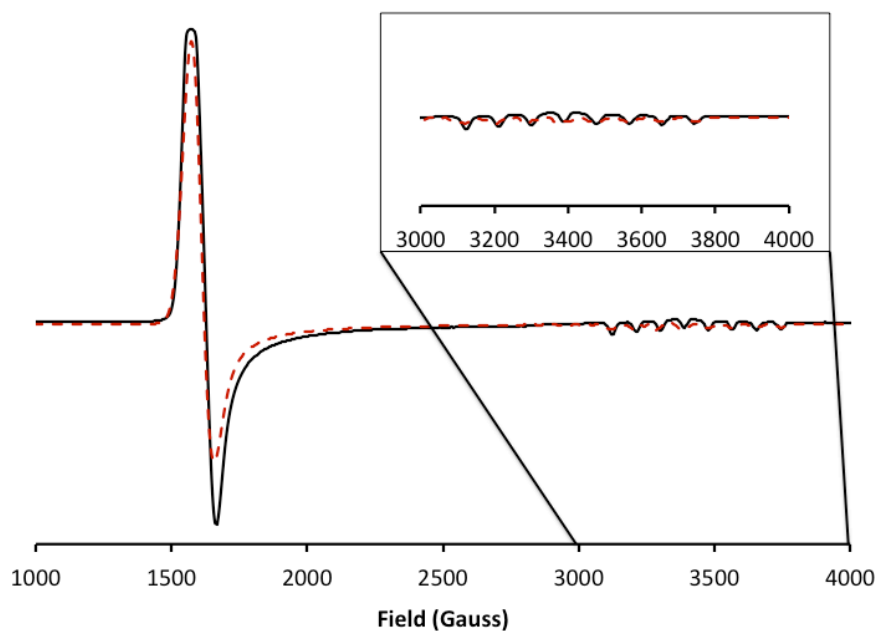


Figure 4.3.9 X-Band EPR spectrum (dX''/dB) of **2** in toluene glass (7 K) shown as solid black line. The dashed red line is the simulated $S = 3/2$ spectrum with anisotropic g values $g = 2.16, 2.16,$ and 2.01 and line widths of $W_x = 100 = W_y = 100, W_z = 50$ G and z -hyperfine tensor for Co ($I = 7/2$) of $A_{zz} = 85 \times 10^{-4} \text{ cm}^{-1}$.

Table 4.3.6 Calculated relative free energies of various possible spin states at the PBE and M06-L levels of theory. Bolded values are the lowest energy spin states.

PBE/Def2-TZVP(Def2-SVP for C and H) at 298.15 K (gas phase)

Compound	<i>S</i>	$\langle S^2 \rangle$	ΔG_{SPIN} [kcal/mol]
1-SiPh₃	1/2	0.77	14.7
	3/2	3.75	0.0
	5/2	8.75	14.4
1-SiPh₂Me	1/2	0.77	15.2
	3/2	3.75	0.0
	5/2	8.75	16
1-SiPhMe₂	1/2	0.77	14.9
	3/2	3.75	0.0
	5/2	8.75	16.8
1-SiMe₃	1/2	0.77	15.1
	3/2	3.75	0.0
	5/2	8.75	20.2

M06-L/Def2-TZVP(Def2-SVP for C and H) at 298.15 K (gas phase)

Compound	<i>S</i>	$\langle S^2 \rangle$	ΔG_{SPIN} [kcal/mol]
1-SiPh₃	1/2	5.04	10.7
	3/2	3.75	0.0
	5/2	8.76	9.7
1-SiPh₂Me	1/2	4.46	12.8
	3/2	3.75	0.0
	5/2	8.76	12.0
1-SiPhMe₂	1/2	4.97	13.6
	3/2	3.79	0.0
	5/2	8.76	12.1
1-SiMe₃	1/2	4.92	16.3
	3/2	3.75	0.0
	5/2	8.76	14.6

Similarly, complex **2** was examined by EPR spectroscopy. The resulting spectrum (Figure 4.3.9) shows a classic axial $S = 3/2$ EPR signal with effective g -values of $g_{\text{eff}} = 4$, 4, and 2. This spectrum can be modeled with anisotropic g -values of $g = 2.16$, 2.16, and 2.01. An 8-line hyperfine splitting is also observed at $g_{\text{eff}} = 2$. This coupling can be modeled as one cobalt nucleus ($I = 7/2$) with a $A_{zz} = 85 \times 10^{-4} \text{ cm}^{-1}$. The similar hyperfine values of **2** compared to **1-SiPh₃** suggest a similar nuclear environment containing the unpaired electrons. Through examination of the structural metrics (*vide supra*) and the observed EPR data, complex **2** is believed to be a Co(II)Co(III) species with non-interacting cobalts. This is further corroborated through DFT calculations (PBE) where the spin density of **2** was found to be isolated on Co_N (Figure 4.3.10) with a spin density of 2.46 electrons, which within DFT error suggests 3 unpaired electrons and essentially no spin density of the low-spin Co(III)_P center.

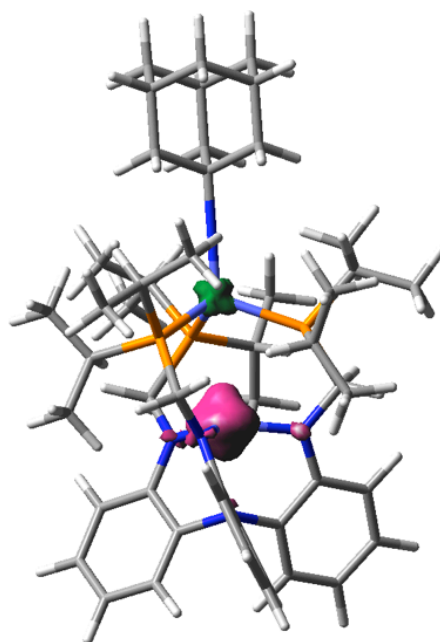


Figure 4.3.10 Spin density isosurface (0.02 a.u.) of **2**, neutral quartet. Fuscian and green density correspond to alpha and beta spin, respectively.

Co_P spin density = -0.238769; Co_N spin density = 2.462085

Complexes **1-SiPh₃**, **2**, and $[\text{LCo}_2(\text{N}_2)]^{2-}$ as well as an independently prepared $[\text{LCo}]^{\cdot-}$ compound present a unique series of $S = 3/2$ bimetallic species (Figure 4.3.11). While all three have a common high-spin Co(II), each has a varying oxidation state of the phosphorous ligated cobalt. The cobalts also act as two independent metals within the ligand scaffold in the bimetallic species (Figure 4.3.12). This flexibility allows for coupling and uncoupling of each metal that coincidentally allows for the stabilization of reactive species. The weaker interactions between the two cobalts can be a potential reason that LCo_2 has high catalytic activity toward dinitrogen silylation relative to the Co heterobimetallic species containing metal-metal multiple bonds.⁴⁴

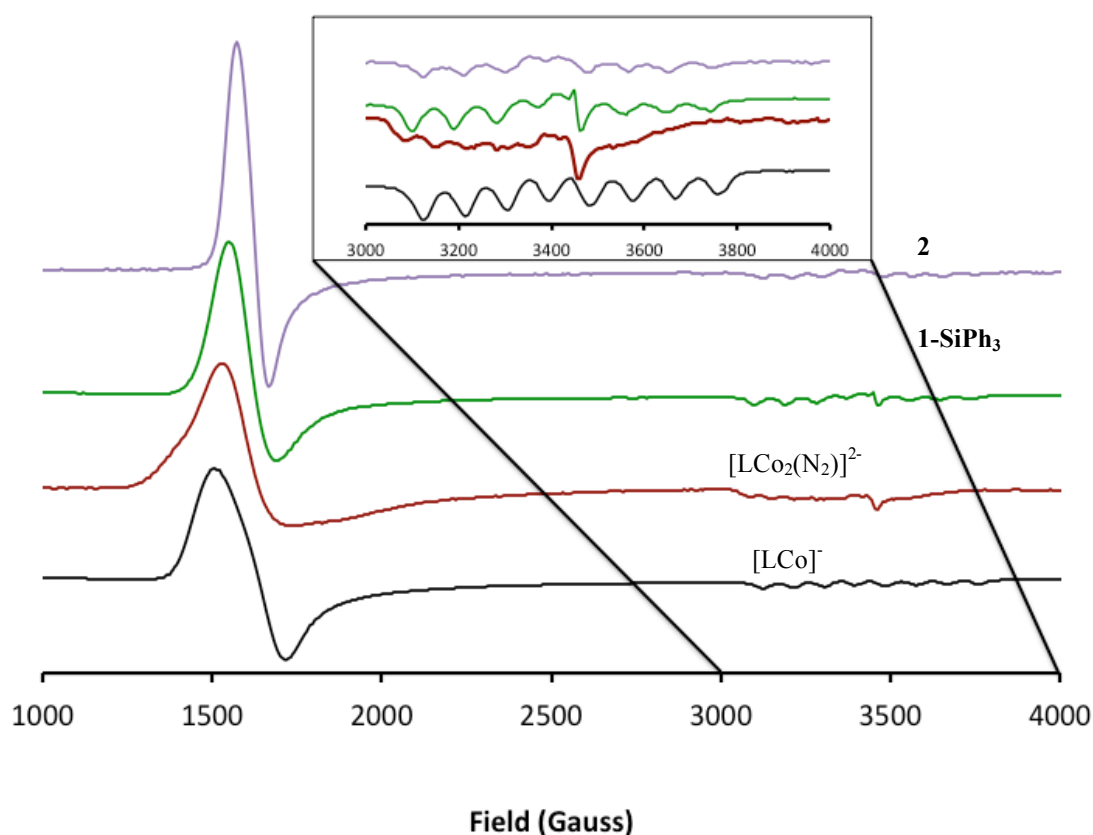


Figure 4.3.11 Overlay of X-Band EPR spectrums (dX''/dB) in THF glass for $[\text{LCo}]^{\cdot-}$ (Black, bottom), $[\text{LCo}_2(\text{N}_2)]^{2-}$ (Red, 2nd from bottom), **1-SiPh₃** (Green, 2nd from top), and **2** (Purple, top). Insert: Zoom of 3000 to 400 Gauss region highlighting Co ($I = 7/2$) hyperfine.

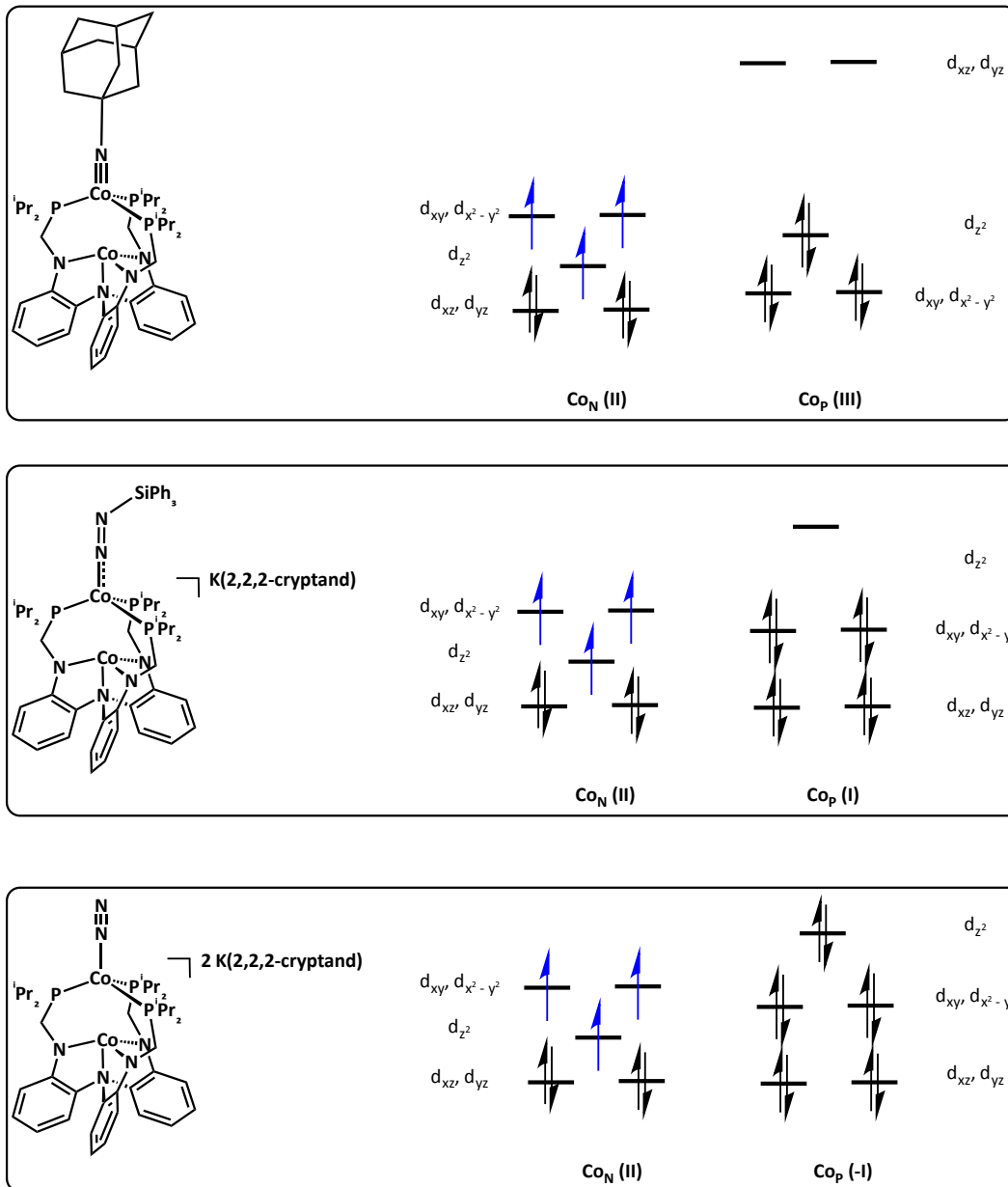


Figure 4.3.12 Qualitative orbital diagrams highlighting the differences in **1-SiPh₃** (top), **2** (middle) and $[\text{LCo}_2(\text{N}_2)]^{2-}$ (bottom).

4.3.5 Infrared Data

As seen in Chapter 2, IR spectroscopy is a great probe for understanding the activation of dinitrogen. The same holds true for examining functionalized dinitrogen species. The solution IR spectrum of complex **1-SiPh₃** shows a band at 1690 cm⁻¹ (1685 KBr) (Figure 4.3.13). This is shifted from the dinitrogen stretching frequencies seen in [LCo₂(N₂)]⁻ and [LCo₂(N₂)]²⁻ at 1994 and 1925 cm⁻¹ respectively. It is hypothesized that the signal corresponds to a silyldiazenido intermediate; and, based on a correlation of N-N stretching frequencies with N-N distances, the interpretation suggests a N-N double bond.⁴ To provide further evidence for the functionalization of N₂, **1-¹⁵N₂SiPh₃** was synthesized and gave a IR stretch of $\nu(^{15}\text{N}_2\text{SiPh}_3) = 1634 \text{ cm}^{-1}$ (Appendix Figure A4.3.3) which gives a shift, $\Delta\nu = 56 \text{ cm}^{-1}$, that is close to the expected shift of $\Delta\nu = 58 \text{ cm}^{-1}$ based on a simple Hooke's law calculation of N-NSiPh₃ versus ¹⁵N-¹⁵NSiPh₃. As well, the stretching frequency is within the range of other silyldiazenido species as summarized in Table 4.3.7.

The IR spectrum of **2** was also examined. Typically, metal-imido stretches for alkyl-imidos give stretches around ~1100 cm⁻¹.¹¹⁴ When examining complex **2**, no stretches were observed in the range of 1200 to 1000 cm⁻¹ that did not correspond to stretches of the ligand backbone. However, a weak band at 1256 cm⁻¹ can be seen. The red shift of the IR stretch could be attributed to increased electron density around the cobalt center due to the electron rich phosphine donors, thus contributing to a weakening of the Co-N bond. Labeling experiments would be essential in order to confirm the assignment of a Co-NR stretch due to the litany of stretches observed in the 1200 to 1000 cm⁻¹ for the ligand itself.

Table 4.3.7 Comparisons of silyldiazenido stretching frequencies

Complex	$\nu(\text{N}=\text{NR}) \text{ cm}^{-1}$	ref
1-SiPh₃	1690	<i>this work</i>
Co[PhB(CH ₂ ⁱ Pr ₂ P) ₃](N ₂ TMS)	1654	<i>40e</i>
Fe[<i>o</i> -(ⁱ Pr ₂ P)C ₆ H ₄] ₃ B](N ₂ TMS)	1741	<i>38d</i>
Mo(1,1'-bis(diethylphosphino)ferrocene) ₂ (N ₂ TMS)OTf	1629	<i>108</i>

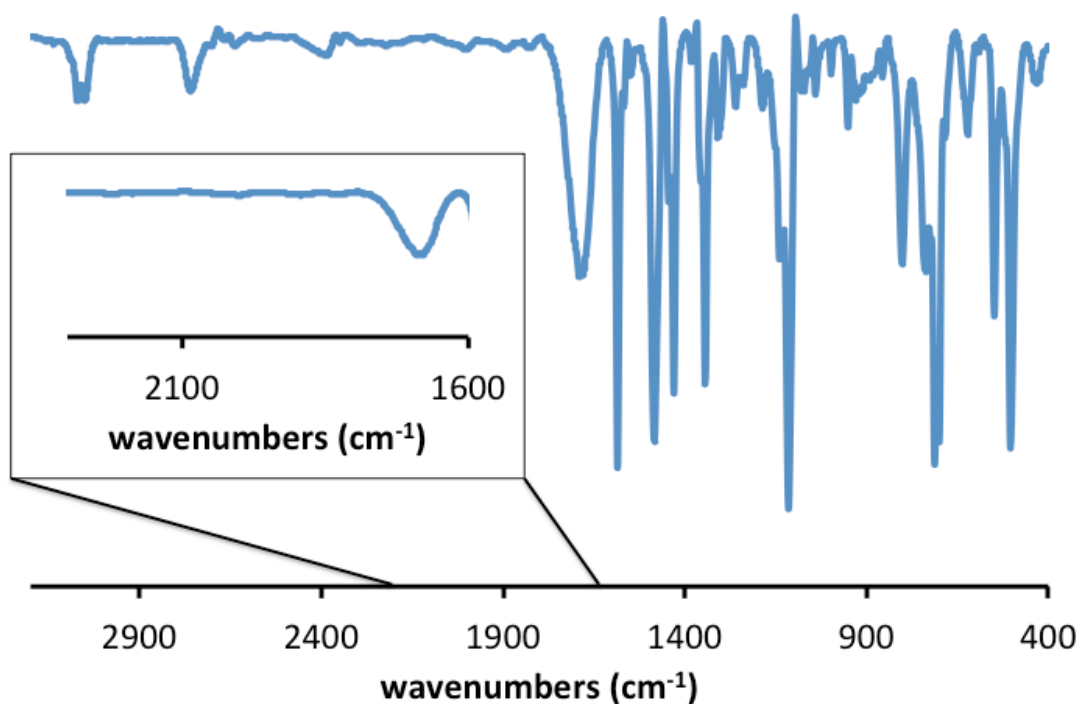


Figure 4.3.13 Solution IR spectrum (THF, 293 K) of **1-SiPh₃**. $\nu(\text{N}=\text{NR})$: 1690 cm^{-1}
Insert: Zoom of region from 1600 to 2300 cm^{-1} .

4.3.6 Cyclic Voltammetry

The electrochemical properties for complex **2** were examined. It was found to have a reversible reductive event and quasi-reversible oxidative event (Figure 4.3.14). The reversibility of the reduction is scan speed dependent (Figure 4.3.15), and has a potential of $E_{1/2} = -1.64$ V versus ferrocene with a peak-to-peak separation of $\Delta E = 95$ mV and current ratio of $i_{pa}/i_{pc} = 0.82$, indicative of a reversible electrochemical event. Preliminary attempts to isolate a chemically reduced **2** by one electron have been unsuccessful. It is hypothesized that a reduced species cannot be isolated because the reduction is based on Co_p . A reduction of the imido bound cobalt center would populate a d-orbital of π^* Co-NR character, thus destabilizing the imido fragment. However, such a redox event is rarely seen among Co(III) imidos.¹¹⁴

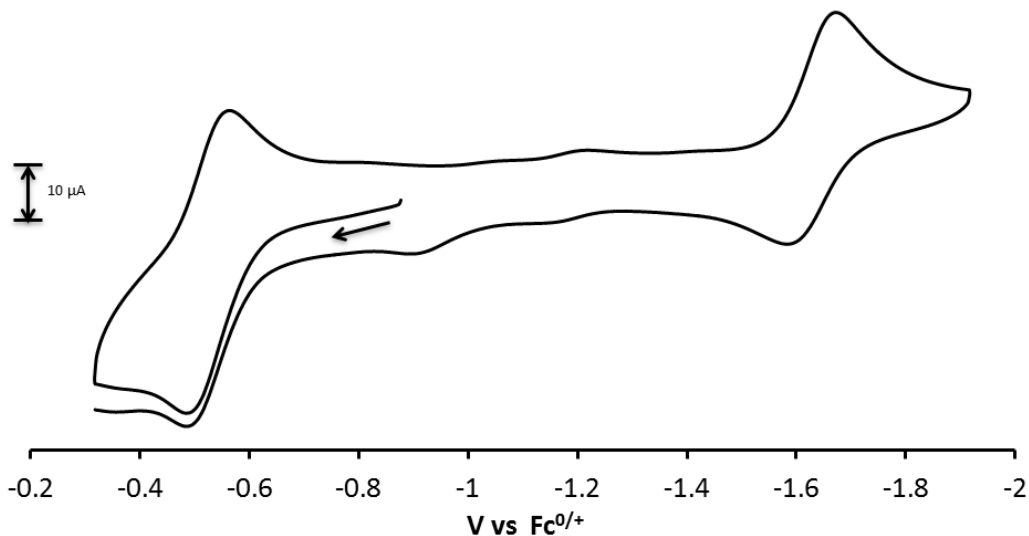


Figure 4.3.14 Full CV of **2** (0.1 M TBAPF₆, 50 mV/s)

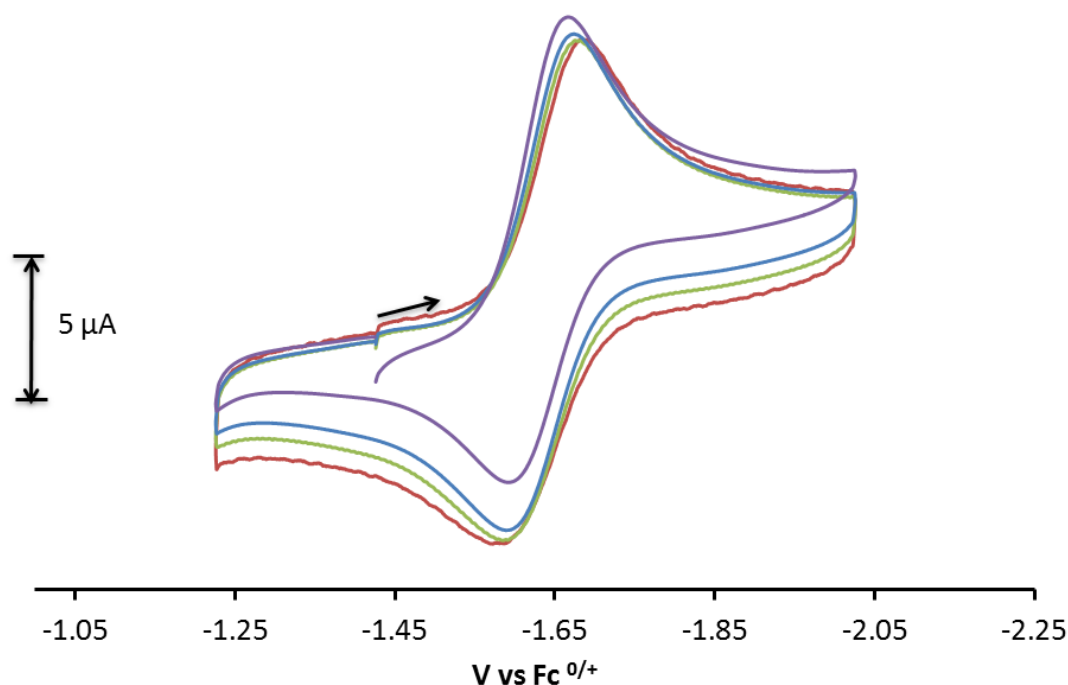


Figure 4.3.15 Scan speed dependence (10 – 250 mV/s) for cathodic electrochemical event of **2**. Current was corrected by dividing by the square root of the scan speed.

The oxidative event for **2** is scan speed independent (Figure 4.3.16) and has a potential of $E_{1/2} = -0.53$ V versus ferrocene with a peak to peak separation of $\Delta E = 79$ mV and current ratio of $i_{pa}/i_{pc} = 0.40$. The poor current ratio suggests that the electrochemical event observed is quasi-reversible instead of fully reversible. The assignment of the oxidation is ambiguous due to the bimetallic nature of **2**. Due to the lack of oxidative redox couples observed for Co(III) imidos, it can be hypothesized that the oxidation occurs at Co_N . However, the oxidation of Co_N from Co(II) to Co(III) should present more reversible electrochemical features due to the stabilization of the trianionic pocket.

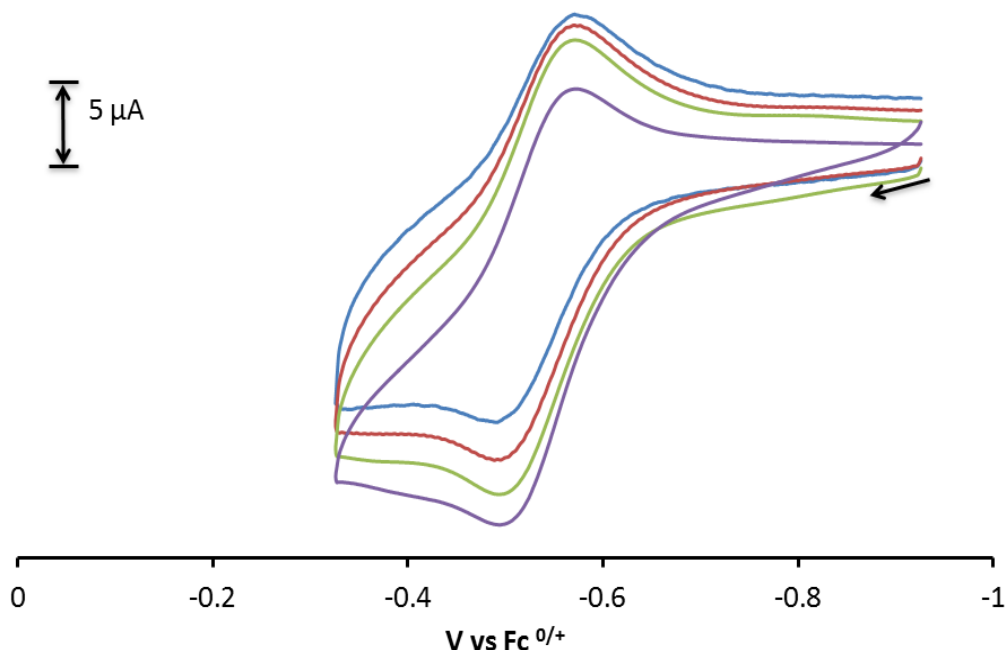


Figure 4.3.16 Scan speed dependence (10 – 250 mV/s) for anodic electrochemical event of **2**. Current was corrected by dividing by the square root of the scan speed.

4.3.7 Catalytic Activity of the Silyldiazenido Intermediate

Complex **1-SiPh₃** was examined as a suitable precatalyst for the generation of silyl amines. When **1-SiPh₃** was subjected to excess ClSiPh₃ and KC₈, no tris(triphenylsilyl)amine was observed via GC/MS. It should also be noted that the color of the reaction solution never deviated from that of the green color seen for **1-SiPh₃**. One hypothesis is the catalytic cycle could not be completed due to the steric bulk of the triphenyl silyl groups. Alternately, catalysis was run under normal catalytic conditions (2000 equiv TMSCl and KC₈) with **1-SiPh₃** as the precatalyst. It was found that **1-SiPh₃** was active in generating tris(trimethylsilyl)amine; however, the expected product bis(trimethylsilyl)triphenylsilyl amine, was not observed while analyzing the GC/MS trace. It is ambiguous whether **1-SiPh₃** would produce the desired product. Due to the higher expected molecular weight of bis(trimethylsilyl)triphenylsilyl amine, the method

of product isolation (vacuum transfer) from the catalyst could potentially leave behind the desired product in the mixture. It should be noted that complex **1-SiPh₃** was seen to decompose to the known mono-anionic species (*vide supra*), which is also catalytically active for the silylation for dinitrogen (Chapter 3).

4.3.8 Preliminary Reactivity Scope of the Dicobalt Imido

Complex **2** was screened as an nitrene transfer reagent (Figure 4.3.17). Unlike the previously known Co(III) imidos, the bimetallic composition complex **2** was hypothesized to be a facile transfer reagent due to the driving force of forming a metal-metal bond upon loss of the imido fragment. Such metal-metal cooperativity has been illustrated throughout the literature with C-H borylation catalysis⁵³, C-C coupling⁴⁸ and carbene and nitrene transfer.¹¹³

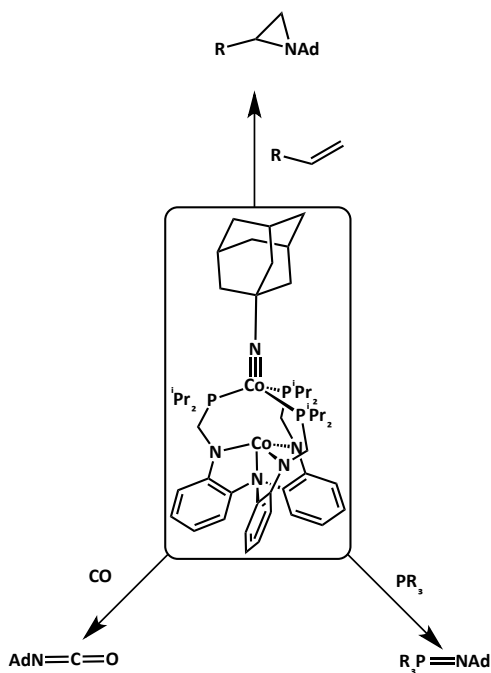


Figure 4.3.17 General scope of nitrene reactions attempted with complex **2**.

Complex **2** readily reacts with 2 equivalents of trimethylphosphine (PMe_3) at room temperature to generate $\text{Me}_3\text{P}=\text{NAd}$ and an assigned $\text{LCo}_2\text{-PMe}_3$ adduct which can be independently synthesized and confirmed through ^1H NMR spectroscopy. The phosphinimide was characterized via ESI-MS (Figure 4.3.18) and ^{31}P NMR spectroscopy. Complex **2** also reacts with CO at 40°C to generate a CO bound product as based by ^1H NMR and IR. However, there was no evidence for adamantylisocyanate formation.

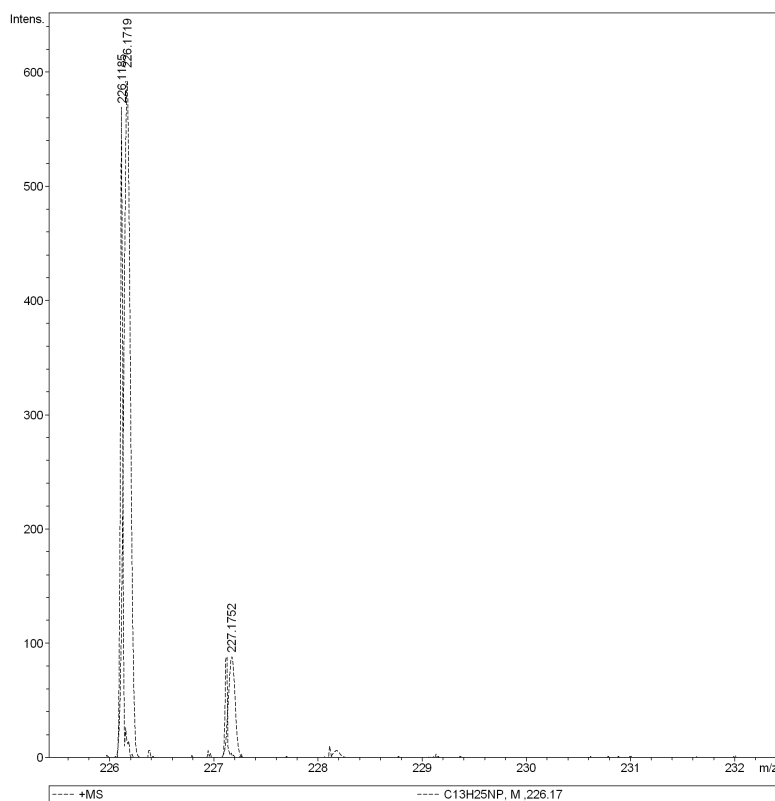


Figure 4.3.18 Positive mode ESI-MS spectrum in acetonitrile of reaction solution of **2** with PMe_3 . Solid line is experimental spectrum. Dashed line is a model of $\text{Me}_3\text{P}=\text{NH-Ad}^+$.

Complex **2** is a potential aziridation reagent. At room temperature, complex **2** does not react with styrene or cyclooctene. However, at elevated temperatures (60°C), ^1H NMR shows complete loss of complex **2**. The resulting ^1H NMR shows proton signals for LCo_2 (Figure 4.3.19) and a possible aziridation product. Conversely, when **2** is heated

with styrene, no formation of LCo_2 is observed by ^1H NMR spectroscopy. Instead, the ^{31}P NMR spectrum shows a signal at ~ 50 ppm which could correspond to an oxidized phosphine. It is hypothesized that high temperatures promote the de-coordination of a phosphine arm, which can then be readily attacked by the imido fragment. For comparison, an analogous trialkyl phosphinimine, $\text{Me}_3\text{P}=\text{NAd}$ has been reported with a ^{31}P chemical shift of -13 ppm.¹¹⁸ The observed upfield ^{31}P chemical shift from the heating of **2** can be due to the electronics of the ligand scaffold and outer sphere interactions with the paramagnetic cobalt centers; however, this hypothesis still needs to be verified. The observation of this ^{31}P chemical shift is also present when ethylene is added to **2** at room temperature and in thermo-stability experiments of complex **2**. This decomposition pathway is insightful in that it shows the lability of the phosphine arms of the ligand scaffold. This notion is also supported in the calculated mechanism for dinitrogen silylation (Chapter 3) in which the phosphine arm lability is important for driving the catalysis forward.

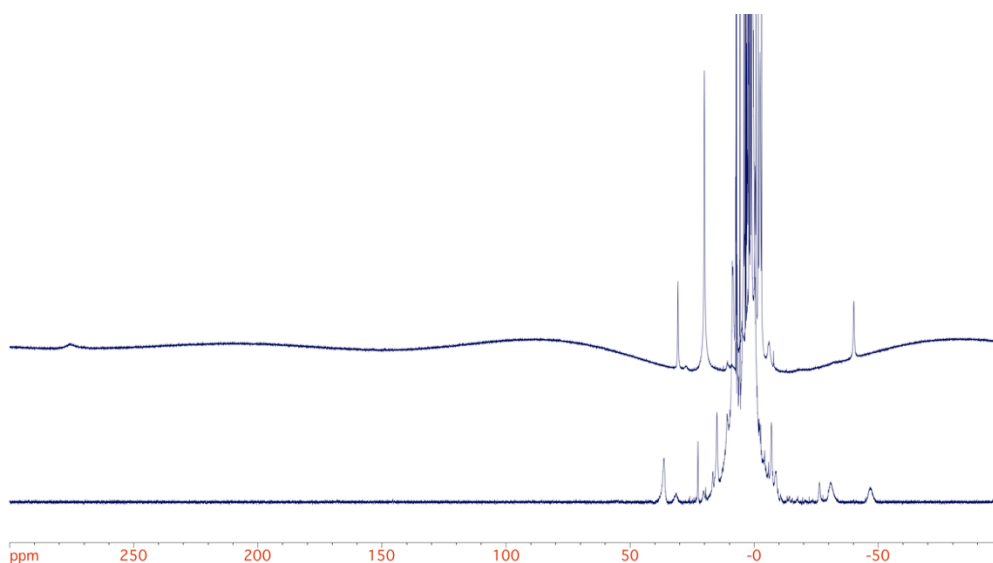


Figure 4.3.19 ^1H NMR spectra (500 MHz, C_6D_6) of reaction of **2** with cyclo-octene (1 equiv) after 10 hours at 40°C . Top: spectrum after 10 hours at rt Bottom: spectrum after 10 hrs at 40°C .

4.4 Conclusions

Two potential intermediates of dinitrogen reduction, a silyldiazenido unit (**1-SiPh₃**) and a dicobalt imido **2** were synthesized and characterized. It was found that each complex has a low spin Co_P center that shows electron density of the supporting cobalt center (Co_N). For complex **1-SiPh₃** it was elucidated that altering the number of phenyl groups leads to a blue shift in electronic absorption. Complex **1-SiPh₃** also undergoes photo-degradation that could suggest partial radical character of the N₂SiR₃ unit. The blue shift in the vis-NIR spectrums also correlates well to the stability of the silyldiazenido intermediates and can be seen in catalytic activity where TMSCl undergoes catalysis whereas Ph₃SiCl does not. Complex **2**, to the best of our knowledge, is the first late-transition metal imido to possess multiple reversible redox events as seen in electrochemical experiments. While the parent complex had limited reactivity, the addition or removal of an electron from **2** may allow more facile nitrene transfer.

4.5 Experimental

4.5.1 General Considerations

Unless otherwise stated, all manipulations were performed under a dinitrogen atmosphere in a Vac Atmosphere glovebox or using standard Schlenk techniques. Standard solvents were deoxygenated by sparging with dinitrogen and dried by passing through activated alumina columns of a SG Water solvent purification system. Deuterated solvents were purchased from Cambridge Isotope Laboratories, Inc., degassed via freeze-pump-thaw cycles, and stored over activated 4 Å molecular sieves. ^1H and ^{31}P NMR spectra were recorded on Varian 300, and 500 MHz and Bruker 400 and 500 MHz spectrometers at ambient temperature unless otherwise stated. Proton chemical shifts were referenced to residual solvent, ^{31}P NMR was referenced to 85% H_3PO_4 at 0 ppm. The synthesis of 2,2,2-tri(diisopropylphosphinomethylamino)triphenylamine ((N(o-(NHCH₂PiPr₂)C₆H₄)₃) (abbreviated as LH₃) has been reported previously.^{69b}

4.5.2 Synthetic Procedures

Preliminary Synthesis of [K(2,2,2-cryptand)]CoL:

LH₃ (0.199 g, 0.292 mmol) was dissolved in 10 mL of toluene. Potassium bis(trimethylsilyl)amide (0.190 g, 0.952 mmol) in toluene was added to the ligand solution. The solution immediately turned yellow and was stirred for 24 hr at rt in which a off-white precipitate formed. The solution was then filtered and washed with toluene to give K₃L as a yellow solid (0.211g). K₃L was then dissolved in THF (8 mL) and cooled to -40 C. Separately, a slurry of cobalt(II) chloride (0.036 g, 0.277 mmol) in THF (4 mL) was cooled to -40 C. The cobalt slurry was then added to the K₃L solution and stirred for 2 hr. The reaction mixture was then warmed to rt and stirred for 2 hr to which a yellow-brown solution formed. The solvent was removed *in vacuo*. The residual solid

was dissolved in hexane and filtered. The filtrate was then dried *in vacuo*, and reconstituted in THF. To the THF solution was added 2,2,2-cryptand (0.106 g, 0.282 mmol) in 2 mL of THF for crystallization purposes and stirred for 10 minutes and the solvent removed *in vacuo* to yield a dark orange-brown solid (202 mg, 60%). Bulk crystals can be attained through layering a concentrated benzene solution with pentane. ^1H NMR (400 MHz, C_6D_6): 232.1, 25.3, 9.9, 4.8, 3.6, 2.8, 1.8, 1.0, -7.7, -35.4. See Figure A4.5.1 for spectrum.

Preliminary synthesis of $[\text{K}(\text{crypt})]\text{LCO}_2\text{N}_2\text{SiPh}_3$ (1-SiPh₃**):**

LCO_2 (100 mg, 0.13 mmol) was dissolved in 4 mL of THF and run through a plug of KC_8 (1/4" in a pipette equipped with filter paper). This was done 3 times to ensure full conversion to generate *in situ* $[\text{LCO}_2(\text{N}_2)]^{2-}$. The reaction vial was then cooled to -78 C, and to it was added a THF solution (4 mL) of chlorotriphenylsilane (38.1 mg, 0.13 mmol) dropwise, in which the solution immediately turned dark green. The reaction was allowed to warm to room temperature in which 2,2,2-cryptand (34 mg, 0.10 mmol) was added and after 5 min the volatiles were removed *in vacuo*. The residue was then washed with benzene. The residue was then concentrated in THF and layered with hexane and placed in a -20 C freezer in which a green precipitate appeared after 1 week (133.1 mg, 75%). Attempts to grow single crystals from the green precipitate have not been successful to date. ^1H NMR (500 MHz, $\text{d}^8\text{-THF}$): 191.9, 182.8, 31.3, 28.5, 15.4, -1.4, -36.9. UV-vis-NIR (THF) $\lambda_{\text{max}}/\text{nm}$ ($\epsilon / \text{M}^{-1} \text{cm}^{-1}$): 590 (1200), 1340 (250). IR (KBr pellet, (THF solution)): 1685 cm^{-1} (1690 cm^{-1}). Similar reaction conditions can be used to make **1-SiPh₂Me**, **1-SiPhMe₂**, and **1-SiMe₃** but their stabilities are much less.

Synthesis of LCO_2NAd (2**):**

LCO₂Cl (0.157 g, 0.189 mmol) was dissolved in 4 mL of THF. To the purple solution was added KC₈ (0.025 g, 0.187 mmol) and the reaction was stirred for 2 hr at room temperature. The reaction mixture was then filtered through a Celite plug and washed with 2 mL THF. To the filtrate was added 1-adamantyl azide (0.037g , 0.208 mmol) and the reaction was stirred for 90 mins at rt. The solvent was removed *in vacuo* and the resulting solvent was reconstituted in diethyl ether (5 mL) and filtered. The insoluble solids were reconstituted in benzene and collected to yield a green solid (47.7 mg, 24 % yield). Crystals suitable for single crystal X-ray diffraction were grown from layering a concentrated benzene solution of **2** with pentane to yield a mixture of fine needles and blocks. ¹H NMR (400 MHz, C₆D₆): 272.2, 30.3, 19.7, 3.6, 3.2, 1.4, 1.2, 1.1, 0.9, -0.4, -0.7, -1.5, -2.9, -6.0, -39.2. UV-vis-NIR (THF) λ_{max}/nm (ε / M⁻¹ cm⁻¹): 450 (1700), 636 (950), 903 (650). Analysis (calcd., found) for C₄₉H₇₅Co₂N₅P₃: C (62.28, 62.19), H (8.00, 7.97), N (7.41, 7.27).

4.5.3 X-ray Crystallographic Data Collection and Refinement of Structure

A dark green block of **2** was placed on the tip of a 0.1 mm diameter glass capillary and mounted on a Bruker APEX II CCD diffractometer for data collection at 123(2) K. The data collection was carried out using Cu Kα radiation (graphite monochromator). The data intensity was corrected for absorption and decay (SADABS). Final cell constants were obtained from least-squares fits of all measured reflections and the structure was solved using SHELXS-08 and refined using SHELXL-08. A direct-methods solution was calculated which provided most non-hydrogen atoms from the E-map. Full-matrix least-squares/difference Fourier cycles were performed to locate the remaining non-hydrogen atoms and all non-hydrogen atoms were refined with anisotropic

displacement parameters. Hydrogen atoms were placed in ideal positions and refined as riding atoms with relative isotropic displacement parameters.

4.5.4 *Physical Measurements*

Elemental analyses were performed by Complete Analysis Laboratories, Inc. (Parsippany, NJ). Cyclic voltammetry was performed with a CH Instruments 600 electrochemical analyzer with a one-cell setup, comprising a glassy carbon working electrode, a platinum wire counter electrode, and Ag/AgNO₃ reference electrode in acetonitrile. Analytes were measured in 0.1 M [TBA]PF₆ THF solutions and internally referenced to the Cp₂Fe/Cp₂Fe⁺ redox couple.

4.5.5 *Computational Details*

TD-DFT calculations were performed to investigate the nature of the electron excitations observed in the electronic absorption spectra for **1-SiPh₃**, **1-SiPh₂Me**, **1-SiPhMe₂**, and **1-SiMe₃**. Full geometry optimization were performed by using the PBE¹²⁹ and M06-L¹³⁰ functionals as implemented in the *Gaussian 09 package*, and TD-DFT calculations were performed at the same level of theory.¹³¹ Solvent effects were considered by using the SMD model with THF as solvent.¹³² The def2-svp basis set for C, and H atoms, and the def2-tzvp¹³³ basis sets for N, P, Si, and Co atoms. An automatic density-fitting set generated by the Gaussian program was used to reduce the computational cost. The optimizations **1-SiPh₃**, **1-SiPh₂Me**, **1-SiPhMe₂**, and **1-SiMe₃** and **2** for were carried out without symmetry constraints and until tight energy and geometry convergence criteria were attained. The DFT integrations were performed with an ultrafine grid. The nature of all stationary points was verified by analytical computation of vibrational frequencies.

Bibliography

1. Huo, Y.-X.; Wernick, D. G.; Liao, J. C., *Curr. Opin. Biotechnol.* **2012**, *23*, 406-413.
2. Wallace, J. M.; Hobbs, P. V., *Atmospheric science: an introductory survey*. Academic press: 2006; Vol. 92.
3. Jia, H.-P.; Quadrelli, E. A., *Chem. Soc. Rev.* **2014**, *43*, 547-564.
4. Holland, P. L., *Dalton Trans.* **2010**, *39*, 5415.
5. (a) Leigh, G. J., **2004**, 33-54; (b) Kandemir, T.; Schuster, M. E.; Senyshyn, A.; Behrens, M.; Schlögl, R., *Angew. Chem. Int. Ed.* **2013**, *52*, 12723-12726; (c) van der Ham, C. J. M.; Koper, M. T. M.; Hetterscheid, D. G. H., *Chem. Soc. Rev.* **2014**, 5183-5191; (d) Averill, B.; Eldredge, P., Prentice Hall: Upper Saddle River, NJ, 2007; Vol. 1.
6. (a) Appl, M., Ammonia, 1. Introduction. In *Ullmann's Encyclopedia of Industrial Chemistry*, Wiley-VCH Verlag GmbH & Co. KGaA: 2000; (b) Brown, T. E.; LeMay, H. E.; Bursten, B. E., *Chemistry: The Central Science*. Pearson: Upper Saddle River, NJ, 2006.
7. Khoenkhoen, N.; de Bruin, B.; Reek, J. N. H.; Dzik, W. I., *Eur. J. Inorg. Chem.* **2015**, 567-598.
8. Burgess, B. K.; Lowe, D. J., *Chem. Rev.* **1996**, *96*, 2983-3012.
9. (a) Eady, R. R., *Chem. Rev.* **1996**, *96*, 3013; (b) Kim, J.; Rees, D. C., *Science* **1992**, *257*, 1677.
10. Hoffman, B. M.; Lukoyanov, D.; Yang, Z.-Y.; Dean, D. R.; Seefeldt, L. C., *Chem. Rev. (Washington, DC, U. S.)* **2014**, *114*, 4041-4062.

11. (a) Lancaster, K. M.; Roemelt, M.; Ettenhuber, P.; Hu, Y.; Ribbe, M. W.; Neese, F.; Bergmann, U.; DeBeer, S., *Science* **2011**, *334*, 974-977; (b) Spatzal, T.; Aksoyoglu, M.; Zhang, L.; Andrade, S. L. A.; Schleicher, E.; Weber, S.; Rees, D. C.; Einsle, O., *Science* **2011**, *334*, 940.
12. Seefeldt, L. C.; Dance, I. G.; Dean, D. R., *Biochemistry* **2004**, *43*, 1401-1409.
13. Seefeldt, L. C.; Hoffman, B. M.; Dean, D. R., *Annu. Rev. Biochem* **2009**, *78*, 701-722.
14. Dos Santos, P. C.; Igarashi, R. Y.; Lee, H. I.; Hoffman, B. M.; Seefeldt, L. C.; Dean, D. R., *Acc. Chem. Res.* **2005**, *38*, 208-214.
15. (a) Lukoyanov, D.; Barney, B. M.; Dean, D. R.; Seefeldt, L. C.; Hoffman, B. M., *Proc. Nat. Acad. Sci.* **2007**, *104*, 1451-1455; (b) Hoffman, B. M.; Dean, D. R.; Seefeldt, L. C., *Acc. Chem. Res.* **2009**, *42*, 609-619.
16. Igarashi, R. Y.; Laryukhin, M.; Dos Santos, P. C.; Lee, H. I.; Dean, D. R.; Seefeldt, L. C.; Hoffman, B. M., *J. Am. Chem. Soc.* **2005**, *127*, 6231-6241.
17. Kinney, R. A.; Hetterscheid, D. G. H.; Hanna, B. S.; Schrock, R. R.; Hoffman, B. M., *Inorg. Chem.* **2010**, *49*, 704.
18. Lukoyanov, D.; Yang, Z.-Y.; Dean, D. R.; Seefeldt, L. C.; Hoffman, B. M., *J. Am. Chem. Soc.* **2010**, *132*, 2526.
19. Brown, K. A.; Harris, D. F.; Wilker, M. B.; Rasmussen, A.; Khadka, N.; Hamby, H.; Keable, S.; Dukovic, G.; Peters, J. W.; Seefeldt, L. C.; King, P. W., *Science* **2016**, *352*, 448-450.
20. (a) Chatt, J.; Elson, C. M.; Leigh, G. J., *J. Am. Chem. Soc.* **1973**, *95*, 2408; (b) Chatt, J.; Pearman, A. J.; Richards, R. L., **1975**; (c) Diamantis, A. A.; Chatt, J.; Leigh, G.

- J.; Heath, G. A., *J. Organomet. Chem.* **1975**; (d) Chatt, J., *Philos. Trans. R. Soc. London, Ser. B* **1977**, *281*, 243-248; (e) Pickett, J. C., *J. Biol. Inorg. Chem.* **1996**, *1*, 601-606.
21. Schrock, R. R., *Acc. Chem. Res.* **2005**, *38*, 955-962.
22. (a) Tanaka, H.; Sasada, A.; Kouno, T.; Yuki, M.; Miyake, Y.; Nakanishi, H.; Nishibayashi, Y.; Yoshizawa, K., *J. Am. Chem. Soc.* **2011**, *133*, 3498-3506; (b) Liao, Q.; Saffon-Merceron, N.; Mézailles, N., *ACS Catalysis* **2015**, 6902-6906.
23. Del Castillo, T. J.; Thompson, N. B.; Peters, J. C., *J. Am. Chem. Soc.* **2016**, jacs.6b01706.
24. Hoffman, B. M.; Lukoyanov, D.; Yang, Z.-Y.; Dean, D. R.; Seefeldt, L. C., *Chem. Rev.* **2014**, *114*, 4041-4062.
25. Dilworth, M. J.; Eady, R. R., *Biochem. J.* **1991**, *277*, 465.
26. Lukoyanov, D.; Yang, Z.-Y.; Barney, B. M.; Dean, D. R.; Seefeldt, L. C.; Hoffman, B. M., *Proc. Nat. Acad. Sci.* **2012**, *109*, 5583-5587.
27. ESEEM. <http://www.epr.ethz.ch/about-epr-research-group/what-are-spin-echoes/spin-echoes/eseem.html> (accessed April 26, 2016).
28. Hoffman, B. M.; Lukoyanov, D.; Dean, D. R.; Seefeldt, L. C., *Abstracts of Papers of the American Chemical Society* **2014**, 247.
29. Bevan, P. C.; Chatt, J.; Leigh, G. J.; Leelamani, E. G., *J. Organomet. Chem.* **1977**.
30. (a) Takahashi, T.; Mizobe, Y.; Sato, M.; Uchida, Y.; Hidai, M., *J. Am. Chem. Soc.* **1979**, *101*, 3405-3407; (b) Tatsumi, T.; Tominaga, H.; Hidai, M.; Uchida, Y., *J. Organomet. Chem.* **1980**; (c) Mizobe, Y.; Ono, R.; Uchida, Y.; Hidai, M.; Tezuka, M., *J. Organomet. Chem.* **1981**; (d) Hidai, M.; Komori, K.; Kodama, T.; Jin, D. M., *J. Organomet. Chem.* **1984**; (e) Komori, K.; Oshita, H.; Mizobe, Y.; Hidai, M., *J. Am.*

- Chem. Soc.* **1989**, *111*, 1939-1940; (f) Hidai, M., *Coord. Chem. Rev.* **1999**, *185-186*, 99-108.
31. Nishibayashi, Y., *Inorg. Chem.* **2015**, *54*, 9234-9247.
32. (a) Yandulov, D. V.; Schrock, R. R., *J. Am. Chem. Soc.* **2002**, *124*, 6252-6253; (b) Yandulov, D. V.; Schrock, R. R., *Science* **2003**, *301*, 76.
33. (a) Arashiba, K.; Miyake, Y.; Nishibayashi, Y., *Nat. Chem.* **2011**, *3*, 120-125; (b) Kuriyama, S.; Arashiba, K.; Nakajima, K.; Tanaka, H.; Kamaru, N.; Yoshizawa, K.; Nishibayashi, Y., *J. Am. Chem. Soc.* **2014**, *136*, 9719; (c) Kuriyama, S.; Arashiba, K.; Nakajima, K.; Tanaka, H.; Yoshizawa, K.; Nishibayashi, Y., *Chem. Sci.* **2015**, *6*, 3940-3951.
34. Leigh, G. J.; Jimenez-Tenorio, M., *J. Am. Chem. Soc.* **1991**.
35. (a) Gilbertson, J. D.; Szymczak, N. K.; Tyler, D. R., *J. Am. Chem. Soc.* **2005**, *127*, 10184-10185; (b) Yelle, R. B.; Crossland, J. L.; Szymczak, N. K.; Tyler, D. R., *Inorg. Chem.* **2009**, *48*, 861-871.
36. Gilbertson, J. D.; Szymczak, N. K.; Tyler, D. R., *Inorg. Chem.* **2004**, *43*, 3341-3343.
37. (a) Rodriguez, M. M.; Bill, E.; Brennessel, W. W.; Holland, P. L., *Science* **2011**, *334*, 780; (b) McWilliams, S. F.; Holland, P. L., *Acc. Chem. Res.* **2015**, *48*, 2059-2065.
38. (a) Anderson, J. S.; Rittle, J.; Peters, J. C., *Nature (London, U. K.)* **2013**, *501*, 84-87; (b) Creutz, S. E.; Peters, J. C., *J. Am. Chem. Soc.* **2014**, *136*, 1105.
39. (a) Anderson, J. S.; Cutsail, G. E., III; Rittle, J.; Connor, B. A.; Gunderson, W. A.; Zhang, L.; Hoffman, B. M.; Peters, J. C., *J. Am. Chem. Soc.* **2015**, *137*, 7803-7809; (b) Anderson, J. S.; Moret, M. E.; Peters, J. C., *J. Am. Chem. Soc.* **2013**, *135*, 534; (c)

- Moret, M. E.; Peters, J. C., *Angew. Chem., Int. Ed.* **2011**, *50*, 2063; (d) Moret, M.-E.; Peters, J. C., *J. Am. Chem. Soc.* **2011**, *133*, 18118-18121.
40. Groom, C. R.; Bruno, I. J.; Lightfoot, M. P.; Ward, S. C., *Acta Crystallogr. Sect. B: Struct. Sci.* **2016**, *72*, 171-179.
41. (a) Rozenel, S. S.; Padilla, R.; Arnold, J., *Inorg. Chem.* **2013**, *52*, 11544; (b) Clouston, L. J.; Bernales, V.; Carlson, R. K.; Gagliardi, L.; Lu, C. C., *Inorg. Chem.* **2015**, *54*, 9263-9270; (c) Bowman, A. C.; Milsmann, C.; Atienza, C. C. H.; Lobkovsky, E.; Wieghardt, K.; Chirik, P. J., *J. Am. Chem. Soc.* **2010**, *132*, 1676; (d) Ding, K.; Pierpont, A. W.; Brennessel, W. W.; Lukat-Rodgers, G.; Rodgers, K. R.; Cundari, T. R.; Bill, E.; Holland, P. L., *J. Am. Chem. Soc.* **2009**, *131*, 9471-9472; (e) Betley, T. A.; Peters, J. C., *J. Am. Chem. Soc.* **2003**, *125*, 10782-10783; (f) Whited, M. T.; Mankad, N. P.; Lee, Y.; Oblad, P. F.; Peters, J. C., *Inorg. Chem.* **2009**, *48*, 2507-2517; (g) Greenwood, B. P.; Forman, S. I.; Rowe, G. T.; Chen, C.-H.; Foxman, B. M.; Thomas, C. M., *Inorg. Chem.* **2009**, *48*, 6251-6260; (h) Setty, V. N.; Zhou, W.; Foxman, B. M.; Thomas, C. M., *Inorg. Chem.* **2011**, *50*, 4647-4655; (i) Suess, D. L. M.; Tsay, C.; Peters, J. C., *J. Am. Chem. Soc.* **2012**, *134*, 14158; (j) Del Castillo, T. J.; Thompson, N. B.; Suess, D. L. M.; Ung, G.; Peters, J. C., *Inorg. Chem.* **2015**, *54*, 9256-9262; (k) Siedschlag, R. B.; Bernales, V.; Vogiatzis, K. D.; Planas, N.; Clouston, L. J.; Bill, E.; Gagliardi, L.; Lu, C. C., *J. Am. Chem. Soc.* **2015**, *137*, 4638-4641; (l) Wu, B.; Gramigna, K. M.; Bezpalko, M. W.; Foxman, B. M.; Thomas, C. M., *Inorg. Chem.* **2015**, *54*, 10909-10917; (m) Rudd, P. A.; Planas, N.; Bill, E.; Gagliardi, L.; Lu, C. C., *Eur. J. Inorg. Chem.* **2013**, *2013*, 3898-3906.
42. Ding, K.; Pierpont, A. W.; Brennessel, W. W.; Lukat-Rodgers, G.; Rodgers, K. R.; Cundari, T. R.; Bill, E.; Holland, P. L., *J. Am. Chem. Soc.* **2009**, *131*, 9471-9472.

43. (a) Kuppuswamy, S.; Bezpalko, M. W.; Powers, T. M.; Wilding, M. J. T.; Brozek, C. K.; Foxman, B. M.; Thomas, C. M., *Chem. Sci.* **2014**, *5*, 1617; (b) Krogman, J. P.; Thomas, C. M., *Chem. Commun.* **2014**, *50*, 5115.
44. Clouston, L. J.; Bernales, V.; Siedschlag, R. B.; Vogiatzis, K. D.; Gagliardi, L.; Lu, C. C., *In manuscript in preparation*.
45. Lindahl, P. A., *J. Inorg. Biochem.* **2012**, *106*, 172-178.
46. Cooper, B. G.; Napoline, J. W.; Thomas, C. M., *Catalysis Reviews* **2012**, *54*, 1-40.
47. Mankad, N. P., *Chemistry – A European Journal* **2016**, *22*, 5822-5829.
48. Thomas, C. M., *Comments on Inorganic Chemistry* **2011**, *32*, 14-38.
49. Krogman, J. P.; Bezpalko, M. W.; Foxman, B. M.; Thomas, C. M., *Inorg. Chem.* **2013**, *52*, 3022-3031.
50. Thomas, C. M.; Napoline, J. W.; Rowe, G. T.; Foxman, B. M., *Chem. Commun.* **2010**, *46*, 5790.
51. Zhou, W.; Marquard, S. L.; Bezpalko, M. W.; Foxman, B. M.; Thomas, C. M., *Organometallics* **2013**, *32*, 1766-1772.
52. Napoline, J. W.; Bezpalko, M. W.; Foxman, B. M.; Thomas, C. M., *Chem. Commun.* **2013**, *49*, 4388-4390.
53. Mazzacano, T. J.; Mankad, N. P., *J. Am. Chem. Soc.* **2013**, *135*, 17258-17261.
54. Bagherzadeh, S.; Mankad, N. P., *J. Am. Chem. Soc.* **2015**, *137*, 10898-10901.
55. Jayarathne, U.; Mazzacano, T. J.; Bagherzadeh, S.; Mankad, N. P., *Organometallics* **2013**, *32*, 3986-3992.
56. (a) Hoffman, B. M.; Lukoyanov, D.; Dean, D. R.; Seefeldt, L. C., *Acc. Chem. Res.* **2013**, *46*, 587-595; (b) Hoffman, B. M.; Lukoyanov, D.; Yang, Z. Y.; Dean, D. R.;

- Seefeldt, L. C., *Chem. Rev.* **2014**, *114*, 4041; (c) Kampa, M.; Pandelia, M.-E.; Lubitz, W.; van Gestel, M.; Neese, F., *J. Am. Chem. Soc.* **2013**, *135*, 3915-3925; (d) Tard, C.; Pickett, C. J., *Chem. Rev.* **2009**, *109*, 2245-2274; (e) Lohmiller, T.; Ames, W.; Lubitz, W.; Cox, N.; Misra, S. K., *Appl. Magn. Reson.* **2013**, *44*, 691-720.
57. Nocera, D. G., *Acc. Chem. Res.* **2012**, *45*, 767-776.
58. (a) Brown-Xu, S. E.; Chisholm, M. H.; Durr, C. B.; Gustafson, T. L.; Spilker, T. F., *J. Am. Chem. Soc.* **2014**, *136*, 11428-11435; (b) Brown-Xu, S. E.; Chisholm, M. H.; Durr, C. B.; Lewis, S. A.; Spilker, T. F.; Young, P. J., *Inorg. Chem.* **2014**, *53*, 637-644; (c) Brown-Xu, S. E.; Chisholm, M. H.; Durr, C. B.; Lewis, S. A.; Spilker, T. F.; Young, P. J., *Chem. Sci.* **2014**, *5*, 2657-2666.
59. McGrady, J. E., Introduction and General Survey of Metal-Metal Bonds. In *Molecular Metal-Metal Bonds : Compounds, Synthesis, Properties*, Liddle, S. T., Ed. Wiley: Berlin, 2015.
60. (a) Murillo, C. A., *Multiple Bonds Between Metal Atoms* **2005**; (b) Chifotides, H. T.; Saha, B.; Patmore, N. J.; Dunbar, K. R.; Bera, J. K., Group 9 Metal-Metal Bonds. In *Molecular Metal-Metal Bonds : Compounds, Synthesis, Properties*, Liddle, S. T., Ed. Wiley: Berlin, 2015.
61. (a) Cotton, F. A.; Daniels, L. M.; Feng, X.; Maloney, D. J.; Matonic, J. H.; Murilio, C. A., *Inorg. Chim. Acta* **1997**, *256*, 291-301; (b) Cotton, F. A.; Daniels, L. M.; Maloney, D. J.; Matonic, J. H.; Murillo, C. A., *Inorg. Chim. Acta* **1997**, *256*, 283-289.
62. Zall, C. M.; Zherebetsky, D.; Dzubak, A. L.; Bill, E.; Gagliardi, L.; Lu, C. C., *Inorg. Chem.* **2012**, *51*, 728-736.

63. Zall, C. M.; Clouston, L. J.; Young, J., Victor G; Ding, K.; Kim, H. J.; Zherebetsky, D.; Chen, Y.-S.; Bill, E.; Gagliardi, L.; Lu, C. C., *Inorg. Chem.* **2013**, *52*, 9216-9228.
64. Tereniak, S. J.; Carlson, R. K.; Clouston, L. J.; Young, J., Victor G; Bill, E.; Maurice, R.; Chen, Y.-S.; Kim, H. J.; Gagliardi, L.; Lu, C. C., *J. Am. Chem. Soc.* **2014**, *136*, 1842-1855.
65. Tereniak, S. J. Synthesis, Characterization, and Reactivity of Metal-Metal Bonded Complexes with Cobalt, Iron, and Manganese. University of Minnesota, 2014.
66. Jones, C.; Schulten, C.; Rose, R. P.; Stasch, A.; Aldridge, S.; Woodul, W. D.; Murray, K. S.; Moubaraki, B.; Brynda, M.; La Macchia, G.; Gagliardi, L., *Angew. Chem. Int. Ed.* **2009**, *48*, 7406-7410.
67. Kuppaswamy, S.; Powers, T. M.; Johnson, B. M.; Bezpalko, M. W.; Brozek, C. K.; Foxman, B. M.; Berben, L. A.; Thomas, C. M., *Inorg. Chem.* **2013**, *52*, 4802-4811.
68. Mathialagan, R.; Kuppaswamy, S.; De Denko, A. T.; Bezpalko, M. W.; Foxman, B. M.; Thomas, C. M., *Inorg. Chem.* **2013**, *52*, 701-706.
69. (a) Miller, D. L. Design and Synthesis of New Ligand Scaffolds and Transition Metal Complexes for Small Molecule Activation. University of Minnesota, 2013; (b) Rudd, P. A.; Liu, S.; Gagliardi, L.; Young, J., Victor G; Lu, C. C., *J. Am. Chem. Soc.* **2011**, *133*, 20724-20727.
70. Cotton, F. A., *Multiple bonds between metal atoms*. 2005.
71. Pauling, L., *J. Am. Chem. Soc.* **1947**, *69*, 542-553.
72. Eisenhart, R. J.; Clouston, L. J.; Lu, C. C., *Acc. Chem. Res.* **2015**, *48*, 2885-2894.
73. Mabbs, F. E., *Chem. Soc. Rev.* **1993**, *22*, 313-324.

74. Badger, R. M., *The Journal of Chemical Physics* **1934**, *2*, 128-131.
75. Clouston, L. J.; Siedschlag, R. B.; Rudd, P. A.; Planas, N.; Hu, S.; Miller, A. D.; Gagliardi, L.; Lu, C. C., *J. Am. Chem. Soc.* **2013**, *135*, 13142-13148.
76. Weare, W. W.; Dai, X.; Byrnes, M. J.; Chin, J. M.; Schrock, R. R.; Müller, P., *Proc. Nat. Acad. Sci. U.S.A.* **2006**, *103*, 17099-17106.
77. (a) Nicholson, R. S.; Shain, I., *Anal. Chem.* **1965**, *37*, 178-190; (b) Nicholson, R. S.; Shain, I., *Anal. Chem.* **1965**, *37*, 190-195.
78. Zhao, Y.; Truhlar, D. G., *J. Chem. Phys.* **2006**, *125*, 194101.
79. Weigend, F.; Ahlrichs, R., *PCCP* **2005**, *7*, 3297.
80. Anquilante, F.; De Vico, L.; Ferre, N.; Ghigo, G.; Malmqvist, P.-A.; Neogrady, P.; Pedersen, T. B.; Pitonak, M.; Reiher, M.; Roos, B. O.; Serrano-Andres, L.; Urban, M.; Veryazov, V.; Lindh, R., *J. Comput. Chem.* **2010**, *31*, 224.
81. Roos, B. O.; Taylor, P. R.; Siegbahn, P. E. M., *Chem. Phys.* **1980**, *48*, 157.
82. Olsen, J.; Roos, B. O.; Jorgensen, P.; Jensen, H. J. A., *J. Chem. Phys.* **1988**, *89*, 2185.
83. Andersson, K.; Malmqvist, P.-A.; Roos, B. O., *J. Chem. Phys.* **1992**, *96*, 1218.
84. Malmqvist, P.-A.; Pierloot, K.; Shahi, A. R. M.; Cramer, C. J.; Gagliardi, L., *J. Chem. Phys.* **2008**, *128*, 204109.
85. (a) Roos, B. O.; Lindh, R.; Malmqvist, P.-A.; Veryazov, V.; Widmark, P.-O., *J. Phys. Chem. A* **2004**, *108*, 2851; (b) Roos, B. O.; Lindh, R.; Malmqvist, P.-A.; Veryazov, V.; Widmark, P.-O., *J. Phys. Chem. A* **2005**, *109*, 6575.
86. (a) Douglas, M.; Kroll, N. M., *Ann. Phys.* **1974**, *82*, 89; (b) Hess, B. A., *Phys. Rev. A: At. Mol. Opt. Phys.* **1986**, *33*, 3742.

87. Aquilante, F.; Pedersen, T. B.; Lindh, R., *J. Chem. Phys.* **2007**, *126*, 114107.
88. Forsberg, N.; Malmqvist, P.-A., *Chem. Phys. Lett.* **1997**, *274*, 196.
89. Riley, F. L., *J. Am. Ceram. Soc.* **2000**, *83*, 245-265.
90. (a) Shiina, K., *J. Am. Chem. Soc.* **1972**, *94*, 9266-9267; (b) Liao, Q.; Saffon-Merceron, N.; Mézailles, N., *Angewandte Chemie International Edition* **2014**, *53*, 14206-14210; (c) Mori, M., *J. Organomet. Chem.* **2004**, *689*, 4210-4227; (d) Ung, G.; Peters, J. C., *Angew. Chem., Int. Ed.* **2015**, *54*, 532; (e) Yuki, M.; Tanaka, H.; Sasaki, K.; Miyake, Y.; Yoshizawa, K.; Nishibayashi, Y., *Nature Communications* **2012**, *3*, 1254-1256.
91. (a) Hazari, N., *Chem. Soc. Rev.* **2010**, *39*, 4044; (b) Arashiba, K.; Miyake, Y.; Nishibayashi, Y., *Nat Chem* **2011**, *3*, 120-125; (c) Anderson, J. S.; Rittle, J.; Peters, J. C., *Nature* **2013**, *501*, 84-87.
92. Imayishi, R.; Tanaka, H.; Matsuo, Y.; Yuki, M.; Nakajima, K.; Yoshizawa, K.; Nishibayashi, Y., *Chemistry - A European Journal* **2015**, *21*, 8905-8909.
93. Anderson, J. S.; Rittle, J.; Peters, J. C., *Nature* **2013**, *501*, 84.
94. Greenwood, B. P.; Forman, S. I.; Rowe, G. T.; Chen, C. H.; Foxman, B. M.; Thomas, C. M., *Inorg. Chem.* **2009**, *48*, 6251-6260.
95. (a) Crabtree, R. H., *Chem. Rev.* **2012**, *112*, 1536-1554; (b) Windegren, J. A.; Finke, R. G., *J. Mol. Catal. A: Chem.* **2003**, *198*, 317-341.
96. Weatherburn, M. W., *Anal. Chem.* **1967**, *39*, 971-974.
97. Fürstner, A.; Weidmann, H., *J. Organomet. Chem.* **1988**, *354*, 15 - 21.
98. (a) Padwa, A.; Snyder, J. P.; Curtis, E. A.; Sheehan, S. M.; Worsencroft, K. J.; Kappe, C. O., *J. Am. Chem. Soc.* **2000**, *122*, 8155-8167; (b) Pirrung, M. C.; Liu, H.; Morehead, A. T., *J. Am. Chem. Soc.* **2002**, *124*, 1014-1023.

99. Rudd, P. A.; Liu, S.; Gagliardi, L.; Young, J. V. G.; Lu, C. C., *J. Am. Chem. Soc.* **2011**, *133*, 20724-20727.
100. Perdew, J. P.; Ernzerhof, M.; Burke, K. J., *J. Chem. Phys.* **1996**, *105*, 9982.
101. Grimme, S.; Antony, J.; Ehrlich, S.; Krieg, H., *J. Chem. Phys.* **2010**, *132*, 154104.
102. Adamo, C.; Barone, V., *J. Chem. Phys.* **1999**, *110*, 6158.
103. (a) Becke, A. D., *J. Chem. Phys.* **1993**, *98*, 5648; (b) Lee, C.; Yang, W.; Parr, R. G., *Phys. Rev. B: Condens. Matter* **1988**, *37*, 785.
104. Peverati, R.; Truhlar, D. G., *J. Chem. Theory and Comput.* **2012**, *8*, 2310.
105. Marenich, A. V.; Cramer, C. J.; Truhlar, D. G., *J. Phys. Chem. B* **2009**, *113*, 6378.
106. Rappoport, D.; Furche, F. J., *Chem. Phys.* **2010**, *133*, 134105.
107. Frisch, M. J.; Trucks, G. W.; Schlegel, H. B.; Scuseria, G. E.; Robb, M. A.; Cheeseman, J. R.; Scalmani, G.; Barone, V.; Mennucci, B.; Petersson, G. A.; Nakatsuji, H.; Caricato, M.; Li, X.; Hratchian, H. P.; Izmaylov, A. F.; Bloino, J.; Zheng, G.; Sonnenberg, J. L.; Hada, M.; Ehara, M.; Toyota, K.; Fukuda, R.; Hasegawa, J.; Ishida, M.; Nakajima, T.; Honda, Y.; Kitao, O.; Nakai, H.; Vreven, T.; Montgomery Jr., J. A.; Peralta, J. E.; Ogliaro, F.; Bearpark, M. J.; Heyd, J.; Brothers, E. N.; Kudin, K. N.; Staroverov, V. N.; Kobayashi, R.; Normand, J.; Raghavachari, K.; Rendell, A. P.; Burant, J. C.; Iyengar, S. S.; Tomasi, J.; Cossi, M.; Rega, N.; Millam, N. J.; Klene, M.; Knox, J. E.; Cross, J. B.; Bakken, V.; Adamo, C.; Jaramillo, J.; Gomperts, R.; Stratmann, R. E.; Yazyev, O.; Austin, A. J.; Cammi, R.; Pomelli, C.; Ochterski, J. W.; Martin, R. L.; Morokuma, K.; Zakrzewski, V. G.; Voth, G. A.; Salvador, P.; Dannenberg, J. J.; Dapprich, S.; Daniels, A. D.; Farkas, Ö.; Foresman, J. B.; Ortiz, J. V.; Cioslowski, J.; Fox, D. J. *Gaussian 09*, Gaussian, Inc.: Wallingford, CT, USA, 2009.

108. (a) Schrock, R. R., *Proc. Nat. Acad. Sci. U.S.A.* **2006**, *103*, 17087-17087; (b) Chatt, J.; Dilworth, J. R.; Richards, R. L., *Chem. Rev.* **1978**, *78*, 589.
109. Hidai, M.; Takahashi, T.; Yokotake, I.; Uchida, Y., *Chem. Lett.* **1980**, 645.
110. Tanaka, H.; Sasada, A.; Kouno, T.; Yuki, M.; Miyake, Y.; Nakanishi, H.; Nishibayashi, Y.; Yoshizawa, K., *J. Am. Chem. Soc.* **2011**, *133*, 3498-3506.
111. Rudd, P. A. Stabilizing Metal-Alanes and Metal-Metal Multiple Bonds to Effect Small Molecule Transformations. University of Minnesota, Minneapolis, MN, 2014.
112. Cramer, S. A.; Sanchez, R. H.; Brakhage, D. F.; Jenkins, D. M., *Chem. Commun.* **2014**, *50*, 13967-13970.
113. Berry, J. F., *Dalton Trans.* **2012**, *41*, 700-713.
114. Saouma, C. T.; Peters, J. C., *Coord. Chem. Rev.* **2011**, *255*, 920-937.
115. (a) Cowley, R. E.; Bontchev, R. P.; Sorrell, J.; Sarracino, O.; Feng, Y.; Wang, H.; Smith, J. M., *J. Am. Chem. Soc.* **2007**, *129*, 2424-2425; (b) Mindiola, D. J.; Hillhouse, G. L., *J. Am. Chem. Soc.* **2001**, *123*, 4623-4624; (c) Mindiola, D. J.; Hillhouse, G. L., *Chem. Commun.* **2002**, 1840-1841; (d) Waterman, R.; Hillhouse, G. L., *J. Am. Chem. Soc.* **2003**, *125*, 13350-13351; (e) Laskowski, C. A.; Hillhouse, G. L., *Organometallics* **2009**, *28*, 6114-6120.
116. Cowley, R. E.; Eckert, N. A.; Elhaik, J.; Holland, P. L., *Chem. Commun.* **2009**, 1760.
117. King, E. R.; Sazama, G. T.; Betley, T. A., *J. Am. Chem. Soc.* **2012**, *134*, 17858-17861.
118. Kogut, E.; Wiencko, H. L.; Zhang, L.; Cordeau, D. E.; Warren, T. H., *J. Am. Chem. Soc.* **2005**, *127*, 11248-11249.

119. Ulrich, H., Metal Substituted Carbodiimides. In *Chemistry and Technology of Carbodiimides*, John Wiley & Sons, Ltd: 2007; pp 213-225.
120. Six, C.; Richter, F., Isocyanates, Organic. In *Ullmann's Encyclopedia of Industrial Chemistry*, Wiley-VCH Verlag GmbH & Co. KGaA: 2000.
121. Liao, Q.; Saffon-Merceron, N.; Mezailles, N., *Angew. Chem., Int. Ed.* **2014**, *53*, 14206-14210.
122. Belle, C.; Beguin, C.; Hamman, S.; Pierre, J.-L., *Coord. Chem. Rev.* **2009**, *253*, 963-976.
123. Glueck, D. S.; Hollander, F. J.; Bergman, R. G., *J. Am. Chem. Soc.* **1989**, *111*, 2719-2721.
124. Waterman, R.; Hillhouse, G. L., *J. Am. Chem. Soc.* **2008**, *130*, 12628-12629.
125. Batsanov, S. S., *Inorg. Mater.* **2001**, *37*, 871-885.
126. Yang, L.; Powell, D. R.; Houser, R. P., *Dalton Trans.* **2007**, 955-964.
127. (a) Yap, G. P. A., CCDC Deposition Number 253991. 2004; (b) Mehn, M. P.; Brown, S. D.; Jenkins, D. M.; Peters, J. C.; Que, L., *Inorg. Chem.* **2006**, *45*, 7417-7427; (c) Shay, D. T.; Yap, G. P. A.; Zakharov, L. N.; Rheingold, A. L.; Theopold, K. H., *Angew. Chem. Int. Ed.* **2005**, *44*, 1508-1510.
128. Saouma, C. T. Iron Mediated Reduction Schemes for Dinitrogen and Carbon Dioxide. California Institute of Technology, 2011.
129. (a) Perdew, J. P. B., K.; Ernzerhof, M., *Phys. Rev. Lett.* **1996**, *77*, 3865; (b) Perdew, J. P., *Phys. Rev. B* **1986**, *33*, 8822.
130. Zhao, Y. T., D. G., *J. Chem. Phys.* **2006**, *125*.

131. Frisch, M. J. T., G. W.; Schlegel, H. B.; Scuseria, G. E.; Robb, M. A.; Cheeseman, J. R.; Scalmani, G.; Barone, V.; Mennucci, B.; Petersson, G. A.; Nakatsuji, H.; Caricato, M.; Li, X.; Hratchian, H. P.; Izmaylov, A. F.; Bloino, J.; Zheng, G.; Sonnenberg, J. L.; Hada, M.; Ehara, M.; Toyota, K.; Fukuda, R.; Hasegawa, J.; Ishida, M.; Nakajima, T.; Honda, Y.; Kitao, O.; Nakai, H.; Vreven, T.; Montgomery, Jr., J. A.; Peralta, J. E.; Ogliaro, F.; Bearpark, M.; Heyd, J. J.; Brothers, E.; Kudin, K. N.; Staroverov, V. N.; Kobayashi, R.; Normand, J.; Raghavachari, K.; Rendell, A.; Burant, J. C.; Iyengar, S. S.; Tomasi, J.; Cossi, M.; Rega, N.; Millam, J. M.; Klene, M.; Knox, J. E.; Cross, J. B.; Bakken, V.; Adamo, C.; Jaramillo, J.; Gomperts, R.; Stratmann, R. E.; Yazyev, O.; Austin, A. J.; Cammi, R.; Pomelli, C.; Ochterski, J. W.; Martin, R. L.; Morokuma, K.; Zakrzewski, V. G.; Voth, G. A.; Salvador, P.; Dannenberg, J. J.; Dapprich, S.; Daniels, A. D.; Farkas, Ö.; Foresman, J. B.; Ortiz, J. V.; Cioslowski, J.; Fox, D. J. *Gaussian*, 09; Gaussian, Inc.: Wallingford CT, 2009.
132. Marenich, A. V. C., C. J.; Truhlar, D. G. , *J. Phys. Chem. B* **2009**, *113*, 6378-6396.
133. Eichkorn, K. W., F.; Treutler, O.; Ahlrichs, R. , *Theor. Chem. Acc.* **1997**, *97*, 119-124.

Appendix

Table A3.3.1: Results of Triplicate Runs for Each Compound for Catalytic N₂ Silylation

Pre-catalyst	Reductant	Solvent	Concentration (mM)	TMS ₃ N Yield % (per TMSCl)	TON [TMS ₃ N]/[catalyst]
1	KC ₈	THF	0.13	34.28	222.94
				27.19	176.82
				28.39	184.67
(N ₂)CoAl(L)	KC ₈	THF	0.13	4.23	28.30
				5.70	38.10
				2.63	17.61
1	KC ₈	DME	0.13	19.83	129.81
				21.49	140.71
				22.65	148.28
1^a	KC ₈	THF (40 + 40)	0.16 (0.08)	24.01	319.59
				25.42	338.37
				22.78	303.14
1 CoCl ₂ + LH ₃	KC ₈	THF	0.13	18.21	120.92
				12.29	81.60
				16.25	107.92
2 CoCl ₂ + LH ₃	KC ₈	THF	0.13	26.52	181.56
				22.42	153.50
				26.26	179.79
1 + PMe ₃	KC ₈	THF	0.13	27.28	178.44
				27.73	181.34
				26.03	172.95
CoCl ₂	KC ₈	THF	0.13	0.89	5.95
				1.10	7.32
				0.61	4.08
CoCl ₂ + 3 PMe ₃	KC ₈	THF	0.13	13.32	88.46
				12.03	79.87
				13.63	90.50
CoCl ₂ + 3 P(iPr ₂ Me) ₃	KC ₈	THF	0.13	12.13	80.56
				12.94	85.96
				17.43	115.74
Co(PPh ₃) ₃ Cl	KC ₈	THF	0.13	7.92	52.34
				4.64	30.69
				7.29	48.20
1	Li	THF	0.13	2.82	18.45
				2.02	13.20
				3.92	25.63
1	Na	THF	0.13	0.78	5.13
				0.42	2.78
				2.00	13.08
1	K	THF	0.13	4.73	30.99
				4.01	26.27
				4.72	30.90
1^c	K	THF	0.13	21.35	139.78
				15.88	103.97
				24.50	160.41
2	KC ₈	THF	0.13	23.30	152.53
				33.80	221.32
				24.61	161.15

a. A second set of reagents (40 mL THF, 2000 equiv KC₈ and TMSCl)

b. Catalysis was run for 95 hrs.

Table A3.3.2. Spin density isosurfaces (0.02 a.u.) of intermediates and transition states. Blue and green density corresponds to alpha and beta spin, respectively. In all cases, $\text{Co}_N(\text{II})$ is $S = 3/2$.

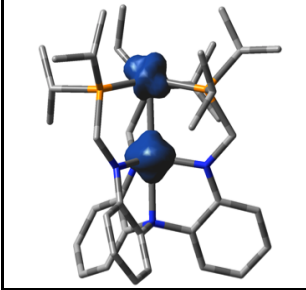
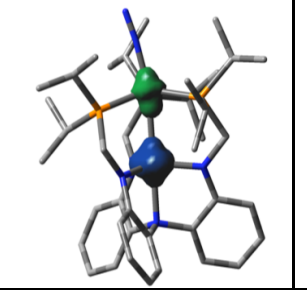
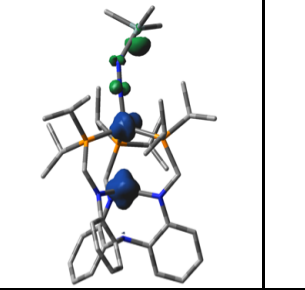
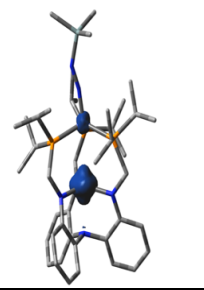
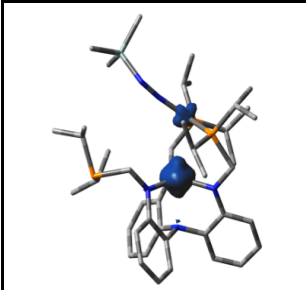
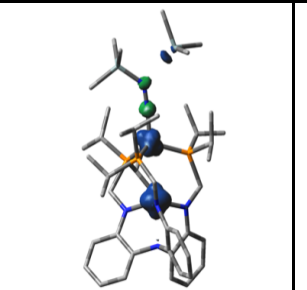
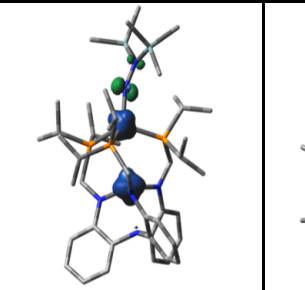
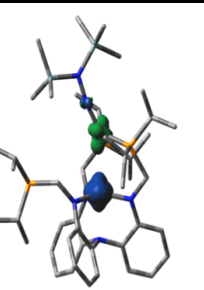
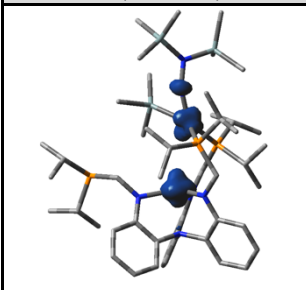
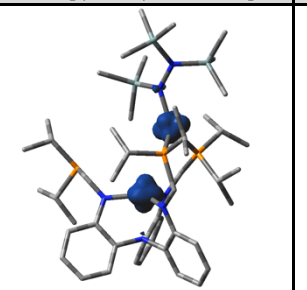
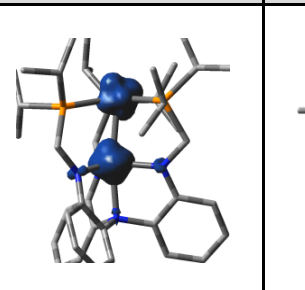
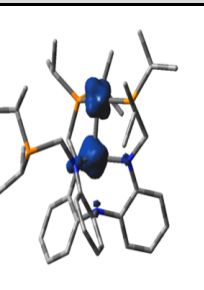
A: $[\text{Co}_2\text{L}]^{1-}$	B: $[\text{N}_2\text{Co}_2\text{L}]^{1-}$	TS(B→C)	C: $[(\text{TMS})\text{N}_2\text{Co}_2\text{L}]^{1-}$
			
$S = 2, \langle S^2 \rangle = 6.01$	$S = 1, \langle S^2 \rangle = 2.08$	$S = 3/2, \langle S^2 \rangle = 3.92$	$S = 3/2, \langle S^2 \rangle = 3.79$
$\text{Co}_P(0), S_{\text{CoP}} = 1/2$	$\text{Co}_P(0), S_{\text{CoP}} = 1/2$		$\text{Co}_P(\text{I}), S_{\text{CoP}} = \sim 0$
C*: $[(\text{TMS})\text{N}_2\text{Co}_2\text{L}]^{1-}$	TS(C→D)	D: $[(\text{TMS})_2\text{N}_2\text{Co}_2\text{L}]^{1-}$	D*: $[(\text{TMS})_2\text{N}_2\text{Co}_2\text{L}]^{1-}$
			
$S = 3/2, \langle S^2 \rangle = 3.75$	$S = 2, \langle S^2 \rangle = 6.04$	$S = 2, \langle S^2 \rangle = 6.03$	$S = 1, \langle S^2 \rangle = 2.19$
$\text{Co}_P(\text{I}), S_{\text{CoP}} = \sim 0$		$\text{Co}_P(\text{II}), S_{\text{CoP}} = 1/2$	$\text{Co}_P(\text{II}), S_{\text{CoP}} = 1/2$
TS(D*→E*)	E*: $[(\text{TMS})_3\text{N}_2\text{Co}_2\text{L}]^{1-}$	Co_2L	Co_2L^*
			
$S = 5/2, \langle S^2 \rangle = 8.84$	$S = 5/2, \langle S^2 \rangle = 8.75$	$S = 5/2, \langle S^2 \rangle = 8.75$	$S = 5/2, \langle S^2 \rangle = 8.82$
	$\text{Co}_P(\text{I}), S_{\text{CoP}} = 1$	$\text{Co}_P(\text{I}), S_{\text{CoP}} = 1$	$\text{Co}_P(\text{I}), S_{\text{CoP}} = 1$

Table A3.3.3. Calculated Bond Lengths (Å), Angles (deg.), and N₁-N₂ bond stretching frequencies (cm⁻¹) through the reaction coordinate (path **I**). All species are in their anionic form, except neutral Co₂L and free N₂.

Species	Spin	Distances					Angles				N ₁ -N ₂ (cm ⁻¹)
		Co-Co	Co _N - N _{eq}	Co _P -P	Co _P - N ₁	N ₁ -N ₂	Co _P -Co _N - N _{ax}	Co _P -Co _N - N ₁	Σ(P-Co _P - P)	Σ(N-Co _N - N) _{eq}	
Free N ₂	-	-	-	-	-	1.095	-	-	-	-	2424
Co ₂ L	2.5	2.522	1.958	2.319	-	-	170.42	-	358.21	355.05	-
A	2	2.625	1.968	2.243	-	-	179.39	-	354.24	355.34	-
B	1	2.648	1.954	2.253	1.817	1.128	178.66	168.7	350.21	355.28	2105
TS(B→C)	1.5	2.886	1.971	2.312	1.804	1.149	179.60	167.8	351.2	337.9	1885
C	1.5	2.927	1.966	2.270	1.660	1.207	178.86	167.4	334.66	351.49	1771
C*	1.5	2.749	1.975	3.281	1.647	1.217	169.73	114.1	330.9	353.2	1702
TS(C→D)	2	2.937	1.969	2.328	1.755	1.230	166.76	172.2	331.12	351.61	1545
D	2	3.042	1.964	2.426	1.800	1.354	174.54	161.9	324.60	352.18	1124
D*	1	2.779	1.960	3.090	1.675	1.349	176.19	145.3	327.8	353.90	1176
TS(D*→E*)	2.5	3.365	1.969	3.460	1.774	1.386	167.00	154.0	302.6	354.5	1068
E*	2.5	3.547	1.968	3.461	1.986	1.482	161.10	140.5	289.9	354.1	1003

The Co_N-N_{eq} and Co_P-P distances are the average of three Co-L distances.

Table A3.5.1. A DFT benchmark study to compare various functionals and basis sets for [(N₂)Co₂L]⁻ (*S* = 1). Differences between the Co-Co, N-N, and Co-L (ligand) bond distances (Å) in the crystal structure and the various optimized geometries are given. The <*S*²> values are also reported.

Functional	Basis Set	D(Co-Co)	D(N-N)	MUE ^a for Co-	< <i>S</i> ² >
PBE	def2-TZVP	-0.071	0.026	0.011	2.26
PBE-D3	def2-TZVP	-0.094	0.026	0.022	2.23
PBE0-D3	def2-TZVP	-0.030	0.001	0.015	2.92
B3LYP-D3	def2-TZVP	-0.012	0.005	0.021	2.87
M06-L	def2-TZVP	-0.025	0.014	0.014	2.76
M06-L	SDD	-0.089	0.014	0.018	2.76
N12	def2-TZVP	-0.119	0.009	0.016	2.22
N12	SDD	-0.098	0.008	0.016	2.56

^aMUE (mean unassigned error for Co-P and Co-N bond distances)

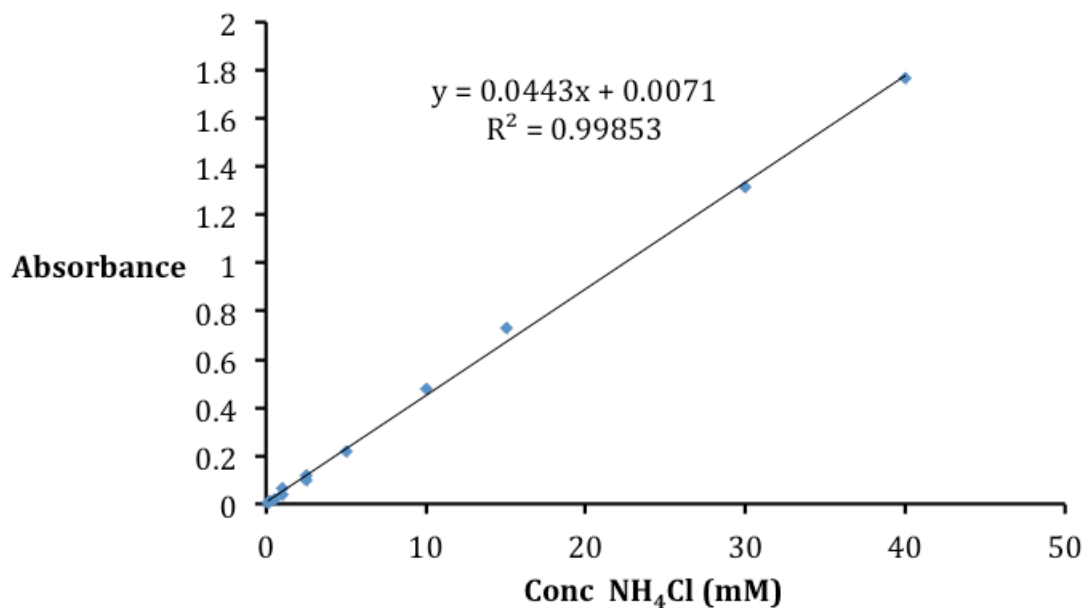


Figure A3.3.1: Indophenol calibration curve ($\lambda_{\text{max}} = 625 \text{ nm}$) for NH₃ quantification.

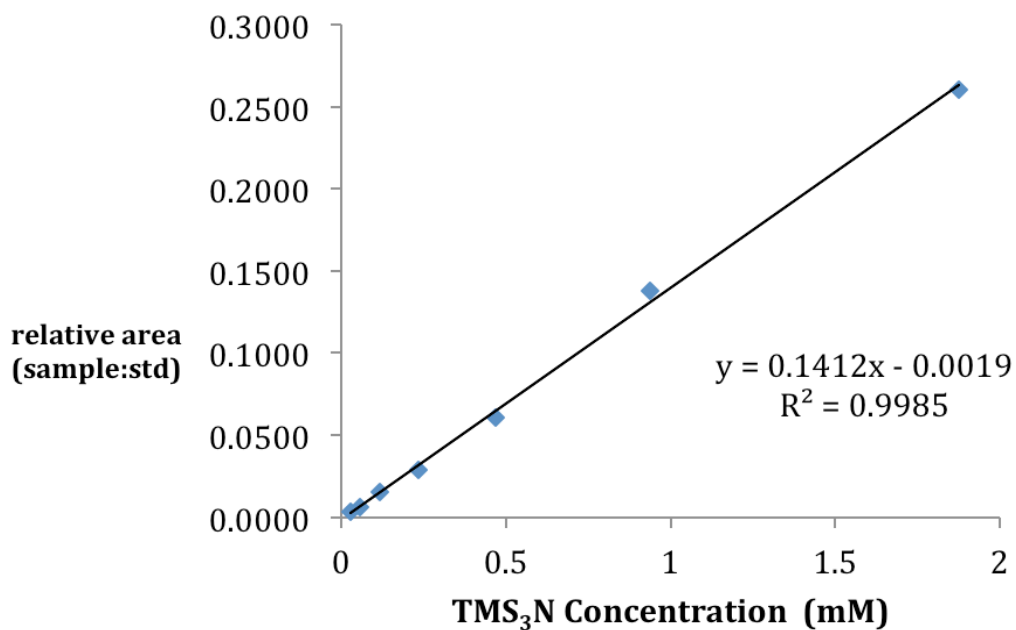


Figure A3.3.2: GC/MS calibration curve of N(SiMe₃)₃ using 9-fluorenone as the internal standard.

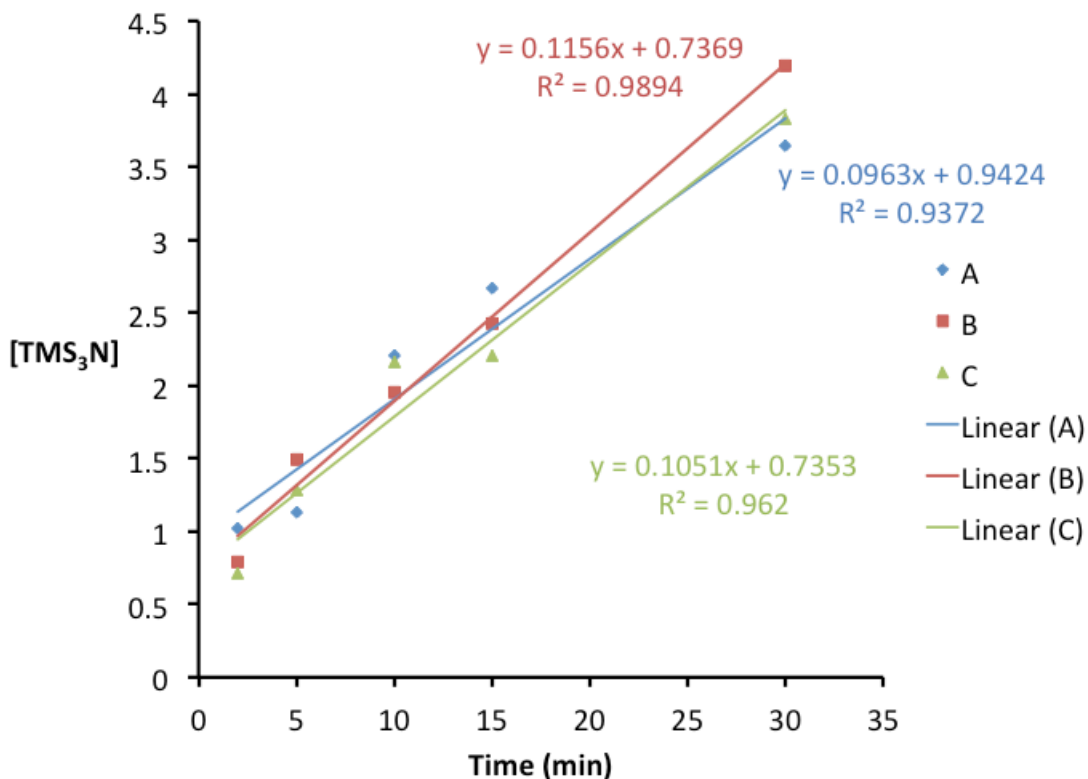


Figure A3.3.3: Triplicate indophenol analysis of $[N(TMS)_3]$ (mM) vs time with $[1]=0.13$ mM. Standard deviation of the slope was used to determine the experimental error of 0.009 mM/min.

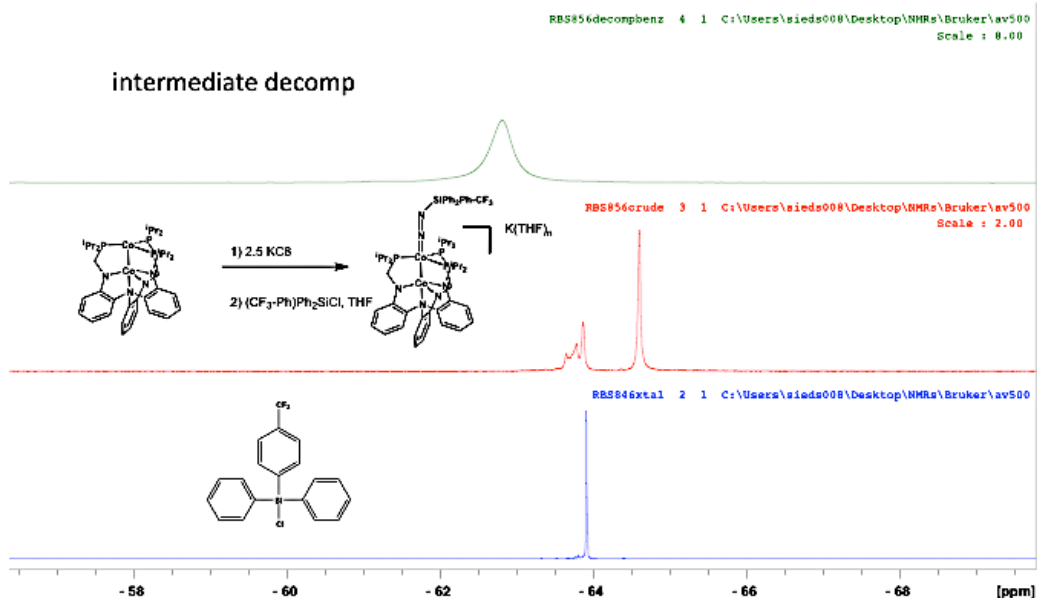


Figure A4.3.1: Stack plot of ^{19}F NMR Spectrum (d^8 -THF, 470 MHz) of ClSiPhAr (bottom), crude **1-SiPh₂Ar** (1.5 equiv ClSiPhAr) (middle) and **1-SiPh₂Ar** after 12 hr photolysis (top).

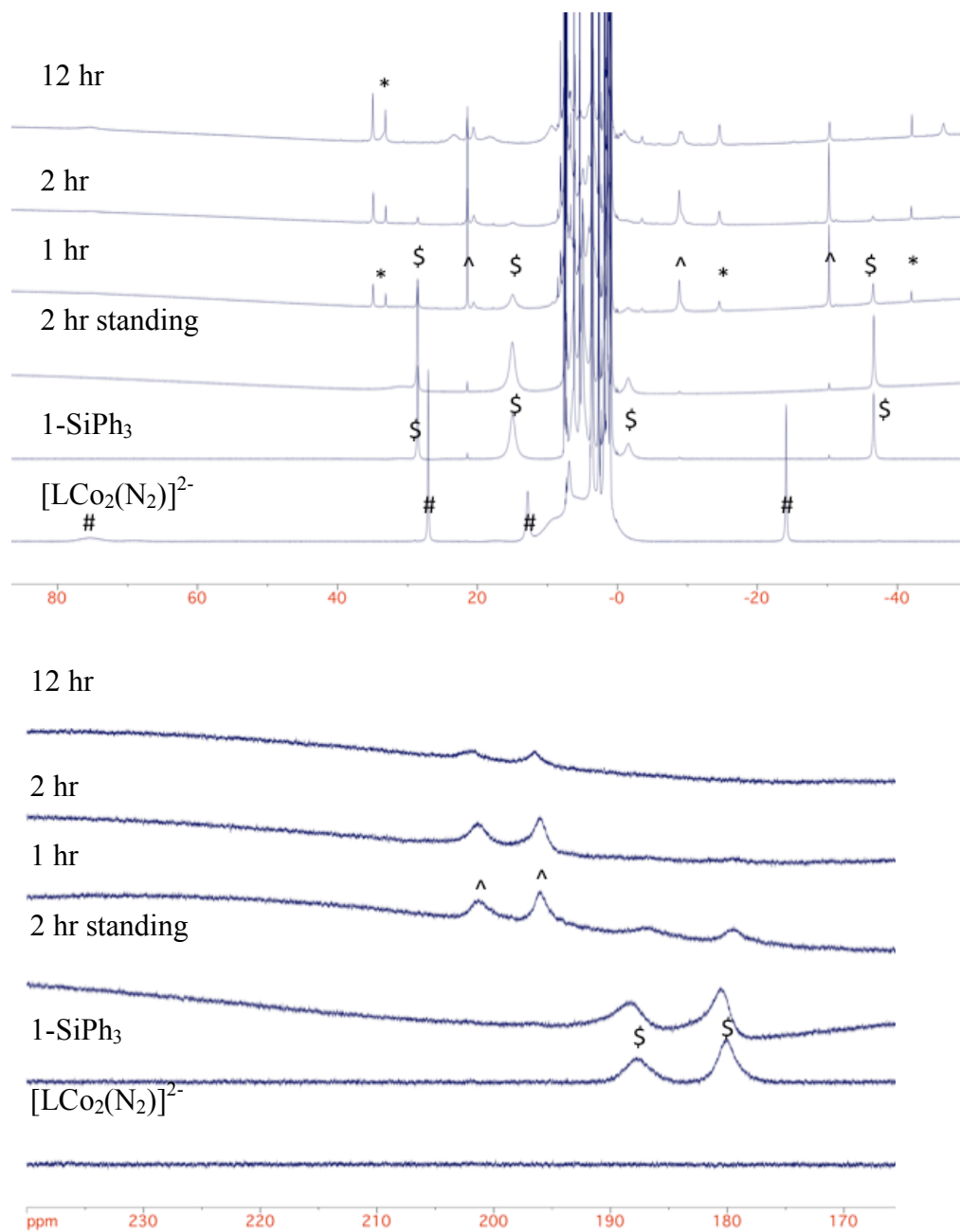


Figure A4.3.2 ^1H NMR (d^8 -THF, 500 MHz) for the photolysis of **1-SiPh₃**
 Top: Wide widow Bottom: Zoom between 240 – 150 ppm.

= $[\text{LCo}_2(\text{N}_2)]^{2-}$

\$ = 1-SiPh₃

^ = $[\text{LCo}_2(\text{N}_2)]^-$

* = unidentified species

